

# Performances of the EUSO mission with neutrinos and other primaries

**Dissertation**

der Mathematisch-Naturwissenschaftlichen Fakultät  
der Eberhard Karls Universität Tübingen  
zur Erlangung des Grades eines  
Doktors der Naturwissenschaften  
(Dr. rer. nat.)

vorgelegt von  
Ms. Sc. Alejandro Daniel Guzmán Cabrera  
aus Ciudad de México (México)

Tübingen  
2015

Gedruckt mit Genehmigung der Mathematisch-Naturwissenschaftlichen Fakultät der Eberhard Karls Universität Tübingen.

Tag der mündlichen Qualifikation:

20. Oktober 2015

Dekan:

Prof. Dr. Wolfgang Rosenstiel

1. Berichterstatter:

Prof. Dr. Andrea Santangelo

2. Berichterstatter:

Prof. Dr. Gustavo Adolfo Medina-Tanco





---

# ZUSAMMENFASSUNG

---

Seit ihrer Entdeckung am Anfang des zwanzigsten Jahrhunderts diente die kosmische Strahlung als ergiebige Quelle für das Wissen der Teilchenphysik. Vor dem Aufkommen der modernen Ära der Beschleuniger, stellte die kosmische Strahlung den Experimentalphysiker ein „Beobachtungsfenster“ zu Energien dar, die weitaus höher waren als was im Labor erreicht werden konnte.

Hundert Jahre später, und trotz enormer Fortschritte im Verständnis der Teilchenphysik und der modernen Beschleunigern, ist unsere aktuelle Technologie immer noch unfähig Teilchen, mit den höchsten in der kosmischen Strahlung beobachteten Energien, zu produzieren. Die höchstenergetischen Teilchen die jemals aufgenommen wurden, übertreffen Energien von  $5 \times 10^{19}$  eV und stellen die extrem energetische kosmische Strahlung (EECR nach *Extreme Energy Cosmic Rays*) dar.

Das Studium der EECR ist das Ziel des Extremen Universum Weltraum Observatoriums an Bord des japanischen Versuchsmodul JEM-EUSO (Extreme Universe Space Observatory on board the Japanese Experimental Module). Das Hauptziel dieses weltraumgestützten Observatoriums ist die Entdeckung und Analyse der Quelle(n) von EECR. Der eher winzige Fluss von EECR Teilchen erfordert ein riesiges Beobachtungsgebiet. Um die Statistiken zu erhöhen, muss das beobachtete Gebiet, das derzeitige Observatorien beobachten, vergrößert werden. Die kann nur durch die Überwachung der Erdatmosphäre vom Weltraum aus erreicht werden.

In dieser Arbeit präsentiere ich Simulationsstudien für die JEM-EUSO Mission in verschiedenen Konfigurationen. Innerhalb des EUSO's Simulation und Analyse Gerüsts ESAF, entwickelte ich zuerst eine Technik (mit dem dazugehörigen Modul) um den Hintergrund vom Signal zu trennen und somit eine bessere Mustererkennung zu erzielen. Dieses Werkzeug ist eine Voraussetzung für eine hochleistungsfähige Winkel- und Energierekonstruktion. Ich erforschte die Leistung der Mission für die Winkel- und Energierekonstruktion von Protonen, Eisenkerne und Photonen als Primärteilchen, welche ausgedehnte Schauer in der Atmosphäre erzeugen. Darüber hinaus habe ich eine sorgfältige Studie über die Leistungsfähigkeit des Detektors für Neutrino-induzierte EAS durchgeführt und erhielt damit zum allerersten Mal die Belichtungszeiten der Mission für die Beobachtung von Neutrinos. Schließlich stellte ich eine Reihe von statistischen Tests vor, die für die experimentellen Daten des Vorgängers des JEM-EUSO Experiments angewandt wurden: den EUSO-Ballon.

# ABSTRACT

---

Since their discovery in the early twentieth century, Cosmic Rays (CR) have been a fruitful source of knowledge for particle physics. Before the advent of the modern area of accelerators, CRs provided experimentalists with an “observational window” to energies beyond what was attainable in the laboratory.

A hundred years afterwards, despite enormous advances in the understanding of particle physics thanks to sophisticated accelerators, our current technology is incapable of experimentally studying particles with the energies observed in the most energetic CR events. These particles are the highest energetic particles ever recorded, with energies exceeding  $5 \times 10^{19}$  eV. They constitute the Extreme Energy Cosmic Rays (EECR)

The study of EECRs is the aim of the JEM-EUSO mission, the Extreme Universe Space Observatory on board the Japanese Experimental Module. The discovery and analysis of the source(s) of EECR is the main objective of this space borne observatory. The rather low flux of EECR particles requires in fact an enormous observation area. To increase statistics we are obliged to enlarge the observed area that current observatories are monitoring. This can only be achieved by monitoring from space the Earth’s atmosphere.

In this thesis I present simulation studies of the JEM-EUSO mission in various configurations. The key goal is the study of the expected performance of the mission. Within the EUSO Simulation and Analysis Framework ESAF, I first developed a technique (and the corresponding module) to separate background from signal, improving pattern recognition. This tool is a precondition for a highly performant angular and energy reconstruction. Second, I developed a module that allows the usage of a hybrid extensive air shower (EAS) generator (CONEX) to provide the capability of studying different primaries. I have explored the performance of the mission for the angular and energy reconstruction of protons, iron nuclei and photon primaries, inducing extended showers in the atmosphere. In addition I have conducted a careful study of the performance of the detector for neutrino induced EAS, obtaining for the first time ever exposures of the mission for observations of neutrinos. Finally, I have introduced a set of statistical tests to be applied to the experimental data of the precursor of the JEM-EUSO experiment: the EUSO-Balloon.

# CONTENTS

---

|  |           |
|--|-----------|
| Zusammenfassung & Abstract                                   | i         |
| <b>1 Introduction</b>  | <b>1</b>  |
| 1.1 Cosmic rays and the extreme universe                     | 3         |
| 1.1.1 The origins of cosmic ray science                      | 3         |
| 1.1.2 The particle channel for astronomy                     | 7         |
| 1.1.3 The highest end of the cosmic ray spectrum             | 11        |
| 1.1.4 The physics of extended air showers                    | 13        |
| 1.2 Extreme Energy Neutrinos                                 | 15        |
| 1.2.1 The neutrino in the Standard Model of particle physics | 15        |
| 1.2.2 Astrophysical neutrinos                                | 18        |
| 1.2.3 UHE- $\nu$ detection from space                        | 22        |
| 1.3 State of the art of the experimental aspects             | 23        |
| 1.3.1 The Pierre Auger Observatory                           | 23        |
| 1.3.2 Telescope Array  | 24        |
| 1.3.3 Comparison between PAO and TA results                  | 26        |
| 1.3.4 IceCube  | 29        |
| <b>2 The Extreme Universe Space Observatory</b>              | <b>31</b> |
| 2.1 Space approach to EECR: the EUSO concept                 | 33        |
| 2.1.1 Overview   | 33        |
| 2.1.2 Scientific potential                                   | 35        |
| 2.2 The JEM-EUSO mission                                     | 38        |
| 2.2.1 Scientific Objectives and Requirements.                | 39        |
| 2.2.2 Optics and Focal Surface subsystems                    | 40        |
| 2.2.3 Atmospheric Monitoring subsystem                       | 45        |
| 2.3 The EUSO pathfinders                                     | 47        |
| 2.3.1 EUSO-Ballon  | 47        |
| 2.3.2 Mini-EUSO  | 48        |
| 2.4 Other EUSO like missions                                 | 49        |
| 2.4.1 SpaceX EUSO  | 50        |
| 2.4.2 K-EUSO   | 52        |
| <b>3 Simulating the EUSO mission</b>                         | <b>55</b> |
| 3.1 The EUSO Simulation and Analysis Framework               | 57        |
| 3.2 The simulation chain: <i>Simu</i>                        | 58        |
| 3.2.1 Light To Euso  | 59        |
| 3.2.2 Detector simulation                                    | 60        |
| 3.3 The reconstruction chain: <i>Reco</i>                    | 63        |
| 3.3.1 Pattern recognition                                    | 64        |
| 3.3.2 Angular Reconstruction                                 | 65        |
| 3.3.3 Energy Reconstruction                                  | 72        |
| <b>4 Space observation of EECR: expected performances</b>    | <b>75</b> |

|          |   |            |
|----------|---|------------|
| 4.1      | Main contributions to ESAF . . . . .                                      | 77         |
| 4.1.1    | Pattern recognition: the <i>PWISE</i> technique . . . . .                 | 77         |
| 4.1.2    | Pattern recognition: the <i>PWISE-R</i> technique . . . . .               | 81         |
| 4.1.3    | The CONEX - ESAF interface . . . . .                                      | 83         |
| 4.1.4    | Configuration of the CONEX-ESAF interface . . . . .                       | 92         |
| 4.2      | Angular reconstruction . . . . .  | 94         |
| 4.2.1    | Simulation sets . . . . .   | 94         |
| 4.2.2    | Summary of angular reconstruction for proton primaries . . . . .          | 96         |
| 4.2.3    | Angular reconstruction for Fe and Proton primaries . . . . .              | 97         |
| 4.2.4    | Angular reconstruction for EE- $\gamma$ primaries . . . . .               | 99         |
| 4.2.5    | Quality cuts . . . . .  | 101        |
| 4.3      | Energy and $X_{max}$ Reconstruction studies . . . . .                     | 104        |
| 4.3.1    | Energy reconstruction for protons, iron nuclei, and photons . . . . .     | 104        |
| 4.3.2    | $X_{max}$ reconstruction for protons, iron nuclei, and photons . . . . .  | 107        |
| <b>5</b> | <b>Space observation of Extremely Energetic Neutrinos</b>                 | <b>111</b> |
| 5.1      | Concepts and definitions . . . . .  | 113        |
| 5.1.1    | Constant flux . . . . .   | 118        |
| 5.1.2    | Power law flux . . . . .  | 120        |
| 5.2      | The neutrino sensitivity as a scaling of the baryon sensitivity . . . . . | 121        |
| 5.2.1    | Tilting . . . . .   | 126        |
| 5.3      | The neutrino exposure . . . . .   | 127        |
| 5.4      | Reconstrucion of EAS induced by a EE- $\nu$ . . . . .                     | 132        |
| 5.4.1    | Angular reconstruction . . . . .  | 132        |
| 5.4.2    | Energy and longitudinal profile reconstruction . . . . .                  | 133        |
| <b>6</b> | <b>Pathfinder simulations and analysis</b>                                | <b>137</b> |
| 6.1      | Statistical analysis of the EUSO-Balloon optics . . . . .                 | 139        |
| 6.1.1    | Definitions . . . . .   | 141        |
| 6.2      | Analysis of selected simulated scenarios . . . . .                        | 143        |
| <b>7</b> | <b>Summary &amp; Outlook</b>  | <b>151</b> |
|          | <b>Appendix</b>   | <b>153</b> |
|          | List of Key Publications . . . . .  | 153        |
|          | Extended list of Publications . . . . .                                   | 154        |
|          | <b>List of Figures</b>  | <b>167</b> |

# INTRODUCTION

---

## Contents

---

|         |  |    |
|---------|--|----|
| 1.1     | Cosmic rays and the extreme universe . . . . .                   | 3  |
| 1.1.1   | The origins of cosmic ray science . . . . .                      | 3  |
| 1.1.2   | The particle channel for astronomy . . . . .                     | 7  |
| 1.1.3   | The highest end of the cosmic ray spectrum . . . . .             | 11 |
| 1.1.3.1 | The Greisen–Zatsepin–Kuzmin mechanism . . . . .                  | 12 |
| 1.1.4   | The physics of extended air showers . . . . .                    | 13 |
| 1.2     | Extreme Energy Neutrinos . . . . .                               | 15 |
| 1.2.1   | The neutrino in the Standard Model of particle physics . . . . . | 15 |
| 1.2.2   | Astrophysical neutrinos . . . . .                                | 18 |
| 1.2.3   | UHE- $\nu$ detection from space . . . . .                        | 22 |
| 1.3     | State of the art of the experimental aspects . . . . .           | 23 |
| 1.3.1   | The Pierre Auger Observatory . . . . .                           | 23 |
| 1.3.2   | Telescope Array . . . . .  | 24 |
| 1.3.3   | Comparison between PAO and TA results . . . . .                  | 26 |
| 1.3.4   | IceCube . . . . .  | 29 |

---



This chapter is devoted to summarize the history and current status of the on-going research of Ultra High Energy Cosmic Rays (UHECR) and Extreme Energy Cosmic Rays (EECR). We begin with a brief historical recapitulation in section 1.1.1. This recap is, by necessity, not thorough and incomplete. Its sole purpose is to bring into historical context the scientific field where the current work is inserted.

## 1.1 Cosmic rays and the extreme universe

### 1.1.1 The origins of cosmic ray science

Cosmic ray research was born at the beginning of the XX century, almost a century after William Herschel's discovery of infrared light and Johann Wilhelm Ritter's discovery of ultra violet light [Herschel 1800] [Ritter 1803]. These invisible forms of radiation were called caloric and chemical rays respectively. The latter being part of what would be known as ionizing radiation. Even though Charles-Augustin de Coulomb realized that electroscopes would naturally discharge in 1785 [Coulomb 1785], it was until Henri Becquerel researched on ionizing radiation that the systematic study of the field truly began in the year 1896 [Becquerel 1896]. A couple of years afterwards, Marie Curie had the vision to study this phenomenon using electroscopes to quantify the discharge rate [Curie 1898].

In these first years, the origin of this penetrating radiation was commonly attributed solely to radioactive material. This radioactive material was believed to reside in the upper layers of the Earth's crust. However, it was observed that even shielded or very well insulated electroscopes would discharge. Studies measuring the discharge rate of electroscopes in different conditions seemed to confirm the hypothesis that this ionizing radiation was indeed of terrestrial origin [Curie 1898].

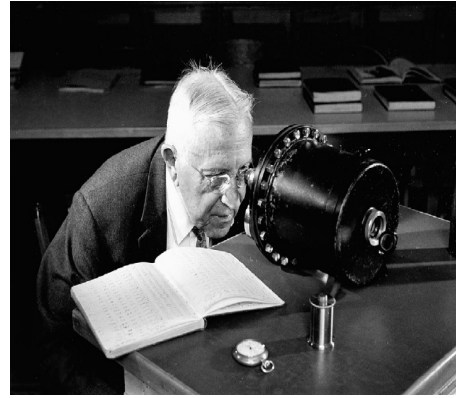
This hypothesis was challenged by the results of the experiments carried out by Theodor Wulf on top of the Eiffel tower [Wulf 1909]. Wulf observed that, although there was a reduction on the ionization rate, the reduction rate was not as high as expected. If the source of this penetrating radiation was of terrestrial origin this reduction should have been higher.

The pioneering work in what is now called cosmic ray research was done almost simultaneously by Viktor Franz Hess and Domenico Pacini [Hess 1912] [Pacini 1912]. Although both researchers worked simultaneously, commonly only credit is given to the former.

Pacini developed a technique to perform his measurements under water. He compared measurements done offshore on a vessel and on the ground. In these measurements, Pacini reported comparable results of the discharge rate. Thus, the immediate surface seemed to have no impact on the amount of ionizing radiation. He concluded that the main source for the penetrating radiation had no relationship with the immediate layer of the Earth's surface [Pacini 1912]. Nevertheless,



(a) Pacini making a measurement. Reproduced from [Angelis 2014].



(b) Hess with a Wulf electroscope. Modified from [Schuster 2014].

Figure 1.1

this assertion did not conclusively prove the extraterrestrial origin of this radiation. It could still be argued that an unknown process within the Earth's atmosphere could be the source.

One year later Hess's balloon experiments finally showed the behavior of the ionization rate as a function of the altitude [Hess 1912]. During the first kilometer of ascension the ionization rate decreased, in accordance with the hypothesis that the main source of radiation were substances encrusted in the Earth's surface. However, roughly after 1 km altitude the ionization losses started to rise again to levels even higher than the ones at surface height.

These experiments are commonly regarded as the discovery or, more precisely, the confirmation of the extraterrestrial origin of the pervading ionizing radiation present in the atmosphere.

Nevertheless, research carried out by Robert Andrews Millikan after the first world war in the US, challenged this conclusion [Millikan 1925]. The nature of this ionizing radiation was still far from settled. Was it pure electromagnetic radiation or was it particle radiation?

It was until 1927 when Jacob Clay settled the issue with experiments performed during a sea voyage from Java to the Netherlands [Clay 1927]. His measurements demonstrated that the ionization rate depended on the geomagnetic latitude. This was the key evidence to support the charged particle nature of cosmic rays. Another evidence to support this argument was the "East-West" effect. If the particles are mostly positively (negatively) charged there will be an increase (decrease) in the detected particles coming from the West compared to the ones coming from the East. An experimental setup and some calculations for these measurements were first proposed in 1930 by Bruno Benedetto Rossi [Rossi 1930], and carried out later by Thomas H. Johnson, Luis Alvarez, and Arthur H. Compton in Mexico City [Alvarez & Compton 1933] [Johnson 1933]. Rossi himself performed his own measurements in Asmara, Eritrea [Rossi 1933].

The invention of the Geiger-Müller detector in 1928 and the coincidence circuits designed by Rossi [Rossi 1930a] led, among many other scientific achievements, to the discovery of Extensive Air Shower (EAS). Rossi observed an increase in the coincidence rate when he introduced some shielding in front of his detectors. This increase would eventually die out when enough shielding material was placed on top of the detectors. Rossi correctly understood that the increase in coincidence rate, came from the interaction of the cosmic rays with the shielding material.

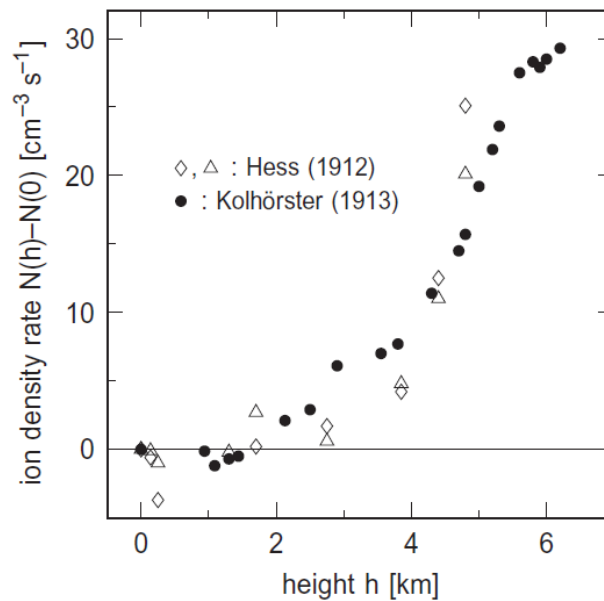


**Figure 1.2:** Ionizing radiation measurements by Kohlhörster and Hess. Reproduced from [Hoffmann 2014].

Pierre Auger and his measurements done in Jungfraujoch demonstrated what Rossi had already anticipated in 1933 with his improved coincidence electronics: that the particles arriving in coincidence come from the same originating event [Auger 1939]. Auger also calculated the energy of the primary particle by summing up the assumed energy of all particles involved in a coincidental detection. His result was astonishing:

*“One of the consequences of the extension of the energy spectrum of cosmic rays up to  $10^{15}$  eV is that it is actually impossible to imagine a single process able to give a particle such an energy [...] (they) acquire their energy along electric fields of great extension.”*  
[Auger 1939]

Throughout the coming decades multitude of researchers conducted experiments in this field in parallel with researchers in particle physics. Let us remember that both fields have common origins, and that some of the first breakthroughs in particle physics came from cosmic ray experiments at the dawn of the era of particle accelerators. The discovery of the positron [Anderson 1933], the muon [Anderson & Neddermeyer 1937] and the pion [Lattes 1947] are a few of the most important examples of this mutual development.

In 1949 Enrico Fermi postulated moving irregularities in the magnetic field of interstellar media as plausible acceleration sites for CR [Fermi 1949]. The basic concept is the interaction of a particle with an interstellar-medium “cloud” which posses a turbulent magnetic field. In this process the energy gain is proportional to the square of the speed of the magnetic cloud divided by the square of the speed of light ( $\beta_{cl}^2$ ). This mechanism however would take too long to accelerate since the energy gain is relatively slow [Stanev 2010]. Nevertheless this idea was the seed concept for shock acceleration, or acceleration at astrophysical shocks [Blandford & Ostriker 1978]. SNRs expansion into the interstellar medium is commonly taken as an example of this type of shocks. The magnitude of the expansion velocity of the SNR is much bigger than the speed of sound in

the medium. In this case the energy gain is taken to increase linearly with  $\beta_{shock}$  [Stanev 2010]. Research in this promising type of acceleration mechanism is still being developed nowadays [Caprioli & Spitkovsky 2014a] [Caprioli & Spitkovsky 2014b] [Caprioli & Spitkovsky 2014c].

With the advent of plastics scintillators, techniques for reconstructing the arrival direction and energy of the primary were developed in the 1950-1960 [Rossi 1959]. By that time already plastic scintillators had superseded Geiger counters for detecting cosmic ray showers. At the beginning of the 1960's, the concept of plastic scintillator arrays was implemented at the "Volcano Ranch" experiment [Linsley 1963]. Benefiting from the precision of this technique, the CR spectrum was measured. It was established that it extended over several orders of magnitude (see Fig. 1.4) following a roughly-featureless power law.

Another milestone that occurred in the sixties was the introduction of the fluorescence technique [Bunner 1967]. The basic idea is to detect the UV photons emitted by the shower front as it transverses the atmosphere. For this purpose an array of UV telescopes was deployed to monitor the clear dark night sky. This was achieved some 10 years later also at Volcano Ranch [Mason et al. 1977].

In 1964 Arno Allan Penzias and Robert Woodrow Wilson discovered the Cosmic Microwave Background [Wilson 1978]. Though perhaps not directly related to the field, this discovery led to the theoretical prediction of a shortening in the propagation lengths for cosmic rays with energies  $\sim 3 \times 10^{19}$  eV [Greisen 1966] [Zatsepin & Kuz'min 1966].

In 1981 the fluorescent technique detector "Fly's Eye" began operation. It was in this experiment that the highest ever particle energy for a CR particle was measured. On October 15<sup>th</sup> 1991 a CR with an energy of  $3.1 \times 10^{20}$  eV was measured [Bird et al. 1995]. In 1993 the experiment was updated and became "HiRes Fly's Eye" for High Resolution Fly's Eye.

Also in the 1990s the Akeno Giant Shower Array (AGASA) was brought into operation. Surprisingly, the AGASA experiment did not see the predicted GZK cutoff which HiRes was reporting to have seen [Yoshida et al. 1995] [HiRes 2011]. This discrepancy fueled the design of bigger observatories which are operating now. We will come back to this point in section §1.3.

In its early stages, cosmic ray research was just tangentially related to astronomy, even at the highest energies. The biggest connection with astronomy was the solar modulation of the cosmic rays. With the advances both in astronomy and particle physics, independent and related, the potential of cosmic rays as astronomical observational tools has slowly flourished. It is now a experimentally established a fact a the highest energy component of cosmic radiation is of astrophysical origin. In particular this high energy component is taken to be the beginning of the particle channel for astronomy, in contrast with thousands of years of relying only in the visible part of the electromagnetic spectrum.

### 1.1.2 The particle channel for astronomy

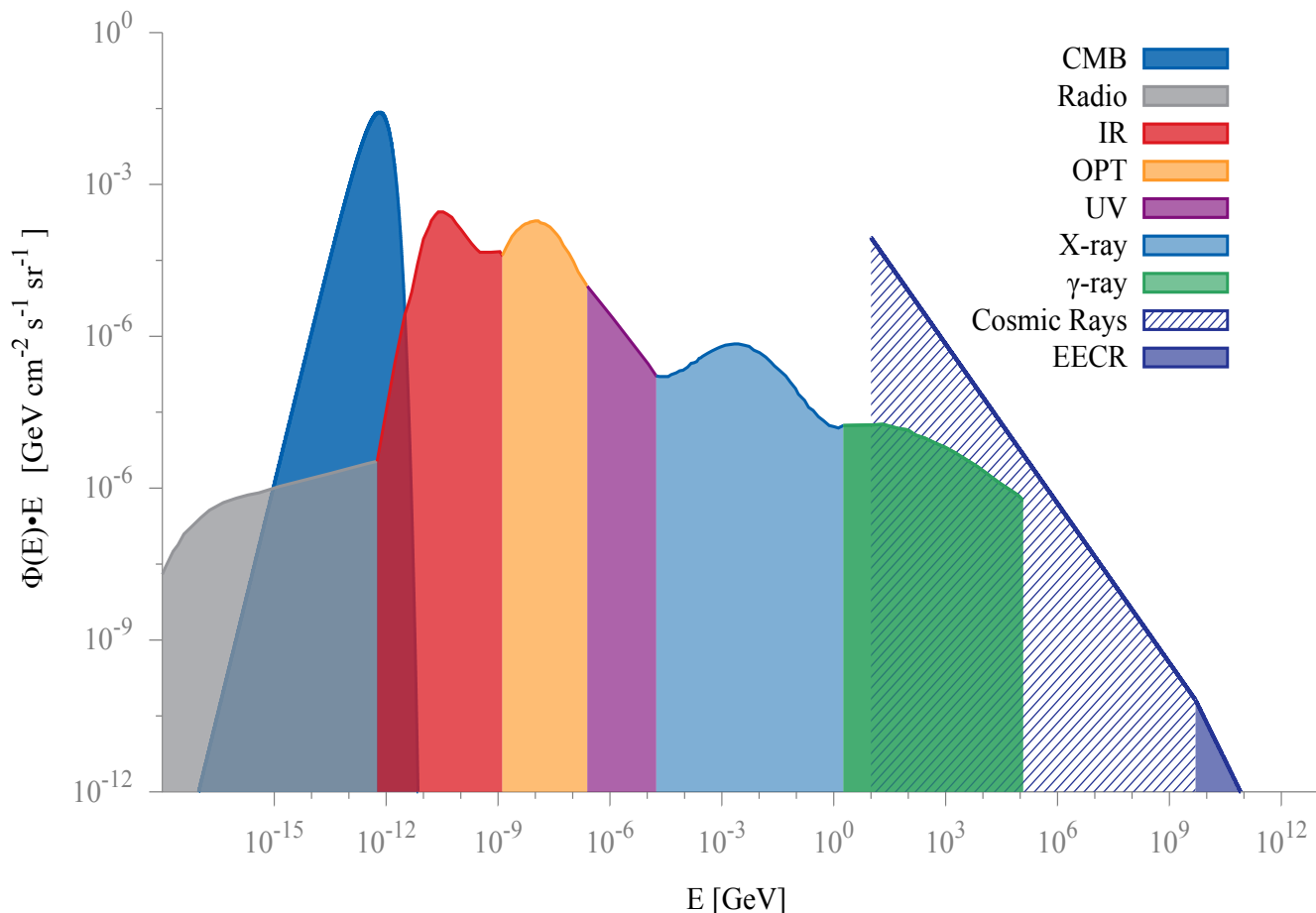


**Figure 1.3:** The particle channel in astronomy. The filled curves represent the different components of the diffuse background spectrum of electromagnetic radiation [Bethérmin 2011]. For comparison the flux of cosmic rays is also plotted. The Extreme Energy Cosmic Rays regime begins at the smallest shaded region, i.e. at energies above 50 EeV ( $5 \times 10^{19}$  eV). Figure modified from [Bethérmin 2011].

The amount of relativistic particles arriving at the Earth's surface per solid angle, per unit area, per unit time, per energy bin is called the cosmic ray spectrum, or differential cosmic ray flux ( $\Phi_{C.R.}$ ). The spectrum as a function of the energy follows a broken power law of the form  $\Phi_{C.R.} \propto E^{-\alpha}$ . The differential flux decreases as the spectral index changes from  $\alpha = 2.7$  to  $\alpha = 3.1$  at energies around 1 PeV (see Fig. 1.4). This feature is called the knee. The main candidate sources for cosmic rays with energies up to the knee and even beyond it, are commonly assumed to be supernovae remnants (SNRs) within the Milky Way. Further candidates within the Galaxy include pulsars and high mass binary systems, where at least one of the partners is a neutron star or even a black hole. Pulsars are taken to be strong candidates because of their extremely intense magnetic fields. In binary systems with a neutron star as one of the partners, the acceleration would take place in the relativistic radio jets around the neutron star (or even black hole).

Coming back to the SNR scenario, in this case the acceleration takes place in the shock fronts of

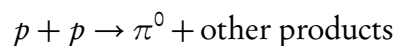
the supernova explosions as they expand in the interstellar medium. Stochastic scattering across the shock front increase the energy of the particle. The spectrum that results from this process, called the first-order Fermi Mechanism [Stanev 2010], follows roughly a power law of the type  $E^{-2}$ . We see that the Galactic energy budget indeed supports, though circumstantially, the claim that SNRs are the main sources for the galactic cosmic rays. The argument goes as follows: the cosmic ray energy density ( $\rho_{CR}$ ) is given by:

$$\rho_{CR} = L \cdot \frac{t_{cont}}{V} \quad (1.1)$$

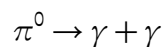
Where  $L$  is the power required to sustain such energy density for a containment time  $t_{cont}$  inside a volume  $V$ .

The average galactic confinement time for particles with energies around GeV is  $15 \pm 1.6$  Mega years [Yanasak et al. 2001] [Blümer, Engel & Hörandel 2009]. Taking  $t_{cont} \approx 10^7$  years as the average containment time of galactic cosmic rays,  $V \approx 10^{67} \text{ cm}^3$  as the volume of Galaxy, and  $L \approx 10^{41} \frac{\text{erg}}{\text{s}}$ , we arrive at  $\rho_{C.R.} \approx 10^{-12} \frac{\text{erg}}{\text{cm}^3} \approx 1 \frac{\text{eV}}{\text{cm}^3}$ . This last values is the observed cosmic ray energy density. The value chosen for  $L$  corresponds to 10% of the average released energy of galactic supernovae over periods for 20-50 years [Katz & Spiering 2012].

This argument is strengthened by a measurement of a diffuse component coming from the galactic disc of TeV photon by the HESS collaboration [H.E.S.S 2014]. On top of that, observations carried out by NASA's Large Area Telescope (LAT), onboard the Fermi Gamma-ray Space Telescope appear to be in agreement with the above reasoning [Ackermann et al. 2013]. Fermi-LAT observed a spectral cutoff in the gamma ray spectrum in supernova remnants IC 433 and W44, which is consistent with neutral pions decaying into gamma rays. The existence of neutral pions at the SNRs is another argument for acceleration of protons occurring at this sites. The argument is as follows: accelerated protons or nuclei encounter interstellar material and produce gamma rays via:



and then:



where the combined energy of the gamma rays in the frame of reference of the neutral pion is  $2 \times \frac{m_{\pi^0}}{c^2} = 135 \frac{\text{MeV}}{c^2}$ . However, the simple observation gamma rays of such energies is not enough evidence for cosmic ray acceleration: high-energy electrons can also produce gamma rays via bremsstrahlung and inverse Compton scattering.

In the process just described above, the  $\pi_0$  spectrum rises steeply below  $\sim 200$  MeV. This characteristic spectral feature identifies gamma rays produced by neutral pion decays, and thereby high-energy protons. Such a feature is not expected in case the gamma rays are produced by high energy electrons. The observations carried out with the Fermi-LAT have seen for the first time such a spectral feature [Ackermann et al. 2013]. We will come back to this process when we talk about neutrino production in astrophysical sources.

At energies between  $10^{17}$  and  $10^{18.5}$  eV the galactic sources run out of power and the extragalactic

sources start dominating [Blümer, Engel & Hörandel 2009]. The precise energy where this transition occurs is still a matter of debate. Even if galactic sources had enough power to accelerate particles to energies exceeding  $10^{18.5}$  eV, these particles would escape right away the Galaxy since their gyro radius is bigger than the size of the Galaxy. It is around this energy ( $10^{18.5}$  eV) that the cosmic ray spectrum index goes back again to  $\alpha = 2.7$ . This feature is known as the “ankle”. For particles exceeding  $10^{18.5}$  eV, which are so called ultra high energy cosmic rays (UHECR), the candidates sources are commonly assumed to be extragalactic. The mains candidates for particle acceleration beyond  $10^{19}$  eV are Active Galactic Nuclei (AGN), Gamma Ray Bursts and starburst galaxies. These objects have the necessary energy budget to accelerate protons to a maximum energy between  $10^{20}$  and  $10^{21}$  eV. In a similar fashion as we discussed for SNRs, the power observed from these sources is enough to reproduce the observed energy density for UHECR. The observed energy density integrated from the ankle till a flux suppression around the GZK cutoff (see section § 1.1.3.1) is  $\sim 10^{-7} \frac{\text{eV}}{\text{cm}^3} \approx 3 \times 10^{-19} \frac{\text{erg}}{\text{cm}^3}$ . This energy density, once normalized to the abundance of AGN, requires a power  $\sim 2 \times 10^{44} \frac{\text{erg}}{\text{s}}$  per AGN [Gaisser 1997]. The latter figure is consistent with the power measured from AGNs.

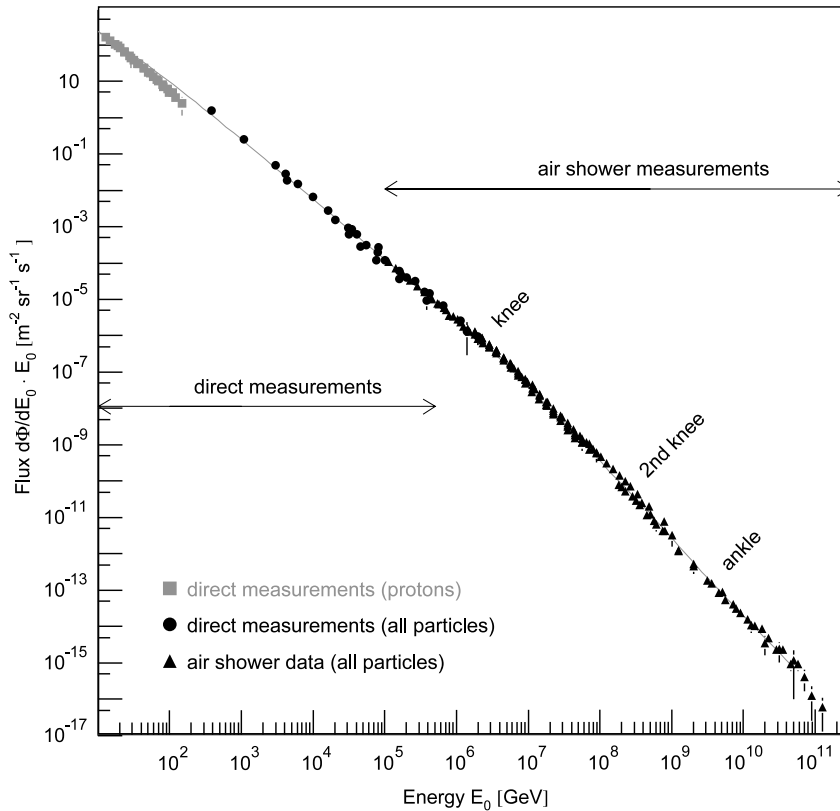
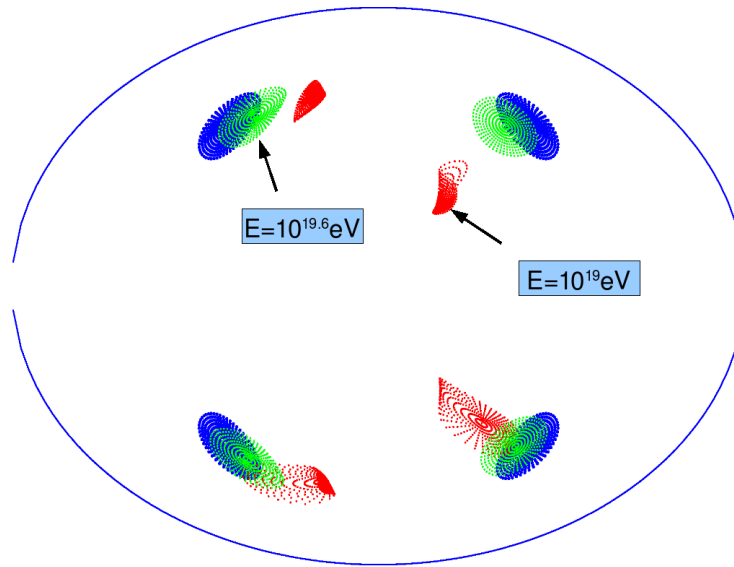


Figure 1.4: The energy spectrum of cosmic rays. Reproduced from [Blümer et al. 2009].

Charged particles are deflected during their propagation from the source to Earth by galactic and extragalactic magnetic fields [Medina-Tanco 2005]. For proton CR primaries at energies  $E < 10^{19}$  eV the arrival direction information is almost independent on the direction of its source, spread out into areas of the sky of tenths of degrees in size [Guzmán 2009] [Rouillé d’Orfeuil et al. 2014]. This also holds for heavier, and hence higher  $Z$ , particles. The deflector is the plethora of intervening magnetic fields. Extra galactic magnetic fields area expected to have intensities around

nG, though many of their properties remain largely unknown [Ryu et al. 1998] [Sig et al. 2004]. On the other hand, galactic magnetic fields are better understood and different models have been put forward to match observations (e.g. polarization of starlight and synchrotron emission) [Han 2001] [Jansso & Farrar 2012]. The interactions with these turbulent and/or not completely understood magnetic fields, make it almost impossible to reconstruct the propagation path of CR for low energies [Guzmán 2009] [Medina-Tanco 2005].

As the energy increases the propagation of the CR becomes less and less affected by magnetic fields. At the energies of the so called Extreme Energy Cosmic Rays (EECR), i.e. above  $\approx 50$  EeV ( $5 \times 10^{19}$  eV), the propagation follows already a semi-ballistic trajectory. This effect is illustrated in Fig. 1.5. In this figure protons were injected at the galactic halo and propagated throughout a model [Han 2001] of the galactic magnetic field.



**Figure 1.5:** Deflection of charged particles (protons) in the galactic magnetic field. In blue is shown the un-deflected injection sites at the galactic halo. In red and green the arrival positions at  $\sim 10$  EeV and  $\sim 38$  EeV respectively [Guzmán 2009].

Fortunately enough, at energies exceeding  $10^{20}$  eV propagation through the galactic magnetic field is semi ballistic. Thus, the arrival direction of the EECR still points out to their potential source.

EECR sources are still to be discovered. However some candidates can already be elucidated by assuming Fermi-acceleration processes or even more exotic accelerating mechanisms. As long as the acceleration mechanism is of electromagnetic origin, we can constrain the accelerating region by the Larmor radius ( $R_L$ ) of an EECR. For a relativistic charged particle of charge  $Z$ , with velocity coefficient  $\beta = \frac{v}{c}$ , with an energy  $E$ , and in a region with field  $B$ ,  $R_L$  is given by:

$$R_L = \frac{E}{2c\beta ZeB}$$

where  $e$  is the electron charge and  $c$  is the speed of light in vacuum. Thus the upper limit on the

energy, is set by the size of the object ( $R_{object}$ ) where  $B$  is present:

$$R_L = R_{object} = \frac{E_{max}}{2c\beta ZeB} \implies E_{max} = 2c\beta ZeBR_{object} \quad (1.2)$$

This limit constrains accelerating sites, and does not require new physics to be postulated. This limit is shown in Fig. 1.6. This is called the Hillas diagram [Hillas 1984]. Candidate astrophysical objects according to their size and magnetic field, are plotted as well as the limit imposed by Eq. 1.2.

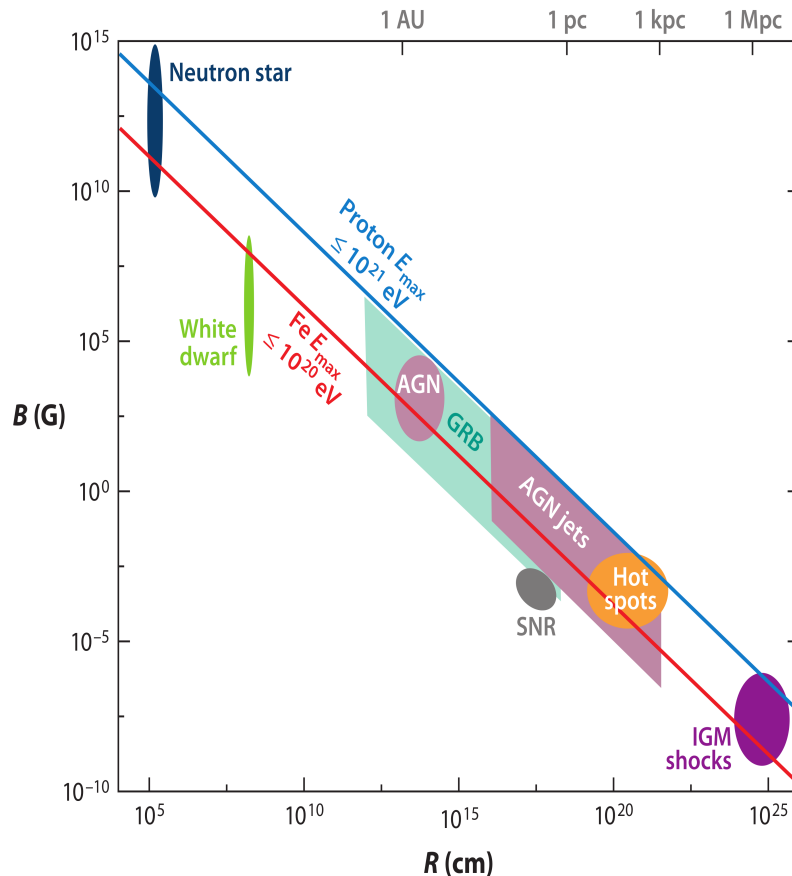


**Figure 1.6:** Hillas diagram. Objects above the lines are capable of trapping Fe with  $10^{20}$  eV (red), and protons with  $E = 10^{20}$  eV (blue). Reproduced from [Kotera & Olinto 2011].

### 1.1.3 The highest end of the cosmic ray spectrum

In Fig. 1.3 we explicitly compare the diffuse electromagnetic background (what we call the electromagnetic channel of astronomy) with the flux of cosmic rays. As it can be seen the flux of “particles” (photons) on the electromagnetic component dominates up to energies  $\sim 100$  MeV. For higher energies the flux is dominated by cosmic rays. However, as we just discussed, only at the highest energies CRs’ arrival direction can be used to infer their source. As it can be seen in Fig. 1.4, EECR have a flux of the order of an event per square kilometer per steradian per millennium.

These are the CRs that will allow us to open the *particle channel for astronomy*. We will discuss further the state of the art of the detection of EECR in section § 1.3. But first we will review the physics of EECR.

### 1.1.3.1 The Greisen–Zatsepin–Kuzmin mechanism

In his famous paper of 1966 Kenneth Greisen already speculated that the integrated number of events in the excess of energies  $2 \times 10^{20}$  eV should not be expected to exceed 1 event per hundred square kilometers in one year [Greisen 1966]. The culprit for this dramatic decrease in the number of events is the Cosmological Microwave Background (CMB). A similar conclusion was also brought forward by Vadim Kuzmin and Georgiy Zatsepin independently [Zatsepin & Kuz'min 1966].

As Greisen explains, regardless of the chemical composition of the primary the flux is expected to dramatically decrease in the decade between  $10^{20}$  eV and  $10^{21}$  eV (see Fig. 1.7). The fact that events with energies up to  $10^{20}$  eV have been observed, is already surprising. This would imply a flatter injection spectrum from extragalactic sources compared to galactic ones. This effect is called the Greisen–Zatsepin–Kuzmin (GZK) mechanism.

The GZK limit however, is an effect on propagation and it does not tell us anything about the power of the sources of the EECR.

At these energies, the principal phenomena responsible for the energy loss for protons, are pair production and photo-pion production, via the  $\Delta$  resonance ( $p + \gamma_{cmb} \rightarrow \Delta^+ \rightarrow \pi^+ + n$ ).

The energy thresholds for pion photo-production (proton interacting with a  $7 \times 10^{-4}$  eV CMB photon) is around  $10^{20}$  eV. The average cross section is  $200 \mu\text{b}$  and the CMB photon density is  $550 \frac{\text{photons}}{\text{cm}^3}$  [Greisen 1966]. This implies a mean free path,  $\ell$ , of:

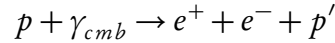
$$\ell = \frac{1}{\rho_{\gamma} \sigma_{\gamma p}} \sim 9 \times 10^{19} \text{km}$$

However, for each interaction there is a corresponding energy loss  $\Delta E$ . In average, in the energetic regime of interest the ratio of initial energy to energy loss is  $\frac{E}{\Delta E} \sim \frac{1}{0.22}$ . Therefore the relevant distance to the source  $\ell_{eff}$  is given by:

$$\ell_{eff} = \frac{E}{\Delta E} \ell \sim \left( \frac{1}{0.22} \right) (9 \times 10^{19}) \approx 4 \times 10^{20} \text{km}$$

In the case when the primary is a heavier atomic nucleus, the situation is slightly different. The main process for energy loss is photo disintegration of the nucleus. In this case the energy threshold is two orders of magnitude below, around  $5 \times 10^{18}$  eV per nucleon. To make matters worse, above 10 EeV most of the photons can excite a giant dipole resonance [Brueckner & Thieberg 1960]. This leads to a mean free path for photo-disintegration  $\sim 10^{17}$  km. The fact that the diameter of the Milky Way is  $\sim 10^{18}$  km, is another strong argument suggesting that the EECR sources

must reside outside of our galaxy. The other main process dominating the energetic losses is pair production, with an energy threshold per proton around  $10^{17}$  eV:



In this process the energy loss depends on the velocities of the  $e^+$ ,  $e^-$ , and the proton ( $p'$ ). Also the scale distance for the energy loss turns out to be the order of half the Hubble length ( $\sim 10^{22}$  km). Hence the energy losses are not so intense for this process as for the previously discussed. Thus, as Greisen showed, this effect (pair creation) decreases the flux by a factor not bigger than 3 in the energy interval  $10^{18} - 10^{20}$  eV [Greisen 1966].

Due to all these effects, the sources for EECR must reside in our cosmological neighborhood the so called GZK-sphere ( $z < 1$  or a radius of 100 Mpc). Powerful enough astrophysical sources are expected to follow the baryonic matter distribution. And this distribution is anisotropic at this scale, hence the flux at trans GZK energies is not expected to be isotropically diffuse.

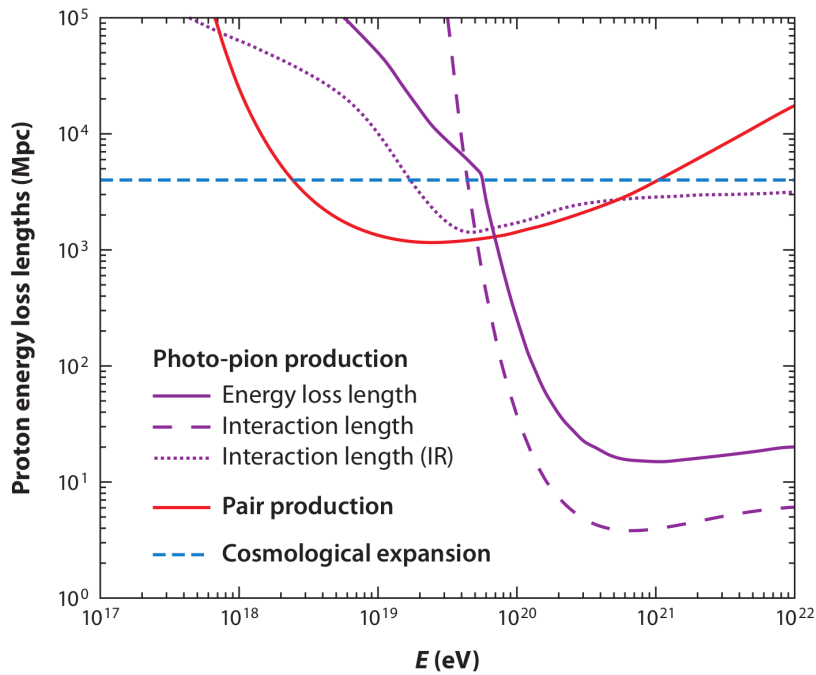
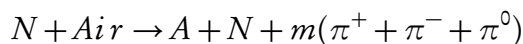


**Figure 1.7:** Proton energy loss for photo pion production (purple), pair production (red) and due to the cosmological expansion (blue). Reproduced from [Kotera & Olinto 2011].

#### 1.1.4 The physics of extended air showers

In this section we will sketch the physics of EAS. When the the primary ( $N$ ) is a nucleon, the EAS begins via an hadronic interaction:



Where  $N$  is any given nucleon (proton or neutron),  $A$  is an excited atmospheric nucleus, and  $m$  is the pion multiplicity. In case the primary was a part of a bigger nucleus a similar expression can be written, adding an excited state of the original nucleus to the right side of the process.

At the beginning of the shower development, the dominant energy loss mechanism is the creation of secondary particles (mostly mesons and baryons). Some of these secondary particles acquire a momentum component transversal to the primaries original direction, creating what is called the *lateral development of the EAS*. The amount of charged particles present at the EAS's front as function of atmospheric depth is called the *longitudinal profile of the EAS*.

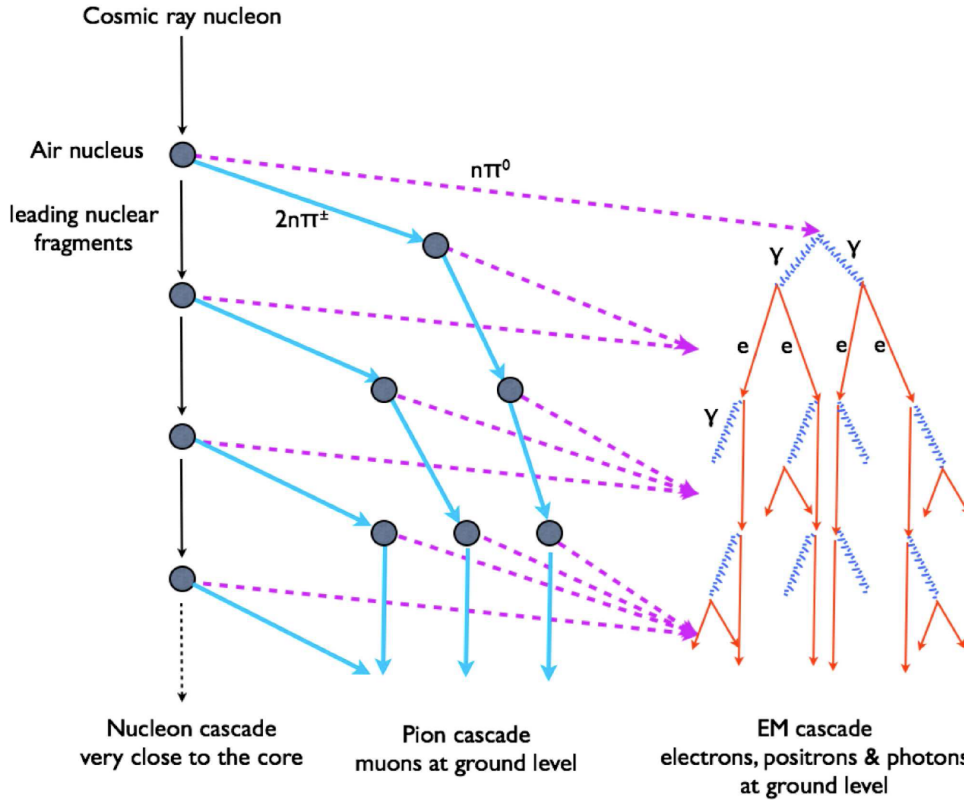


**Figure 1.8:** Scheme of the development of an EAS. At ground level the most abundant component is the electromagnetic component, followed by the muonic one. Figure reproduced from [Letessier & Stanev 2011].

Neutral pions have a half life  $\sim 10^{-17}$ s, and decay mostly into photons:

$$\pi^0 \rightarrow \gamma + \gamma$$

Although the following decays also take place:

$$\begin{aligned} \pi^0 &\rightarrow \gamma + e^+ + e^- \\ \pi^0 &\rightarrow e^+ + e^- + e^+ + e^- \end{aligned}$$

Hence the decay of the pions is the mechanism responsible for the creation of the electromagnetic component of the shower, which carries  $\sim 85\%$  of the EAS energy (particles with an energy range between 1 and 10 MeV). It is possible, however, that some of the photons re-inject some energy

back to the hadronic component. But at ground level the hadronic component carries  $\sim 4\%$  of the EAS energy. The other main component of the EAS is the muonic component. This appears as a consequence of the decays of charged mesons (see Fig. 1.8):

$$\begin{aligned}\pi^\pm &\rightarrow \mu^\pm + \nu \\ K^\pm &\rightarrow \mu^\pm + \nu \\ K^\pm &\rightarrow \pi^\pm + \pi^0\end{aligned}$$

The muonic component carries around 10% of the EAS energy.

## 1.2 Extreme Energy Neutrinos

### 1.2.1 The neutrino in the Standard Model of particle physics

#### The discovery of the neutrino

From its very beginning, neutrino research has proven to be a challenging discipline. Years before the first neutrinos were ever detected, their existence had already been postulated, and debated, within the scientific community.

When in 1914 James Chadwick [[Chadwick 1914](#)] demonstrated the continuum spectrum in beta decay, (the process when an electron is expelled from an atomic nuclei), a huge contradiction arose between his results and what was anticipated. It was expected that beta decay would show discrete levels in accordance with the discrete characteristics of the nuclear spectra. Either the energy levels had to be discrete or energy conservation would not be valid for this type of phenomenon. Therefore in 1930 Wolfgang Pauli [[Pauli 1930](#)] postulated the existence of a particle, never observed before which would carry out an unspecified amount of the energy contained in the nucleus. If one could simultaneously, measure the energy of the electron and this new particle, then one would recover the discrete energies as expected. In 1933 Fermi published a theoretical treatment of  $\beta^-$  decay, which correctly stated that the neutron was decaying into a proton, an electron and an anti-neutrino [[Fermi 1934](#)]. In his paper Fermi also reasons that the neutrino's rest mass should be zero or very small compared to the electron mass. This theory however was super-seeded by the electroweak theory (see below). It was till 1953 when this particle was finally detected by Cowan and Reines [[Cowan & Reines 1956](#)].

#### Neutrino interactions

Nowadays the state of the art theoretical framework is the electroweak theory [[Paschos 2007](#)]. Within this framework there are three flavors of neutrinos. Each one associated with their respective charged lepton, for the three generations in the Standard Model (SM). Originally electroweak Lagrangian contains the simplest assignment for the fermion  $SU(2)$  multiplets that reproduces parity violation. That is left handed doublets and right handed singlets (the neutrino

was thought to be massless):

$$\psi_e = \begin{pmatrix} \nu_e \\ e^- \end{pmatrix}_L, e_R^- \quad , \psi_\mu = \begin{pmatrix} \nu_\mu \\ \mu^- \end{pmatrix}_L, \mu_R^- \quad \text{and} \quad \psi_\tau = \begin{pmatrix} \nu_\tau \\ \tau^- \end{pmatrix}_L, \tau_R^- \quad (1.3)$$

Neutrinos are spin  $\frac{1}{2}$  particles and with zero electric and color charge. Within the SM, neutrinos are described by a bispinor  $\psi(x)$  that obeys Dirac's equation. Following convention, we write a bi-spinor as a vector with 4 complex entries:

$$\psi = \begin{pmatrix} \psi_1 \\ \psi_2 \\ \psi_3 \\ \psi_4 \end{pmatrix} \equiv \begin{pmatrix} \psi_L \\ \psi_R \end{pmatrix}_{\text{Weyl basis}}$$

and Dirac's equation:

$$i \hbar \gamma^\mu \partial_\mu \psi - mc \psi = 0 \quad (1.4)$$

where  $\hbar$  is the reduced Planck's constant,  $c$  is the speed of light in vacuum,  $m$  is the mass of the particle, and  $\gamma^\mu$  are the Dirac matrices. Explicitly these matrices are (again in Weyl's basis):

$$\gamma^0 = \begin{pmatrix} 0 & \mathbb{1} \\ \mathbb{1} & 0 \end{pmatrix} = \begin{pmatrix} 0 & 0 & 1 & 0 \\ 0 & 0 & 0 & 1 \\ 1 & 0 & 0 & 0 \\ 0 & 1 & 0 & 0 \end{pmatrix}, \quad \gamma^1 = \begin{pmatrix} 0 & \sigma_x \\ -\sigma_x & 0 \end{pmatrix} = \begin{pmatrix} 0 & 0 & 0 & 1 \\ 0 & 0 & -1 & 0 \\ 0 & -1 & 0 & 0 \\ 1 & 0 & 0 & 0 \end{pmatrix}$$

$$\gamma^2 = \begin{pmatrix} 0 & \sigma_y \\ -\sigma_y & 0 \end{pmatrix} = \begin{pmatrix} 0 & 0 & 0 & -i \\ 0 & 0 & i & 0 \\ 0 & i & 0 & 0 \\ -i & 0 & 0 & 0 \end{pmatrix}, \quad \gamma^3 = \begin{pmatrix} 0 & \sigma_z \\ -\sigma_z & 0 \end{pmatrix} = \begin{pmatrix} 0 & 0 & 1 & 0 \\ 0 & 0 & 0 & -1 \\ -1 & 0 & 0 & 0 \\ 0 & 1 & 0 & 0 \end{pmatrix}$$

We write them explicitly to introduce the chirality matrix  $\gamma^5$ , which in turn allows us to define the projection operator:  $\frac{1}{2}(\mathbb{1} - \gamma^5)$ , where:

$$\gamma^5 = i \gamma^0 \gamma^1 \gamma^2 \gamma^3 = \begin{pmatrix} 0 & -\mathbb{1} \\ \mathbb{1} & 0 \end{pmatrix}$$

Independently of the basis, this projection operator allows us to get the left or right handed portion of a bispinor. The reason we write this matrix in full is to explicitly show how the Lagrangian of the weak interaction relates to the mass terms and parity violation.

The masses for quarks and leptons are introduced through Yukawa couplings to the Higgs doublet  $\phi$ :

$$\mathcal{L} = g_e \bar{\psi}_e \phi e_R + \dots \quad (1.5)$$

and similar masses for the tau and mu leptons. In the last expression  $\bar{\psi}$  is the Dirac's conjugate of  $\psi$  (i.e.  $\bar{\psi} = \psi^\dagger \gamma^0$ ). This coupling gives the masses to the leptons after the Higgs fields acquires a non-zero expectation value (spontaneous symmetry breaking).

Experimental evidence confirms that weak interaction violates parity conservation. However, the mass terms couple the left-handed and right-handed components of the neutrino bi-spinors:

$$\begin{aligned} m \bar{\psi} \psi &= m (\psi_L^\dagger \psi_R^\dagger) \begin{pmatrix} 0 & 1 \\ 1 & 0 \end{pmatrix} \begin{pmatrix} \psi_L \\ \psi_R \end{pmatrix} \\ &= m \psi_L^\dagger \psi_R + m \psi_R^\dagger \psi_L \end{aligned} \quad (1.6)$$

Since only left handed neutrinos have ever been detected, the neutrinos were thought to be massless. Therefore the interactions in the Lagrangian that involve neutrinos have the form:

$$\mathcal{L}_{CC} = \frac{g}{2\sqrt{2}} \bar{\nu} \gamma^\mu (1 - \gamma^5) e W_\mu + h.c. + \dots$$

for the leptonic charged current interactions.

And for the neutral current interaction, we have:

$$\mathcal{L}_{NC} = \mathcal{L}_{QED} + \mathcal{L}_{NC}^Z$$

where:

$$\mathcal{L}_{QED} = e A_\mu \sum_j \bar{\psi}_j \gamma^\mu Q_j \psi_j \equiv e A_\mu J_e^\mu$$

Hence  $\mathcal{L}_{QED}$  is the usual QED Lagrangian, and summing over the usual fermions we have:

$$\mathcal{L}_{NC}^Z = \frac{e}{\sin 2\theta_W} Z_\mu \sum_f \bar{f}_j \gamma^\mu (v_f - a_f \gamma^5) f_j$$

where  $\theta_W$  is the weak angle. The coupling constants for the first fermion family are:

|        | u                                 | d                                  | e                        | $\nu_e$ |
|--------|-----------------------------------|------------------------------------|--------------------------|---------|
| $2a_f$ | 1                                 | -1                                 | -1                       | 1       |
| $2v_f$ | $1 - \frac{8}{3} \sin^2 \theta_W$ | $-1 + \frac{4}{3} \sin^2 \theta_W$ | $-1 + 4 \sin^2 \theta_W$ | 1       |

It is now evident how this Lagrangian allows only the left-handed neutrinos take part in the interactions. In the original version of the Standard Model, neutrinos are taken to be massless. Hence they would interact with other particles only through the weak interaction mediated by the W and Z bosons.

However neutrino oscillation experiments have demonstrated that the neutrino actually posses

mass. Hence the *ansatz* of Eq. 1.3 must be "extended", including now a right-handed singlet for the neutrino:

$$\psi_e = \begin{pmatrix} \nu_e \\ e \end{pmatrix}_L, \quad \nu_R \quad \& \quad e_R \quad (1.7)$$

As usual  $e_{R,L} = \frac{1}{2}(1 \pm \gamma^5)e$  and the same for the tau and muon families.

### 1.2.2 Astrophysical neutrinos

Due to their low interactions with matter, with cross sections in the range of  $10^{-33} \text{ cm}^{-2}$ , UHE-neutrinos have the potential to present researchers with the opportunity to gaze into the internal processes of supernovae, optically thick astrophysical objects (hidden sources) [Ando et al. 2013], and other extremely energetic astrophysical environments such as GRB's AGN's [Kotera & Olinto 2011]. UHE neutrinos escape their production sites carrying information that cannot be accessed via the electromagnetic channel.

As noted in [Waxman & Bahcall 2001], the UHECR and EECR fluxes guarantee some population of UHE neutrinos. In this scenario the UHE neutrinos are produced by the decay of charged mesons produced by interaction of UHECR and EECR with the cosmic microwave background. This also a consequence of the GZK effect discussed in section § 1.1.3.1. However, this is not the only possible scenario. The interaction may also happen in the acceleration region or somewhere else with ambient radiation or even nuclear material. Let's review the process, assuming for the sake of the example a proton as the UHECR:

$$p + \gamma \rightarrow (\Delta^+) \rightarrow \begin{cases} \pi^+ + n \\ \pi^0 + p \end{cases} \quad p + p \rightarrow \begin{cases} \pi^+ + n + p \\ \pi^0 + p + p \end{cases}$$

or

$$p + N \rightarrow \pi^{\pm,0} + N'$$

in both cases followed by:

$$\begin{aligned} \pi^+ &\rightarrow \mu^+ + \bar{\nu}_\mu \quad \text{and} \quad \pi^- \rightarrow \mu^- + \nu_\mu \\ \mu^+ &\rightarrow e^+ + \bar{\nu}_\mu + \nu_e \quad \text{and} \quad \mu^- \rightarrow e^- + \bar{\nu}_e + \nu_\mu \end{aligned}$$

Regardless of the proton energy the neutrino energy is  $E_\nu \approx 0.05E_p$  [Waxman & Bahcall 1998]. Keep in mind that the neutron will either decay or further interact:

$$n \rightarrow p + e^- + \bar{\nu}_e \quad \text{or} \quad n + \gamma \rightarrow p + \pi^-$$

As a consequence at the sources the flavor ratio is approximately  $\nu_e : \nu_\mu : \nu_\tau = 1 : 2 : 0$  but after propagation (due to neutrino oscillations) the ratio is expected to be  $\nu_e : \nu_\mu : \nu_\tau = 1 : 1 : 1$ . But the key point we want to make explicitly clear is that regardless of the acceleration mechanism,

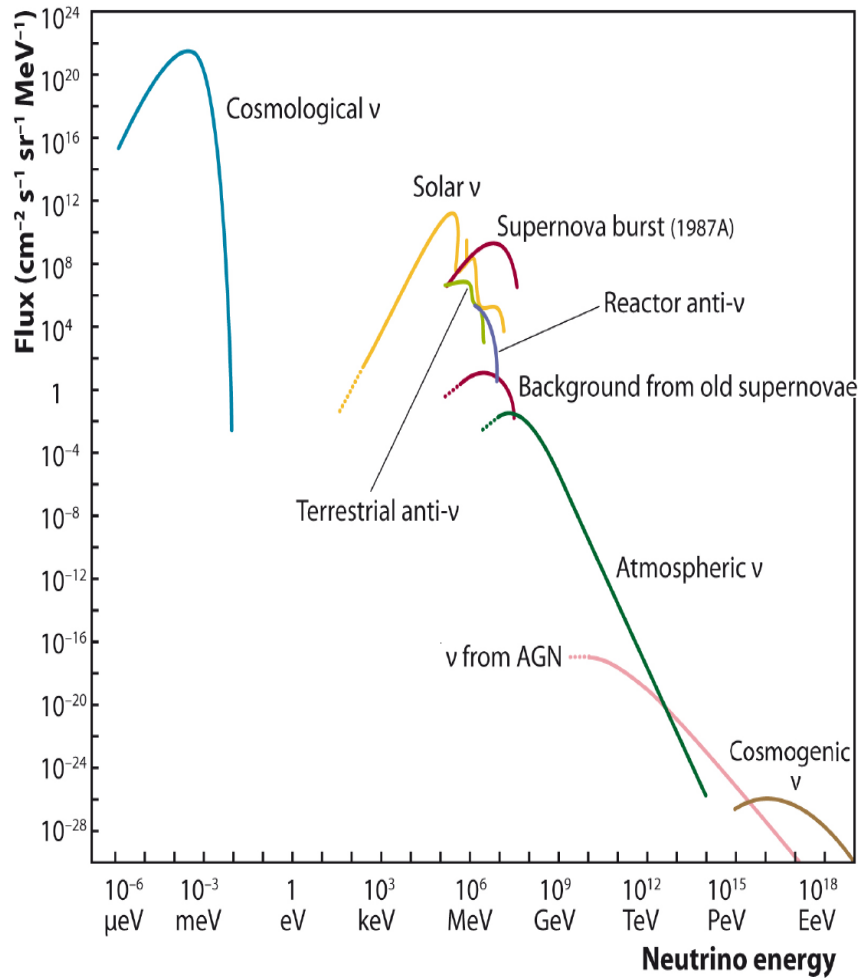


**Figure 1.9:** The “universal” neutrino background. In the energy range where this works concentrate, we can see that there is already an expected contribution from EECR neutrinos as a by product of the GZK effect. Reproduced from [Spiering 2012].

UHE-neutrinos are expected as consequence of the existences of UHECR.

Although the composition of the primary population of UHECR does have an impact in the properties of the expected UHE neutrino flux, both proton dominated or iron dominated scenarios yield a UHE neutrino flux. The kinematic threshold (the minimum energy of the intervening proton) for  $p + \gamma \rightarrow \Delta^+$  depends on the energy of the photon. For example, in many stars or accreting objects the ambient radiation peaks in the UV regime. For  $p + \gamma_{UV} \rightarrow \Delta^+$  the kinematic threshold of the proton is in the range of several  $PeV$ .

As we mention in § 1.1.3.1, this threshold is above  $10^{20}$  eV when the involved photon is CMB photon. In any case, we end up with a “guaranteed” neutrino flux (the GZK flux) is therefore, intimately correlated to the overall UHECR, at least for energies below  $10^{19}$  eV. The precise mechanisms taking places in the sources is not completely understood, and in principle some UHE neutrinos could also be escaping directly from the primary source, pointing directly to the acceleration region. For example lets take Active Galactic Nuclei (AGN). The super massive black holes inside the AGN, transform the gravitational energy into radiation. AGNs, in particular

Seyfert galaxies, are assumed to contribute to the [Stecker 2005] non-thermal component of extragalactic  $MeV\gamma$ -ray background. In this region UHECR acceleration might be taking place. Then in this scenario, the main process for neutrino production is the interaction from ultra-relativistic protons with the ambient radiation field. Also, blazars have been found to be strong gamma emitters at GeV and even at TeV. The  $\gamma$ -ray emission of blazars has been found to be highly variable with changes in order of magnitude in hours time scale. Observation of neutrinos within this time window coming from these sources, would be a strong hint in this direction.

It is instructing, to introduce some upper limits as well as model predictions for the UHE- $\nu$  flux:

- *Waxman-Bahcall upper bound (WB-limit)* [Waxman & Bahcall 1998]. Using the measured UHECR flux, Eli Waxman and John Bahcall calculated the energy-dependent generation rate ( $\dot{N}$ ) for cosmic ray sources with redshift  $< 1$  and energies between  $10^{19}$  and  $10^{21}$  eV assuming an injection spectrum proportional to  $E^2$ . They obtain a value of:  $\frac{d\dot{N}_{CR}}{dE_{CR}} \approx E_{CR}^2 \times 10^{44} \frac{\text{erg}}{\text{Mpc}^{-3} \text{yr}^{-1}}$ . To calculate the amount of neutrinos in the present day they then integrate this generation rate to arrive at:  $\frac{dN_\nu}{dE_\nu} \approx \frac{1}{4} \epsilon t_H \frac{d\dot{N}_{CR}}{dE_{CR}}$ . here the  $\frac{1}{4}$  factor comes from the fact that neutral pions, whose decay yields no neutrino, are equally to be produced as the charged pions. Also, because after the decay of the charged pion the neutrinos carry away almost half the charged pion energy. We take  $\epsilon$  to be the fraction of the energy the CR loses before leaving the source due to photo pion production, and  $t_H$  is the Hubble time.

With the latter expression, Waxman & Bahcall calculate the upper bound on the neutrino intensity as:

$$E_\nu \Phi_\nu \equiv \frac{c}{4\pi} E_\nu^2 \frac{dN_\nu}{dE_\nu} = \frac{\epsilon \xi_z}{2} 1.5 \times 10^{-8} \text{GeV cm}^{-2} \text{s}^{-1} \text{sr}^{-1}$$

In this last expression  $\xi_z \sim 1$  is added to account for hypothetical high redshift sources for UHECR.

- *Mannheim-Protheroe-Rachen upper bound (MPR-limit)*. Postulates a hadronic test spectrum following  $Q_{CR} \propto E^{-1} \exp(-E/E_c)$  (a power law with an energy cutoff value  $E_c$  and spectral index  $\alpha = 1$ ). Using different values of  $E_c$  for different types of sources, Karl Mannheim, Raymond Protheroe, and John Rachen, interpret the observed spectrum as a superposition of the aforesaid sources. We mention this limit for context reasons. Recent measurements by Fermi and ICECUBE, amongst other neutrino telescopes, have ruled out the argument presented in [Mannheim, Protheroe & Rachen 2001], since the expected flux of neutrinos was not measured.
- *Cosmological UHE- $\nu$*

As we mentioned before the observed UHECR and the GZK mechanism, have as a consequence a UHE  $\nu$  flux. However the exact shape and intensity depend strongly on the composition of the UHECR population. Commonly the source injection spectra are taken to be a power law with a cutoff energy. Since the GZK process produces neutrinos with energies proportional to the UHECR, the average injected spectra are expected to be similar but with a different normalization factors. Let us also remember that this injection spectra includes neutrons as a consequences of  $\pi^\pm$  decays. Due to the decay of this neutron component, the cosmogenic  $\nu_e$  and  $\bar{\nu}_e$  spectrum is expected to have a double peak structure. The

decay of the neutrons adds an additional lower energy peak. In a proton dominated composition, the shape of the neutrino spectrum is expected to exhibit this double peak feature [Engel et al. 2001]. With the first peak due to neutron decay in between  $10^{16}$  and  $10^{17}$  eV (electron family) and the second one between  $10^{18}$  and  $10^{19}$  eV (both muon and electron neutrinos). The expected neutrino flux, can also be affected by the energy at which the galactic flux is superseded by an extragalactic component. Generally speaking the lower the crossover energy, the lower flux of UHE- $\nu$  [Ahlers 2010].

On the other hand if we consider a heavier initial composition, the expected number of neutrinos decreases. Multiple photo disintegration of the nuclei create a new excess of lower energy neutrons which produce a third peak at energies around  $10^{14}$ eV [Ave et al. 2005]. However this reduction in the expected flux of UHE- $\nu$ , when iron nuclei are taken as the primary CR, is a factor of a few smaller than predictions using only protons.

The so called “source evolution” also affects the expected neutrino flux. The argument goes as follows: the star formation rate is a tracer of matter in the universe and thus they are assumed to also trace the sources of UHECR. We know that the star formation rate is a function of the redshift, and hence the UHECR sources are also a function of the redshift. This has consequences on neutrino production along the propagation of UHECRs.

|                    | Neutrino Source          | Main characteristics  |
|--------------------|--------------------------|---|
| WB-Limit           | EECR                     | Neutrino flux based on astrophysical “energy budget”.   |
| MPR-limit          | UHECR & EECR             | Assumes extragalactic sources for CR with $10^{16}eV < E < 10^{19}eV$ .   |
| Cosmological (GZK) | AGN, GRBs, UHE- $\gamma$ | Highly dependent of EECR composition, the thermal component (if any) of the extragalactic $\gamma$ -ray background. |

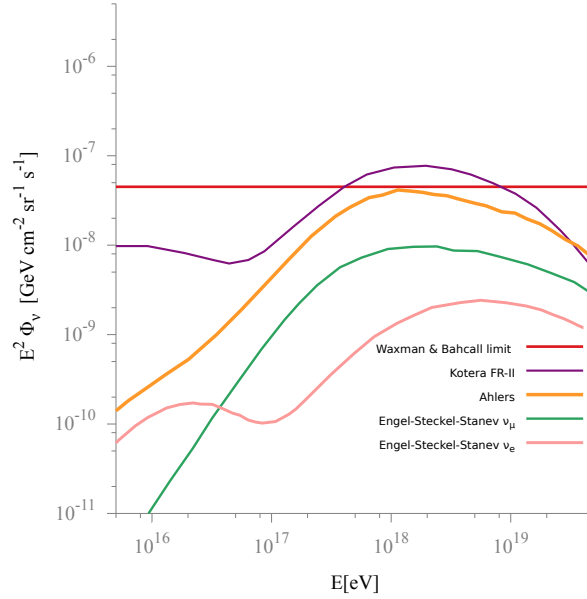


**Figure 1.10:** A summary of models of expected cosmological neutrino flux (see text). Data taken from [Aartsen et al. 2013], [Engel et al. 2001], [Kotera et al. 2010] and [Ahlers 2010].

### 1.2.3 UHE- $\nu$ detection from space

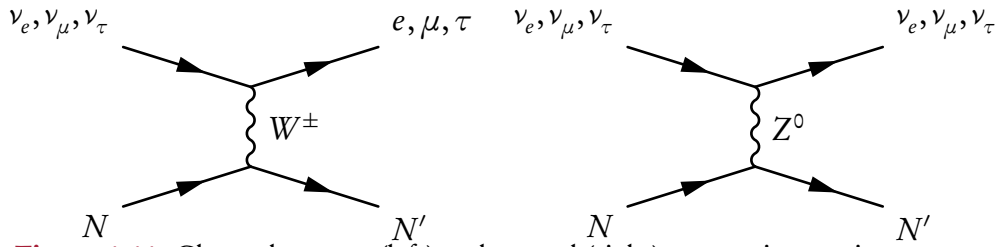


**Figure 1.11:** Charged current (left) and neutral (right) current interactions.

To detect neutrinos on Earth the charged (CC) and neutral current (NC) interactions are exploited. This is illustrated in Fig. 1.11 where  $N(N')$  stands for an (excited) air nucleon and  $l = e, \mu, \tau$ , stands for any of the Standard model families. We will focus our attentions on the CC interaction of electron neutrinos. The reason for this is twofold: first of all, in average the leading lepton takes 80% of EECR energy [Gandhi et al. 1996]; secondly, from the SM leptons we only expect the electrons to trigger a space borne fluorescence detector detectable EAS at this energies. We can make this claim since the muons are too deeply penetrating and the decay length of the tau is too big for the foreseen detector to notice the “double bang” (i.e the initial hadronic cascade followed by the decay of the tau lepton [Kusenko et al. 2002]). This decay length is the order of  $10^5$  km [Kusenko et al. 2002], and therefore highly unlikely to be detected by a space borne detector with a Field of View (FOV) with a characteristic size of the order of hundreds of kilometers. The decay of the tau after propagation could produce a detectable electromagnetic shower. However, we would only see the “second bang”, if the first interaction happens outside the FOV. The first interaction will also produce a small hadronic shower, but the fluorescence yield of this shower will not be sufficient to trigger a space-borne detector.

## 1.3 State of the art of the experimental aspects

---

Currently (2014), talking about the state of the art of EECR research implies talking about mainly about two observatories: The Pierre Auger Observatory (PAO) and the Telescope Array (TA). The latter is the follow up of the HiRes experiment. We will first introduce the experiments and then proceed to discuss their findings.

### 1.3.1 The Pierre Auger Observatory

---

Located in the southern hemisphere, at Argentinian Pampa Amarilla, the PAO is the biggest CR observatory ever built. It consists of more than 1660 water cherenkov detectors and a set of 27 fluorescence telescopes. It covers an area of roughly 3000 km<sup>2</sup>.

PAO started data taking in 2004, before the all of the water-cherenkov tanks were deployed. The baseline design was completed in June 2008. Since then the PAO has been acquiring data almost uninterruptedly.

The principle of detection is to use the water-cherenkov detectors, or SD for surface detector, to measure the amount and arrival time distribution of the particles constituting the EAS. This technique, provides a high duty cycle and is enhanced by the fact that it is complemented with a calorimetric measurement of the energy: the fluorescence technique. We will discuss the fluorescence technique in more detail in the next chapter when we talk about the JEM-EUSO mission. For the moment, it is enough to say that the fluorescence technique measures the UV photon yield of ionized air. This ionization is produced by the EAS as it transverses the atmosphere. The fluorescence technique has been used in the past by other experiments [[HiRes 2011](#)] [[Linsley 1963](#)], and produces a calorimetric measurement of the energy deposited on the atmosphere by the EAS.

PAO is therefore called a “hybrid” detector. By combining both detection methods, the uncertainties in the measurement of the EAS’s characteristics are diminished.

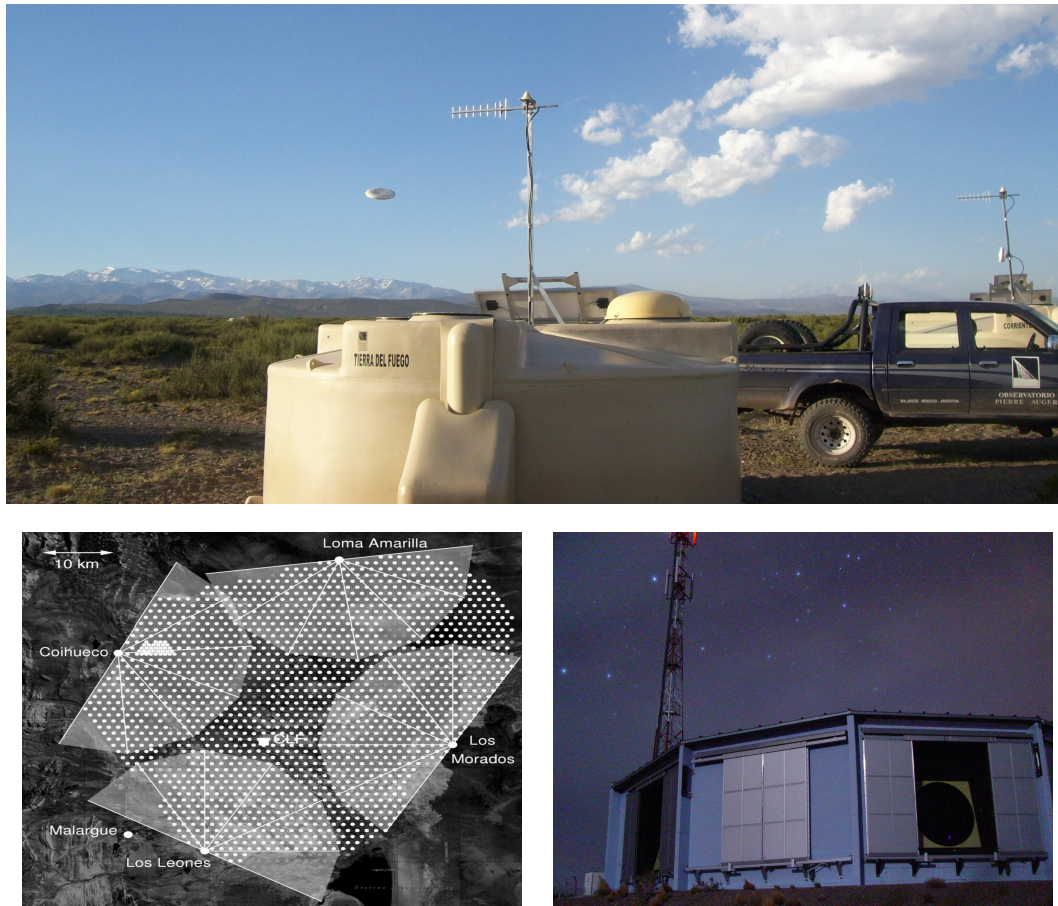


**Figure 1.12:** The main components of the PAO. Upper image: one of the  $\sim 1660$  water cherenkov tanks. Bottom left: The positions of the SD detectors in the final array configuration overlaid on a map of the Malargüe area. The FD's field of view are indicated as shaded semicircles. Reproduced from [Abraham, et al. 2010]. Bottom right: the FD building located at Los Leones. Each of these buildings contains 6 UV-telescopes. Reproduced from [Smida 2014].

### 1.3.2 Telescope Array

The TA is the largest CR experiment in the northern hemisphere. It is situated in western Utah, in the United States, and consists of an array of 507 scintillator detectors covering an area of  $\approx 700 \text{ km}^2$  [Ikeda et al. 2013]. The SD of TA consists of scintillation counters. The spacing of the array is 1.2 km and each scintillation counter has an area of  $3 \text{ m}^2$ . They consist of two separated layers of an organic scintillating material. As the EAS particles go through the scintillator wavelength shifter fiber optics collect the scintillation signal and relay it to a dedicated photo multiplier tube [Abu-Zayyad et al. 2012] (see also Fig. 1.13).

This SD array is surrounded by 3 fluorescence detector stations with 28 UV-fluorescence telescopes. Hence TA is also a hybrid detector. The northern FD station consists of 14 fluorescence telescopes, refurbished from the High Resolution Fly's Eye experiment (HiRes) [HiRes 2011]. The other two FD stations were newly designed specifically for the TA experiment, however, they

all consist of a primary segmented spherical mirror and a photomultiplier camera with 256 PMTs [Tokuno et al. 2012].

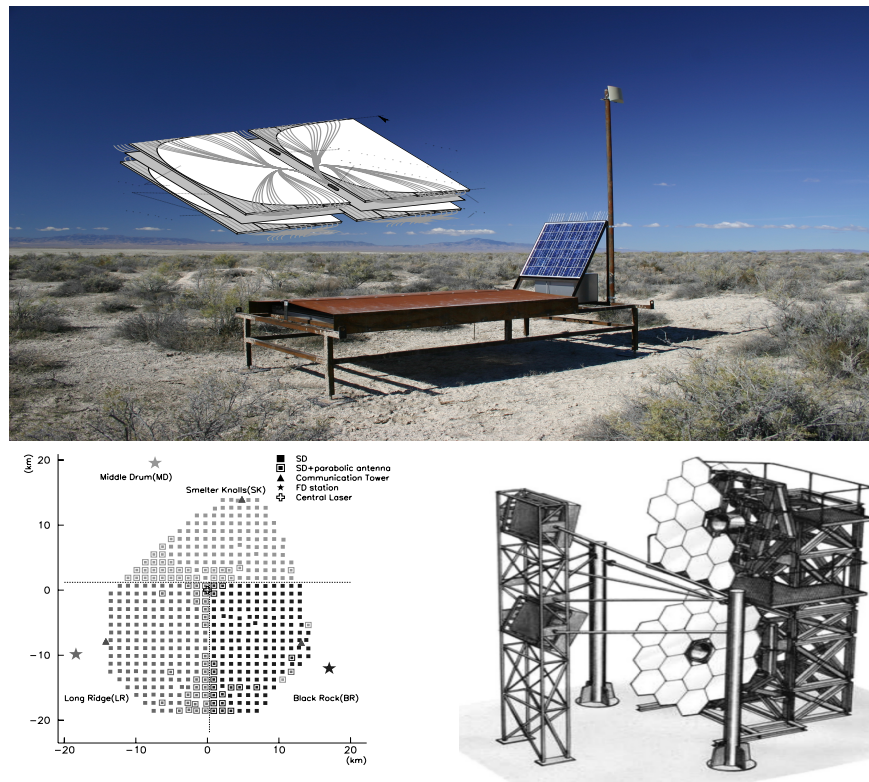


**Figure 1.13:** The main components of the Telescope Array experiment. *Upper image:* one of the 507 scintillation counters. Overlaid on the picture is a diagram of the inner structure of the scintillator (white) separated by metal plates. Modified from [Abu-Zayyad et al. 2012]. *Bottom left:* The layout on ground of the TA experiment (distance between counters is 1.2 km) Reproduced from [Abu-Zayyad et al. 2012]. *Bottom right:* a sketch of new (not HiRes refurbished) FD designed for the TA experiment [Tokuno et al. 2012].

### 1.3.3 Comparison between PAO and TA results

Having introduced both detectors let us now focus on the main results from both experiments:

- UHECR spectrum.* Both PAO's and TA's measurements agree on the overall shape and magnitude of the UHECR flux (within perhaps an unknown shift on the energy scale). Both experiments see a significant reduction of the flux consistent with the expected GZK cutoff (around  $2 - 3 \times 10^{19}$  eV), and the "ankle" feature at energies below the GZK limit ( $\sim 4 \times 10^{18}$  eV). However they differ in the exact energies where these main features occur: PAO reports the flux's suppression at an energy of  $(2.09 \pm 0.2) \times 10^{19}$  eV [PAO 2010b] while TA reports  $(5.4 \pm 0.6) \times 10^{19}$  eV [Tinyakov 2014]. For the "ankle" (a hardening of the spectrum), PAO and TA both report agreeing results. PAO reports this feature at  $(4.07 \pm 1) \times 10^{18}$  eV while TA reports it at  $(4.6 \pm 0.3) \times 10^{18}$  eV. It is worth mentioning that TA results are also in good agreement with its predecessor (HiRes). HiRes reported the values of  $(4.5 \pm 0.8) \times 10^{18}$  eV and  $(5.6 \pm 0.9) \times 10^{19}$  eV for the "ankle" and flux suppression respectively. The energy where these transitions take place indicate that TA and HiRes results favor a model of composition with protons. On the other hand, the results from PAO would point to heavier composition since PAO's relatively softer spectrum is more consistent with an iron dominated composition. A harder energy spectrum would not be expected since heavier nuclei suffer greater energy losses
- Composition* The difference in the measurements is more marked as far as composition is concerned. Although, both experiments are self-consistent (see previous point), PAO finds a heavier composition than TA with  $X_{max}$  analysis.  $X_{max}$ , also sometimes called the elongation rate, is the atmospheric depth (in  $\frac{g}{cm^2}$ ) at which EAS's longitudinal profile reaches its maximum. This analysis consists on comparing the average of value the reconstructed  $X_{max}$  for a sample of detected EAS. Its interpretation is somehow biased since it depends strongly on the hadronic models used in the analysis, particularly for SD detectors. Roughly speaking, in comparison to pure protons, heavy nuclei are expected to have a lower value for  $\langle X_{max} \rangle$  and smaller distribution of this value  $\sigma(X_{max})$ . However, not only do TA and PAO differ in the overall composition. They also differ in how the composition behaves as the energy increases. While TA sees almost no correlation from energy and composition, PAO sees a tendency to heavier primaries as the energy increases.

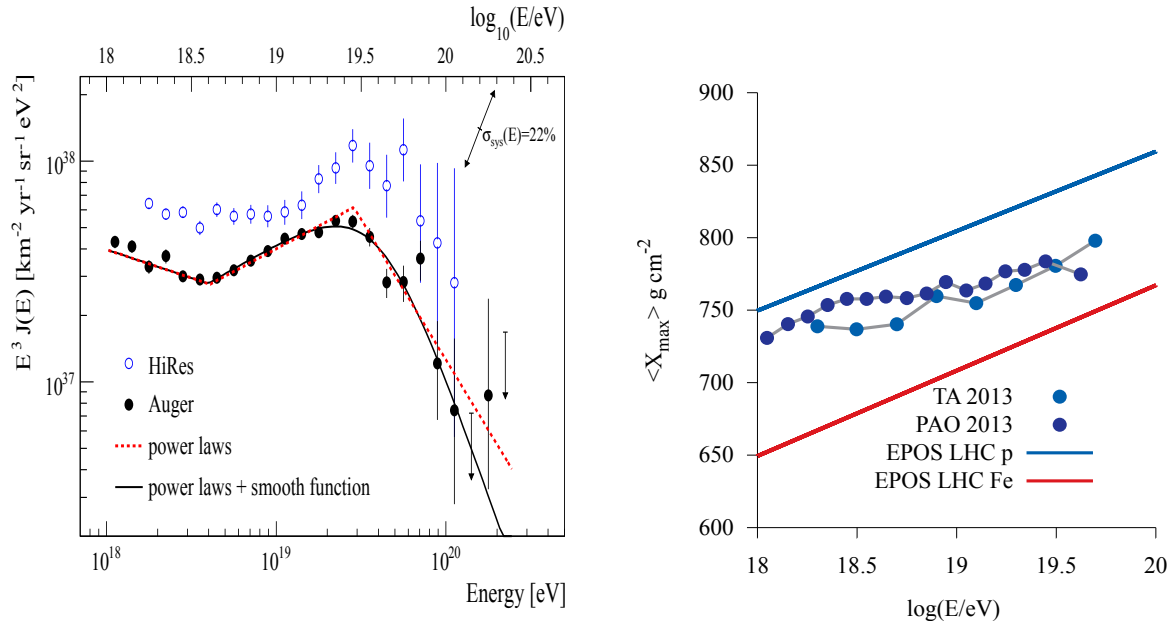


**Figure 1.14:** *Left:* The measured energy spectra from HiRes and PAO. Reproduced from [PAO 2010b]. *Right:* Composition results from TA and PAO. Data taken from [Tinyakov 2014] [PAO 2013b] [Pierog 2013].

- *Anisotropy searches* PAO claimed to have detected an isotropic flux at UHECR [PAO 2007]. Years later the significance of this result diminished [PAO 2013a]. The procedure is to try to correlate the arrival directions with a catalog of astrophysical objects. These correlations is done by determining the probability that, given a set of sources with a given angular separation ( $\psi$ ), uniformly distributed events arrive with a smaller separation. If in the experimental data, we have a significantly high amount of pairs of events separated by  $\psi$  or less, then then we may be dealing with an anisotropic flux. Using a similar analysis, both TA and HiRes have measurements that appear to be contradicting those of PAO at least at energies  $<10$  EeV [Tinyakov 2014] [HiRes 2011]. However we must remember both experiments are looking at different portions of the sky. It also worth mentioning that neither HiRes nor TA have sufficient data to rule-out an isotropic or anisotropic UHECR flux. Nevertheless at energies above 57 EeV TA, has already reported an excess or *hotspot* with a very low probability of being compatible with an isotropic flux [Abbasi et al. 2014]. The result comes after 5 years of data taking, and was found by oversampling using  $20^\circ$  radius circles. This is relatively close to AGASA's similar hot spot and  $19^\circ$  off of the supergalactic plane.

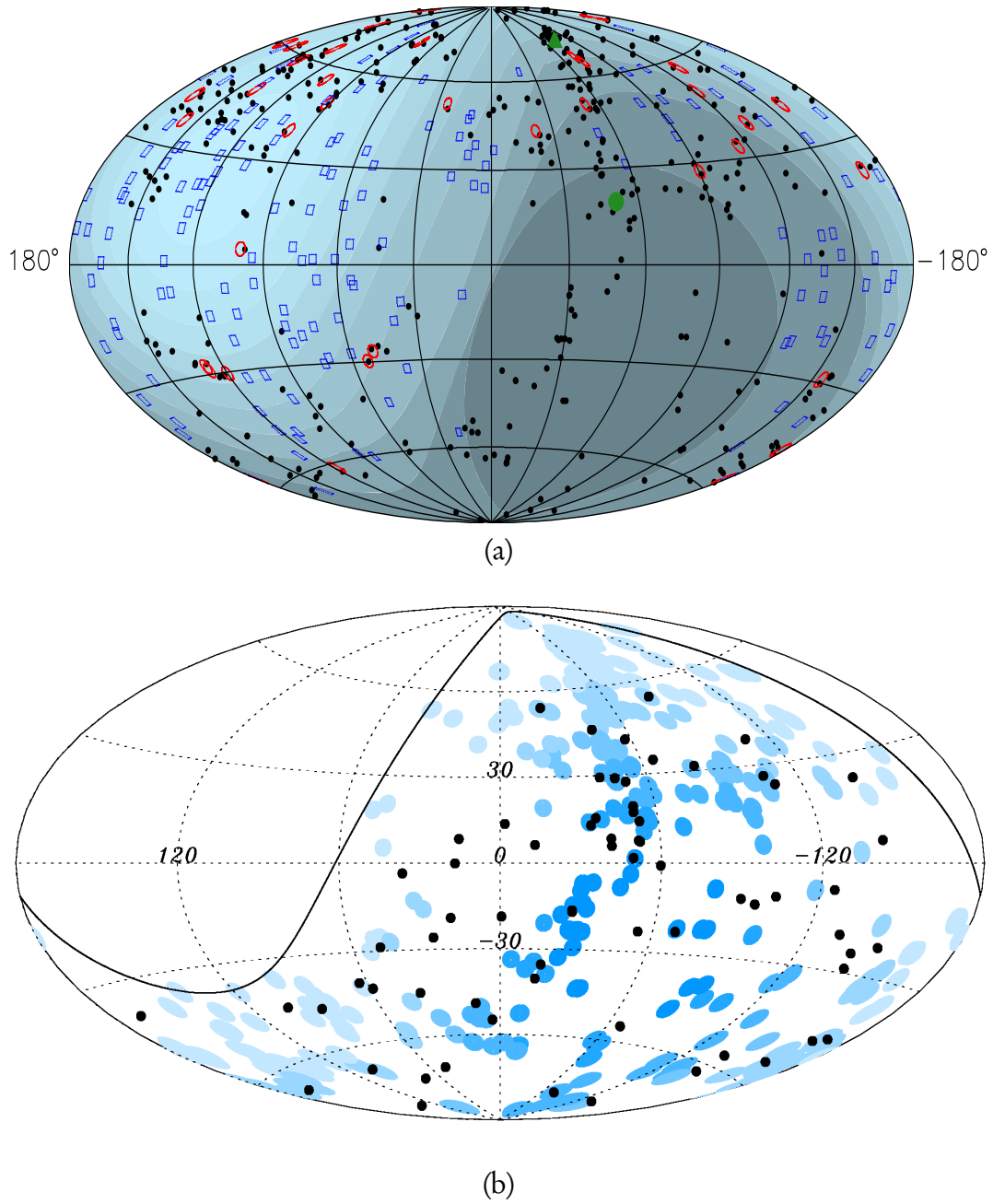


**Figure 1.15:** Arrival directions in an Aitoff-Hammer projection of the sky in galactic coordinates, for HiRes a) and PAO b). Also plotted are the positions of nearby AGNs in the Veron catalogue. To the left: AGNs are shown in black, uncorrelated data and correlated data is shown in blue and red boxes correspondingly. A lighter shadow intensity corresponds to a larger relative exposure. To the right 69 CRs with energy  $E \geq 55 EeV$  detected by PAO are presented as black dots, while circles of radius  $3.1^\circ$  are centered at the positions of the aforesaid AGN. In this figure a darker blue indicates a larger relative exposure. Figures a) and b) reproduced from [HiRes 2011] and [PAO 2010a] respectively.

### 1.3.4 IceCube

Buried in the antarctic ice the IceCube detector is the first kilometer-scale dedicated neutrino detector [Halzen & Gaisser 2014]. IceCube consists of 86 1-km strings spaced 125 m apart and buried at a depth of 1.5 km to shield against background cosmic rays. The instrument is a cubic kilometer of dark and transparent antarctic ice situated at the South Pole. Each string consists of 60  $\sim$  25 cm photomultipliers spaced 17 m from each other. This huge array of photomultipliers detects the Cherenkov light produced after the neutrino interacts with the ice, triggering a cascade of secondary charged particles.

In this experiment, the atmospheric neutrinos are a background for the cosmic neutrino signal. This atmospheric neutrinos are a consequence of the interaction of CR in the atmosphere. As counter measure, the IceCube collaboration has implemented an analysis filter which identifies neutrino interactions that originate inside the detector, as distinct from events originating outside it. The filter divides the instrumented volume into an outer-veto shield and a 420 megatonne inner active volume. As of 2014 [Aartsen et al. 2014a] IceCube has 37 candidate cosmic neutrino events with energies between 30 and 1240 TeV. They are candidates in the sense that, the signal (37 events) is 5.7 sigmas above the expected background. Since the highest neutrino energy ever recorded is around 2 PeV, the neutrinos detected by IceCube do not constitute UHE- $\nu$ , although their cosmological origin is strongly supported by the evidence. However the neutrinos detected by IceCube are in disagreement with the hypothesis that they should follow  $\Phi_\nu(E) = kE_\nu^{-\gamma}$ , with  $\gamma = 2$ , as the CR spectrum. The best value reported is  $\gamma = 2.46 \pm 0.12$  for the energy range between 10 and 100 TeV, thus disfavoring the prediction by Fermi shock-acceleration of  $\gamma = 2$  [IceCube 2015]. However for higher energies in the energy range above 100 TeV, the spectrum hardens again with  $\gamma = 2.26 \pm 0.35$  compatible with previous results [Aartsen et al. 2013] [Aartsen et al. 2014a] [IceCube 2015]. For the region above 60 TeV and 2 PeV IceCube reports  $E^2\Phi(E) = 0.95 \pm 0.3 \times 10^{-8} \text{ GeV cm}^{-2} \text{ s}^{-1} \text{ sr}^{-1}$  which is close to the WB-limit [Aartsen et al. 2014a].

PAO has also conducted its own search of UHE- $\nu$ , though at higher energies than IceCube (i.e.  $0.1 \text{ EeV} < E_\nu < 100 \text{ EeV}$ ). So far PAO has reported an upper limit  $k < 3.2 \times 10^{-8}$  and  $1.7 \times 10^{-7} \text{ GeV cm}^{-2} \text{ s}^{-1} \text{ sr}^{-1}$  for earth-skimming and downward going neutrinos respectively [PAO 2013c].

These promising results and the confirmation ( $5.7\sigma$ ) of the first cosmological neutrinos have researchers propose a high-energy extension to IceCube (IceCube-gen2). This concept aims for a detector with a 10-times-larger instrumented volume, albeit with a higher energy threshold. [IceCube-Gen2]

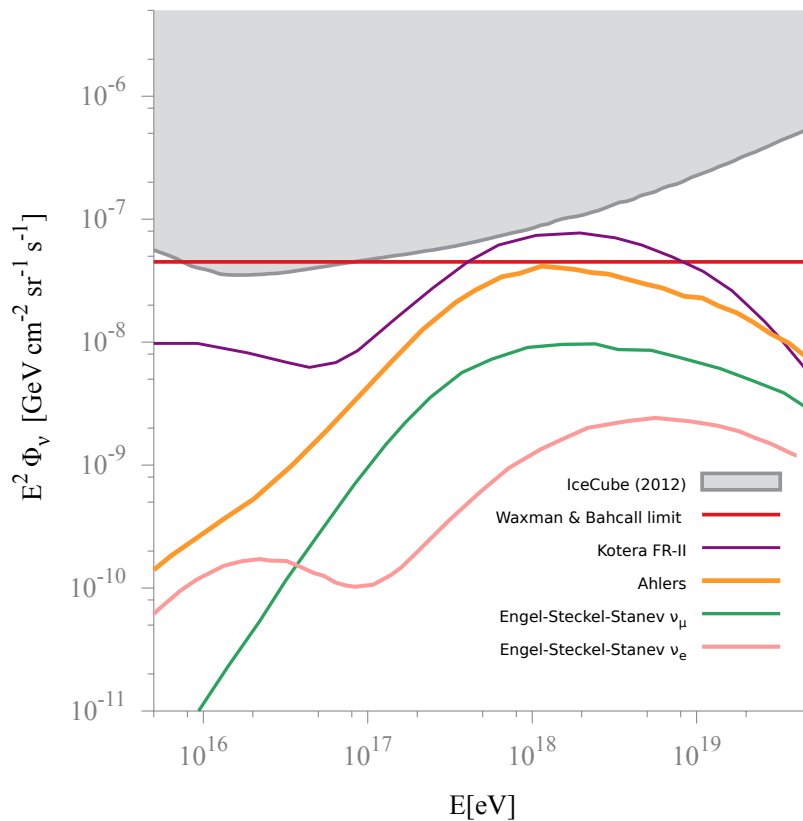
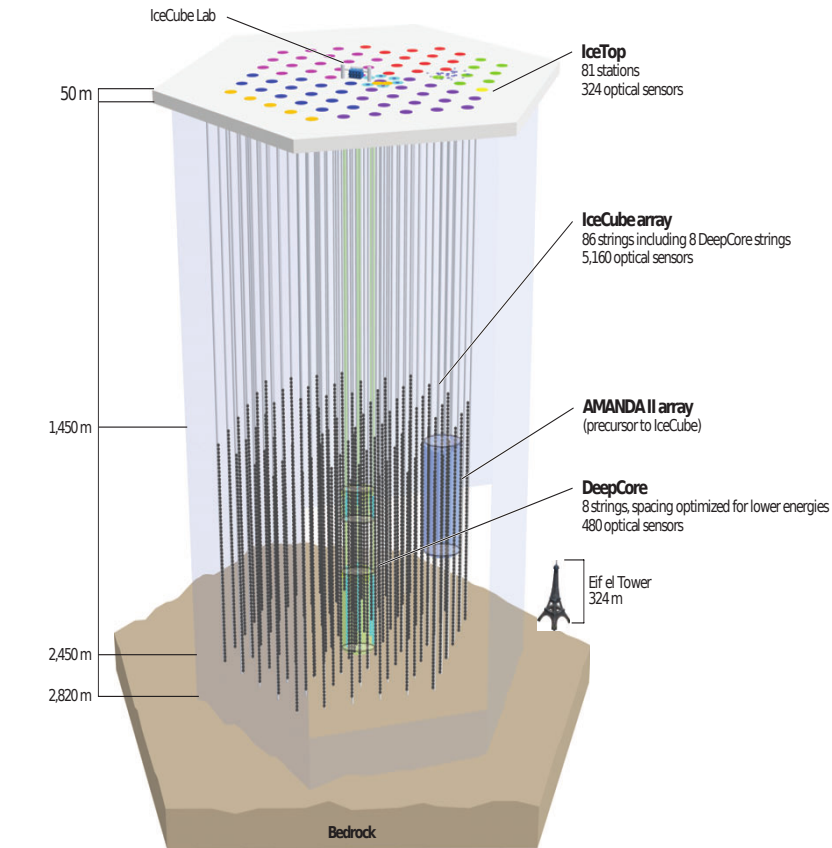


**Figure 1.16:** *Upper panel:* An artistic depiction of the IceCube experiment. Reproduced from [Halzen & Gaisser 2014]. *Lower panel:* Recent constraints to the muon neutrino flux from the ICECUBE experiment compared to proposed models for cosmogenic UHE- $\nu$  [Aartsen et al. 2013].

# 2

## THE EXTREME UNIVERSE SPACE OBSERVATORY

---

### Contents

---

|       |  |    |
|-------|--|----|
| 2.1   | Space approach to EECR: the EUSO concept . . . . . | 33 |
| 2.1.1 | Overview . . . . .                                 | 33 |
| 2.1.2 | Scientific potential . . . . .                     | 35 |
| 2.2   | The JEM-EUSO mission . . . . .                     | 38 |
| 2.2.1 | Scientific Objectives and Requirements. . . . .    | 39 |
| 2.2.2 | Optics and Focal Surface subsystems . . . . .      | 40 |
| 2.2.3 | Atmospheric Monitoring subsystem . . . . .         | 45 |
| 2.3   | The EUSO pathfinders . . . . .                     | 47 |
| 2.3.1 | EUSO-Ballon . . . . .                              | 47 |
| 2.3.2 | Mini-EUSO . . . . .                                | 48 |
| 2.4   | Other EUSO like missions . . . . .                 | 49 |
| 2.4.1 | SpaceX EUSO . . . . .                              | 50 |
| 2.4.2 | K-EUSO . . . . .                                   | 52 |

---



## 2.1 Space approach to EECR: the EUSO concept

### 2.1.1 Overview

The last chapter introduced the state of the art of the research in EECR. Notably, the main question remains unanswered: which are the sources of EECR? The way to elucidate the answer is clear: increase the statistics. Once larger data samples are available for analysis the answer to this, and other enigmas surrounding EECR, should be attainable. Given the tantalizing results on (an)isotropy and trans-GZK particles, a naïve idea would be just to extend our observation time. Nevertheless, it turns out that the biggest problem hindering the increase in statistics is not the exposure time, but the size of the detector. It does not suffice to observe with current-size (e.g.  $PAO \approx 10^5 \text{ km}^2$ ) Earth based observatories. There is indeed an agreement between TA and PAO: the flux of particles with energies above  $E = 5 \times 10^{19} \text{ eV}$ , amounts to one particle per square kilometer per millennia. To improve the statistics drastically, it is not realistic to operate an observatory for tenths of years. Even “just” a 10 fold increase in the involved time scales (i.e. 50 to 70 years) is unfeasible. Instead the only viable option left is to increase the monitored surface. Increasing the monitored surface may sound simple enough. But PAO with its 1600 SD detectors is already closing in to the biggest size that one such array could reach.

Another way of increasing the monitored surface is to “*go to space*”. This idea was already put forward by John Linsley in 1979 [[Benson & Linsley 1981](#)]. The basic concept is to monitor a huge portion of the atmosphere with a space based UV-telescope. The observation of the UV tracks of UHECR is then accomplished using the well established fluorescent technique. This is the Extreme Universe Space Observatory (EUSO) concept in a nutshell, and it is illustrated in Fig. 2.1.

Depending on the orbital characteristics of the instrument’s platform, we can point out some advantages of the space approach:

- ◇ The instantaneously monitored area can be some orders of magnitude larger than the instantaneously monitored area of ground based observatories.
- ◇ A full sky coverage can be achieved with almost uniform exposure.
- ◇ Due to the relatively great distance to the shower, there is a very much attenuated, or even negligible, proximity effect for different showers.

We can also point out some of the specific challenges that the space approach will face:

- ◆ The highly variable observation conditions. The telescope must be ready to make observations in completely different background conditions which depend on the albedo of the monitored area, the presence of spurious lights, and the atmospheric conditions. These conditions will be changing in a matter of minutes for the whole observed area, and it is highly probable that different regions with different background characteristics will be observed simultaneously.

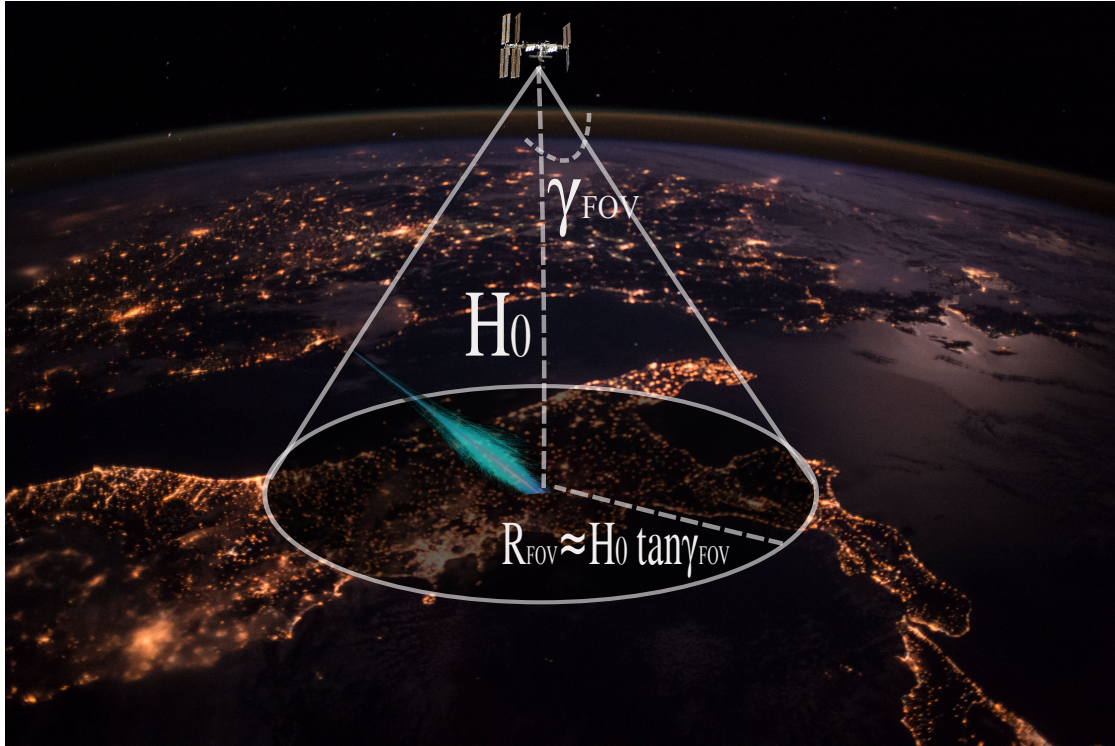


**Figure 2.1:** Artistic depiction of EUSO's concept of operation. UV light originated by the EECR's EAS, is observed from space. This allows for an unprecedented instantaneous exposure. Background image NASA<sup>i</sup>.

- ◆ The distance to the shower. Being so far away from the EAS reduces the signal to noise ratio. This increases the energy threshold for detection.
- ◆ The presence of light (man made or of natural source) and clouds can tamper the measurements, thus effectively reducing the exposure of the instrument.

This last point, the reduction of the duty cycle, plays a key role in the reduction of the total exposure of a space borne detector. Roughly speaking, a detector following an orbit with an altitude of  $\sim 400$  km and an inclination of  $\sim 51^\circ$  (basically the International Space Station's orbit) will have a duty cycle around 20 %. We will come back to a more detailed discussion of this effect later on. However, we must point out that even with its reduced duty cycle a space borne UHECR detector is still able to increase ten fold the exposure of current ground based experiments. The instantaneous monitored area  $S_{obs}$  is a function of the altitude of the detector ( $H_0$ ) and the solid angle subtended by its optics' field of view ( $\Omega_{FOV}$ ). It is expressed as:

$$S_{obs} = \Omega_{FOV} H_0^2 \quad (2.1)$$

<sup>i</sup>Earth Science and Remote Sensing Unit, NASA Johnson Space Center <http://eol.jsc.nasa.gov>

### 2.1.2 Scientific potential

Opening the window to the “particle” channel of astro-particle physics will enable the scientific community to address basic problems of fundamental physics and high-energy astrophysics. The first step would be to find the sources that are producing UHECR. This will help understand the propagation environment, from the source to the Earth, constraining the Galactic and extragalactic magnetic fields in the process. In addition, there will be the opportunity to probe the particle physics’ and particle acceleration mechanisms at energies well beyond the ones achievable in man-made accelerators.

A EUSO like design will allow more than  $10^5 \text{ km}^2 \text{ sr yr}$  annual exposure. With the fluxes discussed in § 1.3 and under current uncertainties, this exposure should amount up to 500-800 events above  $5.5 \times 10^{19} \text{ eV}$ . This expected amount of events should allow for the identification of individual sources by high-statistics arrival direction analysis. Once a potential source(s) is (are) identified, the next step would be the follow up measurement of its (their) energy spectra. In addition we would be able to search for counterpart object(s) with standard modern astronomical observations (visible, UV, X-ray etc.). These observations will provide constrains to the emission/acceleration mechanisms. Current statistics do not allow for a definitive identification of the sources. However, a EUSO-like experiment, like JEM-EUSO, with 10 times the annual exposure would in principle be enough to detect significant anisotropy in the EECR.

This was studied deeply in [Rouillé d’Orfeuil et al. 2014]. In the aforementioned paper, the authors sample galaxies in the 2MRS<sup>ii</sup> catalog, and simulate realistic UHECR maps using these galaxies as sources. It is important to note that the analysis is made on the global anisotropy of the sources (i.e. the average angular distances between two elements of the sample) and does not depend on their specific positions and structure. The 2MRS is used as seed catalog where realizations for a given source density (e.g  $n_s = 10^{-5} \text{ Mpc}^{-3}$ ) is randomly chosen. After simulating the propagation of EECR through the intervening magnetic fields, and taking into account energy losses and photo dissociation, they produce a series of “expected ” sky-maps for each realization. They then proceed to make an statistical study of the intrinsic anisotropy seen by exploring such maps with EUSO’s exposure and PAO’s exposure. We show their results for two example scenarios in Fig. 2.2. The first one is called **MC- 4 EeV**. It assumes a mixed composition case compatible with PAO composition observations, where the maximum energies are dominated by heavier nuclei ( $E_{max} = Z \times 4 \text{ EeV}$ ). Although this model agrees with the PAO composition trend, it requires a rather hard spectral index  $\alpha = 1.4$ . The second model, called **pure-Fe**, is a more pessimistic but “very unrealistic” iron dominated scenario. More scenarios and a larger discussion can be found in [Rouillé d’Orfeuil et al. 2014].

<sup>ii</sup> **2MRS** stands for **2MASS (Two Micron All Sky Survey) Redshift Survey**. It maps the distribution of galaxies and dark matter in the local universe, out to a mean redshift of  $z = 0.03$ . <https://www.cfa.harvard.edu/~dfabricant/huchra/2mass/>

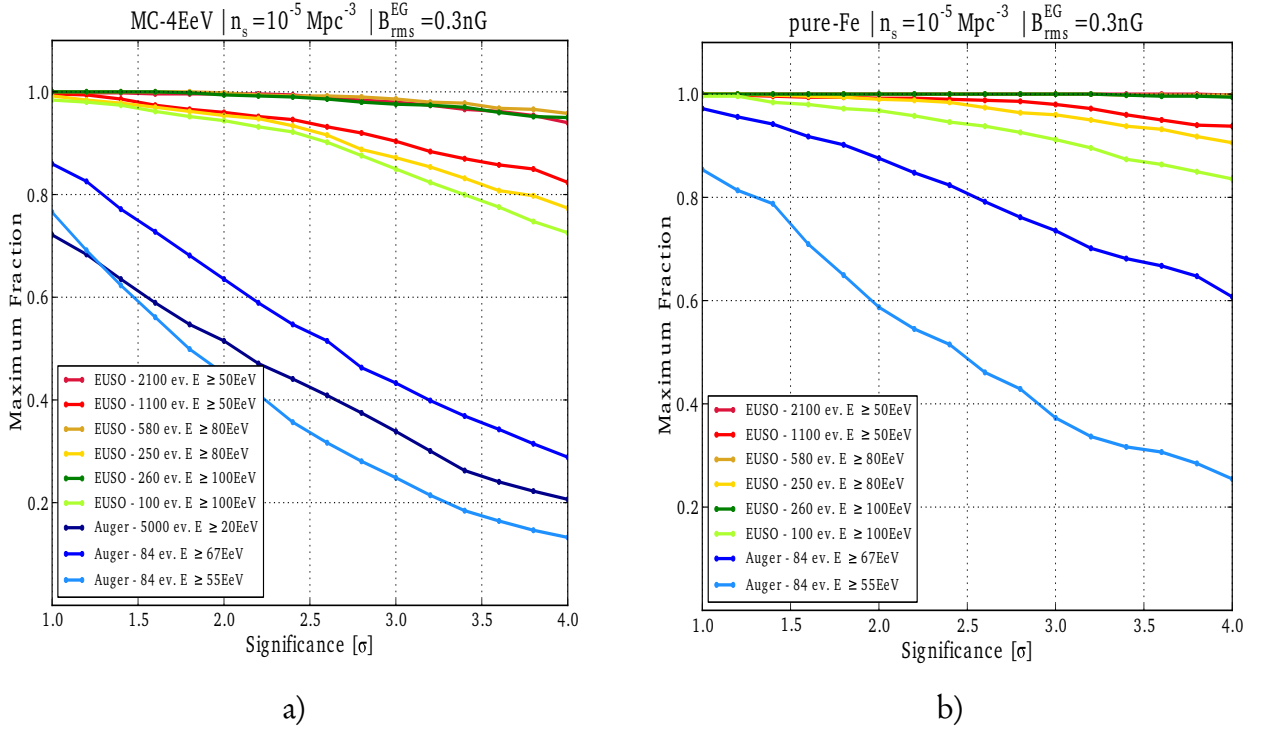


**Figure 2.2:** Fraction of realizations which yield anisotropic results with significance larger than the abscissa for a) 4 EeV model and b) **pure-Fe**, assuming the EUSO exposure. Different colors indicate different number of events above a certain energy. In blue are the results using the same realizations but with PAO exposure (and statistics). Reproduced from [Rouillé d’Orfeuil et al. 2014].

We mention these results now in context of the lack of a clear anisotropic signal in the PAO data [PAO 2015]. In the bottom panel of Fig. 2.3 we see  $f_{\text{min}}$ , the minimum of the fraction of isotropic simulations having an equal or higher number of pairs than the data, as a function of the distance to the objects D (drawn from the 2MRS catalog). In the same plot we see the post-trial probability P, defined as the fraction of isotropic simulations which lead to a value of  $f_{\text{min}}$  smaller than the one obtained with the data. As it can be seen, there is not a strong case for anisotropy. Which is in agreement with what is expected from Fig. 2.2.

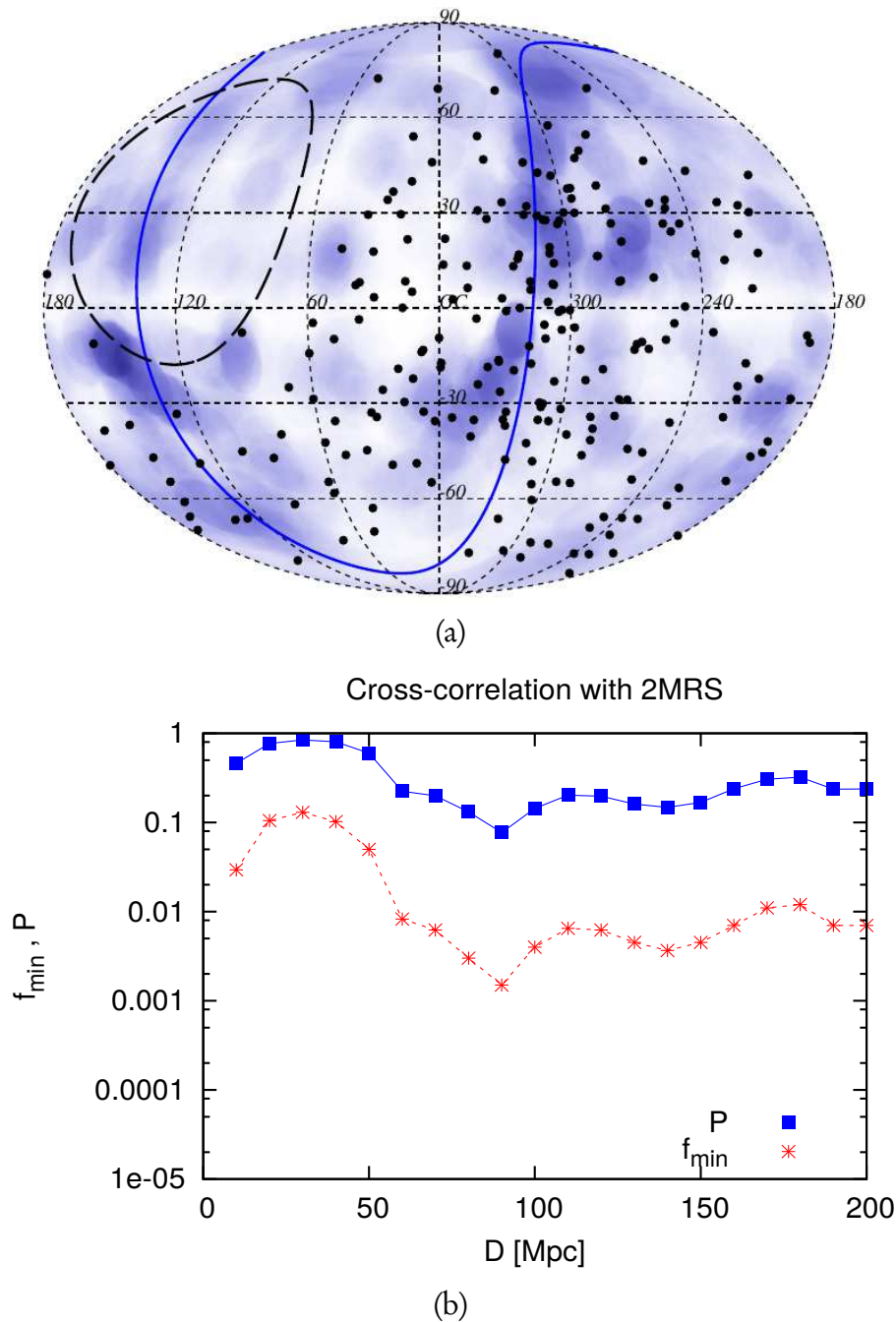


**Figure 2.3:** a) The sky distribution of PAO events with  $E > 52$  EeV (black dots) superimposed on top of the 2MRS objects (blue fuzzy circles). The blue solid line corresponds to the Super-Galactic Plane, and the dashed line is the field-of-view limit for the PAO. b) The values of  $f_{\min}$  and  $P$  (see text) as a function of the maximum distance  $D$  to the galaxies in the 2MRS catalog. Both figures are reproduced from [PAO 2015].

If sources can be identified, another fundamental scientific objective of a EUSO-like mission would be point-source analysis. This kind of study would also benefit enormously from the unprecedented exposure to achieve a high-statistics for this analysis.

Before concluding this overview on the scientific potential, we must mention that exploratory objectives will arise naturally, but depending on the specifics, for any EUSO-like instrument. For example the detection of extreme energy neutrinos and gamma rays, testing of Lorentz invariance and the systematic surveillance of atmospheric phenomena, among many others, constitute some of the possible exploratory objectives

## 2.2 The JEM-EUSO mission

We focus now our attention on the latest example of a mission following the EUSO concept: JEM-EUSO, the Extreme Universe Space Observatory on the Japanese Experiment Module [Adams et al. 2013a]. On-board the International Space Station (ISS), JEM-EUSO will orbit around the Earth approximately every 90 minutes at an altitude of 400 km. Under the current design considerations, JEM-EUSO could initiate a new field of astronomy and astrophysics using the extreme energy particle channel, by achieving more than  $10^5 \text{ km}^2 \text{ sr yr}$  above energies of  $7 \times 10^{19} \text{ eV}$  during its first three years of operation.

JEM-EUSO is a super wide ( $60^\circ$ ) UV-telescope which uses the Earth's atmosphere as the target mass for EECR. It observes transient luminous phenomena taking place in the atmosphere caused by particles coming from Space. Its observational aperture of the ground area is roughly approximated by a circle with a  $\approx 250 \text{ km}$  radius (see Fig. 2.1), and the monitored atmospheric volume is  $\sim 1 \text{ Tera-ton}$  or more. The instantaneous aperture of JEM-EUSO is larger than the PAO by a factor ranging from 65 to 280, depending on its observation mode.

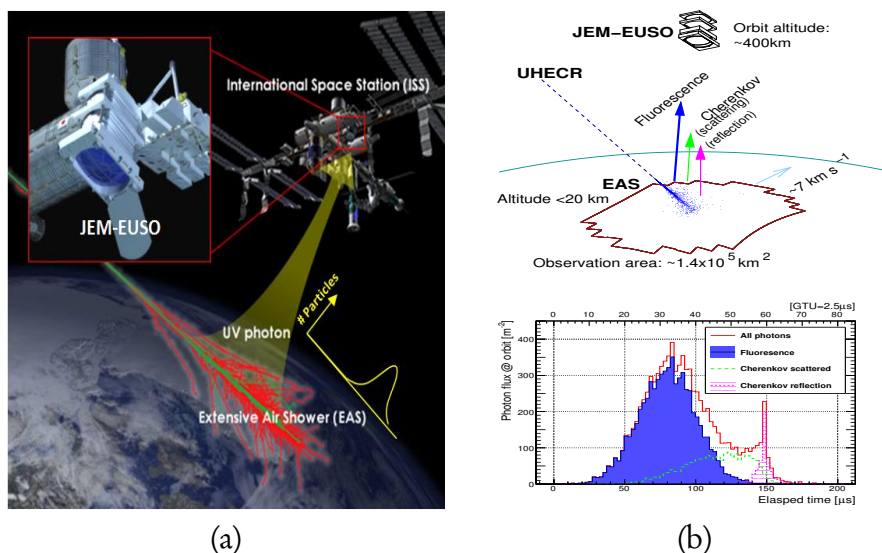


**Figure 2.4:** Artistic depiction of JEM-EUSO's operational principle. The “fluorescence signal” (UV light) produced by the EAS is captured by a telescope mounted on the ISS. Reproduced from [JEM-EUSO 2010] and [Adams et al. 2013a].

JEM-EUSO captures the moving shower front of an EAS. The shower front emits (via ionization processes) UV-photons which are scattered isotropically by the atmosphere. With the aid of its super wide Field of View (FOV), JEM-EUSO shall be capable of recording the EAS-track with a time resolution of  $2.5 \mu\text{s}$  and a spatial resolution of  $0.75 \text{ km}$  in the so called “nadir mode”. In “nadir mode” the telescope points towards the Earth’s atmosphere along nadir. JEM-EUSO is expected to observe the first few years in the “nadir mode”, afterwards to increase the exposure at higher energies the telescope will be then tilted, and will operate in “tilted mode”. This increment in exposure is shown in Fig. 2.5. The “tilted” mode, the threshold energy gets higher since the mean distance from the EAS core to the detector, as well as the atmospheric absorption and dispersion both increase. This effect was studied and quantified in [Fenu 2013] [Mernik 2014].

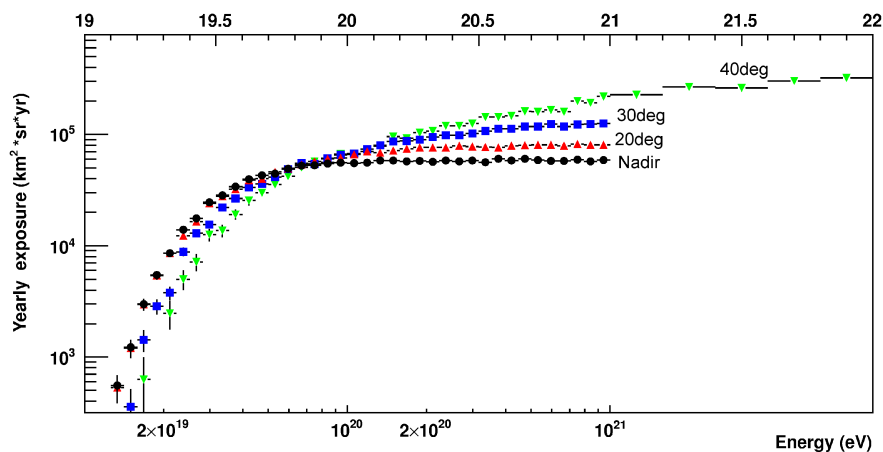


**Figure 2.5:** Modifications to the JEM-EUSO nadir exposure by tilting the instrument at  $20^\circ$  (red),  $30^\circ$  (blue) and  $40^\circ$  (green). Reproduced from [Fenu 2013].

### 2.2.1 Scientific Objectives and Requirements.

The scientific objectives of the mission are [Santangelo et al. 2013]:

- **Main Objective** To explore with high statistics the energy decade around and beyond  $10^{20}$  eV. This will have the side effect of the identification of sources of EECR. As discussed above only a few sources are expected to dominate this energy regime. Therefore, JEM-EUSO will study the anisotropy of the EECR sky. If sources are powerful enough, not only their identification may be possible but also the study of their energy spectra. And finally, the JEM-EUSO mission aims to study with high statistics the spectrum of CR with trans-GZK energies.
- **Exploratory Objectives** Depending on the nature of the EECR, the JEM-EUSO mission can contribute to:
  - i) the study of UHE- neutrinos.
  - ii) the discovery of UHE- gamma rays.

| Parameter   | Requirement                            | Comments  |
|---|--|---|
| Exposure<br>(in three years)  | $\geq 10^5 \text{ km}^2 \text{ sr yr}$ | Imposed by the goal to obtain statistics of hundreds of events above $5 \times 10^{19} \text{ eV}$ .                        |
| Angular Resolution<br>@ $E > 8 \times 10^{19} \text{ eV}$                               | $\leq 3^\circ$                         | To find the EECR sources, and to study the intervening magnetic fields.   |
| Energy Resolution<br>@ $E > 8 \times 10^{19} \text{ eV}$                                | $\leq 30 \%$                           | Expressed in 68% of the distribution. It is desirable to achieve this resolution even for $E > 6 \times 10^{19} \text{ eV}$ |
| $X_{max}$ determination error<br>@ $E > 10^{20} \text{ eV}$ and zenith angle $60^\circ$ | $\leq 120 \text{ g cm}^{-2}$           | Provides the capability to discriminate between nuclei, gamma rays, and neutrinos.  |
| Full-sky observation  | $\leq 30 \%$                           | Check the non-uniformity amongst both hemispheres.  |

**Table 2.1:** The main scientific requirements (see text) of the JEM-EUSO mission (extracted from [Santangelo et al. 2013]).

- iii) the study of the galactic and local extragalactic magnetic fields.
- iv) Atmospheric Science in the ultra violet part of the spectrum, i.e. characterization of the night-glow, of the slow UV-tracks associated to meteors and meteoroids, and of the transient luminous events (TLE).

The fulfillment of these objectives imposes requirements on the JEM-EUSO mission. For example, the first two exploratory objectives require the identification of the different atmospheric depths typical of each type of primaries, i.e. baryons, photons or neutrinos; the third exploratory objective requires the reconstruction of the arrival direction with sufficient precision. Quantify the required precision we arrive at the so-called *scientific requirements* of the mission. We provide a summary of the scientific requirements in Table 2.1

### 2.2.2 Optics and Focal Surface subsystems

We make two important distinctions in the subsystems of the instrument: the Optics & Focal Surface subsystems of the main UV telescope and the atmospheric monitoring subsystems. The former subsystems are more concerned with the acquisition of the UV signal whilst the latter subsystems are concerned with monitoring the target mass of the experiment. The parameters of Optics & Focal Surface subsystems are summarized in Table 2.2.

An artistic view of the main telescope and its components is shown in Fig. 2.6.

| Parameter                          | Value                             |
|------------------------------------|-----------------------------------|
| <i>Optics</i>                      |                                   |
| Optical aperture                   | 4.5 m <sup>2</sup>                |
| Ensquared collection efficiency    | 35%                               |
| Ensquared energy                   | 86%                               |
| Optical bandwidth                  | 300-430 nm                        |
| Field of view                      | 0.85 sr                           |
| Observational area (nadir mode)    | $1.4 \times 10^5$ km <sup>2</sup> |
| <i>FS detector and electronics</i> |                                   |
| Number of pixels                   | $3.2 \times 10^5$                 |
| Spatial angular resolution         | 0.074°                            |
| Pixel size at ground               | 0.51 km                           |
| Quantum efficiency                 | 41%                               |
| Collection efficiency              | 80%                               |
| Cross talk                         | <2%                               |
| Transmittance of UV filter         | 97%                               |

**Table 2.2:** The main parameters of the JEM-EUSO mission (extracted from [Bertaina et al. 2014]).

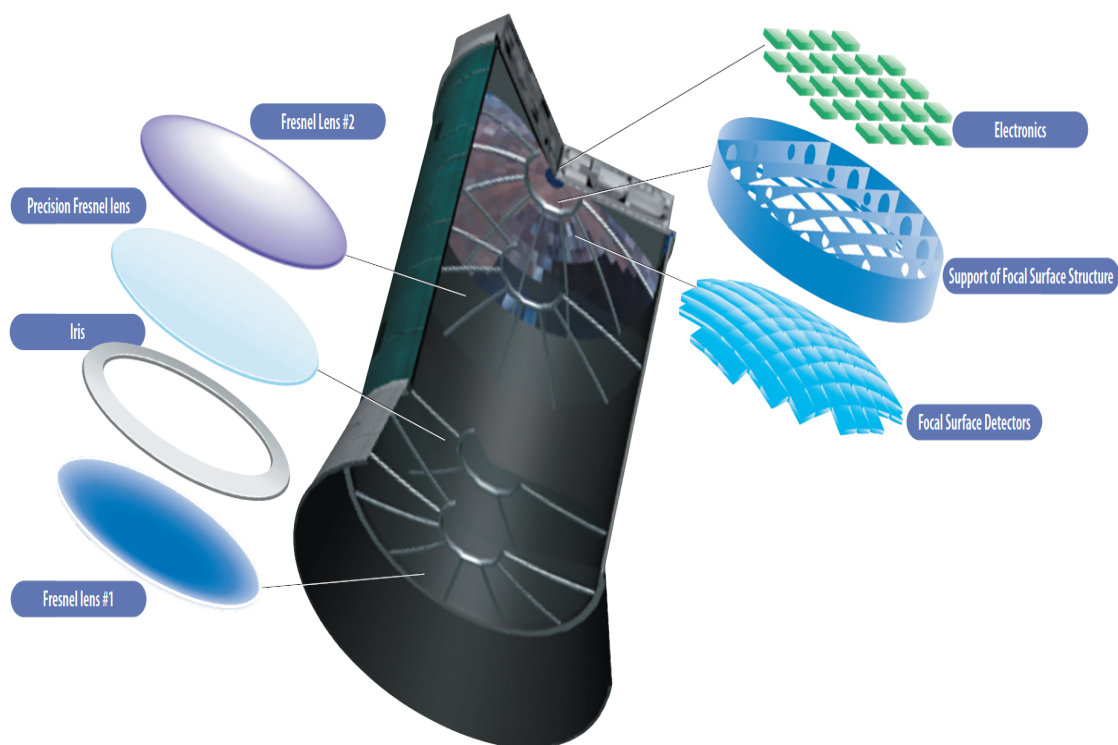


**Figure 2.6:** Artistic depiction of JEM-EUSO summarizing the optics and focal surface layout. Notice that the original cylindrically symmetrical concept of the telescope is illustrated. In order to fit the telescope into the Japanese transfer vehicle, the shape of the telescope had to be modified (see Fig. 2.4). Reproduced from [JEM-EUSO 2010]

### 2.2.2.1 Optics

As already stated, JEM-EUSO will consist of a refractive optics telescope which uses Fresnel lenses. The current (baseline) design is based on a refractive system made of two curved double-sided Fresnel lenses, plus an intermediate lens. The lenses material is PolyMethyl Methacrylate (PMMA) from Mitsubishi Rayon Co., Ltd. [Mitsubishi]. The intermediate lens, with a circularly symmetric diffractive surface on one side and a Fresnel surface on the other, compensates part of the chromatic aberration. An alternative material Cytop (an amorphous fluoropolymer) from Asahi Glass Co.,Ltd [Asahi Glass Co, Ltd.] has also been studied by the JEM-EUSO collaboration [JEM-EUSO 2010]. This option, an advanced option, replaces the front lens with a front curved double-sided Fresnel lens made out of Cytop. Even in this advanced option the PMMA-000 is still used for the middle and back lenses. The reason for this change in materials can be understood by comparing the transmittance of PMMA and Cytop in the UV (see Fig. 2.7). Cytop is also very resistant. However due to a higher cost and fragility Cytop was disfavored as the only material for the three lenses. The telescope's shape presents the so called "side-cut" feature. This is a modification from a traditionally cylindrically symmetrical telescope. To allow the telescope to maximize the collection area but also fit in the foreseen transfer vehicle (the Japanese HTV- "Kounotori" transfer vehicle [JAXA]) the circular optics are cut along one direction (see Fig. 2.8).

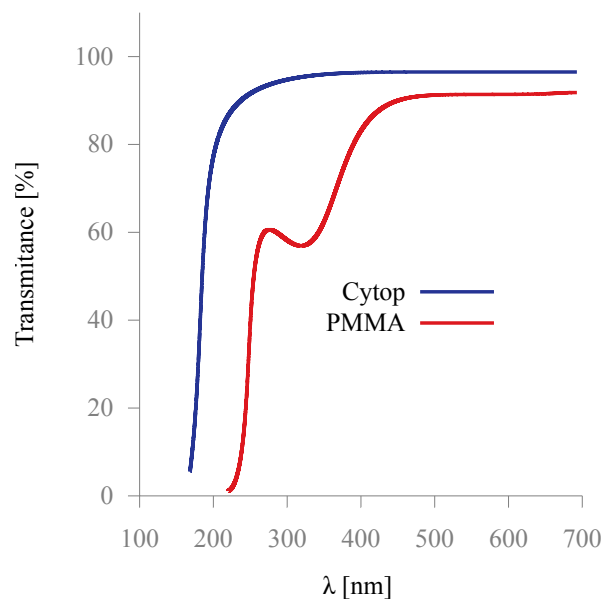


**Figure 2.7:** Comparison of PMMA's and Cytop's transmittance in the near UV/ visible. Data taken from [Asahi Glass Co, Ltd.].

### 2.2.2.2 Focal Surface

The Focal Surface (FS) of JEM-EUSO is deployed on a curved surface of about 2.35 m in diameter. Attached to this surface, are the photo sensitive electronics. The area of the sensitive portion

of the focal surface  $\sim 4 \text{ m}^2$ , whereas each pixel's area is  $\sim 8.29 \text{ mm}^2$ . In combination with the insensitive spaces in between pixels this means that JEM-EUSO will pixelize the FS with more than 300 000 pixels. JEM-EUSO focal surface is arranged in a hierarchy of smaller units which follow the rationale for the modular electronics developed for the mission. This hierarchy is illustrated in Fig. 2.8.

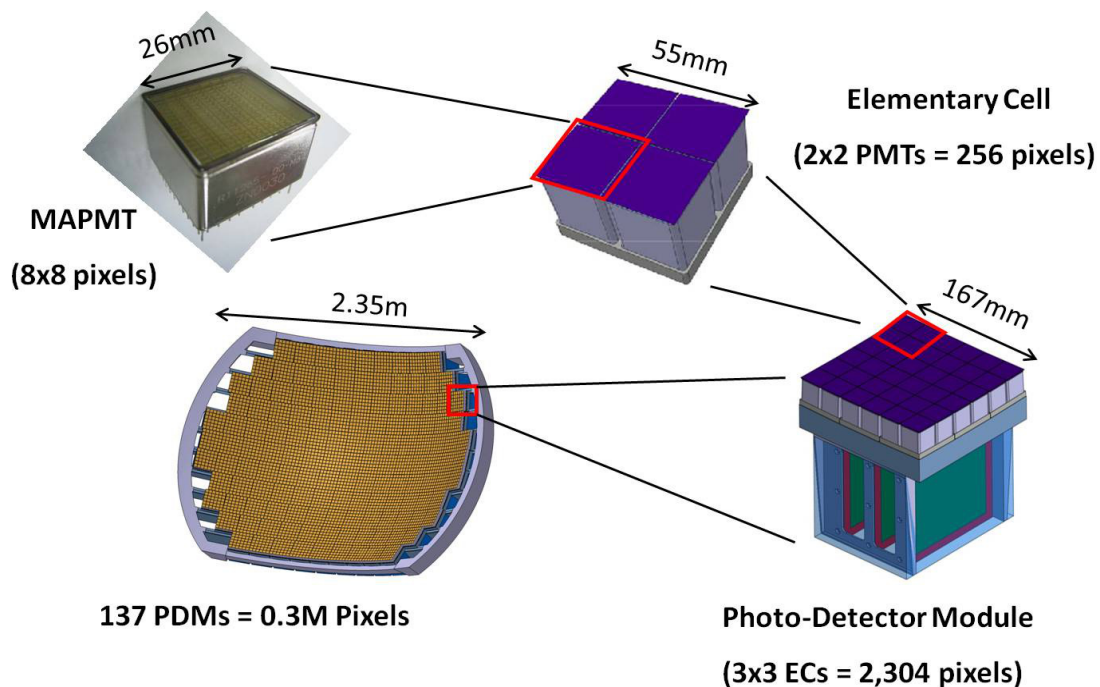


**Figure 2.8:** Focal surface detector and its structure. Reproduced from [Kawasaki et al. 2011].

The hierarchy of the FS, and its respective electronic counter part follows (specifics taken from [Kawasaki et al. 2011] and [JEM-EUSO 2010]):

- **Pixel** The smallest (abstract) detection unit is the pixel which is one individual anode from the multi-anode photomultiplier tube. There are 315 648 pixels. The current design's PMTs have a quantum efficiency of 30% and a gain of  $10^6$  at 900 V.
- **Multi-Anode Photo Multiplier Tube (MAPMT)** The MAPMTs taken for the current design are the Hamamatsu R11265-03-M64 model. This model has  $8 \times 8$  anodes on its base, where the signal is readout. This means that each MAPMT contains 64 pixels. The MAPMTs have a UV-glass transparent window. This window is covered by a UV filter to minimize the contamination from light sources with wavelengths outside the experimental range of interest.
- **Elementary Cell (EC)** An EC constitutes an array of  $2 \times 2$  MAPMTs. The MAPMT analog signal will be processed by a dedicated front end application specific integrated circuit (ASIC). For the JEM-EUSO mission this ASIC is named Spatial Photomultiplier Array Counting and Integrating Read-Out Chip (SPACIROC). The role of the SPACIROC will

be to perform the photon counting, charge to time conversion, apply suitable thresholds and digitalize the photon counters [Ahmad et al. 2012].

- Photo Detection Module (PDM)** The FS detector consists of 137 Photo-Detector Modules (PDMs), each of which is made off  $3 \times 3$  ECs. The first level trigger is implemented at the electronic PDM board. This trigger is called the persistent tracking trigger (PTT). The PTT looks for a signal persistence on the ECs. If the PTT is activated then the next level of trigger is carried out by the so called Cluster Control Board (CCB). The CCB will monitor simultaneously 8-9 PDMs, and when any one of them reports a level 1 trigger, then it applies the so called Linear Tracking Trigger (CCB LTT). The basic working principle of the CCB LTT is to integrate the photon counts along predefined directions. These directions are chosen to resemble the track that would appear as a consequence of the movement of the EAS front when projected onto the FS. More details on the dedicated triggering scheme can be found in [Bayer et al. 2013] and in [Fenu 2013]. The rationale of the electronics of the FS (including the trigger) is illustrated in Fig. 2.9.

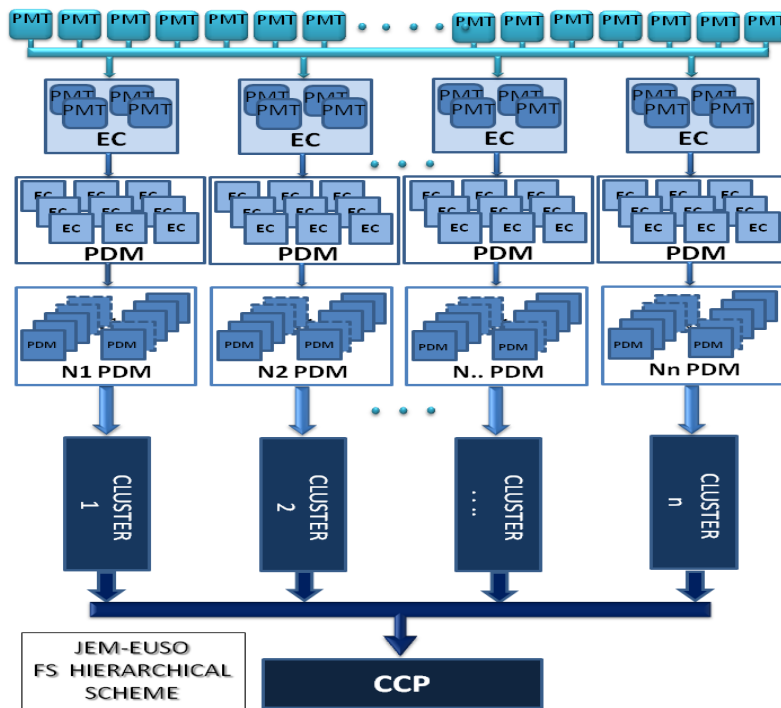


**Figure 2.9:** A diagram of the hierarchical scheme of the JEM-EUSO detector. Reproduced from [JEM-EUSO 2010].

As mentioned before the hierarchy of the FS follows the electronics design, which is intimately related to the trigger capabilities of the detector. These are constrained by telemetry constraints of the whole detector. We show the expected trigger rates for JEM-EUSO in Table 2.3.

|   | Trigger rate at FS [Hz] |
|---|-------------------------|
| 1 <sup>st</sup> trigger level (PTT)     | ~ 1000                  |
| 2 <sup>nd</sup> trigger level (CCB LTT) | ~ 0.1                   |

**Table 2.3:** Expected trigger rates for the 1<sup>st</sup> and 2<sup>nd</sup> level trigger.

### 2.2.3 Atmospheric Monitoring subsystem

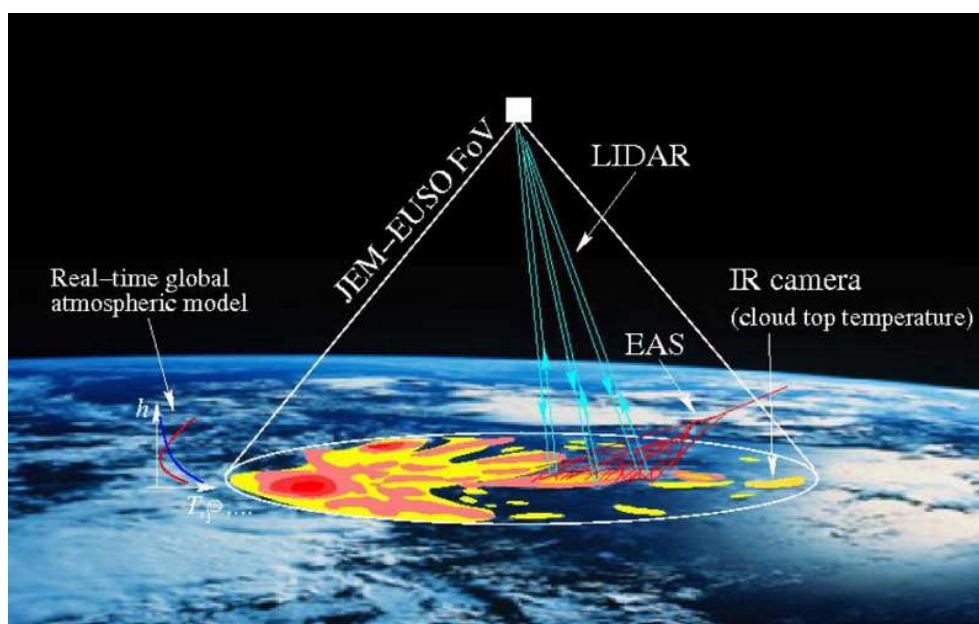


**Figure 2.10:** Atmospheric monitoring subsystem. Reproduced from [JEM-EUSO 2010].

As previously stated, JEM-EUSO will count on a state of the art Atmospheric Monitoring (AM) system to assess atmospheric conditions in the field of view of the JEM-EUSO main telescope. A conceptual illustration of the AM system is shown in Fig. 2.10. The role of the atmospheric conditions is of uttermost importance to properly assess the energy deposited in the atmosphere by the EAS. In addition, the correct knowledge of the cloud coverage by a proper AM system is necessary to estimate the effective observing time with accuracy, and also to increase the confidence level in the events just above the energy threshold of the telescope. The experiment's exposure also depends on the capacity of the AM system to recognize the different atmospheric conditions present (sometimes simultaneously) within the FOV.

#### 2.2.3.1 Infrared camera

The Infrared (IR) camera is a dual band bolometric imaging system used to detect the presence of clouds. The current baseline of the IR camera consists of a refractive optics made of germanium (Ge) and zinc selenide (ZnSe) and an uncooled micro-bolometer array detector. Plastic filters limit the wavelength band to 10-12  $\mu\text{m}$ . The emission in the IR will be translated into temperature

and subsequently into height by using dedicated cloud and atmosphere radiance models and/or profiles [Rodríguez Frías et al. 2013]. The main parameters of the IR camera are summarized in Table 2.5

**Table 2.4:** IR Camera Current requirements

| Parameter                     | Specification  |
|-------------------------------|--|
| Measurement temperature range | 200 ÷ 300 K (accuracy of 3 K)                          |
| Wavelength                    | 2 bands 10 ÷ 12 $\mu\text{m}$ plus one for calibration |
| Angular Resolution            | 0.25°  |
| Number of pixels              | 320 × 340  |

**Table 2.5:** Specifications of JEM-EUSO's IR [Toscano et al. 2014].

### 2.2.3.2 Lidar

Complementing the IR-camera, and providing a deeper understanding of the vertical structure of the cloud top, a lidar is contemplated to make measurements at specific points within the JEM-EUSO's FOV. This will determine the cloud-top altitude with high accuracy in a more robust way since this technique does not depend on a temperature-height model of clouds present in the atmosphere. Also this technique is, in principle, more capable of detecting optically thin clouds (or clouds with low IR radiance). The idea is to shoot a Nd:YAG laser, exciting its third harmonic ( $\lambda = 355 \text{ nm}$ ). As the receiver element of the LIDAR, the JEM-EUSO telescope itself will be used to detect the backscattered signal. The expected LIDAR design parameters are summarized in Table 2.6 [Toscano et al. 2014]. The ranging (distance estimation) resolution for the lidar is set by the timing resolution of its receiver unit. In this case JEM-EUSO's FS is the receiver unit which will translate the signal from its time domain to the corresponding distances. In the current design the timing resolution is expected to be 2.5  $\mu\text{s}$ . This unit of time is referred to as a Gate Time Unit (GTU). Therefore the lidar for the JEM-EUSO system has range resolution of 375 m. This and other parameters of JEM-EUSO's lidar are listed in Table 2.6.

| Parameter        | Specification               |
|------------------|-----------------------------|
| Wavelength       | 355 nm                      |
| Repetition rate  | 50Hz                        |
| Pulse width      | 5 ÷ 15ns                    |
| Pulse energy     | 20 mJ/pulse                 |
| Beam divergence  | 0.1 mrad                    |
| Detector         | MAPMT(JEM-EUSO's telescope) |
| Range resolution | 375 m                       |

**Table 2.6:** Specifications for the JEM-EUSO Lidar [Toscano et al. 2014].

### 2.2.3.3 Global Light System and ground calibration

It is foreseen to provide JEM-EUSO with a system of UV-leds to perform an on-board calibration of the instrument. However this will be enhanced by a dedicated system of ground calibration. This system is called the Global Light System (GLS). The GLS is a combination of ground-based xenons flash and lamps, and UV lasers. Unlike the signal from natural UV-sources (EECR, auroras, lighting, albedo. etc), the elements of the GLS will provide calibrated signals whose precise luminosity, timing, and direction is well known. A total of 12 ground based sites is foreseen in the current design of the GLS [Adams et al. 2013b]. These sites will be chosen for low background light and distribution along different latitudes within the range of the ISS's orbit. All of the sites will have calibration flash lamps, while only half will have a UV-laser. It is also envisaged to mount an airborne GLS unit inside a P3B Orion aircraft to be deployed monthly from Wallops Flight Facility/ NASA. The main characteristics of the GLS are summarized in Table 2.7.

| GLS Unit | Sources                 | Number | Specifications   |
|----------|-------------------------|--------|--|
| GLS-X    | Xe Flash-Lamps (XF)     | 6      | Hamamatsu model L6604 fitted with filters to pass $\lambda = 357, 337 \text{ \& } 391 \text{ nm}$ only. Flash duration $\sim 24 \mu\text{s}$ |
| GLS-XL   | XF and Laser            | 6      | A 5 mJ laser with $\lambda = 355 \text{ nm}$ and $0.25^\circ$ pointing accuracy.   |
| GLS-AXHL | XF and Laser (Airborne) | 1      | Flights to be conducted on a monthly basis over the ocean at different altitudes   |

**Table 2.7:** GLS units and specifications from [Adams et al. 2013b].

## 2.3 The EUSO pathfinders

### 2.3.1 EUSO-Balloon

On August 24<sup>th</sup> 2014 the first down-scaled prototype of JEM-EUSO was launched from the Timmins Stratospheric Balloon Base of the Canadian Space Agency by the French Space Agency CNES (Centre National d'Études Spatiales) [EUSO-Balloon 2015]. The launch and a sketch of the payload is shown in Fig. 2.11. The EUSO-Balloon flew at an altitude of  $\sim 36 \text{ km}$  and tested the JEM-EUSO's detection principle [EUSO-Balloon 2013]. It consisted of a scaled down version of the JEM-EUSO's telescope, with a squared FOV of  $12^\circ \times 12^\circ$ . The same material

and manufacturing process was used to produce the fresnel lenses of the balloon instrument. Although in the last moment only two lenses were used. On the electronics side, only a single PDM was present in the focal surface. This is the smallest detection unit within the JEM-EUSO's modular design. Also, a calibration light system (a laser and a flasher) was flown on board a helicopter underneath the balloon. The scientific goal of the mission was to measure the UV background (albedo) of different terrains. The calibration lights provided laser "events" which demonstrated with measurement the feasibility of detecting UHECR with the system proposed by the JEM-EUSO collaboration. In §6 we discuss some statistical analysis, proposed to be done once the calibration data is produced and validated.

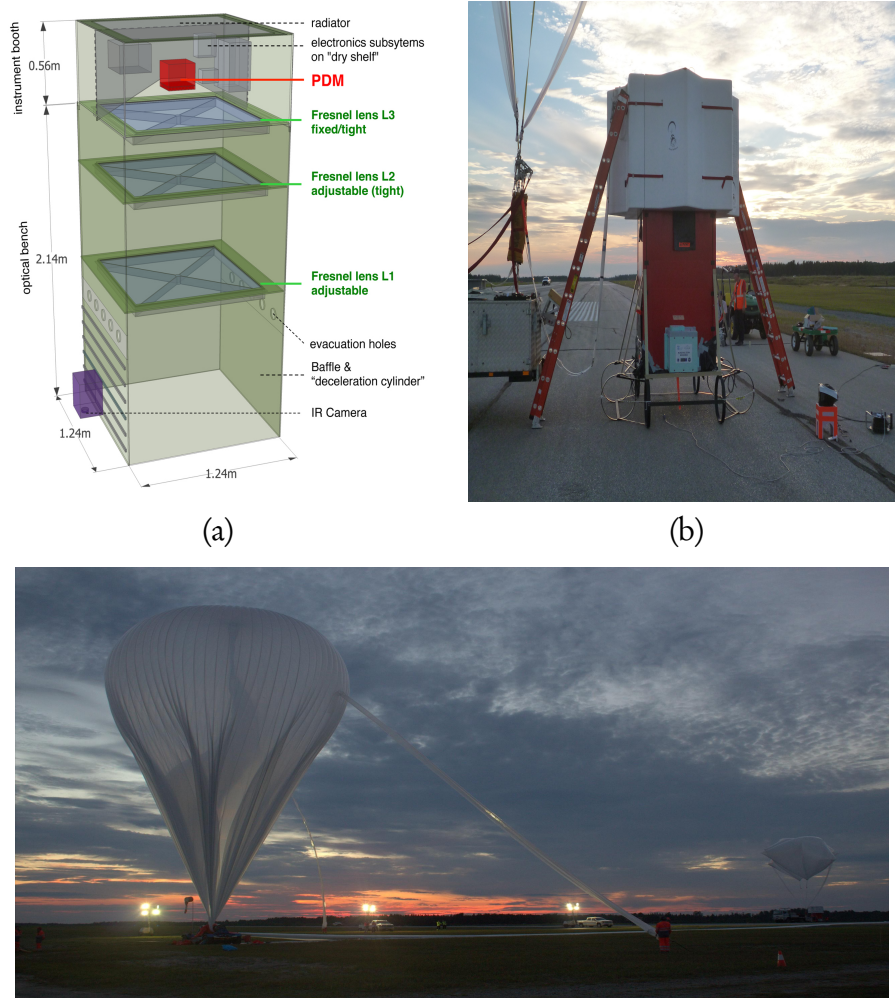


**Figure 2.11:** *Upper panel:* a) A diagram showing the inner structure of the instrument. Reproduced from [Dagoret & Mot 2014], and b) the EUSO-balloon gondola. Image credit Karine Mercier. *Lower panel:* EUSO-Balloon minutes before launch. Image credit Michael Wille.

### 2.3.2 Mini-EUSO

Another pathfinder for the JEM-EUSO mission will be the so called Mini-EUSO on board the ISS [Mini-EUSO 2015]. Once again a down scaled version of the telescope will be attached to one

PDM. The electronics and data readout system will be similar, though not exactly the same as the ones used in the balloon, and possibly closer to the final version of the JEM-EUSO mission electronics (see Fig. 2.12). Due to its small size, the Mini-EUSO can be transported in any of the regular resuppliers of the ISS. Once in orbit, the detector will be flying inside the pressurized Zvezda Russian module on board the ISS (see Fig. 2.12). This module has a 16'' transparent window for nadir mode observations of the Earth [NASA 2000]. The Fresnel lenses will have a 25 cm diameter, which is considerably smaller than JEM-EUSO proper. However, this mission will boost the technical readiness level of the JEM-EUSO consortium and will perform background UV light measurements at the same height and with the same orbital characteristics as the main mission. It is also foreseen to use the GLS for a better estimation of the performance of the detector.

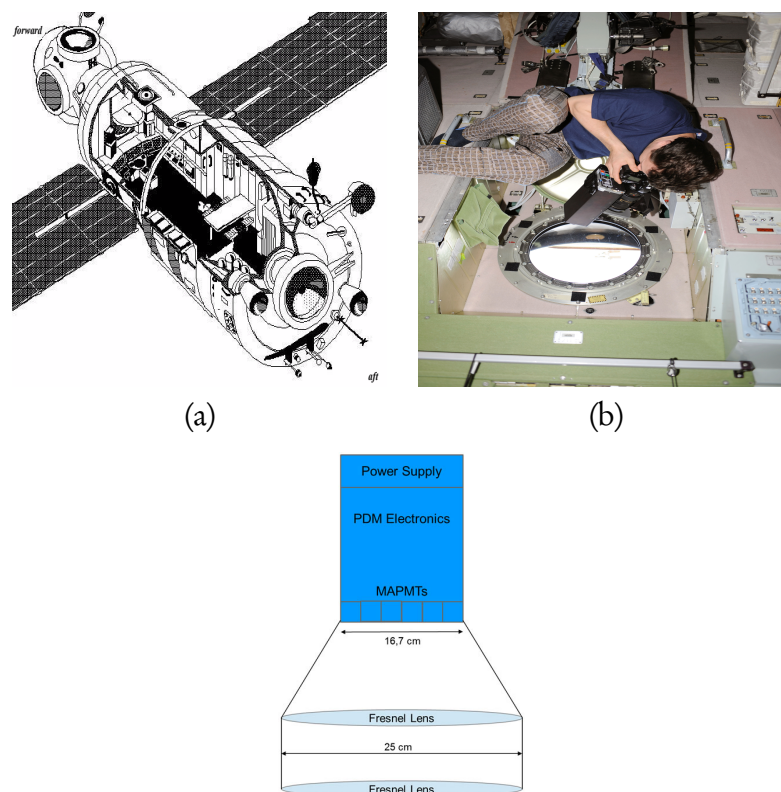


**Figure 2.12:** *Upper panel:* a) The Zvezda service module. Reproduced from [NASA 2000]. b) The nadir looking window that is foreseen to allocate the mini-EUSO experiment. Reproduced from [NASA 2009]. *Lower panel:* An schematic representation of the Mini-EUSO instrument. Reproduced from [Mini-EUSO 2015].

## 2.4 Other EUSO like missions

It is often the case in space investigation that alternative designs of the same mission co-exist and even are co-developed before a final decision is taken. Albeit, this does not pertain solely to space industry or space missions. Within this context we introduce the currently (as of 2015) alternative designs: the so called “EUSO like missions”.

### 2.4.1 SpaceX EUSO



**Figure 2.13:** The Dragon spaceship berthed to the International Space Station. Image reproduced from [Dragon].

Since the retirement of the space shuttle fleet from service, commercial private companies have been contracted by NASA to resupply the ISS. One such company is the Space Exploration Corporation or SpaceX [SpaceX]. The SpaceX EUSO mission would use a Dragon spacecraft to bring the main telescope to the ISS [Adams et al. 2013c]. Due to the different characteristics of this vehicle a version of JEM-EUSO without side cuts could be flown. This new configuration of the JEM-EUSO mission is called the *dragon configuration*. Preliminary results lead to the conclusion that this will have a positive impact on many scientific aspects of the mission; particularly on the angular reconstruction [Mernik 2014]. The main reason for this is, that the detectors response is expected to be more uniform across the entire FOV and suffer less from *border* effects that arise when a EAS occurs in the border of the FOV. In the present work, we performed our simulations studies using this dragon-configuration and compared our results with what was published in [Adams et al. 2013a].

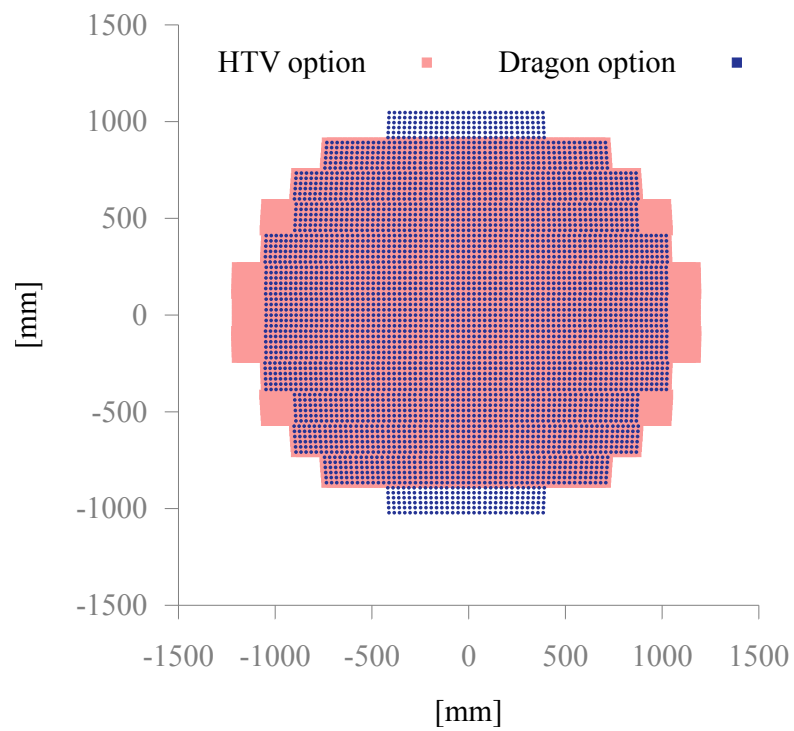


**Figure 2.14:** The reallocation of the FS elements in the SpaceX EUSO design. In blue are shown the positions of the MAPMT superimposed on the outline of the FS for the HTV configuration. It can be seen that the newer design is more symmetric whilst conserving the monitored area.

### 2.4.2 K-EUSO

A Russian space observatory similar to the JEM-EUSO concept has been around since the beginning of the 21<sup>st</sup> century [Khrenov et al. 2001]. The main experiment is called KLPVE (original Russian acronym for extreme energy cosmic rays) or KLYPVE to facilitate its pronunciation to non-Russian speakers [Khrenov et al. 2004]. It is based upon another Russian prototype called TUS (Tracking Ultraviolet Setup). The main difference between EUSO and KLPVE/TUS is the optics. KLYPVE/TUS relies on a segmented fresnel mirror to collect the incoming UV light onto the photo sensitive components of the detector [Panasyuk et al. 2014]. A preliminary artistic conception of the instrument can be appreciated in Fig. 2.15. The original KLPVE mission was also foreseen to be attached to the ISS, though in this case to the Russian segment of the ISS.

The preliminary design stage of the KLYPVE reflector type telescope for EECR measurements has already been concluded at the Skobeltsyn Institute of Nuclear Physics of Moscow State University in 2012 [Panasyuk et al. 2014]. The mirror has a reflective surface of about 10 m<sup>2</sup> and the FOV a diameter of 15°. The angular resolution (in this case pixel size) was estimated to be around 5 mrad. This milestone however revealed some new problems, the observation area and image quality would not allow good enough reconstruction of the principal EECR parameters (energy and arrival direction). The changing (increasing) spot size was found to be the culprit of this reduced quality. In 2013 a joint working group with the JEM-EUSO collaboration, proposed the addition of a corrective element to eliminate off-axis chromatic aberration. A PMMA Fresnel lens was introduced into the telescope system thus improving the spot size of the optical system [Panasyuk et al. 2014]. Many design parameters are still to be fixed. These parameters optimal configuration depends on the size and complexity of the forms of the individual optical elements (e.g. grooves of the fresnel lenses, focal length, mirror area, etc). This new concept is called the **K-EUSO** project.

Within the K-EUSO system there is already a baseline system concept. Its main characteristics are (taken from [Panasyuk et al. 2014]):

- Diameter of the reflector and the lens-corrector equals 3.4 m and 1.7 m respectively.
- The length of the system (see Fig. 2.15) is 4 m.
- FOV has a maximum size of  $\pm 14^\circ$ .
- The pixel spot on ground is  $\sim 0.4$  km.

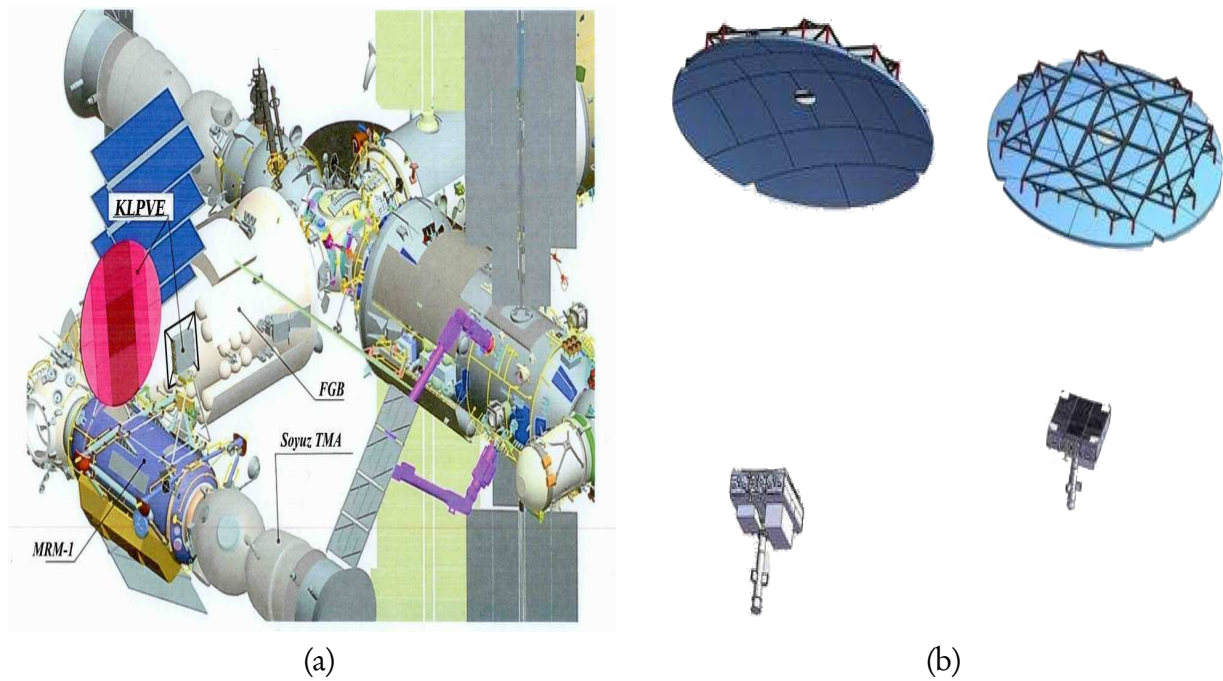


**Figure 2.15:** a) KLYPVE segmented mirror-concentrator and photo-detector. Viewed from the front side and viewed from the rear side. b) The foreseen docking spot on MRM1 on-board the Russian segment for the ISS. Both images reproduced from [Panasyuk et al. 2014].



# 3

## SIMULATING THE EUSO MISSION

---

### Contents

---

|       |  |    |
|-------|--|----|
| 3.1   | The EUSO Simulation and Analysis Framework . . . . . | 57 |
| 3.2   | The simulation chain: <i>Simu</i> . . . . .          | 58 |
| 3.2.1 | Light To Euso . . . . .                              | 59 |
| 3.2.2 | Detector simulation . . . . .                        | 60 |
| 3.3   | The reconstruction chain: <i>Reco</i> . . . . .      | 63 |
| 3.3.1 | Pattern recognition . . . . .                        | 64 |
| 3.3.2 | Angular Reconstruction . . . . .                     | 65 |
| 3.3.3 | Energy Reconstruction . . . . .                      | 72 |

---



## 3.1 The EUSO Simulation and Analysis Framework

The EUSO Simulation and Analysis Framework (ESAF) was developed with the aim to provide the necessary software tools to perform studies for any EUSO-like mission [Berat et al. 2010]. Its development began at the time of the phase-A review of the former EUSO mission. It is structured in a modular scheme and its purpose is to provide an end-to-end simulation of the whole mission. A conceptual sketch of the different processes involved in the simulations is shown in Fig. 3.1. The different modules deal with different aspects of the simulation chain, taking into account the relevant physical processes. The chain includes (but not exclusively): the UV-light production, light transmission in the atmosphere, photon-tracking inside the optics of the detector, the electronics response, the trigger algorithms, filtering and energy/angular reconstruction. To achieve this outstanding amount of intrinsically-different tasks, ESAF takes full advantage of its modular design. To begin with, ESAF is divided in two main components: *Simu*, which is designed for the simulation part; and *Reco*, which deals with the reconstruction of the simulated/measured data. In the following section we further describe *Simu* and *Reco*.

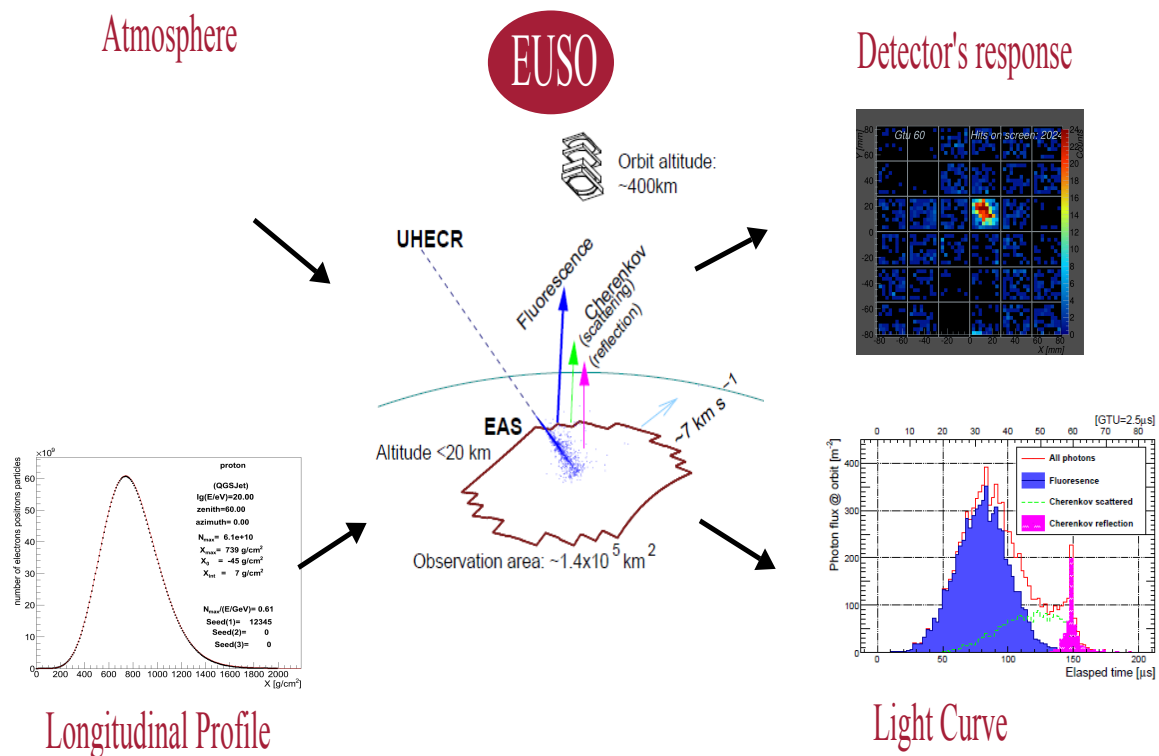
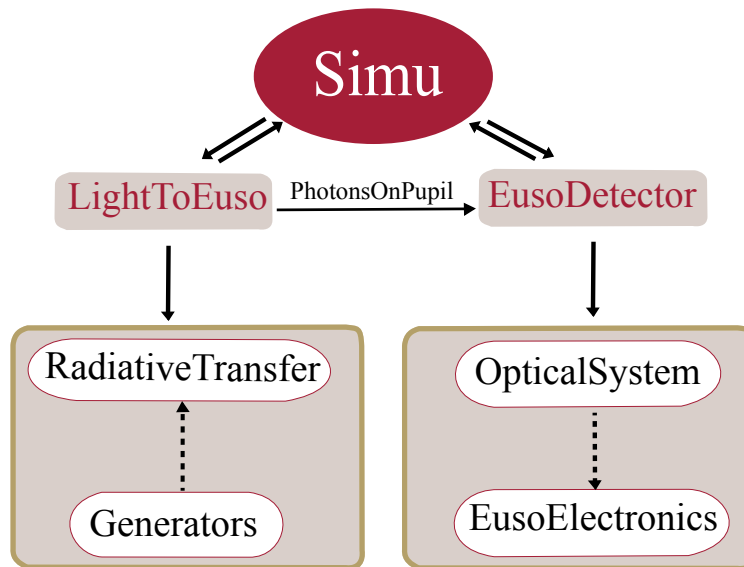


Figure 3.1: An illustration of the concepts involved in the simulations with ESAF.



**Figure 3.2:** The general structure of *Simu* as included in ESAF.

## 3.2 The simulation chain: *Simu*

The simulation chain is performed by the *Simu* program. *Simu* is the part of ESAF which for simulating the behavior of EUSO-like instruments in the presence of specific physical phenomena (EAS-tracks, lighting, Earth's UV albedo, etc.). A conceptualized sketch is shown in Fig. 3.2. In this figure we can distinguish the two main components of *Simu*: light production and propagation (*LightToEuso*), and the detector simulation (*EusoDetector*). The output produced by a *Simu* execution is contained in three files:

- *simu.ConfigDump.cfg*. A configuration summary for the ESAF run at hand (configuration dump).
- *simu.log*. A log file of the runtime messages produced during execution of the *Simu* program.
- *simu.root*. This file contains the information saved by the different modules called during the *Simu* run. Hence, its content depends on the intention of the aforesaid modules to save data to this file. For example the most common information blocks, to name a few, are: the simulated EAS main characteristics, a list of photons in the atmosphere with their properties, the history of the photons before and after propagation through the optics, the trigger results of the simulated events, as well as the photon-counts from the FS electronics. The general concept is shown in Fig. 3.1. We will be referring to the photon-counts detected in the whole detector taken as a function of time, with the term *light curve*. This concept is illustrated in Fig. 3.3.

### 3.2.1 Light To Euso

This part of *Simu* is in charge of creating a light source object within the framework and propagate the source's photons to the entrance pupil of the detector. The output of this process is delivered to the next stage of the simulation via the list of *PhotonsOnPupil*. It is separated into two main components:

- ◇ **Light Source Generators.** In ESAF, as well as in nature, light sources are not limited to fluorescence traces induced by an EAS. Alternative light sources are also implemented, not only to test the simulation chain, but to assess the performance of the EUSO telescope under different conditions. For example a meteor and/or its fireball can occur within EUSO's operating time. Therefore a suitable light source has been coded and implemented into ESAF. Artificial light sources with the potential of simulating calibration lights (see §2.2.3.3) are provided in ESAF as well. Within the scope of this work, the most relevant light source generator is an EAS. Therefore, we make a more detailed description of the EAS, the physics within, and the induced ultraviolet photon yield in §4.1.3. For the moment, we introduce the standard EAS generator within ESAF, i.e. SLAST [Naumov 2003]. SLAST stands for *Shower Light Attenuated to Space Telescope* and uses the so-called GIL parametrization (Greisen-Ilina-Linsley) for the number of electrons  $N_e$  on the shower front as a function of the shower age  $s^*$  [Ilina et al. 1992] [Berat et al. 2010]. Namely:

$$N_e(s^*) = \frac{E}{N_{E_0}} e^{(t(1-2\log s^*) - t_{max})} \quad (3.1)$$

Where:

$$t = \frac{X - X_0}{X_{int}}, \quad s^* = \frac{2t}{t + t_{max}}, \quad t_{max} = 1.7 + 0.76 \left( \log \frac{E}{0.81e8} - \log(A) \right)$$

Here  $X$  and  $X_0$  are the shower's slant depth and first interaction point.  $E$  and  $A$  are the primary's energy and atomic mass number, while  $X_{int}$  is a scaling factor related to the interaction length of the shower (in grammage).  $N_{E_0}$  is a normalization factor with units the units of  $[\frac{eV}{N_e}]$ .

We point out the non-standard definition of shower age  $s^*$ . Although at the shower maximum  $s^* = 1$ , the limit  $\lim_{X \rightarrow \infty} s^* = 2 \neq 3$ . This is not the case for other standard definitions of shower age [Matthews et al. 2010]. All the numeric constants are "semi-empirical" constants that reproduce the output of full MC codes [Ilina et al. 1992].

Although interfaces to other existing EAS codes (e.g. CORSIKA [Pierog & Heck 2011]) are available, till 2015 the standard within ESAF is still SLAST.

One of the main outcomes of the present work was the implementation, testing and validation of a CONEX to ESAF interface to simulate with EAS more realistic showers and to provide a more coherent shower description throughout the code. We will explore this in

detail in §4.1.3

- ◇ **Radiative transport.** Within ESAF the propagation of photons across the atmosphere until the detector's entrance pupil is accomplished by this module. There are two main versions of this process: the *Bunch transfer algorithm* and the *Monte-Carlo* multiple scattering algorithm.

The *Bunch transfer algorithm* takes into account just the leading scattering at the emission site of the photons. The individual photons are grouped in so-called bunches. Each bunch is rescaled with the fraction of photons emitted directly in the direction of the detector. A probability of survival, based on absorption and scattering in the atmosphere, is assigned to each bunch and “reconstructed” at the detector's pupil. This procedure is particularly tuned for EAS. The bunches are defined at different points along the longitudinal development of the EAS. This method also takes care of the ground-reflected Cerenkov photons and of the first-scattered Cerenkov photons.

The *Monte-Carlo* algorithm is a much more computing intensive algorithm, that tries to reproduce nature more truthfully. Besides propagating photons which are originally emitted towards the telescope, this module simulates the scattering up-to  $N$  times ( $N^{th}$ -order scattering) of other photons. The MC method rejects photons which are not scattered at all (but also not emitted towards the detector), not scattered  $N$  times, not scattered in the detector's solid angle, or not transferred to the detector (absorbed). Performing the previously mentioned process for the  $\sim 10^{15}$  photons produced in average by a  $10^{20}$  eV EAS would make the computing time involved excessive for any practical purpose. To reduce the number of photons to be tracked, an assumption is made: at a given maximum height ( $h_{max}$ ) the atmospheric density becomes low enough that photons propagating towards the detector suffer insignificant scattering [Berat et al. 2010]. This height (typically taken to be 30 km), introduces a minimum distance from the top of the atmosphere till the detector. This distance ( $D_{min}$ ) and the sensitive surface of the detector ( $S_{det}$ ), define a maximum solid angle  $\Omega_{max} = \frac{S_{det}}{D_{min}^2}$ . The probability of a photon scattering towards the detector has a maximum at:

$$P_{max} = \Phi_{max} \Omega_{max}$$

where  $\Phi_{max}$  is the maximum of all the phase functions in the simulation. Taking the Poisson distribution as a limit to the binomial distribution, the original number of photons available for propagation ( $N_0$ ) is reduced to  $N_{red} = Poisson(N_0 \Phi_{max} \Omega_{max})$  [Berat et al. 2010]. The net effect accounting for higher orders of scattering is both a spatial extension on the FS and a bigger time window of their arrival times. Nevertheless, multiple-scattered photons will not be distinguishable from the background photons, because they arrive relatively uncorrelated at the focal surface. Studies about the impact of these higher scattering were studied in [Mernik 2014], in the scope of angular reconstruction. We will come back to this topic and discuss its effects on pattern recognition in section 4.1.2.

### 3.2.2 Detector simulation

This part of *Simu* is designed to simulate the UV telescope of any EUSO-like mission. This part of ESAF is closely related to the specifications of the actual detector at hand (optics type, focal

surface layout, electronics, etc.). To fix our example, we focus on the JEM-EUSO detector as implemented in ESAF.

- ◇ **Optical Sytem.** This module is responsible for the internal transport of each photon arriving at the entrance pupil of detector. This process is sometimes referred as “ray-tracing”. It begins with a list of *PhotonsOnPupil*, and proceeds to propagate them through the optics and provides a list of the photons at the focal surface. Within ESAF there are mainly two categories of the available ray-trace options: an ESAF-native implementation of the Optical System or a likewise implementation with GEANT4 [Geant4 Collaboration 2003]. Both options account for different performance of the optics as a function of wavelength, incident angle and position at entrance pupil of the photons being propagated. The GEANT4 option is the newest implementation of an optical system and was not used in the studies presented in this work. We used the so called *RIKEN raytrace code*; specifically the *NOpticalSystem*. For even faster simulations there are options which perform almost no ray-tracing and are just parametrized versions of the behavior of the optics [Fenu 2013]. It is important to mention that in order to avoid spending unnecessary CPU time, background photons are not propagated through the detector. Instead of that, a poissonian background is randomly added at the electronic level (see below). The mean value of this poissonian background is a configurable parameter of the simulation and it is typically taken as 1.2 counts per pixel per GTU.
- ◇ **EuSoElectronics.** The electronics simulation aims to reproduce the behavior of the electronic hardware responsible for the transformation of photons impinging on the FS to electronic signals. The end product, which is saved to the *simu.root* file, is the *telemetry* of the event at hand. The latter consists basically of a list of photon counts with their respective timing and position information. One of the most important tasks performed by this module is the application of the trigger algorithms on the detected signals [Fenu 2013]. The electronics simulation begins translating the photons at the FS into an electronic signals (in current). To decide if a photon created a signal, a random number between 0 and 1 is compared with the detection efficiency  $\varepsilon_{phdet}$ . The detection efficiency consists of 3 factors:

$$\varepsilon_{phdet} = \varepsilon_{quant}(\lambda) \times \varepsilon_{ang}(\vartheta) \times \varepsilon_{collec}(Pixel) \quad (3.2)$$

In this last expression  $\varepsilon_{quant}(\lambda)$  is the quantum efficiency of the pixel, at least the part which depends solely on the wavelength of the photon. This quantity represents the probability that an electron is expelled by the photo-cathode when hit by a photon of wavelength  $\lambda$ . The quantum efficiency also depends on the photon’s incident-angle, although to a lesser extent. This dependence on the incident angle is taken into account by the factor  $\varepsilon_{ang}(\vartheta)$ . In ESAF all pixels are taken to have the same value of  $\varepsilon_{quant}(\lambda)$ . For  $\lambda$  between 300-400 nm,  $\varepsilon_{quant}(\lambda)$  varies between 0.35 and 0.42. Whereas the values for  $\varepsilon_{ang}(\vartheta)$  decrease monotonically from 1 to 0.95 for  $\vartheta$  between  $0^\circ$  and  $60^\circ$  [Fenu 2013]. After an electron is expelled by the photo-cathode it is still necessary to focus it onto the anode. This is expressed by the quantity  $\varepsilon_{collec}(Pixel)$ , which in principle depends on each pixel’s capacity to collect the electrons expelled by the photon. This value must be measured for each pixel. In this work we used a version of ESAF which sets  $\varepsilon_{collec}(Pixel) = 0.8$  for all pixels. After a photon creates a signal (in current), this signal must be translated into photon-counts. By photon counts

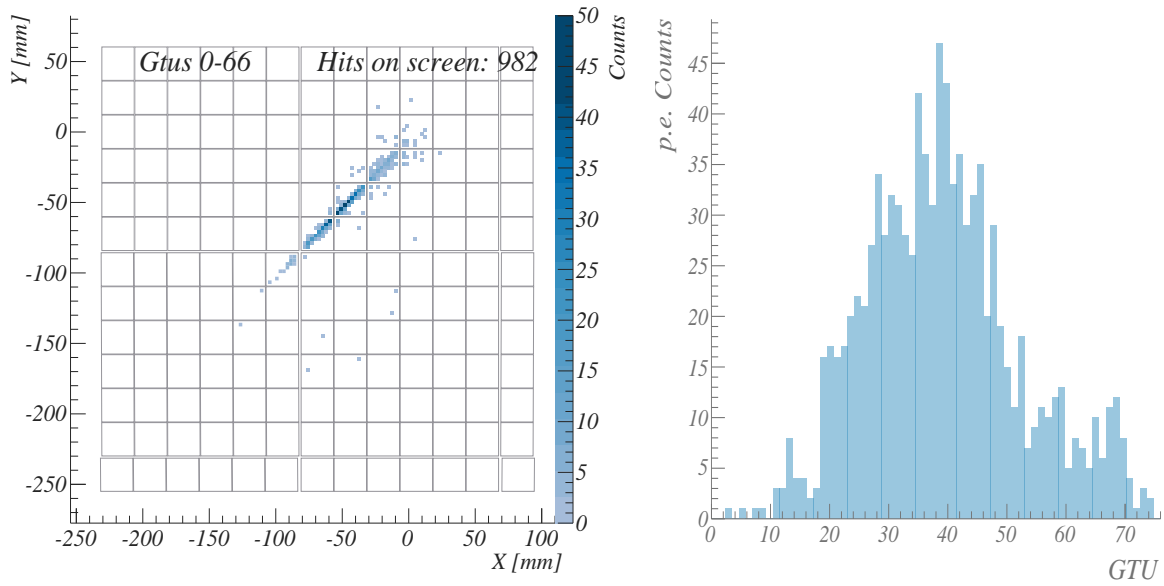


**Figure 3.3:** *Left:* The (integrated) track of the moving spot produced by the fluorescence photons on the FS. *Right:* The *light curve* of the EAS's track on the left. This simulated example EAS has a proton primary with  $E = 10^{20}$ eV and  $\Theta = 60^\circ$ .

we refer to the *single photo-electron count*, which is a term that tells us how many photons were detected. This last process is modulated by the conversion factor between the detected photo-electron and the final pulse charge. This pulse is amplified with a random gaussian distribution. If the amplitude of the amplified pulse crosses a given pixel-preset threshold, then the photo-electron is transformed into a photon count. At this stage, the background is randomly added to the pixels counts.

The last step of the detector's simulation is the application of the trigger algorithms to the photon counts. The reasoning behind the trigger is to reduce the data rate produced by the detector without missing any EAS that occurs inside the FoV. It is a technical impossibility to record the information of 300 K pixels with microsecond precision for year long runs [Adams et al. 2013a]. Within ESAF there are several triggering schemes, but the *de facto* trigger scheme, is a two tier triggering scheme referred as PTT & CCB-LTT. PTT stands for Persistent Tracking Trigger, and its duty is to search for persistent patterns inside an EC. These patterns are defined as boxes of  $3 \times 3$  pixels, whose integrated counts exceed a given threshold for a predefined amount of time [Bertaina et al. 2014] [Fenu 2013]. The ECs selected by the PTT are passed onto the next trigger level: the Cluster Control Board Persistent Tracking Trigger (CCB-LTT) [Bayer et al. 2013]. This trigger (implemented on hardware at the CCB) is tasked with further filtering the EAS signal from the background. The idea is to perform time integrations along a predefined set of directions, taking as a starting point the PTT. The predefined set of directions are defined by the projection on the focal surface of ideal EASs with different polar and zenith angles. If the integral exceeds a given threshold then the CCB-LTT trigger selects the event.

Besides these main components, ESAF also has some underlying common (singleton where necessary) classes available throughout the framework for both *Simu* and *Reco*. These classes are

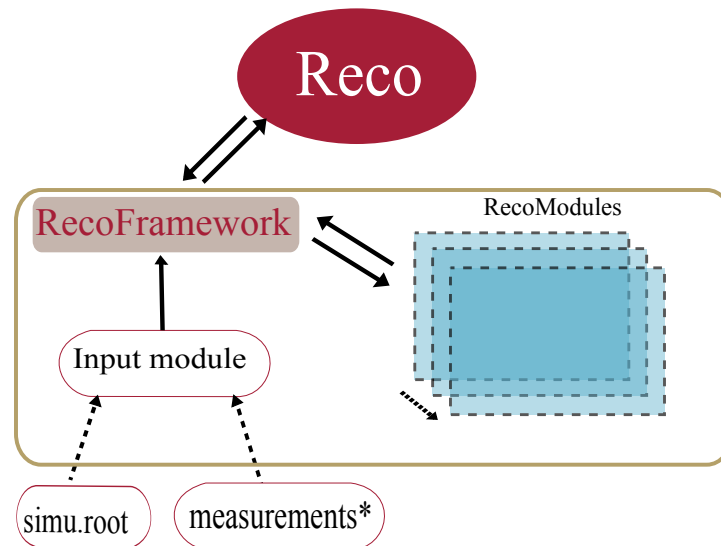


**Figure 3.4:** The general structure of *Reco* as included in ESAF. \*Measurements are foreseen to be interchangeable with the simulated data.

intended for different purposes: input and output of information, system of units conversions, parsing configuration files, object containers for the root files, transformations between systems of reference, etc. Of utmost physical importance is the class dedicated to encapsulate the atmospheric conditions: *EsafConfigurable::Atmosphere*. It is common practice to use the *US-Standard 1976* parametrization of the atmosphere [NOAA & NASA 1976]. Also available in ESAF are the complements to the *US-Standard 1976*, like the MSISE empirical model [Berat et al. 2010]. Both of these possibilities are available for computation of the atmospheric transmission conditions within LOWTRAN 7. LOWTRAN 7 is a standard program to calculate atmospheric transmission [LOWTRAN7 1986]. Unlike the rest of the ESAF code, this package is written in FORTRAN. For the atmospheric properties ESAF calls this package, which in turn provides a layered atmosphere model and with specific transmission coefficients for different wavelengths, aerosol content, amongst other relevant physical properties required by the radiative transfer algorithms implemented in ESAF.

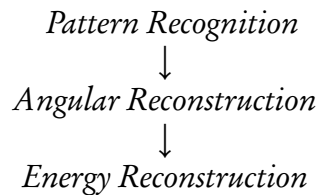
### 3.3 The reconstruction chain: *Reco*

While *Simu* covers the simulation part, *Reco* is in charge of the analysis of the simulations produced by ESAF. Although ESAF has been under development for a considerable time (more than 10 years) the fact that the EUSO mission has been changing configuration has made it harder for the always small group of developers (mainly PhD students and post-docs) to keep up with the current configuration; or to develop analysis tools for an end-user. In this case the end-user is taken to be a physicist with no particular training in software development, who uses ESAF to understand the performance of the mission or to analyze real data. *Reco* is the first step towards that direction.

*Reco* is configured in a less strict program-flow as *Simu*. The starting point is always a *simu.root*

file. ESAF provides a sub-framework, the *RecoFramework* to have access to the members of the classes saved into the *simu.root* file. The analysis depends strongly on what wants to be studied. To perform a particular analysis the user must provide a list of modules in order to carry out the necessary tasks. For example, to analyze just the background fluctuation, a user would need a dedicated module which does exactly background studies and any ancillary modules that the background module should require. The file management, interface between different reco-modules, and the execution of them, is controlled by the *RecoFramework*. The application of a reco-module after the other is what we refer to as the reconstruction chain.

For the present thesis we only used ESAF to analyze simulations of EAS. Therefore we will illustrate just one possibility of a reconstruction chain. Namely:



The only other possible reconstruction chains available at the moment, are sub-steps of the above. They are basically the same reconstruction chain but omitting (bypassing) some of the steps. For example: *Pattern Recognition* → *Energy Reconstruction* (skip the angular reconstruction and use the real simulated geometrical characteristics of the event), or *Angular Reconstruction* → *Energy Reconstruction* (perform the angular and energy reconstruction using an idealized detector without background photons).

### 3.3.1 Pattern recognition

---

This module is in charge of dis-entangling the signal from the background. It serves as a filter to the raw data which intends to provide a clean (background free) signal to other modules' fitting procedures. This means that the *Pattern Recognition* aims to select the photon counts coming from the EAS and not the ones due to the natural UV background. Inside ESAF (inside the code), pattern recognition is also referred to as "clustering". This can be slightly misleading since not all pattern recognitions look for "clusters" of signal but for moving spots, and has nothing to do with the Cluster Control Board which is related to electronics hierarchy. On the other hand, one could regard the signal as a cluster of pixels in space and time, hence the term clustering.

All pattern recognition modules search for this sets of excess-counts inside the focal surface. Then they proceed to select the ones that remain together either in space or in time [Berat et al. 2010]. This is further refined by ruling out groups of pixels that cannot be fitted by a line on the FS of the detector.

At the beginning of the present work (early 2012), there were some attempts to provide this first step inside ESAF. Actually, none was working in a proper way; either *Reco* crashed during execution or the results were extremely unsatisfactory. One of the most promising ones, involved the use



**Figure 3.5:** The definition of the *MES* (see text). In red is also shown the definition of  $\hat{\Omega}$ : the unitary vector parallel that characterizes the EAS's arrival direction.  $\hat{\Omega}$  point in the opposite direction of the EAS's propagation.

of the a modified Hough-transform to try to fit a line to the projected data [Immerkaer 1998] [Berat et al. 2010]. This can be done either in the  $XY$  plane (the FS) or in the  $Xvt$  and  $Yvt$  projections. The line that better fits the data (with noise) would be taken to be the *fitting seed*  $\hat{x}$ .

One of the scientific products delivered by the present thesis is the development, testing, and implementation a working pattern recognition technique which allows the reconstruction of the energy and arrival direction (angular reconstruction) of the primary EECR. This technique is called PWISE and will be discussed in detail in §4.1.2.

### 3.3.2 Angular Reconstruction

Currently only one angular reconstruction module is fully implemented within ESAF: the *TrackDirection2* module. The algorithms of this module were coded into ESAF at the time of the ESA-Phase A report for the EUSO mission [JEM-EUSO 2010] [Taddei 2004]. A detailed simulation study on the overall angular reconstruction performance of the JEM-EUSO mission has already been presented by the author in collaboration with S. Biktemerova and T. Mernik in [Guzmán, Mernik et al. 2014]. The following is a revised description of the algorithms, developed by the original ESAF developers, as implemented and improved by us for the aforementioned publication [Berat et al. 2010] [Taddei 2004].

The *TrackDirection2* reconstruction module consists of a series of algorithms and routines that interpret the photon counts in the FS and translate them into zenith ( $\Theta$ ) and polar ( $\Phi$ ) angles. The two main assumptions are: first, it is assumed that the photon-counts handed in by the pattern recognition constitute the projection of the three dimensional *linear track* of the EAS trajectory onto the FS. Secondly, that this track is moving with the speed of light ( $c$ ) in vacuum. The second assumption is clearly not true since the EAS, consists (to some extent) of massive particles which, according to relativity, cannot propagate with a speed of  $c$ . Even the photons (gamma-rays) of the shower front are not propagating with  $c$ , since they are propagating through a medium. Regardless of this, the impact of the second assumption is negligible, because the actual speed differs less than 1 % from this value.

The geometrical description of the shower begins with the definition of a system of reference. Within ESAF the so-called Master ESAF System of reference *MES* is defined as follows: a right handed Cartesian system of reference whose origin is where the nadir axis intersects the ground. In other words, the *MES*'s origin is the point on the Earth's surface that is directly below the telescope. The  $z$  axis is the elongation of the line that passes through the *MES* origin and the Earth's center, i.e. normal to the Earth's surface. The  $xy$  plane is defined as a plane containing the *MES* origin and whose normal is the previously defined  $z$  axis. In principle, one could simply assign a East-North-Up for positive  $x$ - $y$ - $z$  convention, but unfortunately inside ESAF there is still no clear relation between the *MES* and geographic coordinates. Therefore, the election of the direction of  $x$  or  $y$  is quite arbitrary. To fix ideas and since the side-cut optics of JEM-EUSO introduce an asymmetry in the  $XY$  plane, it is common practice to take the  $X$  axis along the major axis of the FS, unequivocally defining the *MES*. A related system of reference is the optics system of reference (OS), which has a similar definition of the  $xy$  plane but with a reversed direction of the  $z$ -axis, and the origin is translated to the center of the FS. In other words  $(0, 0, 0)_{MES} = (0, 0, -400 \text{ km})_{OS}$ . The definition of the *MES* as well as the arrival direction vector  $\hat{\Omega}$  is illustrated in Fig. 3.5. The three dimensional components of  $\hat{\Omega}$  are given by:

$$\hat{\Omega} = \begin{pmatrix} \cos(\Phi) \sin(\Theta) \\ \sin(\Phi) \sin(\Theta) \\ \cos(\Theta) \end{pmatrix} \quad (3.3)$$

with  $\Theta$  and  $\Phi$  defined within the *MES*.

Of particular importance is the so called Track Detector Plane or TDP (it is also referred as the shower detector plane SDP [Baltrusaitis et al. 1985]). The TDP is defined as the plane that contains both the EAS's axis and the center of the FS. The normal vector  $\hat{V}$  that characterizes this plane is given by:

$$\hat{V} = \frac{1}{\sin \alpha_{ij}} \cdot \hat{n}_i \times \hat{n}_j \quad (3.4)$$

here  $\hat{n}_i$  and  $\hat{n}_j$  are unitary vectors which go from the detector's center  $(400\text{km}, 0, 0)_{MES}$  to points  $i$  and  $j$  of the EAS's track respectively (see Fig. 3.6). The direction vectors  $\hat{n}_i$  are coded in the so-called *Pixel Angle Map*. This map assigns to each pixel a direction ( $\alpha$ ), so for any two points on the FS a TDP can be thus defined. If more than two points are given, they are expected to be collinear (a shower track).

A base for the TDP is then constructed as follows:

$$\begin{aligned} \hat{W} &= \frac{\hat{z} \times \hat{V}}{|\hat{z} \times \hat{V}|} \\ \hat{U} &= \frac{\hat{V} \times \hat{W}}{|\hat{V} \times \hat{W}|} \end{aligned} \quad (3.5)$$

and the EAS direction vector can be now treated two dimensionally in the TDP via:

$$\hat{\Omega} = \cos \beta \hat{W} + \sin \beta \hat{U} \quad (3.6)$$

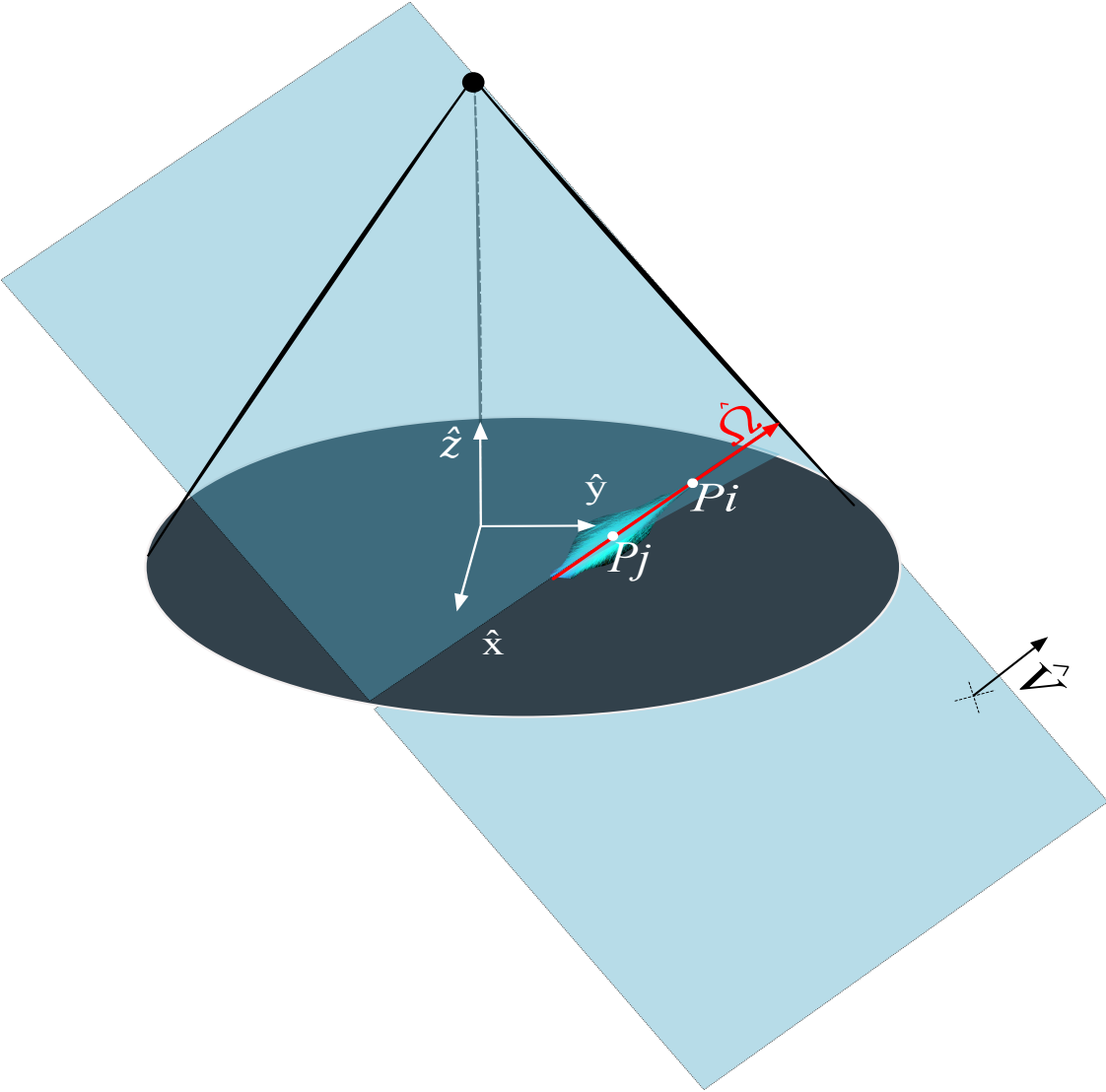


**Figure 3.6:** The Track Detector Plane: defined by the shower axis and the center of the detector. Its normal vector,  $\hat{V}$ , is also shown.

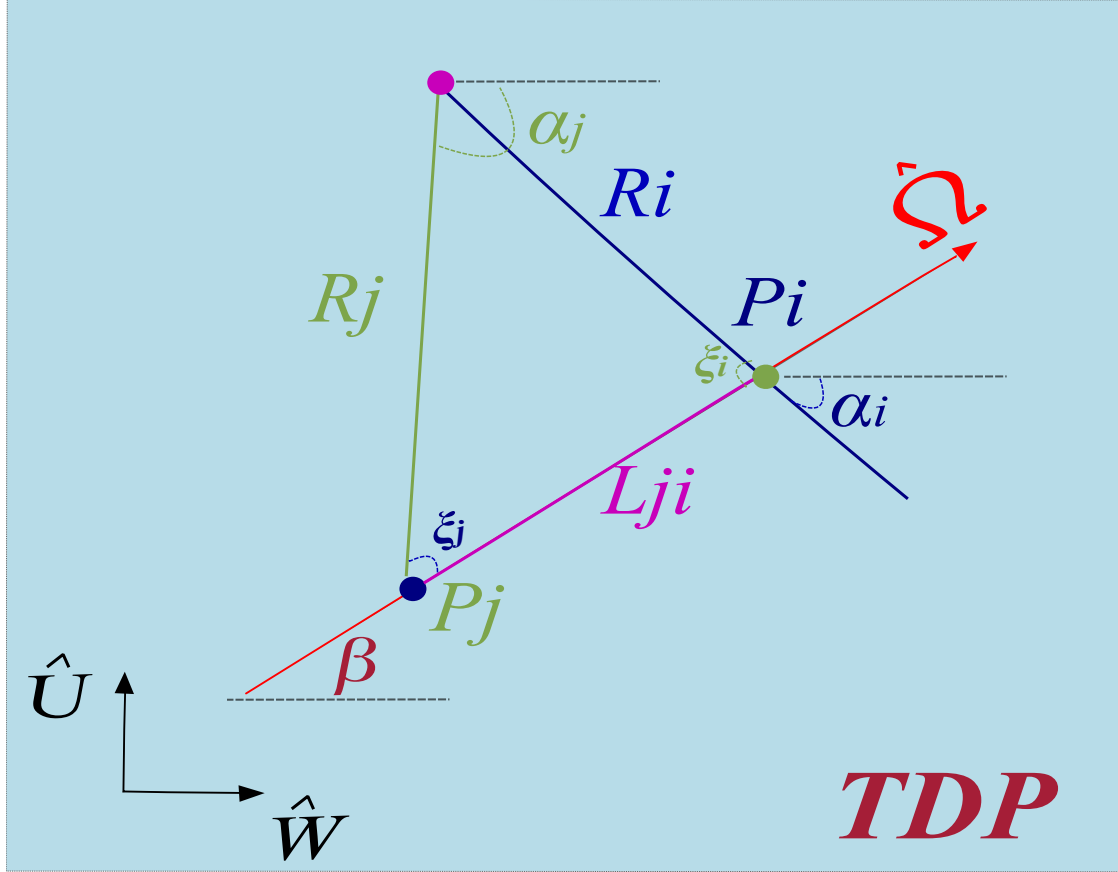


**Figure 3.7:** Geometrical illustration of the triangles referred by Eqs. 3.8, 3.7, and 3.9.

where  $\beta$  is the angle between  $\hat{U}$  and  $\hat{W}$  within the TDP. As it can be seen in Fig. 3.7, the time  $\Delta t$  elapsed between the detection of the photons emitted from point  $P_i$  and the ones emission from point  $P_j$  along the shower track is given by:

$$\Delta t = \frac{|L_{ji}|}{c} + \frac{|R_i| - |R_j|}{c} \quad (3.7)$$

where  $|L_{ij}|$  is the distance between points  $P_i$  and  $P_j$  and  $|R_i|$  and  $|R_j|$  the distance from the center of the detector to the aforementioned points. With these three line segments we can construct a triangle to help us derive the rest of the necessary angles. This triangle is shown in Fig. 3.7. We write down the definition of the involved angles explicitly:

$$\xi_{i,j} = \pi - (\beta + \alpha_{i,j}) \quad (3.8)$$

The law of sines gives us:

$$\frac{L_{ji}}{\sin \alpha_{ji}} = \frac{R_i}{\sin \xi_j} = \frac{R_j}{\sin \xi_i} \quad (3.9)$$

which inserted into Eq. 3.7 yields:

$$\begin{aligned}\Delta t &= \frac{|R_j|}{c} \left( \frac{\sin \alpha_{ji} + \sin \xi_j - \sin \xi_i}{\sin \xi_i} \right) \\ t_j - t_i &= \frac{|R_j|}{c} \left( \frac{\sin \alpha_{ji} + \sin(\pi - \beta - \alpha_j) - \sin(\pi - \beta - \alpha_i)}{\sin(\pi - \beta - \alpha_i)} \right) \\ t_j - t_i &= \frac{|R_j|}{c} \left( \frac{\sin \alpha_{ji} + \sin(\beta + \alpha_j) - \sin(\beta + \alpha_i)}{\sin(\beta + \alpha_i)} \right)\end{aligned}\quad (3.10)$$

This last expression is used to calculate the angular velocity  $\omega$  of the EAS.

$$\begin{aligned}\omega &\equiv \lim_{\Delta t \rightarrow 0} \frac{\Delta \alpha}{\Delta t} = \lim_{i \rightarrow j} \frac{\alpha_j - \alpha_i}{t_j - t_i} \\ &= \lim_{i \rightarrow j} \frac{c \cdot \sin(\beta + \alpha_i)}{|R_j|} \left( \frac{\alpha_j - \alpha_i}{\sin(\alpha_j - \alpha_i) + \sin(\beta + \alpha_j) - \sin(\beta + \alpha_i)} \right)\end{aligned}\quad (3.11)$$

Using the trigonometric identity  $\sin \theta - \sin \phi = 2 \sin(\frac{\theta - \phi}{2}) \cos(\frac{\theta + \phi}{2})$ , the latter expression reduces to:

$$\begin{aligned}\omega &= \lim_{i \rightarrow j} \frac{c \cdot \sin(\beta + \alpha_i)}{|R_j|} \left( \frac{\alpha_j - \alpha_i}{\sin(\alpha_j - \alpha_i) + 2 \sin(\frac{\beta + \alpha_j - (\beta + \alpha_i)}{2}) \cos(\frac{\beta + \alpha_j + (\beta + \alpha_i)}{2})} \right) \\ &= \lim_{i \rightarrow j} \frac{c \cdot \sin(\beta + \alpha_i)}{|R_j|} \left( \frac{\alpha_j - \alpha_i}{\sin(\alpha_j - \alpha_i) + 2 \sin(\frac{\alpha_j - \alpha_i}{2}) \cos(\beta + \frac{\alpha_j + \alpha_i}{2})} \right) \\ &= \lim_{i \rightarrow j} \frac{c \cdot \sin(\beta + \alpha_i)}{|R_j|} \cdot \lim_{i \rightarrow j} \left( \frac{\alpha_j - \alpha_i}{\sin(\alpha_j - \alpha_i) + 2 \sin(\frac{\alpha_j - \alpha_i}{2}) \cos(\beta + \frac{\alpha_j + \alpha_i}{2})} \right)\end{aligned}\quad (3.12)$$

We calculate the limit in parenthesis, via its inverse limit:

$$\begin{aligned}\lim_{i \rightarrow j} \left( \frac{\sin(\alpha_j - \alpha_i) + 2 \sin(\frac{\alpha_j - \alpha_i}{2}) \cos(\beta + \frac{\alpha_j + \alpha_i}{2})}{\alpha_j - \alpha_i} \right) &= \\ &= \lim_{i \rightarrow j} \frac{\sin(\alpha_j - \alpha_i)}{\alpha_j - \alpha_i} + \lim_{i \rightarrow j} \frac{2 \sin(\frac{\alpha_j - \alpha_i}{2})}{\alpha_j - \alpha_i} \cdot \cos(\beta + \frac{\alpha_j + \alpha_i}{2}) \\ &= 1 + \cos(\beta + \alpha_j)\end{aligned}$$

Finally we substitute this value in Eq.3.12 to arrive at a closed form for the angular velocity of the shower track:

$$\begin{aligned}
\omega &= \lim_{i \rightarrow j} \frac{c \cdot \sin(\beta + \alpha_i)}{|R_j|} \lim_{i \rightarrow j} \left( \frac{\alpha_j - \alpha_i}{\sin(\alpha_j - \alpha_i) + 2 \sin\left(\frac{\alpha_j - \alpha_i}{2}\right) \cos\left(\beta + \frac{\alpha_j + \alpha_i}{2}\right)} \right) \\
&= \frac{c \cdot \sin(\beta + \alpha_j)}{|R_j|} \left( \frac{1}{1 + \cos(\beta + \alpha_j)} \right) \\
&= \frac{c}{|R_j|} \cdot \left( \frac{\sin(\beta + \alpha_j)}{1 + \cos(\beta + \alpha_j)} \right) = \frac{c}{|R_j|} \cdot \tan\left(\frac{\beta + \alpha_j}{2}\right)
\end{aligned} \tag{3.13}$$

$$\tag{3.14}$$

In summary: the position of the pixels identified as the projection of the shower track are used to calculate the TDP, and its base vectors  $\hat{W}$  and  $\hat{U}$ ; the timing between arriving signals is used to calculate  $\beta$ . Once these three elements are known  $\Omega$  is calculated using Eq. 3.6. Thus there is sufficient information to determine the angles for the direction vector, at least mathematically. However, all vectors parallel to  $\hat{\Omega}$  that lie in the TDP could be solutions, but only one of them contains the shower. This ambiguity is constrained by the knowledge of the approximate distance to the shower. This information is needed to properly solve Eq. 3.10, since we need a starting (ending) point to calculate the distance  $R_0(R_{last})$  to the first (last) point in the shower. A common practice is also to make an educated guess on the position of the shower maximum, hence getting the distance  $R_{max}$ . The most promising method is the detection of the reflected Cherenkov light by the Earth's surface. This is sometimes called the "Cherenkov peak" method, because the light curve on the detector features a second short but clear rise due to the arrival of the reflected Cherenkov light. This allows to pin-point the impact point of the shower with high accuracy making the angular reconstruction more robust.

For the vast majority of cases, the brighter part of the EAS is always contained within the first 5 km of the atmosphere. Compared to the 400 km distance to the EUSO telescope, this uncertainty is negligible and has not a great impact in the angular reconstruction.

The method described above is necessary for the discussion in §4.2. Before we move on to the next element of the reconstruction chain, we make a brief description of the 4 algorithms used in this work for arrival direction retrieval.

1. *Analytical Approximate 1 (AA1)*. This method is the base method used within the *Track-Direction2* module. As a first step, it finds the TDP. Next it performs a linear fit of the data-points in the  $t$  vs.  $\alpha_i$  plane, to estimate  $\omega = \frac{d\alpha}{dt}$ . This approximation needs the assumption that  $\omega$  remains constant in the FS. Then it uses Eq. 3.14 to calculate  $\beta$ . To do so, the angular position of the maximum of the data points  $\alpha_{max}$  is estimated via a gaussian fit. Then the distance to the maximum  $R_{max}$  is calculated via:

$$R_{max} = (R_{\oplus} + H_{EUSO}) \cdot \cos\Theta_{max} - \sqrt{(R_{\oplus} + H_{max})^2 - (R_{\oplus} + H_{EUSO})^2 \cdot \sin^2\Theta_{max}} \tag{3.15}$$

Where  $H_{max}$  and  $H_{EUSO}$  are the altitude of the EAS's maximum and the EUSO detector, and  $R_{\oplus}$  is the Earth's radius. Typically the latter is taken simply to be the altitude of the ISS.  $\Theta_{max}$  is the zenith angle (in *MES*) of the unitary vector from the detector to  $P_{max}$ . To fix

ideas the reader is invited to follow Fig. 3.7. The AA1 method is reiterative, the first value of  $H_{max}$  is just a initial guess which is typically taken as 5 km. This initial guess yields a value of  $\Theta$  that is then used for the calculation of a second  $H_{max}$  using a shower parametrization as a reference model. With this new  $H_{max}$ , the whole process is performed a second time.

2. *Analytical Approximate 2 (AA2)*. This method requires the TDP as well as  $\alpha_{max}$  to be calculated before hand by the AA1 method. Instead of using the angular velocity on the detector the EAS track is projected to the  $XY_{MES}$  plane. Afterwards the magnitude of this velocity and  $\alpha_{max}$  are used to calculate  $\beta$ . Once  $\beta$  is known then Eq. 3.6 is used to find  $\Omega$ .
3. *Numerical Exact 1 (NE1)*. The method carries out a  $\chi^2$  minimization varying  $\beta$ ,  $H_{max}$  and  $t_{max}$ . The  $\chi^2$  function to minimize is given by:

$$\chi^2(\beta, H_{max}, t_{max}) \equiv \sum_{i=1} \left( \frac{t_i^{data} - t_i(\beta, H_{max}, t_{max})}{\sigma_i} \right)^2 \cdot N_i^{counts} \quad (3.16)$$

This  $\chi^2$  function compares the time measured  $t_i^{data}$  with the expected  $t_i(\beta, H_{max}, t_{max})$  given by Eq. 3.10. Each squared difference is summed up for every  $i^{th}$  pixel with a weight defined as the number of counts in the  $i^{th}$  pixel ( $N_i^{counts}$ ) divided by the square of the uncertainty in the time measurement  $\sigma_i^2$ . However this last step is for the moment superfluous, since all pixels are taken to have the same value of  $\sigma$ , i.e  $\sigma = 1$  GTU (2.5  $\mu$ s). The NE1 method uses as seed values for the minimization the values calculated by the AA1 method.

4. *Numerical Exact 2 (NE2)*. This algorithm assumes the last point of the FS-track to correspond with the impact point of the EAS with the Earth's surface. Hence, it has a fixed point ( $\vec{P}_{impact}$ ) with known coordinates from where it constructs test directions varying  $\Theta$  and  $\Phi$ . Taking this into consideration, the position of the  $i^{th}$  point on the EAS is given by:

$$\vec{P}_i = \vec{P}_{impact} + c \cdot (t_{impact} - t_i) \cdot \hat{\Omega}_{test}(\Theta, \Phi) \quad (3.17)$$

Let us remember that the *Pixel Angle Map* provides direction vectors ( $\hat{n}_i$ ) for each pixel. We expect that the vector  $\vec{R}_i = \vec{P}_i - \vec{P}_{EUSO}$  which goes from the detector's center to the  $i^{th}$  point on the shower  $P_i$ , to be parallel to its corresponding  $\hat{n}_i$ . We define:

$$\Psi_i(\Omega_{test}) \equiv \arccos(\hat{n}_i^{data} \cdot \hat{R}_i) \quad (3.18)$$

and we construct the following  $\chi^2$  function:

$$\chi^2(\Omega_{test}) = \sum_i \left( \frac{\Psi_i(\Omega_{test})}{\sigma_i} \right)^2 \cdot N_i^{counts} \quad (3.19)$$

Again the sum is performed for all pixels with a similar weight as for the NE1 method. The difference is that in this case  $\sigma_i$  is the angular uncertainty for each pixel (inaccuracy of the  $\hat{n}_i$ 's). Currently  $\sigma_i$  is taken to be  $0.1^\circ$  for all pixels.

### 3.3.3 Energy Reconstruction

To conclude our review we will now describe the reconstruction module responsible for the reconstruction of longitudinal profile of the EAS. This module is in charge of transforming the information available in the light curve measured by the detector into the originating EAS's longitudinal profile. Within ESAF the only working module performing this rather important task is the “*PMTToShowerReco*” module developed by Francesco Fenu in the context of his PhD Thesis at the University of Tübingen [Fenu 2013].

Let us remember that the number of charged particles at the shower front  $N_e$  (mostly electrons) is a function of the shower depth  $X$ , primary's energy  $E$  and first interaction point  $X_0$ . The curve  $N_e(X; E, X_0)$  is called the longitudinal profile. We use the measured number of measured photon-counts  $N^{counts}$  per shower step (in depth  $X$ ) to recover the longitudinal profile. Mathematically this is expressed as solving the following equation for  $N_e(X; E, X_0)$ :

$$\frac{dN^{counts}}{dX} = \int_{\lambda_{min}}^{\lambda_{max}} \underbrace{(\psi_{fluor}(N_e, \lambda) + \psi_{ch}(N_e, \lambda))}_{EAS} \underbrace{(T_s(\lambda, X) \cdot T_a(\lambda, X))}_{atmo} \underbrace{\left( \frac{A_{opt} \cos \theta}{R^2} \cdot \varepsilon_{det}(\lambda, \theta) \right)}_{EUSO} d\lambda \quad (3.20)$$

Let us discuss Eq. 3.20 by parts:

- *EAS sector.* Here we have two main components the fluorescence yield  $\psi_{fluor}$  and the Cherenkov yield  $\psi_{cher}$ . These give the number of photons produced in the shower segment. Both have their own respective spectrum and their intensity varies as the shower develops in the atmosphere. The latter is coded in the shower depth. Let us remember that the shower depth depends on the shower position for a particular shower segment ( $\Delta L$ ):

$$\Delta X = \int_{\Delta L} \rho(\vec{r}) dL$$

Where  $\rho$  is the atmospheric density at position  $\vec{r}$ . We will discuss them both in more detail in the following chapter. For the moment we highlight that the main difference is that the fluorescence light is isotropic and allows for a calorimetric measurement of the EAS's energy. On the other hand, the Cherenkov yield is focused in the direction of propagation of the EAS, though through scattering these photons arrive at the detector. Although the presence of a Cherenkov peak in the EAS's light curve is highly beneficial for the angular reconstruction, Cherenkov light contaminates the fluorescent signal worsening the calorimetric measurement of the energy.

- *Atmosphere sector.* The scattering and absorption of the photons by the atmosphere is included in  $T_s(\lambda, X)$  and  $T_a(\lambda, X)$  respectively. These parameters depend on the wavelength  $\lambda$ , and the path between the emission point and the detector. Within the *MES*, this is coded by the atmospheric depth  $X$  for this specific shower.
- *EUSO sector.* Again we have two main components the geometrical part which is the ratio of the effective area of the pupil  $A_{opt} \cos \theta$  to the square of the distance to the emission point

$R^2$ . The  $\cos\theta$  is there to account for the photon's arrival angle. The detector efficiency  $\varepsilon_{det}$  is defined as:

$$\varepsilon_{det}(\lambda) = \varepsilon_{opt}(\lambda) \cdot T_{BG3}(\lambda) \cdot \varepsilon_{phdet}^*(\lambda) \quad (3.21)$$

where  $\varepsilon_{opt}$  the throughput efficiency of the optics,  $T_{BG3}$  is the transmittance of the BG3 filter and  $\varepsilon_{phdet}^*$  is an average photo detection efficiency analog to Eq. 3.2. The integral in Eq. 3.20 is done between a suitable range of wavelengths ( $\lambda_{min} \div \lambda_{max}$ ) dictated by the detector's configuration.

The steps followed to solve this complicated problem are conceptually visualized in Fig. 3.8. After the pattern recognition (a.k.a. clustering) the light curve on the detector is constructed "filling in" the GTUs when the EAS track went through insensitive parts of the FS, like the spaces between PDMs, MAPMT, or even pixels. Once this curve is constructed the mean background is subtracted. To fully characterize the relevant functions and parameters from Eq. 3.20 the geometrical characteristics of the EAS need to be known, in order to calculate the amount of photons produced at each shower point. Of special importance is the distance to the distinct shower points. As for the angular reconstruction this distance can be calculated by spotting a point within the EAS track that can be assigned a position close to the real value. The *PMTToShowerReco* module utilizes two methods:

1. *Cherenkov method*. It uses the Cherenkov Peak to determine the impact point of the EAS. With this information the position of the maximum and, as a consequence, its depth  $X_{max}$  is computed.
2. *Slant depth method* This method depends on the angular reconstruction and tries to fit a GIL parametrization Eq. 3.1. Once the fit is done the value of the  $X_{max}$  is obtained.

After the longitudinal profile has been calculated, a dedicated iterative method within the *PMTToShowerReco* module takes care of determining the amount of Cherenkov photons emitted at each point of the shower.

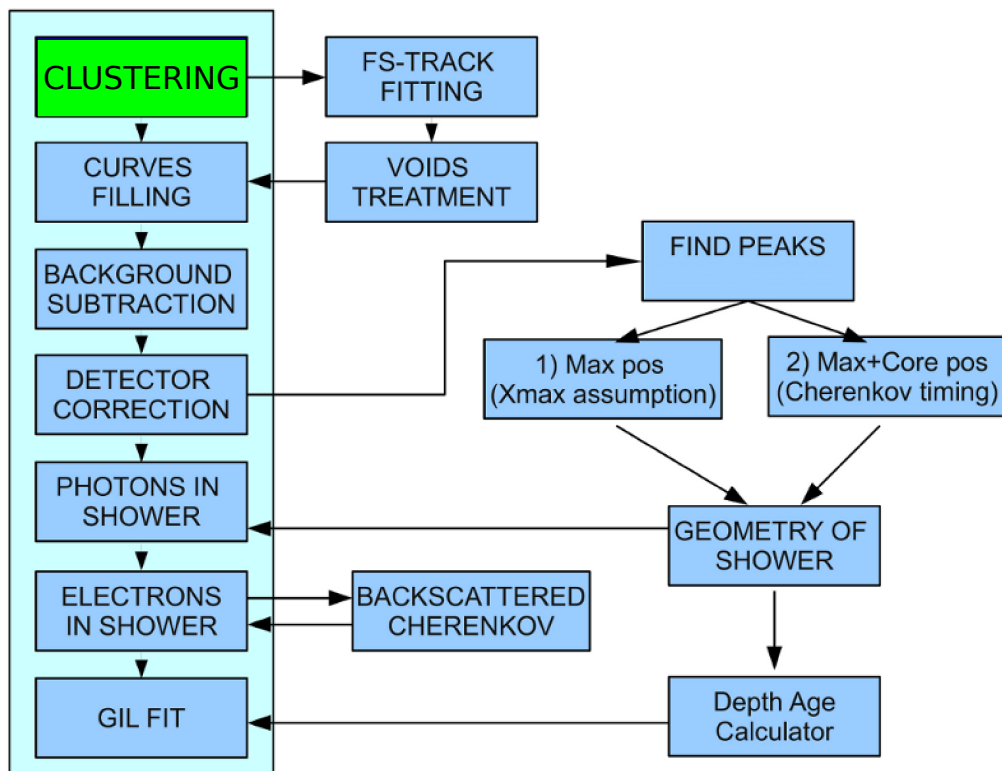


**Figure 3.8:** A flow diagram representation of the *PMT Shower Reco* module. Modified from [Fenu 2013].

# 4

## SPACE OBSERVATION OF EECR: EXPECTED PERFORMANCES

---

### Contents

---

|       |  |     |
|-------|--|-----|
| 4.1   | Main contributions to ESAF . . . . .                                     | 77  |
| 4.1.1 | Pattern recognition: the <i>PWISE</i> technique . . . . .                | 77  |
| 4.1.2 | Pattern recognition: the <i>PWISE-R</i> technique . . . . .              | 81  |
| 4.1.3 | The CONEX - ESAF interface . . . . .                                     | 83  |
| 4.1.4 | Configuration of the CONEX-ESAF interface . . . . .                      | 92  |
| 4.2   | Angular reconstruction . . . . .   | 94  |
| 4.2.1 | Simulation sets . . . . .  | 94  |
| 4.2.2 | Summary of angular reconstruction for proton primaries . . . . .         | 96  |
| 4.2.3 | Angular reconstruction for Fe and Proton primaries . . . . .             | 97  |
| 4.2.4 | Angular reconstruction for EE- $\gamma$ primaries . . . . .              | 99  |
| 4.2.5 | Quality cuts . . . . .   | 101 |
| 4.3   | Energy and $X_{max}$ Reconstruction studies . . . . .                    | 104 |
| 4.3.1 | Energy reconstruction for protons, iron nuclei, and photons . . . . .    | 104 |
| 4.3.2 | $X_{max}$ reconstruction for protons, iron nuclei, and photons . . . . . | 107 |

---



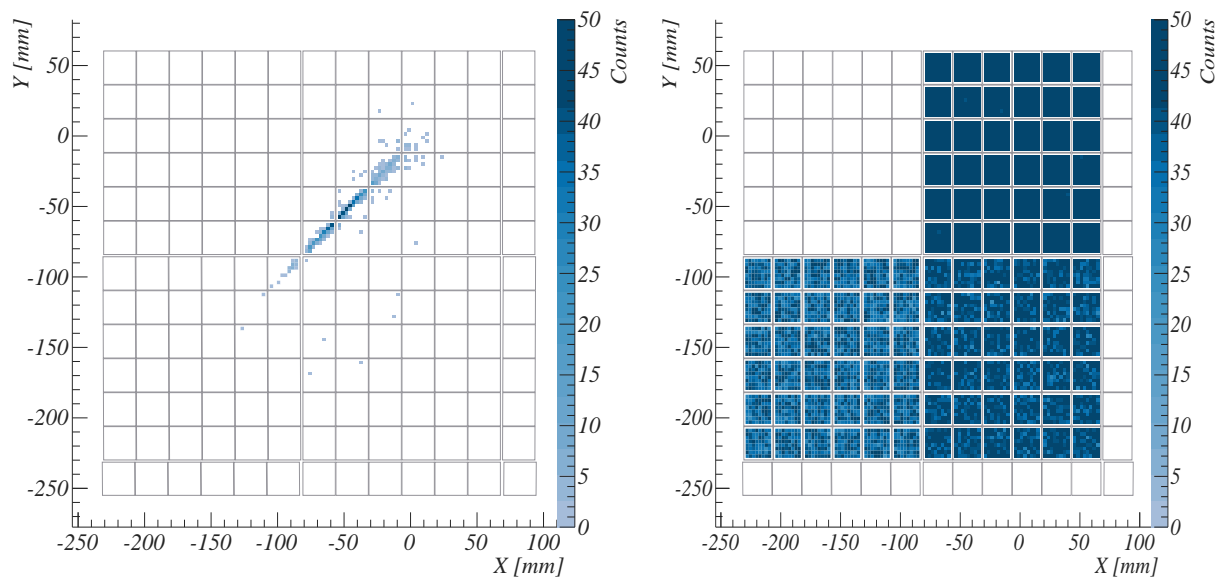


**Figure 4.1:** *Left:* The (integrated) track of the *signal* photons **neglecting** the background. *Right:* Same as left but with the background included. The job of the pattern recognition is to extract the image on the left from the image on the right.

## 4.1 Main contributions to ESAF

As detailed in the previous chapter, within ESAF a prerequisite for both the angular reconstruction and energy reconstruction modules is the successful disentanglement of the photons produced by the EAS and the ones from the natural background. This process is also sometimes referred as disentangling the signal from background. Within *Reco*, the *Pattern Recognition* module is responsible for executing this task. We will concern ourselves with the pattern imprinted by the EAS's UV-photons on the FS: a small cluster or excess of counts, moving across the FS in a straight line. UHE signals can be detected on top of the background mainly because of their higher intensity.

### 4.1.1 Pattern recognition: the *PWISE* technique

To this end, we developed the *Peak and Window SEarching (PWISE)* technique. The main idea behind it is to search through all available pixels for a count-peak and a suitable time window. This is done via what we call *pixel-traces*. These are the counts as a function of time of any given pixel. It is what one would see if the readout electronic would be read with an oscilloscope. An example of a *pixel-trace* is shown in Fig. 4.2.

The count-peak we are looking for is an excursion above the background. This provides the first hint of a pixel containing signal counts. The persistence in time of the signal counts on a given pixel depends on the shower geometry. Selecting a pixel is not enough information. We also need

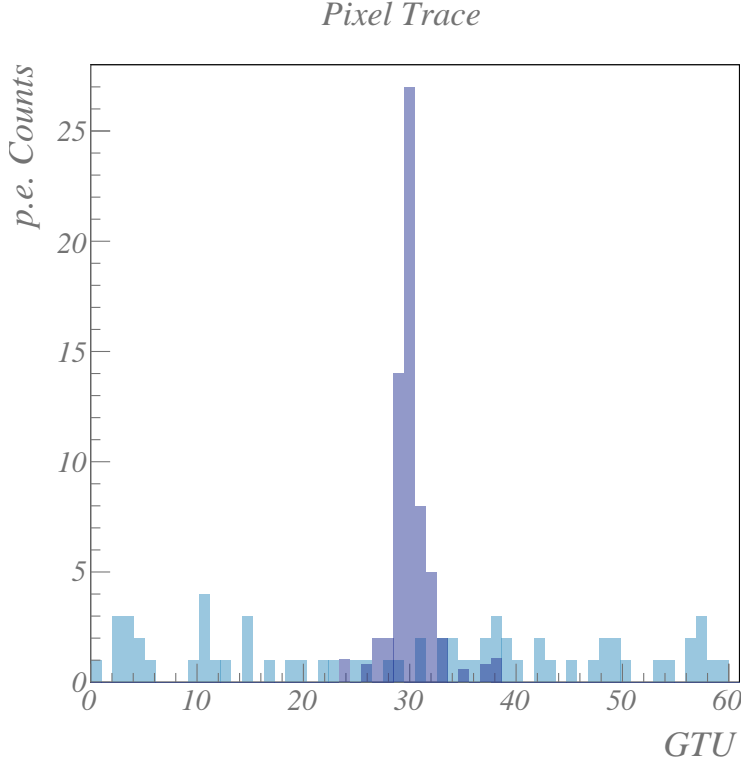


**Figure 4.2:** An example of the *pixel-trace* from a single pixel. On the  $X$ -axis we see the time in units of GTUs and in the  $Y$ -axis the photo electron counts. The highlighted counts are coming from the EAS. All other counts are background photons.

to know which counts of the *pixel-trace* belong to the signal. That is the reason we need to adjust a time window to select the counts that occurred when the signal was present on the selected pixel.

This process is outlined as follows:

- Step 1** We select pixels whose *pixel-trace* exceeds a pre-defined *peak-threshold* for at least one GTU. We label the time (GTU) when this excess occurs as  $t_{peak}$ . We disregard all other pixels.
- Step 2** On the selected pixels, we calculate the root-mean-square  $RMS$  of the counts in the *pixel-trace* with:

$$RMS = \frac{1}{T} \sqrt{\sum_{t=0}^T (pc(t))^2},$$

where  $T$  is the event's total duration time (in GTUs), and  $pc(t)$  are the counts present on the pixel at time  $t$ . Then we calculate the signal-to-noise ratio given by:

$$SNR(\Delta t) = \frac{1}{RMS \cdot \Delta t} \cdot \sum_{t=t_{peak}-\frac{\Delta t}{2}}^{t_{peak}+\frac{\Delta t}{2}} pc(t) \quad (4.1)$$

In other words: we sum all the  $pc(t)$  within a time window of length  $\Delta t$  centered to the time of the maximum  $t_{peak}$ .

- Step 3** We calculate the  $SNR(\Delta t)$  for all possible  $\Delta t$ . Remember that by definition  $\Delta t \leq T$ . We

keep the maximum value maximum  $SNR_{max}$  with its associated time window  $\Delta t_{max}$ .

**Step 4** We compare  $SNR_{max}$  with a previously defined  $SNR-threshold$ . If:

$$SNR_{max} > SNR-threshold$$

Then we select all counts in this pixel occurring in the interval:

$$t_{peak} - \frac{\Delta t_{max}}{2} < t < t_{peak} + \frac{\Delta t_{max}}{2}$$

The implementation of this algorithm in *ESAF* includes the configuration parameters to control the behavior of the *PWISE* technique.

---

—Extract from *PWISEModule.cfg*—

`PWISEModule.fThreshold= 6 # Peak Threshold in counts`

`PWISEModule.fSNRejection= 1.5 # Only pixel-traces with SNR equal or higher will be selected.`

---

Where `fThreshold` corresponds to the *peak-threshold* mentioned in **Step 1** and `fSNRejection` corresponds to the *SNR-threshold* mentioned in **Step 4**.

This rough first implementation has some caveats. The definition of *SNR* centered on the *pixel-trace*'s maximum  $t_{max}$  has as a consequence that all possible choices for time windows are restricted to an uneven number of GTUs. Since the time windows are taken symmetrically around the maximum, we can write:

$$\Delta t(n) = 1 + 2n, \text{ with } n = 0, 1, 2, 3, 4 \dots T.$$

Therefore Eq. 4.1 can be written as:

$$SNR(n) = \frac{1}{RMS \cdot (1 + 2n)} \cdot \sum_{t_{peak} - \frac{1+2n}{2}}^{t_{peak} + \frac{1+2n}{2}} pc(t) \quad (4.2)$$

Let us define:

$$\mathbf{Sum}(n) = \sum_{t_{peak} - \frac{1+2n}{2}}^{t_{peak} + \frac{1+2n}{2}} pc(t)$$

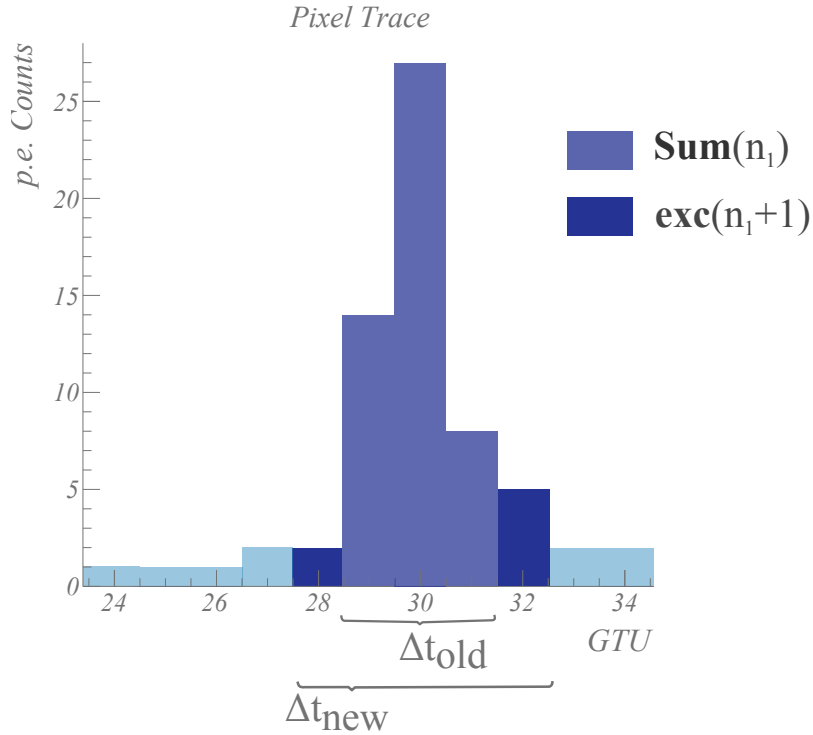


**Figure 4.3:** Illustration of the excess  $exc(n_1 + 1)$  added to the new sum  $\mathbf{Sum}(n_1)$  when increasing the time window from  $\Delta t_{old}$  to  $\Delta t_{new}$ . (see text).

Now let us take  $n_1 < n_2$ . This implies that  $\mathbf{Sum}(n_2) = \mathbf{Sum}(n_1) + exc(n_2)$ . Here we have introduced the term  $exc(n_2)$ , which represents the extra counts added to the sum  $\mathbf{Sum}(n_1)$ . This concept is exemplified in Fig. 4.3.

In order to select a bigger time window we need to fulfill:

$$SNR(n_1) < SNR(n_2)$$

$$\frac{\mathbf{Sum}(n_1)}{RMS \cdot (1 + 2n_1)} < \frac{\mathbf{Sum}(n_2)}{RMS \cdot (1 + 2n_2)}$$

$$\frac{1 + 2n_2}{1 + 2n_1} < \frac{\mathbf{Sum}(n_2)}{\mathbf{Sum}(n_1)}$$

$$\frac{1 + 2n_2}{1 + 2n_1} < 1 + \frac{exc(n_2)}{\mathbf{Sum}(n_1)}$$

With this expression, we arrive to the condition that the ratio  $\frac{exc(n_2)}{\mathbf{Sum}(n_1)}$  must fulfill, to guarantee that  $SNR(n_1) < SNR(n_2)$  holds when we take two consecutive windows; i.e.  $n_2 = n_1 + 1$ . This

implies:

$$\frac{1 + 2(n_1 + 1)}{1 + 2n_1} - 1 < \frac{exc(n_1 + 1)}{\text{Sum}(n_1)}$$

$$\frac{2}{1 + 2n_1} < \frac{exc(n_1 + 1)}{\text{Sum}(n_1)} \quad \text{with } n_1 = 0, 1, 2, 3 \dots T \quad (4.3)$$

$$\implies \frac{exc(n_1 + 1)}{\text{Sum}(n_1)} > 2, \frac{2}{3}, \frac{2}{5}, \frac{2}{7}, \text{etc.}$$

The first case is extremely improbable, since  $\frac{exc(n_1+1)}{\text{Sum}(n_1)} < 1$  unless the height of the other peaks is the same as the height of the centered peak. Let us remember that the time window is centered around the maximum; i.e. the height of the other peaks is expected to be less or equal to the maximum. The other cases,  $\frac{exc(n_1+1)}{\text{Sum}(n_1)} > \frac{2}{3}, \frac{2}{5}, \frac{2}{7}$ , are more plausible; but they would become increasingly difficult to find since we would need high enough peaks far away from the maximum with a few or zero counts in between.

To circumvent this problem, and to assure we select bright pixels where the signal was contained just for 1 or 3 GTUs regardless of the SNR, we have added another step:

**Step 5** If:

$$SNR_{max} < SNR\text{-threshold} \quad \text{and} \quad pc(t_{peak}) > \text{Absolute-threshold}$$

We select all counts in this pixel occurring in the interval  $t_{peak} - \frac{\Delta t}{2} < t < t_{peak} + \frac{\Delta t}{2}$  with  $\Delta t = 1$  or 3 GTU, depending on which  $\Delta t$  has the biggest *SNR*.

This new step provides a new parameter which is also included in the implementation of the algorithm in *ESAF*. Namely:

—Extract from *PWISEModule.cfg*—

`PWISEModule.fAbsThreshold= 9 # AbsoluteThreshold in counts.`

Using this 5-step technique in combination with the *TrackDirection2* module, we were able to successfully reconstruct a large sample of simulated protons with different energies and inclinations. These results will be discussed in §4.2.

#### 4.1.2 Pattern recognition: the *PWISE-R* technique

To further refine the *PWISE* technique, we added a second iteration in what we call the **Refined** version, hence the name *PWISE-R*. The *PWISE* technique works on the “pixel” level, i.e. it does not look for correlations in space or time between different pixels. Although this rough first approach proved successful to some extent, we decided we could benefit from a second iteration looking for casual correlation in time and position within the FS. The idea is as follows: we run the *PWISE* algorithm once but with strict thresholds that will allow, in principle, only very few pixels to be selected. Then we make a second run, where we select pixels above a *Low-threshold*

that are not too far away, in both space or time, to the previously selected pixels. This is achieved by adding the following steps:

**Step 6** Make a linear fit in the  $tx$  and  $ty$  planes with the pixels selected by the first run of *PWISE*.

**Step 7** Look again at all  $pc(t)$  for all  $t$ . Select those  $pc(t)$  that fulfill the following three criteria:

1.  $pc(t) > \text{Low-threshold}$ .
2.  $\mathcal{L}_{x(y)} < |Pix|$ . Where  $|Pix|$  is the size of the pixel's diagonal;  $\mathcal{L}_{x(y)}$  is the distance along the  $x(y)$  direction between the  $pc(t)$ 's pixel  $x(y)$  coordinate and the fitted line in the  $tx(y)$  plane, from step 6.
3.  $\mathcal{L}_t < \text{Time-Threshold}$ . Where  $\mathcal{L}_t$  is the time-distance to the fitted line in the  $tx(y)$  plane, from step 6.

This step is illustrated in Fig. 4.4 and Fig. 4.5 for the  $tx$  and  $ty$  planes respectively. In these figures, we also show in green the  $pc(t)$  pertaining to the signal, but nevertheless too low to be separated from the background.

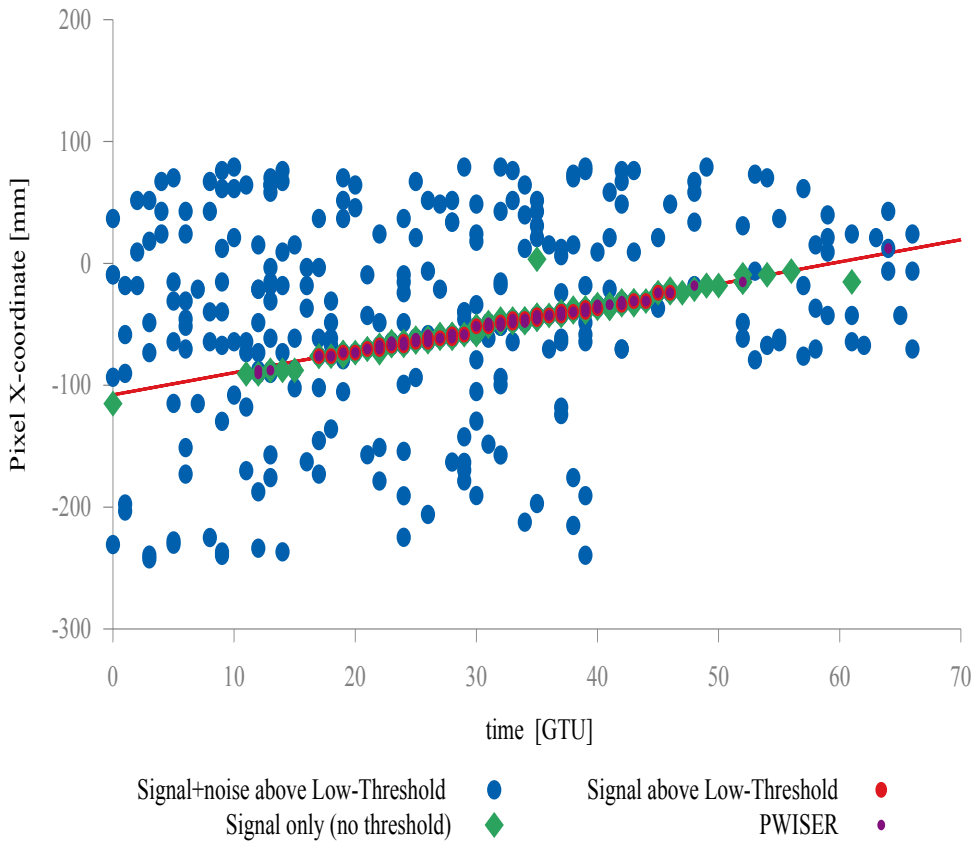


**Figure 4.4:** An illustration of *PWISE-R* technique. Here we show the points in the  $xt$  plane. The solid line is the result of the linear fit performed after the *PWISE* as a first stage (see text).

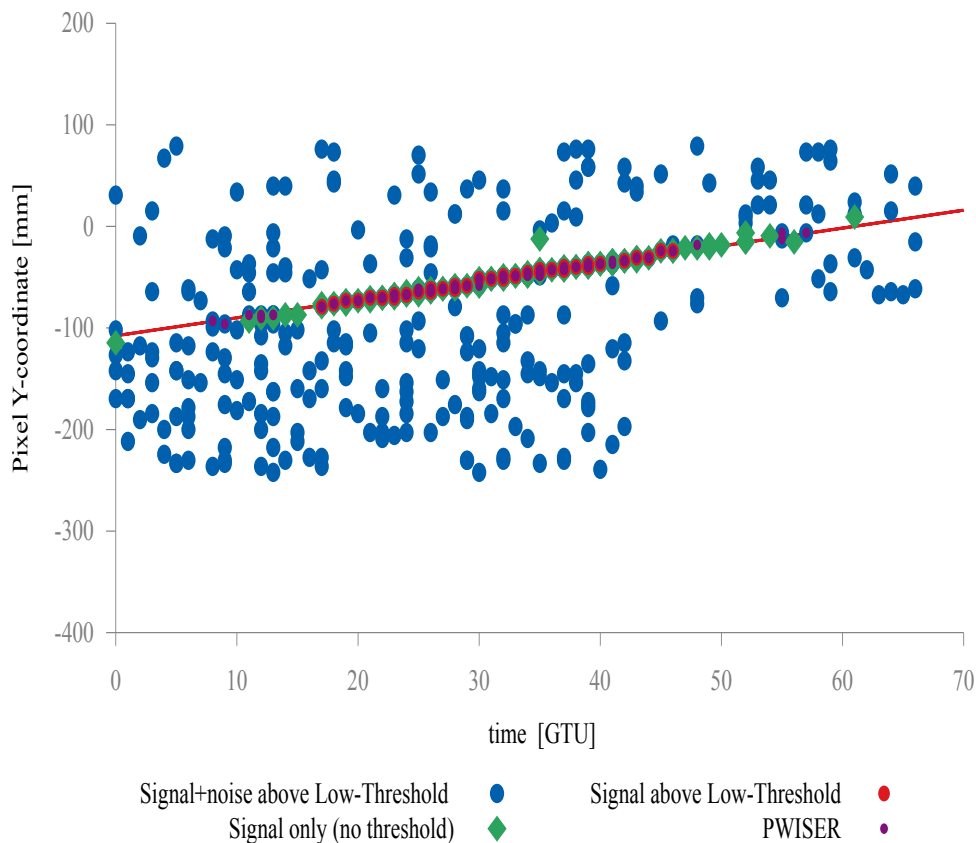


**Figure 4.5:** An illustration of *PWISE-R* technique. Here we show the points in the  $yt$  plane. The solid line is the result of the linear fit performed after the *PWISE* as a first stage (see text).

Again we need to introduce new parameters which are included in the implementation of the algorithm in *ESAF*:

—Extract from *PWISEModule.cfg*—

```
PWISEModule.fLowThreshold= 5 # Low-Threshold in counts.
PWISEModule.fTimeThreshold= 2 # Time-Threshold in GTUs.
```

This approach has provided an overall improvement compared to the simpler *PWISE* technique. We will discuss these results further in in § 4.2.2.

### 4.1.3 The CONEX - *ESAF* interface

The CONEX - *ESAF* interface was developed during the present thesis to provide a more realistic simulation of EAS than the one provided for default by the *SLAST* module (see § 3.2.1). Let us remember that the standard EAS simulator within *ESAF* is the *SLAST* shower simulator, based upon the GIL parametrization. Since any EUSO-like detector will observe the EAS from afar, *ESAF* does not concentrate on the detailed follow-up of the particles pertaining to the shower. Although this approach may seem convenient as a first study, it has its shortcomings when we try to study more fluctuating phenomena like neutrino or gamma induced EAS. For lower-energy

ground-based observatories, where the inner details of the EAS are indeed studied, suitable full Monte Carlo (MC) tools have been developed. For example, AIRES [Sciutto 1997] and CORSIKA [Pierog & Heck 2011] are state of the art software used in experiments like the PAO. The idea is to simulate the interactions of the secondary particles produced during the EAS development. Depending on the energy range this type of simulation could involve following  $\sim 10^{10}$  particles. Therefore some cuts or *thinning* techniques are applied to save computer resources. The MC softwares need to be constantly fine tuned and updated using data from accelerators and UHECR experiments [Pierog 2013] [Ostapchenko 2014].

In the scope of this thesis, the major setback of a full MC simulation of an EECR would be the huge amount of computer resources it requires. Besides this fact, we are only interested in the fluorescence signal produced by the shower front. We will begin by describing the CONEX simulations and then proceed to explain the interface to use them in ESAF.

#### 4.1.3.1 CONEX

---

An alternative simulating procedure is to describe EAS development numerically, based on the solution of the corresponding cascade equations. Combining this with an explicit MC simulation of the most high-energy part of an air shower allows one to obtain accurate results both for average EAS characteristics and for their fluctuation. This is essentially the backbone of CONEX [Bergmann 2007], which is the code we will be using in the present work. A CONEX EAS simulation is divided in two stages: the Monte-Carlo simulation and the cascade equations' solution. We begin by describing the MC simulation and follow with the cascade equations. For this sections we will follow the description of the physical process and their simulation as presented in [Bergmann 2007].

#### 4.1.3.2 Explicit MC simulation

---

CONEX follows individual particles such as nucleons, charged pions, charged and neutral kaons, lambdas, etc. using a MC approach. This hadronic cascade is simulated recording all secondary particles at a number of pre-chosen depth levels and energy intervals, until all produced secondaries have an energy lower than a given energy threshold. Other hadrons are assumed to decay immediately, and the decay products are the ones being followed. In this work we only used the EPOS-LHC hadronic interaction model [Pierog 2013]. The main reason is that EPOS-LHC has been tuned to be able to reproduce LHC data, whereas other hadronic interaction models within CONEX do not. Nevertheless, selecting a different (updated) hadronic interaction model (e.g. QGSJET-II -04 [Ostapchenko 2011]) would be negligible for the studies presented in this thesis. The electromagnetic component is also simulated in MC fashion via the Electron Gamma Shower code [Nelson et al. 1985]. The latter is supplemented by an account of the Landau-Pomeranchuk-Migdal effect for UHE electrons, positrons and photons [Landau & Pomeranchuk 1953] [Migdal 1956]. If the primary is a photon or an electron, the simulation process starts with the calculation of possible interactions with the geomagnetic field using a PRESHOWER routine (this accounts for the geomagnetic pair production and bremsstrahlung). This is of particular importance for EUSO-like missions since it will be flying across different zones of the geomagnetic field. For both the MC and the cascade equations, each step's output becomes an input for the next stage of the simulation.

### 4.1.3.3 Numerical solution of the cascade equations

All the secondary particles with energies below the energy threshold are then fed as sources in a set of nuclear-electro-magnetic cascade equations. These equations are used to describe sub-cascades of smaller energies. The equations are separated in a hadronic, electron/positron, and photon cascade equations. We now show them and discuss their overall behavior. First of all, all three equations are a description of the differential energy spectra of particles at different atmospheric depths along a straight line trajectory;  $h_a(E, X)$  for  $a$ -type hadrons,  $l_{e^\pm}(E, X)$  for electrons/positrons, and  $l_\gamma(E, X)$  for photons. Muons are treated like hadrons, but without interaction term (see below). All of them include both source and “sink” terms, that dictate the variations in the population of particles in the shower front. To fix ideas we reproduce the equations as they appear in [Bergmann 2007]. For the hadronic sector we have:

$$\frac{\partial h_a(E, X)}{\partial X} = \overbrace{-\frac{h_a(E, X)}{\lambda_a(E)} - h_a(E, X) \frac{\frac{dL}{dX}}{c \cdot \tau_a(E)} + \frac{\partial}{\partial E} (\beta_a^{ion}(E) h_a(E, X))}^{sinks} + \underbrace{\sum_d \int_E^{E_{max}} dE' h_d(E', X) \left[ \frac{W_{d \rightarrow a}(E', E)}{\lambda_d(E')} + D_{d \rightarrow a}(E', E) \frac{\frac{dL}{dX}}{c \cdot \tau_d(E)} \right]}_{sources} + S_a^{had}(E, X) \quad (4.4)$$

As *sinks* we have: a decrease due to interactions with air nuclei, parametrized with the mean free path  $\lambda_a$ ; particle decay on a path  $dL$ , characterized by the propagation distance during the life time of the hadron  $a$  in the laboratory system  $c \cdot \tau_a$ . As *sources* we have: production of  $a$ -type hadrons via interactions or via decays of  $d$ -type hadrons, with their corresponding mean free paths and decay lengths, represented by  $\frac{W_{d \rightarrow a}(E', E)}{\lambda_d(E')}$  and  $D_{d \rightarrow a}(E', E) \frac{\frac{dL}{dX}}{c \cdot \tau_d(E)}$  respectively. Here  $W_{d \rightarrow a}$  and  $D_{d \rightarrow a}$  are the corresponding differential energy spectra of the secondary particles; and the MC hadronic source  $S_a^{had}(E, X)$  which sets the initial conditions. The latter is determined during the MC simulation of above-threshold particle cascading plus a contribution from the electromagnetic cascade equations (see below).

For the electromagnetic component of the shower we have:

$$\frac{\partial l_{e^\pm}(E, X)}{\partial X} = \overbrace{-\sigma_{e^\pm}(E) l_{e^\pm}(E, X) + \frac{\partial}{\partial E} (\beta_{e^\pm}^{ion}(E) l_{e^\pm}(E, X))}^{sinks} + \underbrace{\left. \begin{aligned} & \int_E^{E_{max}} dE' l_{e^\pm}(E', X) W_{e^\pm \rightarrow e^\pm}(E', E) + \\ & \int_E^{E_{max}} dE' l_\gamma(E', X) W_{\gamma \rightarrow e^\pm}(E', E) + \\ & \text{(only for electrons)} \rightarrow \int_E^{E_{max}} dE' l_{e^-}(E', X) W_{e^+ \rightarrow e^-}(E', E) + \\ & S_{e^\pm}^{e/m}(E, X) \end{aligned} \right\}}_{sources}$$

for electrons and positrons; and for photons we have:

$$\frac{\partial l_\gamma(E, X)}{\partial X} = \overbrace{-\sigma_\gamma(E)l_\gamma(E, X)}^{\text{sinks}} + \underbrace{\left( \int_E^{E_{max}} dE' l_\gamma(E', X) W_{\gamma \rightarrow \gamma}(E', E) + \int_E^{E_{max}} dE' l_{e^-}(E', X) W_{e^- \rightarrow \gamma}(E', E) + \int_E^{E_{max}} dE' l_{e^+}(E', X) W_{e^+ \rightarrow \gamma}(E', E) + S_\gamma^{e/m}(E, X) \right)}_{\text{sources}}$$

For these equations' sinks we have losses due to interactions with the medium characterized by the cross sections  $\sigma_{e^\pm, \gamma}(E, X)$  (in units mass/area) and, in the case of  $e^\pm$ , also ionization losses. For  $\sigma_{e^-}$ , Bremsstrahlung and Møller scattering (electron-electron scattering) are taken into account; whereas for  $\sigma_{e^+}$  the processes taken into account are bremsstrahlung, annihilation, and Bhabha scattering (electron-positron scattering). For  $\sigma_\gamma$  the processes taken into account are pair-production, Compton scattering, photonuclear interactions and muon-pair production. The corresponding differential energy spectra take ( $W_{l_a \rightarrow l_b}$ ) into account all of the previous process.

As we mentioned above there is a coupling between the hadronic cascade equations and the electromagnetic ones. This is introduced by photo-production of hadrons (photonuclear interactions) and by  $\mu^\pm$  pair-production. As a consequence we can write the source term for type  $a$ -hadrons in the hadronic cascade equations as:

$$S_a^{had}(E, X) = S_a^{MC}(E, X) + S_a^{\gamma \rightarrow a}(E, X) + \delta_a^\mu \cdot S_a^{\gamma \rightarrow \mu}(E, X).$$

The output of the CONEX program is a ROOT file with the simulation parameters, the EAS's longitudinal profile, as well as some run-time information. Particularly important for this work are:

- **H** A fixed array of floats (4 byte precision), which contains the height above sea level in meters.
- **D** A fixed array of floats, which contains the distance to the observation point (the origin of the CONEX system of reference).
- **dEdX** A fixed array of floats which contains the energy deposited by the EAS in the atmosphere  $\frac{dE}{dX}(X, E)$ .
- **dNdX** A fixed array of floats, which contains the number of charged particles  $\frac{dN}{dX}(X, E)$ .

Also the first interaction point and the primary particles information are saved in the ROOT file. A sample energy deposition profile is shown in Fig. 4.6

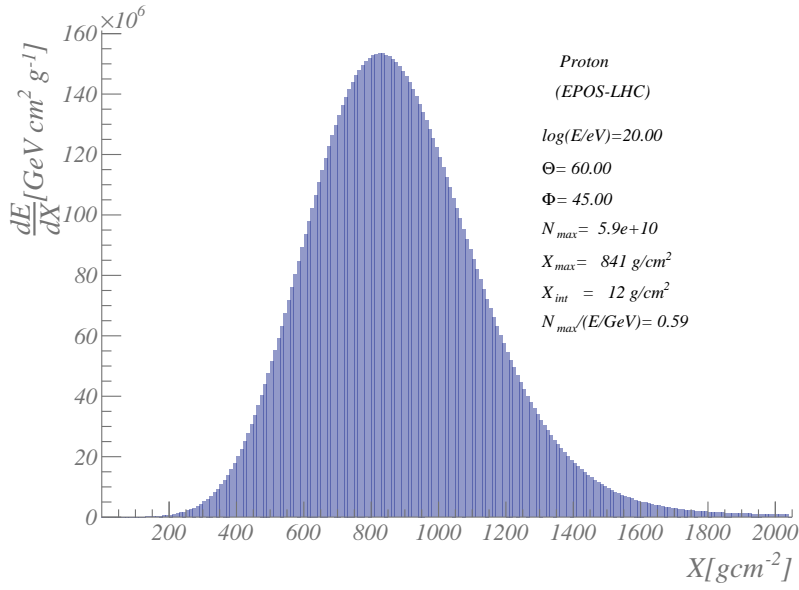


**Figure 4.6:** Energy deposition as a function of slant depth for a typical shower simulated using CONEX. Energy is  $10^{20}$  eV and zenith angle is  $60^\circ$ .

#### 4.1.3.4 Fluorescence Yield

We turn now our attention back to EUSO specific software. Inside *ESAF* the number of EAS-generated fluorescence-photons  $dN_{fluoro}$  per distance  $dL$ , with wavelength  $\lambda$  and at a depth  $X$  is calculated with [Berat et al. 2010]:

$$\frac{dN_{fluoro}}{dL} = N_e(X) FY(T, \rho; E_{ref}, \lambda) \cdot \frac{\left\langle \frac{dE}{dX} \right\rangle(X)}{\frac{dE}{dX}(E_{ref})} \quad (4.5)$$

Where  $FY(T, \rho; E_{ref}, \lambda)$  is the number of photons per electron, per unit distance; with a wavelength  $\lambda$ , generated by an electron with energy  $E_{ref}$  as it transverses an air mass with temperature  $T$  and density  $\rho$  [Nagano et al. 2004]. The factor  $\frac{\left\langle \frac{dE}{dX} \right\rangle(X)}{\frac{dE}{dX}(E_{ref})}$  is the average energy deposited by an electron in the shower at the depth  $X$  divided by the energy deposited by an electron with the reference energy. In other words

$$\left\langle \frac{dE}{dX} \right\rangle(X) = \int_E P_e(E; X) \frac{dE}{dX}(E) dE$$

Where  $P_e(E; X) = \frac{1}{N_e} \frac{dN_e}{dE}$  is the normalized energy distribution of the electrons present in the shower front at a depth  $X$ .

Normally, Eq. 4.5 is written not in terms of  $X$  but in terms of the shower age  $s$ . However as we mentioned in § 3.2.1 two different definitions of shower age are used throughout the *ESAF*'s code.

Even if this lack of consistency could be neglected, it is clear that the assumed energy distribution plays a major role in the parametrization of the amount of photons created at each shower's step. This is crucial when talking about EAS with a strong LPM effect or non-baryonic primaries. In this case SLAST cannot reproduce multiple peaks or account for shower to shower fluctuations in a realistic way (see § 3.2.1). Nevertheless, SLAST does provide sufficient information in the case of proton primaries and has been used for thorough studies regarding the exposure of a EUSO-like detector [Adams et al. 2013a].

In this work, we deviate from the standard ESAF way of calculating the fluorescence yield and we take advantage of the fact that CONEX provides us with the total energy deposited in the atmosphere by the shower front, and not only the electrons as assumed above. We calculate the photon yield at each point of the shower following [Nagano et al. 2004]:

$$FY(T, \rho; E, \lambda) = \left( \frac{1}{N_e(X)} \right) \frac{\left( \frac{dE}{dX} \right)_E}{\left( \frac{dE}{dX} \right)_{0.85 \text{ MeV}}} \frac{A_\lambda \rho}{1 + \rho B_\lambda \sqrt{T}} \quad (4.6)$$

In this last expression  $A_\lambda$  and  $B_\lambda$  are experimentally assigned constants. Inserting Eq. 4.6 into Eq. 4.5 gives the total number of fluorescent photons of wavelength  $\lambda$  per unit distance without any assumption on the energy distribution of the particles present in the EAS's front and independently of the shower age definition. The total fluorescence yield of each EAS step is calculated by summing the contributions of all different involved wavelengths.

#### 4.1.3.5 Cherenkov Yield

In a similar way to what is done for the fluorescent component, ESAF's standard approximation is to use a parametrization of the electrons' energy distribution, to calculate the Cherenkov photons per unit length (here the wavelength sum is done before hand) [Berat et al. 2010]:

$$\frac{dN_{ckov}}{dL} = N_e(X) \int_{E_{thres}}^{\infty} \left( \frac{1}{N_e} \frac{dN_e}{dE} \right) CY(E, \eta) dE \quad (4.7)$$

Where  $\eta$  is the atmosphere's refractive index.

We introduce a small change to the overall scheme, by using a parametrization of the Cherenkov yield as a function of the energy deposition taken from [Nerling et al. 2006].

#### 4.1.3.6 Conventions and usage of the CONEX ESAF interface

To import the EAS simulations from CONEX into ESAF, we have to account for the difference in the age definition and the geometrical transformations between the frames of reference of both programs. In CONEX the shower-local system of reference is introduced. Since CONEX performs the simulations in only one dimension, it suffices to define the point of minimum approach to the Earth's surface as the origin for this system of reference (see Fig. 4.7). We begin by defining the variables involved in the relevant transformations:

- $R_\oplus$  Earth's Radius.

- $M$  EUSO Position  $(0, 0, H_{iss})_{MES}$ .
- $N$  Nadir center of the Field of View. By definition  $H_{ISS} = \overline{MN}$  or  $(0, 0, 0)_{MES}$ .
- $O$  Center of the Earth  $(0, 0, -R_{\oplus})_{MES}$ .
- $P$  Point of closest approach ON the Earth's surface. It is the impact point in case there is one. This is referred as the observation point in CONEX, i.e. the origin of CONEX's system of reference.
- $P'$  Point of closest approach to the Earth's surface. Only relevant when there is no impact point.
- $\zeta$  Angle measured from Earth's center between  $O$  and the point of closest approach  $P$ .
- $s$  Arc length between  $(0, 0, 0)_{MES}$  and point of closest approach ( $s = \zeta R_{\oplus}$ ).
- $d$  Minimum distance between  $(0, 0, 0)_{MES}$  and point of closest approach ( $\overline{NP}$ ).
- $r$  Radial distance in MES to the the impact point. That is  $r^2 = x_p^2 + y_p^2$  with  $x$  and  $y$  in the MES frame.
- $h_{loc}$  Local height of  $P'$ .
- $\alpha$  Auxiliary angle. Defined as the angle between segment  $\overline{MP}$  and  $\overline{MO}$ .

#### 4.1.3.7 Geometrical cases

To insert a CONEX-simulated EAS we need to “place” the EAS inside ESAF, and transform both  $\Phi$  and  $\Theta$  from the local coordinate system to the MES (as introduced in § 3.3.2). In other words we need to define or characterize the transformation of:

$$\begin{pmatrix} x \\ y \\ z \end{pmatrix}_{local} \rightarrow \begin{pmatrix} x \\ y \\ z \end{pmatrix}_{MES} \quad \text{and} \quad \begin{pmatrix} \Theta \\ \Phi \end{pmatrix}_{local} \rightarrow \begin{pmatrix} \Theta \\ \Phi \end{pmatrix}_{MES}$$

The first part is done by selecting the coordinates of the origin of the local coordinate system within the FOV. To transform the different angles, in principle we would need to perform a three dimensional rotation. However since we know CONEX is a one dimensional simulation program we can simplify the problem as 1 dimensional one, i.e. we only have to perform a rotation along the  $Y$  to align both systems of references. This could have an impact since CONEX introduces a North-East reference system within the PRE-SHOWER routine. However, this is only relevant for gamma and electron primaries. Currently ESAF has no convention to orientate the  $X$  and  $Y$  axis, and most importantly in cylindrical versions of a EUSO-like mission this would implicate no impact.

In this work we will take  $\Phi_{local} = \Phi_{MES}$ . This simplified approach is illustrated in on Figure 4.7 and Figure 4.8. This reduces the problem to finding  $\vec{r}_{impact}$  and  $\Theta_{MES}$ .

We distinguish 4 possible cases to carry out the transformations, based upon the information available/given by the user. Namely:

1. The EAS has an impact point (sometimes referred as “shower core” (see Figure 4.7) and :

- a) we are given the arc length( $s$ ) to the impact point ( $P$ )  
or  
b) we are given the radial distance ( $r$ ) to the the impact point ( $P$ ).
2. Without an impact point (see Figure 4.8). This is the case for (locally) horizontal showers. This are characterized by the local height  $h_{loc}$ . We distinguish two user dependent cases:  
a) we are given the arc length ( $s$ ) to the point of closest approach ( $P'$ ) and its local height  $h_{loc}$   
or  
b) we are given the radial distance ( $r$ ) to the point of closest approach ( $P'$ ) and its local height  $h_{loc}$ .

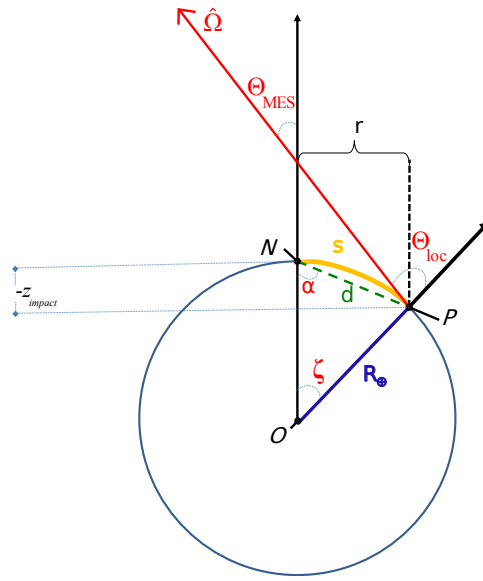


**Figure 4.7:** Diagram of the geometrical characteristics on the plane containing the EAS's track and the center of the Earth. The shower track (in red) is supposed to impact on the Earth's surface. Remember that the EAS's propagation is in the  $-\hat{\Omega}$  direction.

For case 1.a we have the following solution (to follow see Figure 4.7):

$$\Theta_{MES} = \Theta_{loc} - \zeta, \quad \alpha = \frac{\pi - \zeta}{2}, \quad d = R_{\oplus} \frac{\sin \zeta}{\sin \alpha} = R_{\oplus} \frac{\sin \zeta}{\cos \frac{\zeta}{2}}$$

$$\Rightarrow z_{MES} = -d \cos \alpha = -d \sin \frac{\zeta}{2} = -R_{\oplus} \sin \zeta \tan \frac{\zeta}{2}$$

$$\Rightarrow r = d \sin \alpha = d \cos \frac{\zeta}{2} = R_{\oplus} \sin \zeta$$

Which suffices to set the impact point by selecting a random direction  $\phi_{core}$  in the FoV. This is:

$$\vec{r}_{impact} = \begin{pmatrix} R_{\oplus} \sin \zeta \cos \phi_{core} \\ R_{\oplus} \sin \zeta \sin \phi_{core} \\ - R_{\oplus} \sin \zeta \tan \frac{\zeta}{2} \end{pmatrix} \text{ and } \Theta_{MES} = \Theta_{loc} - \zeta, \quad \Phi_{MES} = \Phi_{loc} \quad (4.8)$$

For case 1.b we have the following solution (to follow see Figure 4.7):

$$\begin{aligned} z_{MES} &= \sqrt{R_{\oplus}^2 - r^2} - R_{\oplus}, & \zeta &= \arctan\left(\frac{r}{R_{oplus}}\right) \\ \Theta_{MES} &= \Theta_{loc} - \zeta, & \Phi_{MES} &= \Phi_{loc} \end{aligned} \quad (4.9)$$

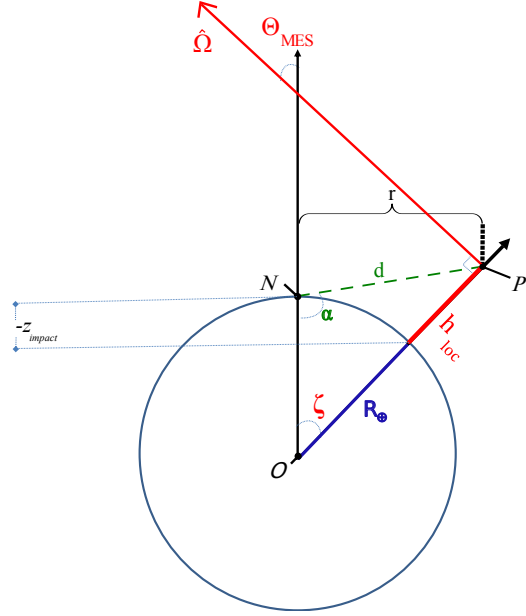


**Figure 4.8:** Diagram of the geometrical characteristics on the plane containing the EAS's track and the center of the Earth. The shower track (in red) has no impact point but rather a local height of maximum approximation  $h_{loc}$ .

For case 2(a) we have the following solution (to follow see Figure 4.8):

$$\Theta_{MES} = \frac{\pi}{2} - \zeta \quad d'^2 = R_{\oplus}^2 + (R_{\oplus} + h_{loc})^2 - 2R_{\oplus}(R_{\oplus} + h_{loc})\cos(\zeta)$$

Since we do not have an impact point, we use  $P'$  as reference to define an injection point. The injection point allows us to create the EAS by moving step by step using the shower's direction vector  $\hat{\Omega}$ . We have, in a similar way as in Eq. 4.8:

$$\vec{r}_{P'} = \begin{pmatrix} (R_{\oplus} + h_{loc}) \sin \zeta \cos \phi_{core} \\ (R_{\oplus} + h_{loc}) \sin \zeta \sin \phi_{core} \\ (R_{\oplus} + h_{loc}) \cos \zeta - R_{\oplus} \end{pmatrix} \quad \text{and} \quad \Theta_{MES} = \frac{\pi}{2} - \zeta, \quad \Phi_{MES} = \Phi_{loc} \quad (4.10)$$

It is worth noticing that Eq. 4.10 reduces to Eq. 4.8 when  $h_{loc} = 0$ . Because of the way CONEX reference system is defined, we need to keep both approaches [Bergmann 2007].

Finally for case 2(b) we have the following solution (see Figure 4.8):

$$\begin{aligned} z_{MES} &= \sqrt{(R_{\oplus} + h_{loc})^2 - r^2} - R_{\oplus}, & \zeta &= \arctan\left(\frac{r}{R_{oplus}}\right) \\ \Theta_{MES} &= \frac{\pi}{2} - \zeta, & \Phi_{MES} &= \Phi_{loc} \end{aligned} \quad (4.11)$$

As expected, this last expression reduces to Eq. 4.9 when  $h_{loc} = 0$ .

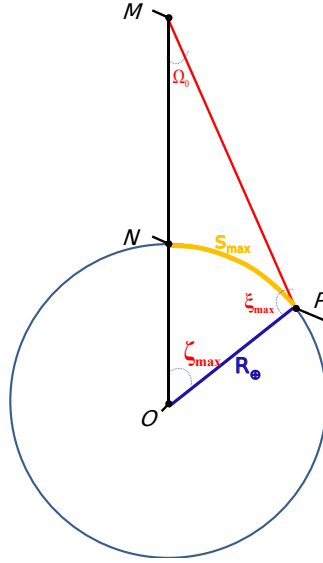


**Figure 4.9:** Diagram of the relevant geometrical characteristics for the calculation of  $\zeta_{max}$  (see text).

It is also illustrative to take an extreme case based on the maximum angular distance to a point inside the FOV. This maximum angular  $\zeta_{max}$  is constrained by the FOV aperture  $\Omega_0$ , the altitude of the EUSO detector  $H_{ISS}$ , and the Earth's Radius. Using the variables defined in Fig. 4.9, we can write:

$$\begin{aligned} \zeta_{max} &= \pi - \arcsin\left(\frac{(R_{\oplus} + H_{ISS})\sin\Omega_0}{R_{\oplus}}\right) \approx 148^\circ & \zeta_{max} &= \pi - \Omega_0 - \xi_{max} \approx 2.0995^\circ \\ \implies s_{max} &= R_0 \cdot \zeta_{max} \approx 233.461 \text{ km} & r_{max} &= R_0 \cdot \sin \zeta_{max} \approx 233.409 \text{ km} \end{aligned} \quad (4.12)$$

Where we have taken  $\Omega_0 = 15^\circ$ ,  $R_{\oplus} = 6371 \text{ km}$  and  $H_{ISS} = 400 \text{ km}$ . It is important to highlight that although not negligible, the differences in zenith angles is quite small. But for the local heights it becomes a very important factor since almost 50 % of the atmosphere is in the first 5 km. We illustrate how big is the difference in local height for a few angles in Table 4.1.

#### 4.1.4 Configuration of the CONEX-ESAF interface

During the course of this dissertation a new *EventGenerator* was implemented inside ESAF: the *ConexFileShowerGenerator*. To control the different geometrical scenarios and to provide a way to

| $\zeta$      | Earth's arc (s) | $z_{diff}$ |
|--------------|-----------------|------------|
| $1^\circ$    | 111.19 km       | 0.97 km    |
| $2.01^\circ$ | 223.89 km       | 3.91 km    |
| $2.24^\circ$ | 249.07 km       | 4.86 km    |

**Table 4.1:** Difference in local height and *MES* height for different distances to the center of the FOV. See Fig. 4.9 for the definition of  $\zeta$ .

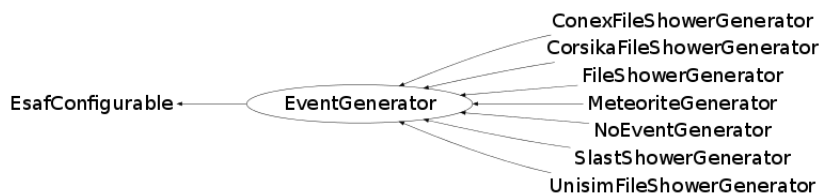


**Figure 4.10:** Inheritance diagram for the *EventGenerator* class. The *ConexFileShowerGenerator* does not generate a new CONEX-simulated shower, but rather reads a CONEX output file and introduces the EAS into ESAF.

manually select the injection point, the *ConexFileShowerGenerator* uses a configuration file. The user can manually fix either the point of first interaction, the first interaction grammage or the impact point (core location). Only one of the last three options is allowed to avoid unphysical behavior. The user can also manually override  $\Theta$  and/or  $\Phi$  effectively selecting the direction vector. This provides the user with whole control of the geometrical characteristics of the inserted EAS. This options are summarized as:

—Extract from *ConexFileShowerGenerator.cfg*—

**# Override  $\Theta$  value?**

`ConexFileShowerGenerator.fForceTheta= no # yes/no`

`ConexFileShowerGenerator.fTheta=80. # [deg]`

**# Override  $\Phi$  value ?**

`ConexFileShowerGenerator.fForcePhi= no # yes/no`

`ConexFileShowerGenerator.fPhi=45 # [deg]`

**# Override first interaction depth?**

`ConexFileShowerGenerator.fForceX1= no # yes/no`

`ConexFileShowerGenerator.fX1=40 # in [g/cm2]`

**# Fix the first interaction point.**

`ConexFileShowerGenerator.fFixedInitPos= no`

`ConexFileShowerGenerator.fXini= 10 # Xcoordinate in MES [km]`

`ConexFileShowerGenerator.fYini= 10 # Ycoordinate in MES [km]`

`...etc`

**# Fix the core (impact point)**

`ConexFileShowerGenerator.fFixedCore= no # Fix the core position`

`ConexFileShowerGenerator.fXCore= 10 # Xcoordinate in MES [km]`

`...etc`

The above options however have to be used with caution. Although the EAS's depth, its direction and position may be consistent, they may not represent what was originally simulated with CONEX. An automatic shower introduction is also available via the following configuration options:

---

—Extract from ConexFileShowerGenerator.cfg—

# Insert showers automatically? If yes ESAF sets a random core.

ConexFileShowerGenerator.fGeometryRNDMCore=yes# yes/no

# Flat distribution or sin(x) ditribution

ConexFileShowerGenerator.fGeometryRNDMZetaDist=flat # flat or sin

ConexFileShowerGenerator.fGeometryZetaMin=0; # Min  $\zeta$  [deg]

ConexFileShowerGenerator.fGeometryZetaMax=2.0; # Max  $\zeta$  [deg]

ConexFileShowerGenerator.fGeometryPhiCoreMin=0; # Min  $\phi_{core}$  [deg]

ConexFileShowerGenerator.fGeometryPhiCoreMax=360; # Max  $\phi_{core}$  [deg]

---

## 4.2 Angular reconstruction

### 4.2.1 Simulation sets

In this section we will present the results of applying the techniques discussed in the previous chapter to simulate and/or reconstruct EAS. We begin by showing a selection of what we published in [Guzmán, Mernik et al. 2014], where we used the default shower generator from ESAF as well as *PWISE* as the pattern recognition. We will then continue with a similar sample of EAS, but this time the results will be obtained using CONEX and *PWISE-R*.

For the SLAST proton-simulations we used a set of fixed conditions in energy and inclination angle as a starting point. This conditions are summarized in Table 4.2. We injected  $\sim 1000$  showers per energy-angle combination. The impact points of the showers were set randomly in a  $300 \text{ km} \times 300 \text{ km}$  square (at sea level). This reduced the number of triggering events when the shower was not visible to the instrument. Because of the very large computing times involved, the simulations at the highest energies and inclinations included a smaller number of events.

For the CONEX simulation we used a similar but smaller set of fixed conditions:

We characterize the error in the reconstructed arrival direction as the angle between the vectors  $\hat{\Omega}_{True}$  (the simulated arrival direction) and  $\hat{\Omega}_{Reco}$  (the reconstructed arrival direction). We define:

$$\gamma = \arccos(\hat{\Omega}_{True} \cdot \hat{\Omega}_{Reco}) \quad (4.13)$$

as the *error in the reconstruction*. To be able to compare the results with similar studies previously published [Bonifazi 2009] we define the *angular resolution* as the value where the cumulative distribution of the reconstruction's error reaches 68%. We shall refer to this value as  $\gamma_{68}$ . This definition is mathematically expressed as:

$$0.68 = \int_0^{\gamma_{68}} P(\gamma) d\gamma \quad (4.14)$$

| $E[eV]$            | $\Theta$ [deg] | Number of events |
|--------------------|----------------|------------------|
| $7 \times 10^{19}$ | 30°            | 654              |
|                    | 45°            | 675              |
|                    | 60°            | 684              |
|                    | 75°            | 648              |
| $10^{20}$          | 30°            | 712              |
|                    | 45°            | 694              |
|                    | 60°            | 672              |
|                    | 75°            | 1126             |
| $10^{21}$          | 30°            | 703              |
|                    | 45°            | 714              |
|                    | 60°            | 726              |
|                    | 75°            | 428              |

**Table 4.2:** The set of EAS simulations with a proton as a primary using SLAST and the default ESAF configuration with the side cut optics. This set of showers will be referred as the *EA-Benchmark*. The numbers vary due to the triggering efficiency and the amount of injected events per energy-angle combination (see text).

| $E[eV]$            | $\Theta$ [deg] | Number of events |
|--------------------|----------------|------------------|
| $5 \times 10^{19}$ | 30°            | 1000             |
|                    | 45°            | 1000             |
|                    | 60°            | 1000             |
|                    | 75°            | 1000             |
| $10^{20}$          | 30°            | 1000             |
|                    | 45°            | 1000             |
|                    | 60°            | 1000             |
|                    | 75°            | 1000             |

**Table 4.3:** The set of EAS simulations with a proton or an iron nucleus as CR-primary, using CONEX as the event generator. This set of showers will be referred as the *CONEX-Benchmark*.

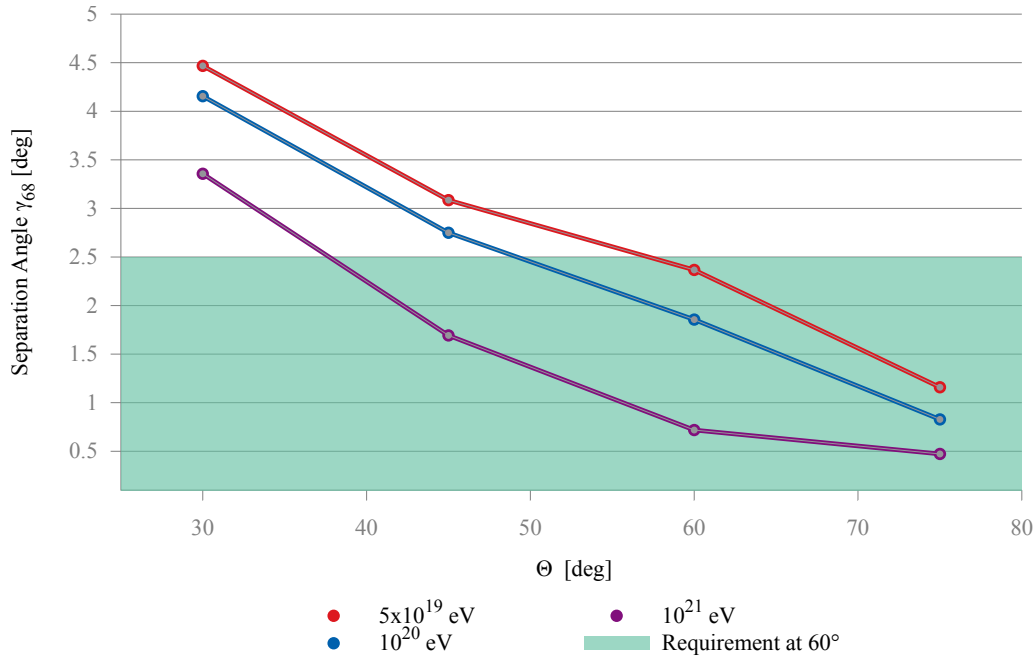


**Figure 4.11:** Our results for SLAST protons, as presented at [Guzmán, Mernik et al. 2014]. Here only *PWISE* was used as pattern recognition.

where  $P(\gamma)$  is the normalized distribution of the error.

#### 4.2.2 Summary of angular reconstruction for proton primaries

The first goal of the *PWISE* technique was to select a sufficient number of signal counts coming from the EAS, to provide enough information so that the angular reconstruction can meet the scientific requirements. As mention in § 2.1.2, within th GZK-sphere the galactic and intergalactic magnetic fields already spread the EECR-source’s spot in the sky. Even in the hypothetical case where we could reconstruct the arrival direction with absolute precision, the uncertainties in the back-calculation of the propagation of the EECR would “blur out” absolute precision.

The *PWISE* method, derived in this work, working in combination with the *TrackDirection2* module, has proven to fulfill the scientific requirement of the mission for angular reconstruction. This requirement states that the angular resolution of the experiment must be below  $2.5^\circ$  for EECR with an energy above  $10^{20}$  eV. Let’s focus on Fig. 4.11. The less vertical (higher  $\Theta$ ) a shower is the better is the angular reconstruction. At higher energy the angular reconstruction uncertainty decreases. Both of these behaviors can be explained as a consequence of a longer signal component at the FS. Either because there is more light (higher energy) or simply because there are more pixels activated (generally speaking more horizontal showers remain longer in the FoV).

For these results we selected the best performing algorithm in a case by case scenario. Although this will not be possible on the real data, these results remain a conservative first approach as will be discussed below. The key point is that even selecting just one algorithm the angular reconstruction does not suffer much worsening. Also in [Guzmán, Mernik et al. 2014] we used a rudimentary approach to pattern recognition. A better pattern recognition plus some “quality

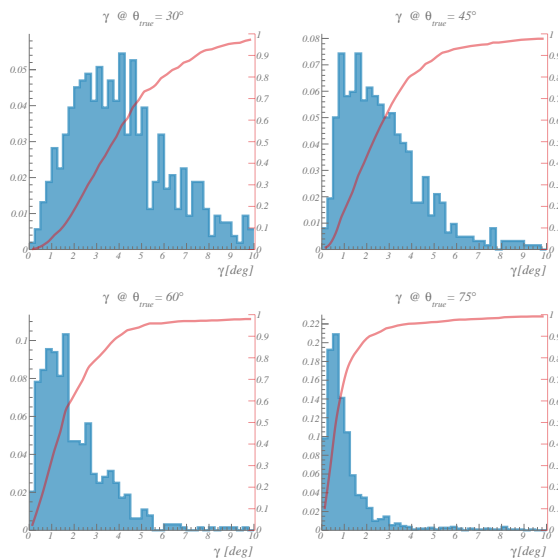


**Figure 4.12:** The normalized distribution of the reconstruction's error for SLAST proton showers at  $10^{20}$  eV (results presented in [Guzmán, Mernik et al. 2014]). In red the accumulated distribution is shown to illustrate how to calculate  $\gamma_{68}$ .

cuts" have shown to improve the former results even when selecting only the NE2 algorithms.

### 4.2.3 Angular reconstruction for Fe and Proton primaries

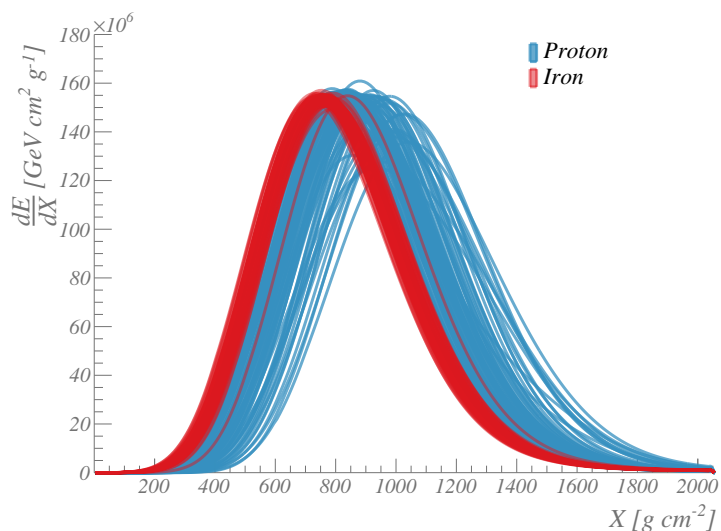


**Figure 4.13:** The longitudinal profiles of EAS initiated by protons and iron nuclei. For both primaries we show a subsample of 100 showers with an energy of  $10^{20}$  eV and  $\Theta = 60^\circ$ . The greater intrinsic fluctuation in proton initiated EASs can be clearly appreciated.

As previously discussed in this chapter, this thesis's work has provided the necessary tools and modifications to ESAF to allow it to simulate more realistic EECR. As it is shown in Fig. 4.13,

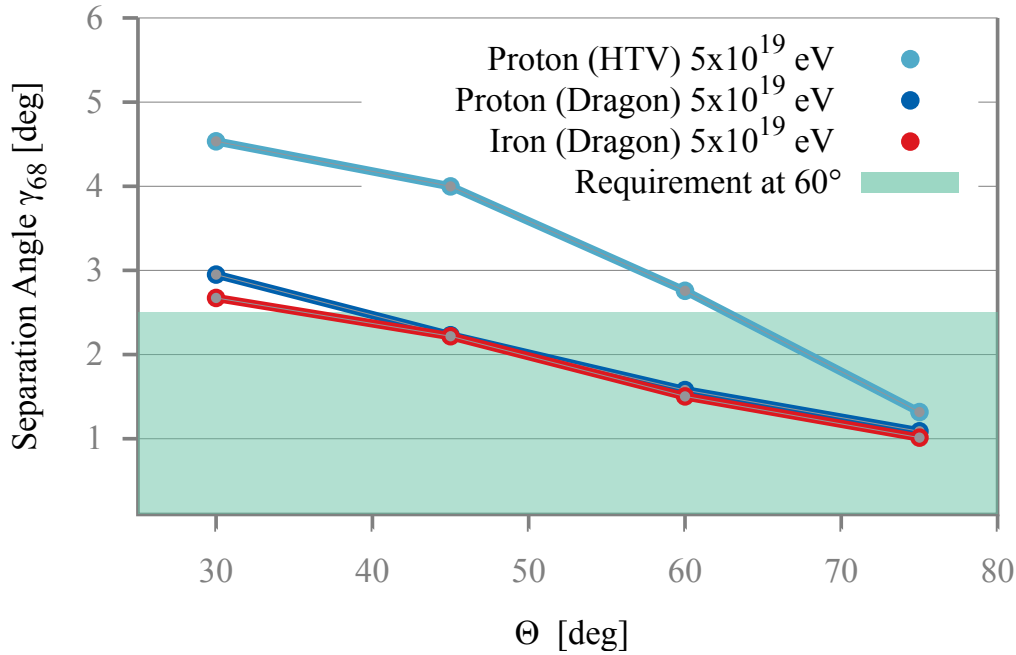


**Figure 4.14:** The angular resolution for proton and iron primaries using the *PWISE-R* technique and CONEX simulated showers with  $E = 5 \times 10^{19}$  eV. Results with the HTV configuration for protons at  $10^{20}$  eV are shown for comparison [Guzmán, Mernik et al. 2014].

using CONEX showers, we simulate the intrinsic fluctuations of the longitudinal profile, not only more manifestly but also using an updated hadronic process calculator. In this part of the thesis we were particularly interested to see if the assumptions of the *TrackDirection2* about the position and nature of the shower would have an impact on the angular reconstruction. For the rest of the thesis, unless stated otherwise, we used the dragon configuration of the instrument. Our results for CONEX-simulated protons and CONEX-simulated Fe are shown in Fig. 4.14 and Fig. 4.15 at energies  $5 \times 10^{19}$  eV and  $10^{20}$  eV respectively. As it can be seen, the angular reconstruction is robust enough to handle the intrinsic shower to shower fluctuations present in the proton primaries.

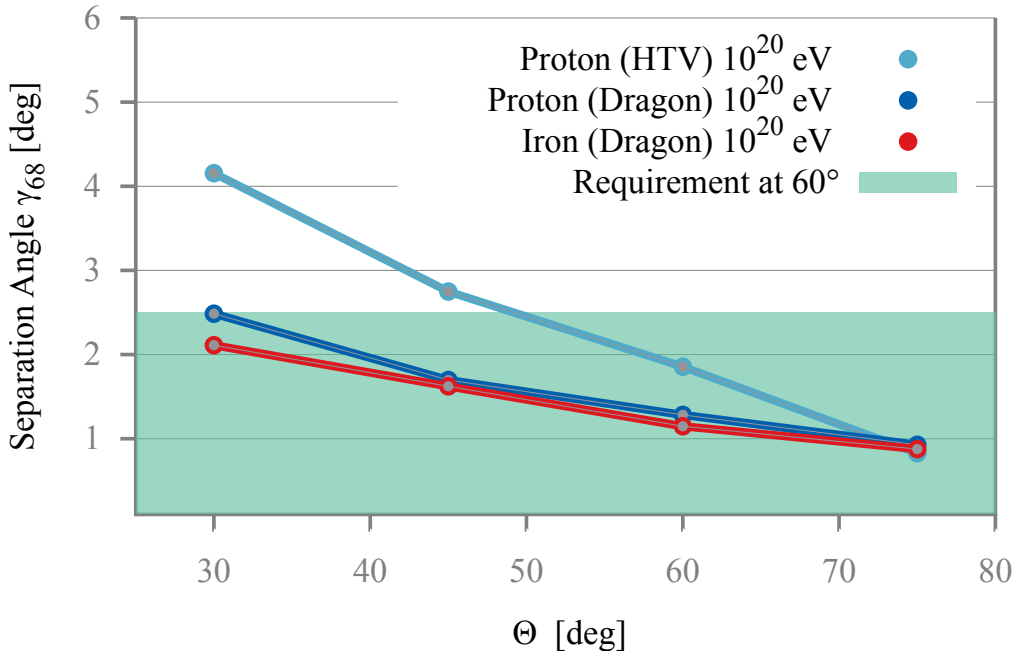


**Figure 4.15:** The angular resolution for proton and iron primaries using the *PWISE-R* technique and CONEX simulated showers with  $E = 10^{20}$  eV. Results with the HTV configuration for protons at  $10^{20}$  eV are shown for comparison [Guzmán, Mernik et al. 2014].

#### 4.2.4 Angular reconstruction for EE- $\gamma$ primaries

We also took advantage of the tools developed in this thesis and test even further the performance of the angular reconstruction for photon primaries. Due to possible interactions with the geomagnetic field, special care has to be taken when performing the photon simulations. The pair production process depends strongly on the magnetic component transverse to the photon's direction of motion, and therefore the event simulation is sensitive to the value and direction of the local geomagnetic field [Homola et al. 2005]. We accounted for this effect in our simulations by sampling the longitude and latitude position of the ISS along its orbit. The difference in longitudinal profiles between protons and photons is more dramatic than what it is between protons and irons. This can be clearly seen in Fig. 4.16. We show the performance of the angular reconstruction for EE-photons in Fig. 4.17. Again we can see that the overall performance is robust enough. Nevertheless we must point out the fact that we suffer from a low triggering ratio for the showers that exhibit a strong Landau-Pomeranchuk-Migdal effect [Landau & Pomeranchuk 1953] [Migdal 1956]. Showers with a strong LPM appear less bright, as a consequence of their extended longitudinal profile. The latter works as a selection filter only allowing the brightest photon showers to trigger the detector and are therefore available for reconstruction. Again this is mostly relevant at the lower zenith angles, whereas for higher zenith angles the impact is less dramatic.

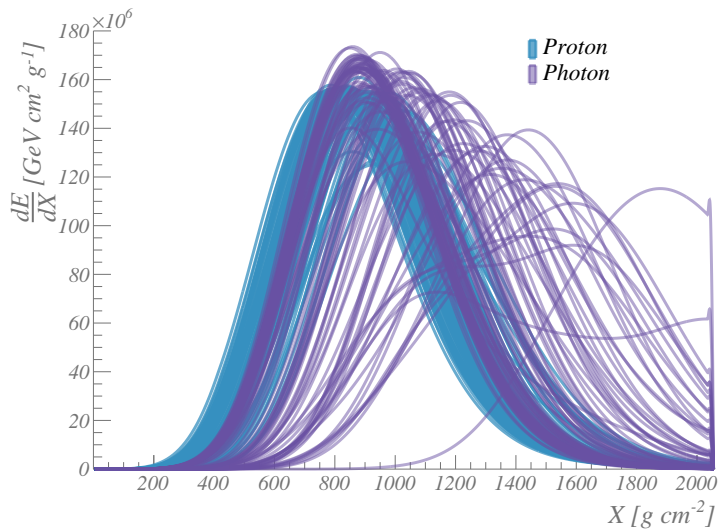


**Figure 4.16:** A comparison of the longitudinal profiles of EAS initiated by protons and photons( $\gamma$ ). For both primaries we show a subsample of 100 showers with an energy of  $10^{20}$  eV and  $\Theta = 60^\circ$ . The abrupt end of the deeply penetrating photon EAS at  $\sim 2000$  g cm $^{-2}$  marks the shower front reaching the ground.

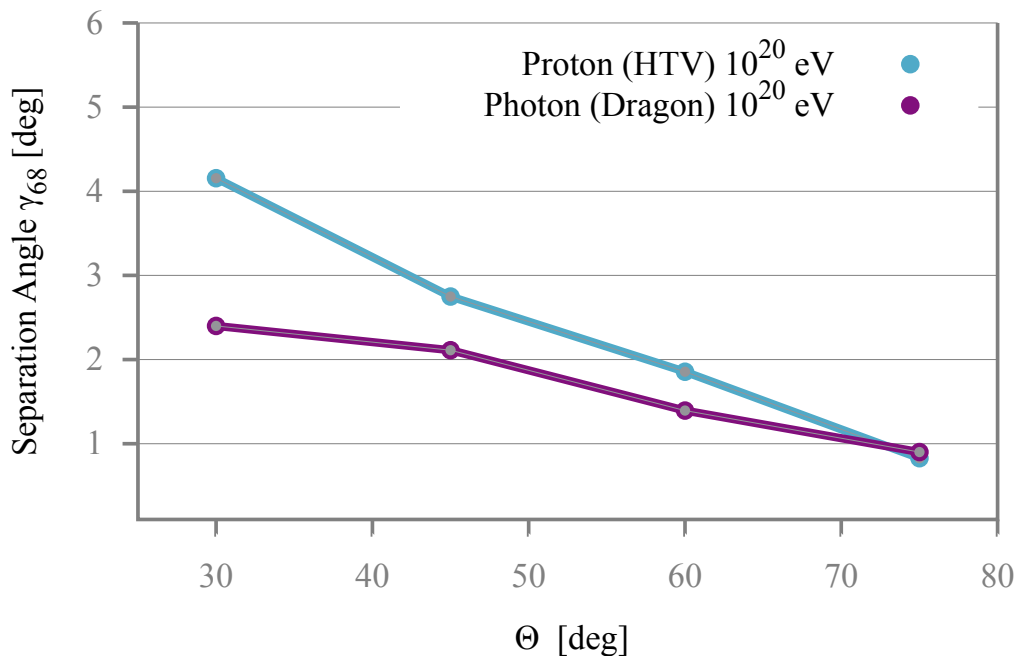


**Figure 4.17:** The angular resolution for photon primaries. The apparent improvement upon hadronic primaries comes to the expense of losing events (non-triggering). Shown are simulated showers with  $E = 10^{20}$  eV. Results with the HTV configuration for protons at  $10^{20}$  eV are shown for comparison [Guzmán, Mernik et al. 2014].

### 4.2.5 Quality cuts

To talk about a general angular resolution of a EUSO-like detector makes sense only for back-of-the-envelope calculations. This type of calculations is commonly encountered when discussing the scientific possibilities of the mission while is still in its design phase. Nevertheless, due to the small number of expected events, in the data analysis of a flying observatory each event will be analyzed with much more focus than the automatic tools discussed in the previous section. Hence the accuracy of the angular resolution will fluctuate in an event by event basis. In this spirit we will now turn our attention to what we define as “quality cuts”. The quality cuts are specific characteristics of each event, that provide a handle to the uncertainty in the reconstruction. In other words, the quality cuts allow us to discern specific events with a robust event-reconstruction from the events where the uncertainty is higher. Within the scope of the angular reconstruction, we introduce two quality cuts: the **Position in the FoV** and the **Number of Points** used by the fitting algorithms.

#### 4.2.5.1 Position in the FoV

An EUSO-like detector, like many other optic instruments, is not expected to have a perfectly uniform response across all wavelengths across the entire FS. Geometrical conditions, for example the sensitive area of the FS, may hinder the proper detection of EASs occurring in a particular spot on the FS. In our case, if we restrict our attention to events occurring in a region closer (farther) to the center of the FS, we show an improvement (worsening) of the angular resolution. This effect is shown in the upper panel of Fig. 4.18. Clearly in the outer parts of the FS the angular reconstruction fails more often as in the inner part. This allows us to introduce our first quality cut: **Position in the FoV**. To exemplify this idea, we show in the lower panel of Fig. 4.18 the angular resolution restricting ourselves to EAS whose light was detected by the inner most PDMs. That is, for the analysis in the lower panel of Fig. 4.18 we neglect EASs whose impact position was farther than 150 km from the center of the FoV. This is a consequence of the inhomogeneity of the detector itself. The events occurring within a few km from the center of the FoV are less deformed by the optics and also are closer to the instrument, than events farther away from the center of the FoV. However, the tools developed in this thesis have not been adapted to this expected real-life scenario. That is we do not use one configuration (a set of reconstruction parameters) for events occurring in one region of the FS and another configuration for other regions.

We do not do so because at this stage in the design phase the inhomogeneities are not completely and/or quantitatively characterized. Thus making any adaptation of the techniques to special conditions artificial and perhaps even a bit biased. The assumption that the detector is indeed homogeneous is a common first step. Afterwards we have to analyze the deviations from the ideal (simulated) scenario once construction and characterization of the detector is underway. The knowledge acquired with the studies here presented will prove crucial when tackling the actual instrument’s behavior.

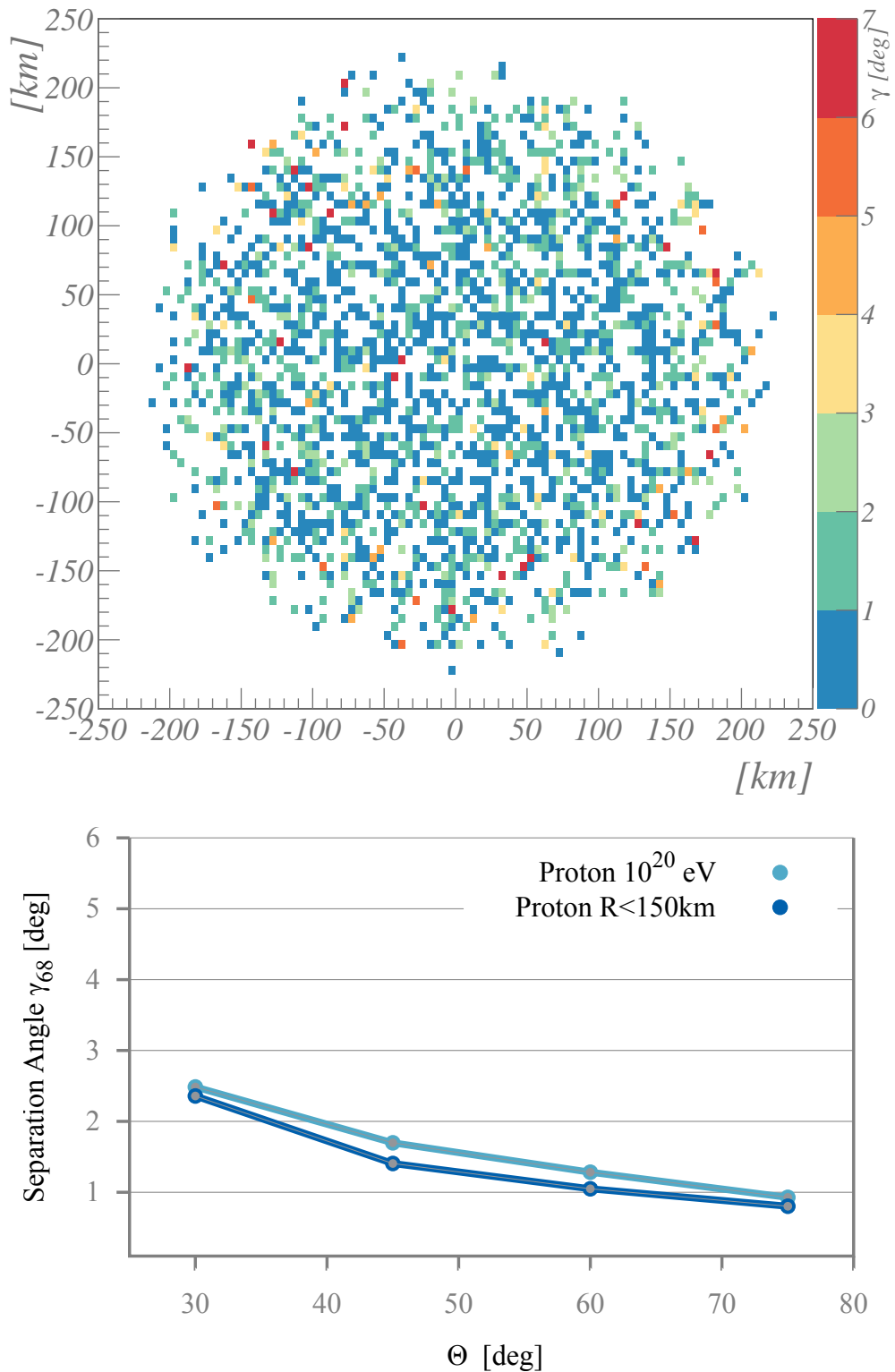


**Figure 4.18:** *Upper panel:* A scatter plot the distribution at the FS of the error in the angular reconstruction, primaries are protons with  $10^{20}$  eV. *Bottom panel:* The angular resolution of the same sample, restricting the results to showers with an impact position within 150 km from the center of the FoV.

## 4.2.5.2 Points selected

The second quality cut we will discuss is the **number of points selected** by the pattern recognition and therefore used by the angular reconstruction. This parameter has a straight forward interpretation: the more information available the better the reconstruction. There is an obvious caveat: the points selected must pertain to the EAS's signal, else the fitting procedures would be fed mostly background photons, rendering the reconstruction ineffective. Fortunately the latter is not the case as can be seen in the upper panel of Fig. 4.19. The tendency is, as expected, showing a smaller error (better angular resolution) with a higher number of points selected. The impact on the angular resolution is shown in the bottom panel of Fig. 4.19. At  $\Theta = 30^\circ$  there is almost no improvement since most of the showers in this condition do not surpass the quality cut. We see an improvement for  $\Theta > 45^\circ$  but for the highest zenith angles it is not so dramatic since these cases are almost always including more than 20 points for the reconstruction.

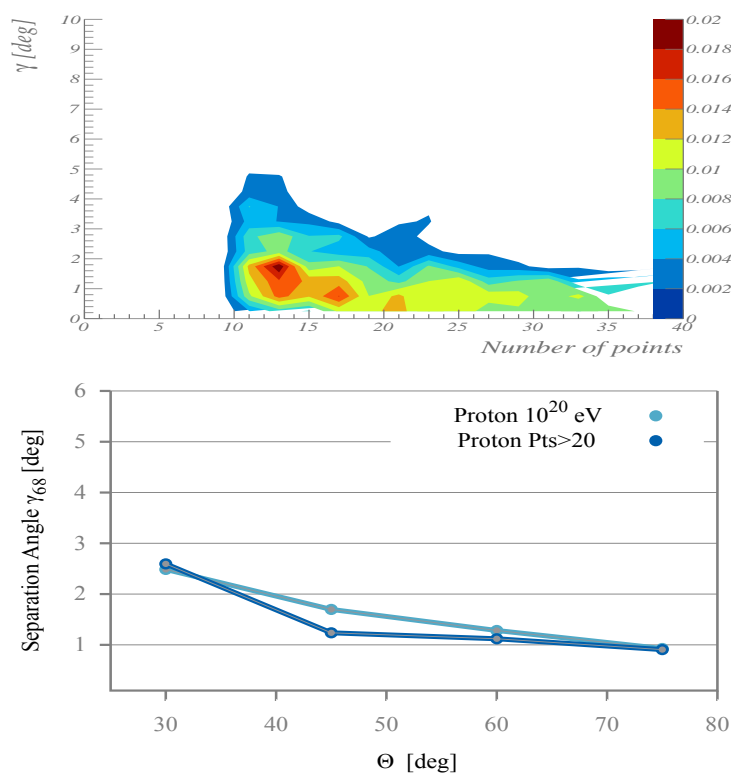


**Figure 4.19:** *Upper panel:* A scatter plot showing the correlation between the number of selected points available for the *TrackDirection2* module and the error in the angular reconstruction. The energy for this data is  $10^{20}$  eV, and the particles simulated were all protons (CONEX). *Bottom panel:* The angular resolution obtained applying a quality cut in the **number of points selected**. For this plots only reconstructed showers with more than 20 points are shown.

### 4.3 Energy and $X_{max}$ Reconstruction studies

#### 4.3.1 Energy reconstruction for protons, iron nuclei, and photons

To conclude the results obtained using CONEX simulated EAS, we performed the longitudinal profile reconstruction. For this purpose we will use the default module provided in ESAF: the *PmtToShowerReco* module [Fenu 2013]. It is important to mention that the *PmtToShowerReco* module was designed and tested only for SLAST simulated showers. Therefore most of the default parameters within the module are not optimized for an overall reconstruction of the EAS's characteristics. Nevertheless, it is illustrative to see how the default configuration of these parameters performs in combination with the tools developed in this thesis.

We implemented the energy reconstruction chain available in ESAF revision 3125. Since extensive tests have already been conducted with the SLAST shower generator [Fenu 2013], we only concentrate on testing the energy reconstruction in new conditions: with iron nuclei and photons as the primary cosmic rays. However we use more stringent quality cuts than what was previously used in [Fenu 2013]. We used results with *Degrees of Freedom* (DOF) bigger than 10 and  $\chi^2 < 2$ . We see an example of a reconstructed profile in Fig. 4.20

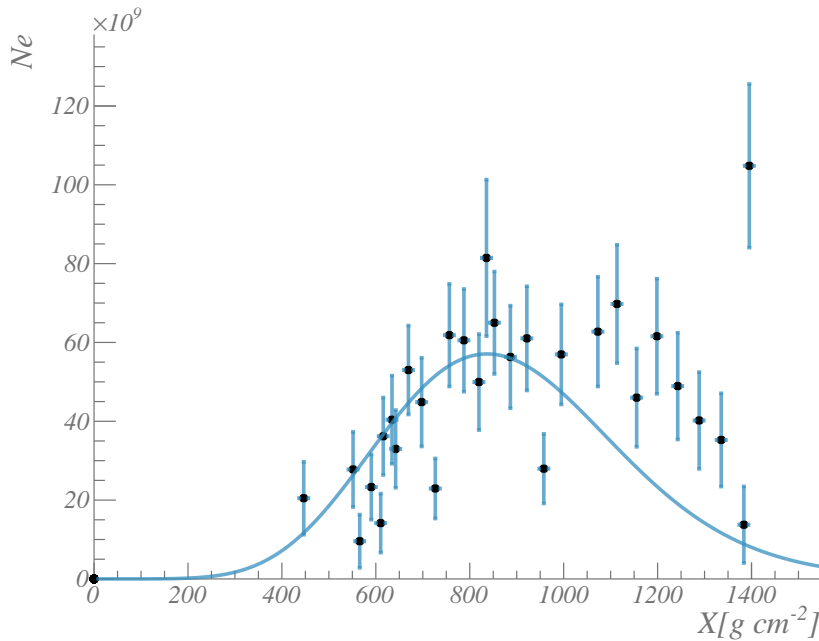


**Figure 4.20:** An example of the reconstruction of the longitudinal profile of a proton-initiated EAS with an energy of  $10^{20}$  eV and  $\Theta = 60^\circ$ . The points represent the reconstructed longitudinal profile with the associated uncertainty. The solid line is the originally simulated EAS.

In Fig. 4.21, Fig. 4.22, and Fig. 4.23 we present the error distribution in the energy reconstruction

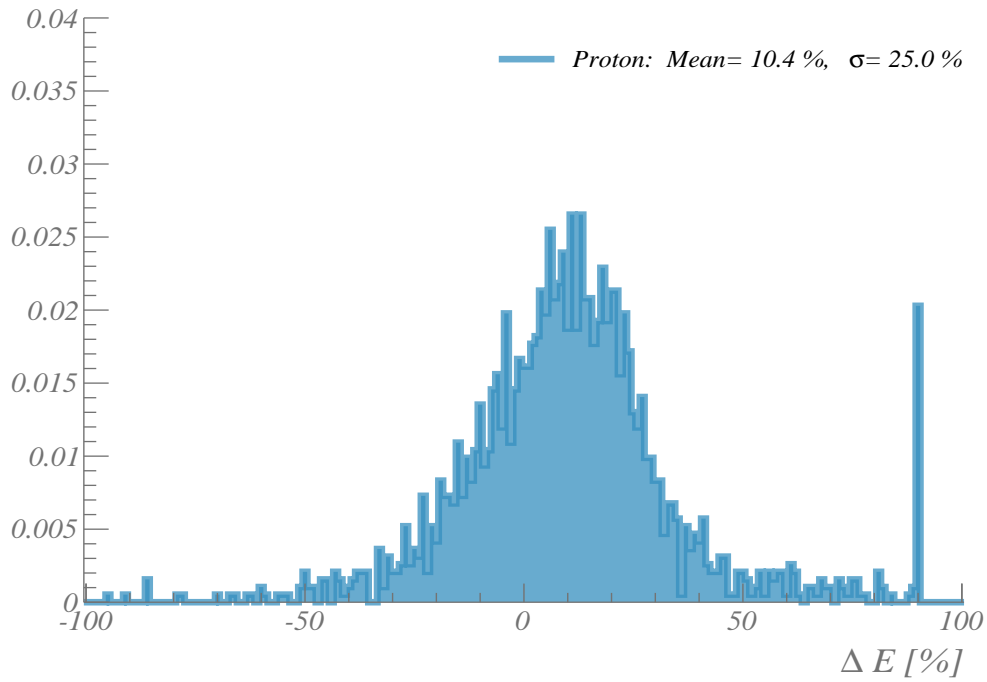


**Figure 4.21:** The energy-reconstruction error distribution for the protons in our *CONEX-benchmark* data sample.

for *CONEX-benchmark*. We define this error (in percentage) as:

$$\Delta E_{\%} \equiv \frac{\Delta E}{E} \times 100 = \frac{E_{Reco} - E_{Simu}}{E_{Simu}} \times 100 \quad (4.15)$$

where  $E_{Simu}$  and  $E_{Reco}$  are the simulated and reconstructed energies, respectively. Also shown in these figures, is the standard deviation  $\sigma$  from the  $\Delta E_{\%}$  distribution.

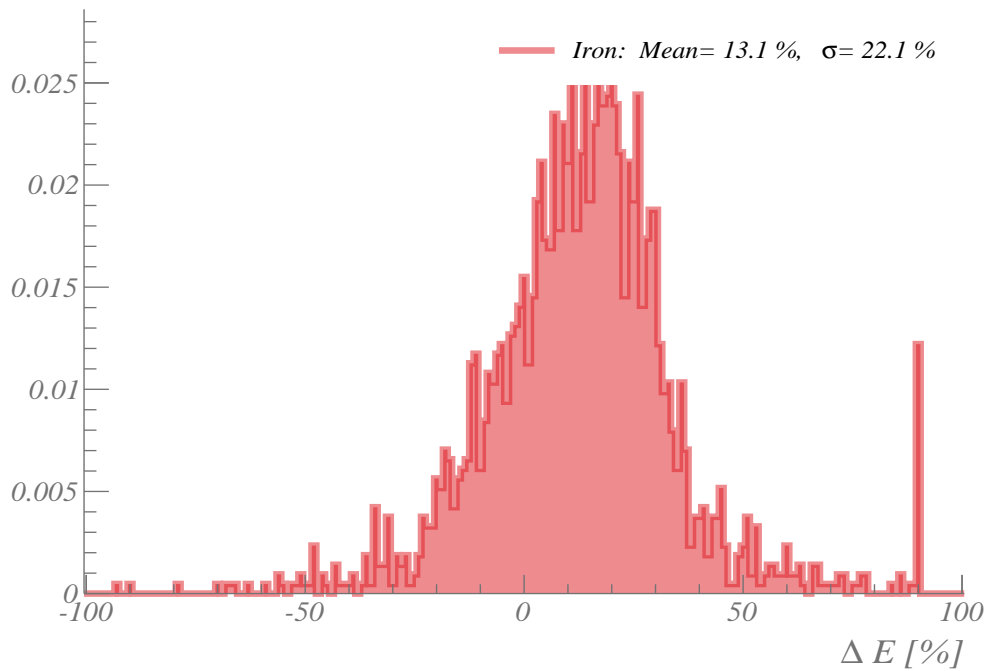


**Figure 4.22:** The energy-reconstruction error distribution for the iron nuclei in our *CONEX-benchmark* data sample.

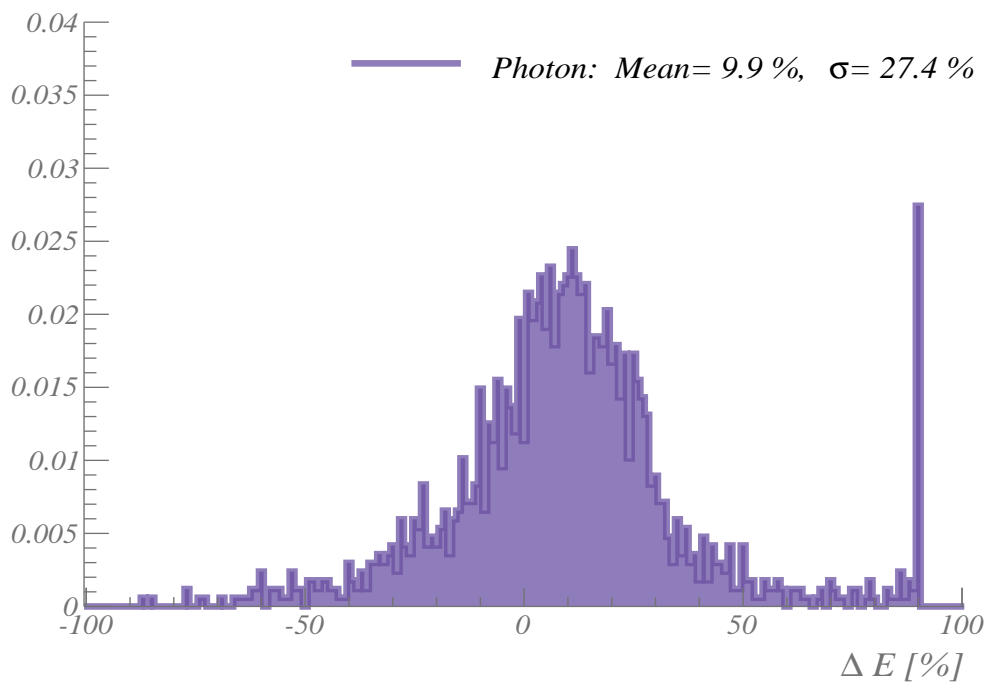


**Figure 4.23:** The energy-reconstruction error distribution for the photons in our *CONEX-benchmark* data sample.

We can appreciate a systematic overestimation of the energy, even in the case for protons. However this is still within the scientific requirements of the mission  $\sigma_E < 30\%$  [Fenu 2013]. To correct this, it seems reasonable to expect that only a fine tuning of the inner parameters, instead of a mayor rewriting of the *PmtToShowerReco* module, would be necessary.

### 4.3.2 $X_{max}$ reconstruction for protons, iron nuclei, and photons

We show the distribution of this error in Fig. 4.24, Fig. 4.25, and Fig. 4.26 for protons, irons, and photons, respectively. As it can be readily seen in the aforementioned figures, the panorama is not so promising on the side of  $X_{max}$  reconstruction. Let us remember that these parameter is of uttermost importance in composition studies. As it is illustrated in Fig. 4.13 and Fig. 4.16 the atmospheric depth of the maximum of the shower depends very strongly on the nature of the primary. We define the error in the  $X_{max}$  determination in a similar fashion as we did for the energy. This is:

$$X_{max}^{Error} \equiv \Delta X_{max} = X_{max}^{Reco} - X_{max}^{Simu} \quad (4.16)$$

The results obtained with the *PmtToShowerReco* module, are not particularly bad for protons and irons but for photons the situation is indeed not so good. For iron initiated shower the results can be explained if we remember that these EAS have less shower-to-shower fluctuations, as can be seen in Fig. 4.13. We have to remember that the *PmtToShowerReco* module is optimized for proton (hadrons) on a parametrized way that does not account very well for the shower-to-shower fluctuations. On the other hand for photons, due to the stronger LPM effect, a shower maximum is not so well defined. For example we can see at the multi-peaked showers in Fig. 4.16. Again, we have to keep in mind that the *PmtToShowerReco* module is optimized for proton (hadrons) initiated EAS. The fitting procedures are performed assuming a hadronic origin of the EAS (based on the GIL parametrization). This time discriminating on an event by event basis is not so straightforward to reduce the uncertainties, since the main uncertainty factor is hard to circumvent: the uncertainty in the local height of the EAS's points. Even a few km, although small compared to the expected observation height (400km), are crucial in the proper determination of the atmospheric depth. The atmospheric mass is condensed in the first 5 km of altitude and the slant depth estimation is strongly affected by the miscalculation of the shower's altitude. This situation can occur anywhere in the FS and therefore there is no strong correlation with the position within the FoV. We summarize the behavior in Table 4.4 and Table 4.5 for energy and  $X_{max}$  respectively.

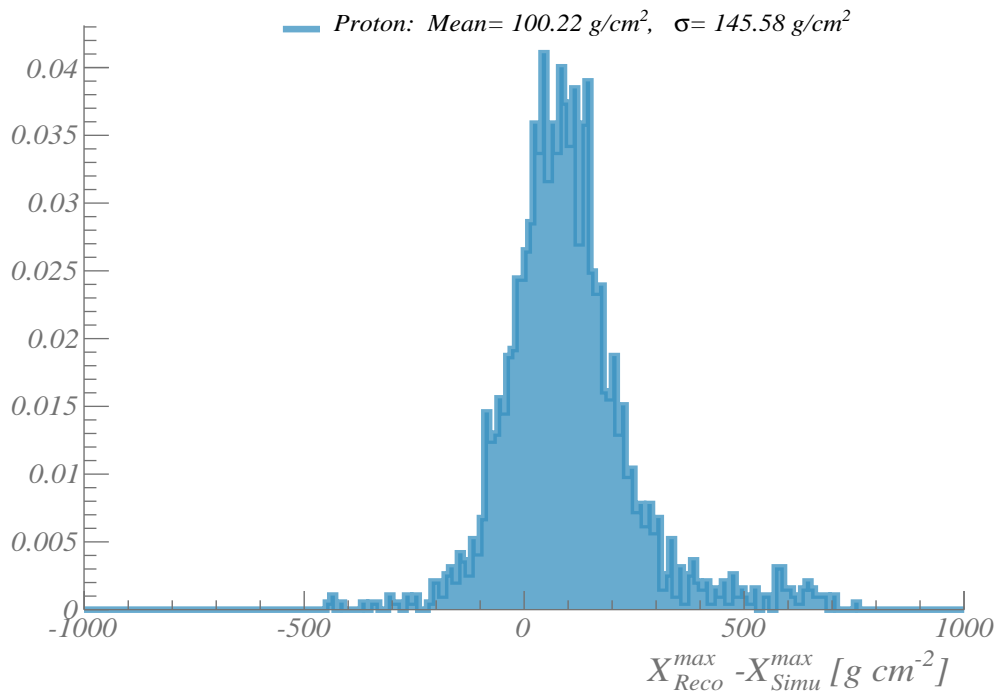


**Figure 4.24:** The  $\Delta X_{max}$  distribution for the protons in our *CONEX-benchmark* data sample.

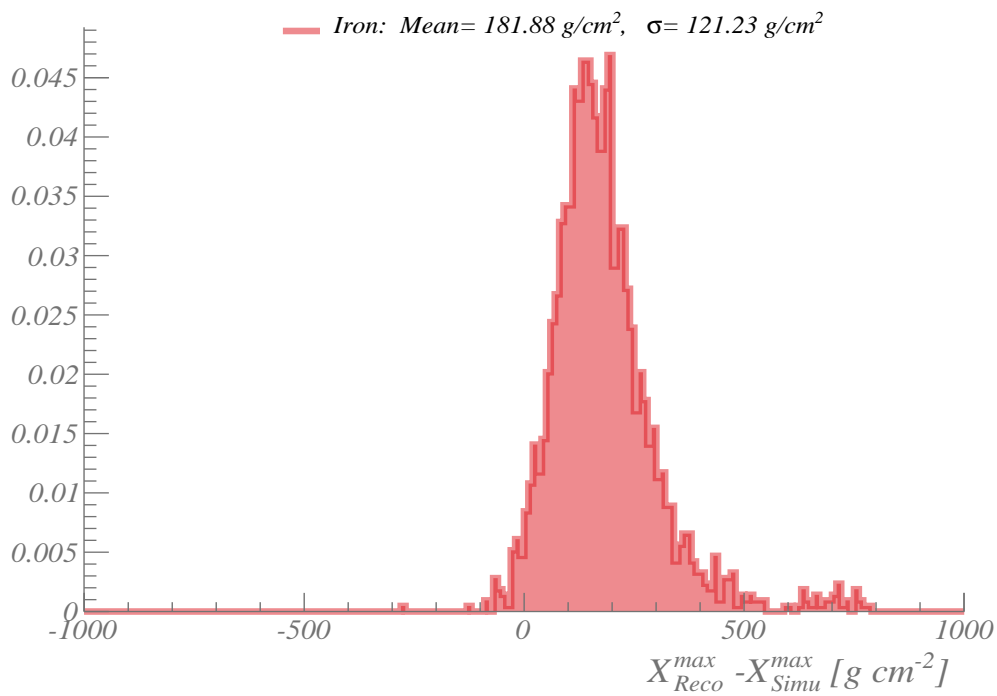


**Figure 4.25:** The  $\Delta X_{max}$  distribution for the iron nuclei in our *CONEX-benchmark* data sample.

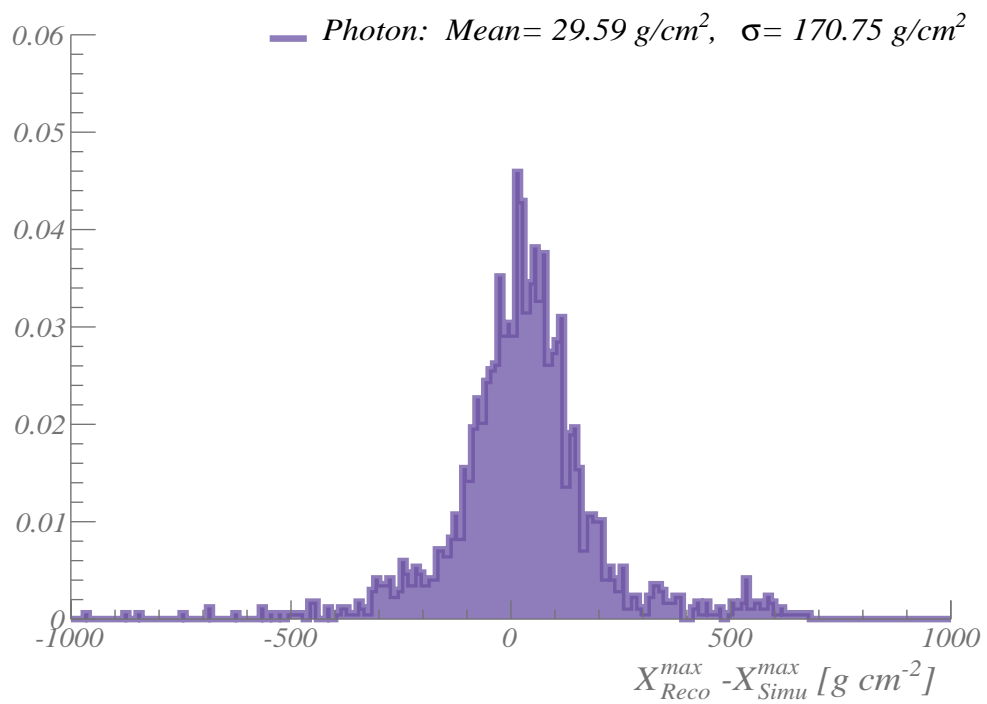


**Figure 4.26:** The  $\Delta X_{max}$  distribution for the photons in our *CONEX-benchmark* data sample.

| EECR primary | $\langle \Delta E \rangle [\%]$ | $\sigma [\%]$ |
|--------------|---------------------------------|---------------|
| Proton       | 10.4                            | 25            |
| Iron         | 13.1                            | 22.1          |
| Gamma        | 9.9                             | 27.4          |

**Table 4.4:** The summary of the energy reconstruction for protons, iron nuclei and photos. The data used are all with  $E=10^{20}$  eV from our *CNX-Benchmark*.

| EECR primary | $\langle \Delta X_{max} \rangle [g\ cm^2]$ | $\sigma [g\ cm^2]$ |
|--------------|--|--------------------|
| Proton       | 100.22                                     | 145.58             |
| Iron         | 181.88                                     | 121.23             |
| Gamma        | 29.59                                      | 170.75             |

**Table 4.5:** The summary of the  $X_{max}$  reconstruction for protons, iron nuclei and photos. The data used are all with  $E=10^{20}$  eV from our *CNX-Benchmark*.

# 5

## SPACE OBSERVATION OF EXTREMELY ENERGETIC NEUTRINOS

---

### Contents

---

|       |   |     |
|-------|---|-----|
| 5.1   | Concepts and definitions . . . . .  | 113 |
| 5.1.1 | Constant flux . . . . .   | 118 |
| 5.1.2 | Power law flux . . . . .  | 120 |
| 5.2   | The neutrino sensitivity as a scaling of the baryon sensitivity . . . . . | 121 |
| 5.2.1 | Tilting . . . . .   | 126 |
| 5.3   | The neutrino exposure . . . . .   | 127 |
| 5.4   | Reconstrucion of EAS induced by a $EE-\nu$ . . . . .                      | 132 |
| 5.4.1 | Angular reconstruction . . . . .  | 132 |
| 5.4.2 | Energy and longitudinal profile reconstruction . . . . .                  | 133 |

---



The possible detection of UHE neutrinos is an exploratory objective of the JEM-EUSO mission with a high scientific reward. In this part of our work we have estimated the neutrino exposure. This plays a key role in the calculation of the expected number of neutrino-induced events. The goal of this chapter is to present the steps we took in the electron-neutrino ( $\nu_e$ ) simulations to assess the exposure of JEM-EUSO for neutrino observations, and to present our results on this exposure.

## 5.1 Concepts and definitions

Before going directly into the neutrino exposure we need to address the discrepancies among the usage of some key concepts. Therefore we begin by explicitly mentioning the definition of the concepts which play a major role in the following discussions. These definitions are to a certain extent arbitrary and are taken solely for the purpose of fixing ideas and concepts for this work. In addition, we wish to bring some uniformity in what found in literature. We try to use a generalized approach for any EECR, but we will be concentrating in  $\nu_e$  studies.

◆ **Differential Flux ( $J_\nu$  or  $\Phi_\nu$ ) [ $\text{ev}^{-1} \text{sr}^{-1} \text{km}^{-2} \text{s}^{-1}$ ]**

$$J_\nu(E) = \frac{d^4 N_{\nu \text{ inc}}}{dE dS d\Omega dt} \quad (5.1)$$

Where  $dN_{\nu \text{ inc}}$  is the number of neutrinos in the energy bin  $E + dE$  incident on a surface element  $dS$  with a solid angle  $d\Omega$ , during the time interval  $dt$ .

◆ **Aperture ( $\mathcal{A}$ ) [ $\text{km}^2 \text{sr}$ ]**

Also referred as the instantaneous aperture. We distinguish two cases:

i **Geometrical Aperture ( $\mathcal{A}_{geo}$ )**

$$\int_{\Omega_0} \int_S \cos\Theta dS d\Omega \quad (5.2)$$

ii **Effective Aperture ( $\mathcal{A}_{eff}(E, t, \Theta, \phi, \vec{r}_{FOV})$ )**

$$\int_{\Omega_0} \int_S \epsilon_\nu(E, t, \Theta, \phi, \vec{r}_{FOV}) \cos\Theta dS d\Omega \quad (5.3)$$

Here  $\Theta$  and  $\phi$  are the zenith and azimuth angles respectively,  $\Omega_0$  and  $d\Omega = d \cos\Theta d\phi$  are the total and differential solid angles observed by the detector respectively. The quantity  $\cos\Theta dS$  is the projected differential surface element,  $S$  is the area of the detector, and  $\vec{r}_{FOV}$  is the position of the event inside the detector's field of view (FOV). The overall detection efficiency  $\epsilon_\nu(E, t, \Theta, \phi, \vec{r}_{FOV})$ , is explained below. Let us stress here the fact that this detection efficiency will depend on the event's characteristics. In the most naïve approximation we may be tempted to calculate the expected number of events using only the geometrical aperture. Extreme caution should be taken in these cases, to avoid neglecting the fact that we are implicitly assuming a perfect detector, i.e. we see everything that interacts and/or everything interacts.

◆ **Number of Events ( $N_\nu(\Delta E_\nu, T)$ ) [no dimension]**

This is simply the number of neutrinos producing an EAS inside the detector during a time interval  $T$ , and within an energy range ( $\Delta E_\nu$ ). To give a quantitative estimate of this factor, we need to assume a given flux and some detector's geometry. We must be careful to remember that this number does not directly translate into the number of detected events, unless we assume the probability of detection equal to unity [Supanitsky Medina-Tanco 2011] [Kusenko et al. 2002].

The probability that an UHE neutrino produces an EAS  $\mathcal{P}_{\nu \rightarrow EAS}(E_\nu, \Theta, \phi, \vec{r}_{FOV}; \sigma_{CC})$  (or just  $\mathcal{P}_{\nu \rightarrow EAS}(E_\nu)$  for short), depends on the physical process at hand and can be theoretically extrapolated to our energy regime. In this last expression  $\sigma_{CC}$  stands for the charged current cross section.

$$N_\nu(\Delta E_\nu, T) = \int_T \int_{\Delta E_\nu} \int_{\Omega_0} \int_S \Phi_\nu \mathcal{P}_{\nu \rightarrow EAS}(E, \Theta, \phi, \vec{r}_{FOV}; \sigma_{CC}) dS d\Omega dE dt$$

$$N_\nu(\Delta E_\nu, T) = \int_T \int_{\Delta E_\nu} \Phi_\nu(E_\nu) \otimes \mathcal{P}_{\nu \rightarrow EAS}(E_\nu) \otimes \mathcal{A}_{geo} dE dt$$
(5.4)

Where  $\mathcal{P}_{\nu \rightarrow EAS}(E_\nu) \otimes \mathcal{A}_{geo}$  represents the probability of a neutrino of energy  $E$  producing a extensive air shower (EAS) in the detector with a geometrical aperture  $\mathcal{A}_{geo}$ . The symbol  $\otimes$  means the coupling between flux, and probability of interaction. Basically we are just multiplying the functions under the integral in a sort of convolution.

For an appropriate context, this number is given within an energy range. We have different cases:

i **Number of events with energies up to  $E_\nu$**

$$N_\nu(E_\nu, T) = \int_T \int_0^{E_\nu} \Phi_\nu(E_\nu) \otimes \mathcal{P}_{\nu \rightarrow EAS}(E_\nu) \otimes \mathcal{A}_{geo} dE dt$$
(5.5)

ii **Number of events with energies above  $E_\nu$**

$$N_\nu(E_\nu < E, T) = \int_T \int_{E_\nu}^{\infty} \Phi_\nu(E_\nu) \otimes \mathcal{P}_{\nu \rightarrow EAS}(E_\nu) \otimes \mathcal{A}_{geo} dE dt$$
(5.6)

If instead of the geometrical aperture, we use the effective aperture, we arrive at the very important:

◆ **Number of DETECTED events in the energy interval  $\Delta E_\nu$**

$$N_\nu(\Delta E_\nu, T) = \int_T \int_{\Delta E_\nu} \int_{\Omega_0} \int_S \Phi_\nu \mathcal{P}_{\nu \rightarrow EAS}(E, \Theta, \phi, \vec{r}_{FOV}; \sigma_{CC}) \epsilon_\nu(E, t, \Theta, \phi, \vec{r}_{FOV}) \cos(\Theta) dS d\Omega dE dt$$
(5.7)

$$N_\nu(\Delta E_\nu, T) = \int_T \int_{\Delta E_\nu} \Phi_\nu(E_\nu) \otimes \mathcal{P}_{\nu \rightarrow EAS}(E_\nu) \otimes \mathcal{A}_{eff} dE dt$$

We will come back to discuss this number in more detail. First we explain the overall detection efficiency  $\epsilon$ .

◆ **Overall detection efficiency**  $\epsilon_\nu(E, t, \Theta, \phi, \vec{r}_{FOV}) \in [0 : 1)$

This is the trickiest concept we introduce here. We have to take into account the duty cycle, role of clouds, civil lights, lighting, natural sources of background light, detector's death time, the wearing out of the detector, trigger efficiency, discrimination efficiency (especially for neutrino events) and possibly even some extra selection criteria. In the following steps we will proceed to simplify it. It is important to remember these factors which will hinder detection, especially when discussing neutrino detection.

As a first approximation, we will separate the time dependent part as:

$$\epsilon_\nu(E, t, \Theta, \phi, \vec{r}_{FOV}) = \eta(t) \cdot \epsilon'_\nu(E, \Theta, \phi, \vec{r}_{FOV}) \quad (5.8)$$

so that we can write the effective aperture as:

$$\mathcal{A}_{eff}(E, t, \Theta, \phi, \vec{r}_{FOV}) = \eta(t) \int_{\Omega_0} \int_S \epsilon'_\nu(E, \Theta, \phi, \vec{r}_{FOV}) \cos \Theta dS d\Omega \quad (5.9)$$

In this expression  $\eta(t)$  is the duty cycle. For the the time being we will take it as representing the fraction of the time JEM-EUSO can perform a measurement. It is a combination of different factors: the excess of natural and man-made background light, the occultation of the fluorescence signal by clouds/aerosols in the atmosphere and the dead time of the detector, to name a few. Although putting together all these factors is a good first approximation, we must keep in mind that many of these factors also depend on the position in the FOV and geometrical characteristics of each event (e.g. city light will only pollute a portion of the FOV, cloud coverage will also be localized, etc.).

The time independent detection efficiency  $\epsilon'_\nu(E, \Theta, \phi, \vec{r}_{FOV})$  is defined to be the coupling between the trigger efficiency and the quality (selection) efficiency of the event (i.e.  $\epsilon'_\nu(E, \Theta, \phi, \vec{r}_{FOV}) \equiv \epsilon_{trig} \otimes \epsilon_{sel}$ ). The definition of  $\epsilon_{sel}$  currently is out of the scope of the present work. There is still no definitive analysis that defines this selection cut.

We used the symbol  $\otimes$  to explicitly express the coupling between  $\epsilon_{trig}$  and  $\epsilon_{sel}$ , which once again are not independent. The simulations we intend to carry out, have the purpose of estimating  $\epsilon_{trig}$  for electron-neutrinos. And from this basic information estimate the exposure and the sensitivity.

◆ **Exposure** ( $\varepsilon(E_\nu)$ ) [ $\text{km}^2 \text{ sr yr}$  ]

This corresponds to the integral of the aperture  $\mathcal{A}_{eff}(E_\nu)$  over a period of time  $T$ , folding it with the conversion probability and the overall detection efficiency [PAO-hybrid 2012]. When not integrated it is taken as the instantaneous aperture. It should reflect the deviations from the ideal detector introduced by the fact that the overall efficiency is different than one. We define it as:

$$\begin{aligned} \varepsilon_\nu(E_\nu) &= \int_T \int_{\Omega_0} \int_S \epsilon_\nu(E_\nu, t, \Theta, \phi, \vec{r}_{FOV}) \cos \Theta dS d\Omega dt \otimes \mathcal{P}_{\nu \rightarrow EAS}(E_\nu) \\ &= \int_T \mathcal{A}_{eff} \otimes \mathcal{P}_{\nu \rightarrow EAS}(E_\nu) dt \end{aligned} \quad (5.10)$$

Or separating the time dependence:

$$\varepsilon_\nu(E_\nu) = \int_T \eta(t) dt \int_{\Omega_0} \int_S \epsilon'_\nu(E_\nu, \Theta, \phi, \vec{r}_{FOV}) \cos \Theta dS d\Omega \otimes \mathcal{P}_{\nu \rightarrow EAS}(E_\nu) \quad (5.11)$$

◆ **Event rate**  $\frac{dN_\nu(E_\nu)}{dt}$  [yr<sup>-1</sup>]

Its calculation is straightforward, but we include it for completeness. The number of neutrinos producing an EAS inside the detector (i.e. the atmosphere) per unit time with and within an energy interval  $\Delta E_\nu$ .

$$\begin{aligned} \frac{dN_\nu(\Delta E_\nu)}{dt} &= \int_{\Delta E_\nu} \int_{\Omega_0} \int_S \Phi_\nu \mathcal{P}_{\nu \rightarrow EAS}(E, \Theta, \phi, \vec{r}_{FOV}; \sigma_{CC}) \cos \Theta dS d\Omega dE \\ \frac{dN_\nu(\Delta E_\nu)}{dt} &= \Phi_\nu(\Delta E_\nu) \otimes \mathcal{P}_{\nu \rightarrow EAS}(\Delta E_\nu) \otimes \mathcal{A}_{geo} \end{aligned} \quad (5.12)$$

Note that we do not require the events (EAS) to be detected, hence, we use the geometrical aperture.

◆ **Sensitivity** ( $\mathbb{S} \equiv E_\nu^2 \Phi_\nu^{\mathbb{S}}(E_\nu)$ ) [GeV cm<sup>-2</sup> sr<sup>-1</sup> s<sup>-1</sup>]

For easy comparison with published results, we use these units and not the more “natural” ones for the EUSO perspective, i.e. [eV km<sup>-2</sup> sr<sup>-1</sup> yr<sup>-1</sup>]. We define  $\mathbb{S}$  as:

*the (minimum) flux  $\Phi_\nu^{\mathbb{S}}(E_\nu)$  that can produce at least  $N_{\mathbb{S}}$  DETECTED event(s) with an energy up to  $E_\nu$ , during an observational period  $T$  multiplied by the square of its energy  $E_\nu^2$ .*

Using Eq.5.7, we see that,  $\Phi_\nu^{\mathbb{S}}$  is such that, for a given  $N_\nu$ , the following expression holds:

$$\begin{aligned} N_{\mathbb{S}}(E_\nu, T) &= \int_{E_{thr}}^{E_\nu} \int_T \int_{\Omega_0} \int_S \Phi_\nu^{\mathbb{S}}(E_\nu) \mathcal{P}_{\nu \rightarrow EAS}(E_\nu) \epsilon_\nu(E, t, \Theta, \phi, \vec{r}_{FOV}) \cos \Theta dS d\Omega dt dE \\ &= \int_{E_{thr}}^{E_\nu} \Phi_\nu^{\mathbb{S}}(E_\nu) \int_T \int_{\Omega_0} \int_S \mathcal{P}_{\nu \rightarrow EAS}(E_\nu) \epsilon_\nu(E, t, \Theta, \phi, \vec{r}_{FOV}) \cos \Theta dS d\Omega dt dE \\ &= \int_{E_{thr}}^{E_\nu} \Phi_\nu^{\mathbb{S}}(E_\nu) \cdot \varepsilon_\nu(E) dE \quad (Integrated) \end{aligned} \quad (5.13)$$

In this last expression we use  $E_{thr}$  as the energy threshold for of the detector. Eq. 5.13 is referred as the integrated form of the sensitivity. As we can see this definition has the caveat that Eq. 5.13 has not a unique solution for  $\Phi_\nu^{\mathbb{S}}$ . This definition can be different in literature. For example in [Abraham et al. 2008] [Abraham et al. 2009] [Abreu et al. 2012]  $\mathbb{S}$  is defined as the inverse of the exposure multiplied by  $2.3 \times E_\nu$ . The 2.3 is due to the 90% confidence level for the upper limit that corresponds to not observing an event (assuming poissonian statistics) [Feldman & Cousins 1998]. This is different than what used to calculate confidence intervals

in [Anchordoqui et al. 2013]. When comparing different sensitivities from different experiments one has also to mention with what "probe" spectrum the calculations were made. If that is not the case, it complicates even further the interpretation and comparison to other published results. The most used probe spectrum follows a simple power law with an index equal to minus two.

A similar concept is used in the literature interchangeably: the **limit on the diffuse flux of UHE neutrinos** [PAO 2013c] [Anchordoqui et al. 2002]. Both references use another concept which we will be using: the **differential form of the sensitivity**. The ansatz behind the concept of a differential limit on the flux of UHE neutrinos is that:  $\Phi_\nu^{\mathbb{S}}(E_\nu) \cdot \varepsilon_\nu(E) \propto E^\Gamma$ , holds for small logarithmic bins of width  $\Delta$  [Anchordoqui et al. 2002]. Then we proceed to integrate Eq. 5.13 in this range:

$$\begin{aligned}
N_{\mathbb{S}}(E_\nu, T) &= \int_{\langle E \rangle e^{-\frac{\Delta}{2}}}^{\langle E \rangle e^{\frac{\Delta}{2}}} \Phi_\nu^{\mathbb{S}}(E_\nu) \cdot \varepsilon_\nu(E) dE = \int_{\langle E \rangle e^{-\frac{\Delta}{2}}}^{\langle E \rangle e^{\frac{\Delta}{2}}} \Phi_\nu^{\mathbb{S}}(E_\nu) \cdot \varepsilon_\nu(E) E \frac{dE}{E} \\
&= \int_{\log(\langle E \rangle) - \frac{\Delta}{2}}^{\log(\langle E \rangle) + \frac{\Delta}{2}} \Phi_\nu^{\mathbb{S}}(E_\nu) \cdot \varepsilon_\nu(E) E d(\log E) = \int_{\log(\langle E \rangle) - \frac{\Delta}{2}}^{\log(\langle E \rangle) + \frac{\Delta}{2}} e^{(\Gamma+1)\log(E)} d(\log E) \\
&= \frac{1}{\Gamma+1} \left( e^{(\Gamma+1)E} \right) \Big|_{\log(\langle E \rangle) - \frac{\Delta}{2}}^{\log(\langle E \rangle) + \frac{\Delta}{2}} = \frac{e^{(\Gamma+1)\log(\langle E \rangle)}}{\Gamma+1} \left( e^{(\Gamma+1)\frac{\Delta}{2}} - e^{-(\Gamma+1)\frac{\Delta}{2}} \right) \\
&= \langle E \rangle \langle E \rangle^\Gamma \Delta \cdot \left( \frac{e^{(\Gamma+1)\frac{\Delta}{2}} - e^{-(\Gamma+1)\frac{\Delta}{2}}}{(\Gamma+1)\Delta} \right) \\
&= \langle E \rangle \langle \Phi_\nu^{\mathbb{S}}(E_\nu) \cdot \varepsilon_\nu(E) \rangle \Delta \cdot \frac{\sinh((\Gamma+1)\Delta)}{(\Gamma+1)\Delta} \tag{5.14}
\end{aligned}$$

Where the terms in brackets  $\langle \rangle$  represent the average value within the energy bin. If the functions involved are smooth enough we can separate the products inside the bracket as the products of the individual brackets. This is in principle guaranteed by our ansatz. Since this definition is based on setting an upper bound for the number of events, using  $\frac{\sinh(x)}{x} < 1$  we arrive at the so-called "model independent" differential limit (or in our case sensitivity) [Anchordoqui et al. 2002]:

$$\begin{aligned}
\langle E \rangle \langle \Phi_\nu^{\mathbb{S}}(E_\nu) \rangle \langle \varepsilon_\nu(E) \rangle \Delta \cdot \frac{\sinh((\Gamma+1)\Delta)}{(\Gamma+1)\Delta} &\leq N_{\mathbb{S}} \\
\implies \langle E \rangle \langle \Phi_\nu^{\mathbb{S}}(E_\nu) \rangle \langle \varepsilon_\nu(E) \rangle &< \frac{N_{\mathbb{S}}}{\Delta} \tag{5.15} \\
\therefore \mathbb{S} \equiv E_\nu^2 \Phi_\nu^{\mathbb{S}}(E_\nu) &= \frac{N_{\mathbb{S}} \langle E_\nu \rangle}{\Delta \langle \varepsilon_\nu(E) \rangle} \quad (\text{Differential})
\end{aligned}$$

The reason this limit is called model independent is that the particular behavior of  $\Phi^{\mathbb{S}}$  (which is coded in  $\Gamma$ ) does not appear explicitly in the last expression. However the less restrictive version which includes the hyperbolic sine function does not hide this factor. In that, with everything else

remaining the same, the sensitivity will be orders of magnitude lower if the spectral index changes. For example, the authors of [Anchordoqui et al. 2002] quote variations from  $\sim 10^{-5}$  to  $\sim 10^{-7}$  for power law fluxes with spectral indexes of  $\alpha = 2$  and  $\alpha = 1.5$  respectively. The harder the assumed spectrum is, the better the sensitivity. The selection of  $\Delta$  in Eq. 5.15 depends on the experiment. For example, the PAO collaboration uses a decimal logarithmic bin, which introduces a factor of  $\log(10)$  times the size of the bin [PAO 2013c]. We will return to the differential form of the sensitivity. But first we illustrate the impact of oversimplifying the assumptions for the detector. This provides us a first upper limit to the achievable sensitivity of the JEM-EUSO mission. Having mentioned the caveats of our definitions, we can start giving some values to the terms. First of all we will simplify the problem by taking the time dependent part as a dimensionless constant  $\eta_0$ . We assume the detector to be planar with surface  $S_0$  and symmetrical on the azimuthal angle  $\phi$ . Also we will take the detector's efficiency constant in time. We rewrite Eq.5.13 as:

$$\begin{aligned} N_\nu(E_\nu, T) &= \int_{E_{thr}}^{E_\nu} \int_T \eta_0 dt \int_0^{2\pi} d\phi \int_0^{\frac{\pi}{2}} \int_S \Phi_\nu^{\mathbb{S}}(E_\nu) \mathcal{P}_{\nu \rightarrow EAS}(E_\nu) \epsilon_\nu(E, \Theta, \vec{r}_{FOV}) \frac{\sin(2\Theta)}{2} dS d\Theta dE \\ &= T \eta_0 \pi \int_{E_{thr}}^{E_\nu} \int_0^{\frac{\pi}{2}} \int_S \Phi_\nu^{\mathbb{S}}(E_\nu) \mathcal{P}_{\nu \rightarrow EAS}(E_\nu) \epsilon_\nu(E, \Theta, \vec{r}_{FOV}) \sin(2\Theta) dS d\Theta dE \end{aligned} \quad (5.16)$$

As general rule we will take the product of  $\mathcal{P}_{\nu \rightarrow EAS} \cdot \epsilon_\nu$  to be piece-wise constant when doing the integrations. We will begin with a constant flux and then elaborate using a power law flux.

### 5.1.1 Constant flux

We can get an upper limit for the sensitivity, assuming a constant flux  $\Phi_{max}^{\mathbb{S}}$  to produce  $N_{\mathbb{S}} = 2.44$  events. The latter is the value at 90% confidence limit with no expected background events and no candidates (no detection) [Feldman & Cousins 1998]. Using Eq.5.16, and setting  $\mathcal{P}_{\nu \rightarrow EAS}(E, \Theta, \vec{r}_{FOV}) = \epsilon'_\nu(E, \Theta, \vec{r}_{FOV}) \equiv 1$ , we arrive at:

$$\begin{aligned} N_{\mathbb{S}} = 2.44 &= T \eta_0 \pi \int_{E_{thr}}^{E_{max}} \int_0^{\frac{\pi}{2}} \int_S \overbrace{\Phi_{max}^{\mathbb{S}}(E_\nu) \mathcal{P}_{\nu \rightarrow EAS}(E_\nu) \epsilon_\nu(E, \Theta, \vec{r}_{FOV})}^{\text{Constant}} \sin(2\Theta) dS d\Theta dE \\ &= T \eta_0 \pi \Phi_{max}^{\mathbb{S}} \int_{E_{thr}}^{E_{ax}} dE \int_0^{\frac{\pi}{2}} \sin(2\Theta) d\Theta \int_{S_0} dS \\ &= T \eta_0 \pi \Phi_{max}^{\mathbb{S}} (E_{max} - E_{thr}) S_0 \\ \Rightarrow \mathbb{S}_{max}^{int} &\equiv E_{max}^2 \Phi_{max}^{\mathbb{S}} = \frac{2.44}{T \eta_0 \pi S_0} \cdot \frac{E_{max}^2}{(E_{max} - E_{thr})} \quad (\text{Integrated}) \\ \Rightarrow \mathbb{S}_{max}^{diff} &\equiv E_\nu^2 \Phi_{max}^{\mathbb{S}} = \frac{E_\nu}{0.05 \log(10)} \cdot \frac{2.44}{T \eta_0 \pi S_0} \quad (\text{Differential}) \end{aligned} \quad (5.17)$$

In our differential case we have used a decimal logarithmic bin of 0.05. We use the fiducial values of  $\eta_0 = 0.13$ ,  $T = 5$  years,  $E_{max} = 10^{21}$ ,  $E_{tbr} = 10^{19}$  and  $S_0 = 1.3 \times 10^5$  km<sup>2</sup> we see that the maximum sensitivity would then be:

$$\begin{aligned} \mathbb{S}_{max}^{int} &\simeq \frac{E_{max}^2}{(E_{max} - E_{tbr})} \cdot 2.914 \times 10^{-23} [\text{GeV cm}^{-2} \text{s}^{-1} \text{sr}^{-1}] \\ &\simeq 2.943 \times 10^{-12} [\text{GeV cm}^{-2} \text{s}^{-1} \text{sr}^{-1}] \\ \mathbb{S}_{max}^{diff} &\simeq E_\nu \cdot 2.531 \times 10^{-22} [\text{GeV cm}^{-2} \text{s}^{-1} \text{sr}^{-1}] \end{aligned} \quad (5.18)$$

Where  $E$  should be given in GeV. If we take  $E_{tbr} = 10^{19}$  eV and  $E_\nu = 10^{21}$  eV, we get  $\mathbb{S}_{max} \simeq 1.2 \times 10^{-13}$  GeV cm<sup>-2</sup> s<sup>-1</sup> sr<sup>-1</sup>. This value is an upper limit. For its calculation most of the assumptions made are unrealistic and therefore, it should not be cited and/or used for further calculations. However, we can compare this maximum hypothetical sensitivity, with a given neutrino flux  $\Phi_\nu^{ref}$ . This is shown in Fig. 5.1 where we compare with the upper limit for the flux from [Waxman & Bahcall 1998] and [Abreu et al. 2012].

The next step will be to compare with the baryon sensitivity, still assuming a constant flux. We will use the proton exposure published in [Adams et al. 2013a] to calculate the electron-neutrino sensitivity. It follows from Eq. 5.13, that if we assume a constant flux, we only need to integrate the exposure to get the sensitivity:

$$\begin{aligned} N_p^{\mathbb{S}}(E_p) &= \Phi_p^{\mathbb{S}} \int_{E_{tbr}}^{E_{max}} \varepsilon_p(E) dE \\ \implies \mathbb{S}_p^{int} &\equiv E_p^2 \Phi_{max}^{\mathbb{S}} = \frac{E_p^2 N_p^{\mathbb{S}}(E_p)}{\int_{E_{tbr}}^{E_{max}} \varepsilon_p(E) dE} \end{aligned} \quad (5.19)$$

Since we are taking the exposure piecewise constant, the differential form is simply:

$$\mathbb{S}_p^{diff} \equiv E_p^2 \Phi_{max}^{\mathbb{S}} = \frac{E_p}{0.05 \log(10)} \cdot \frac{N_p^{\mathbb{S}}}{\langle \varepsilon_p(E) \rangle} \quad (5.20)$$

In Fig. 5.1 we show in red the differential value of  $\mathbb{S}_{max}$  (labeled JEM-EUSO ideal). In the same figure we can see in blue the differential baryon sensitivity ( $\mathbb{S}_p$ ), and, to bring these values into context, the published limits from [Waxman & Bahcall 1998] [Abreu et al. 2012]. It can be seen that for baryons the sensitivity is already very close to the ideal case for  $E \approx 4 \times 10^{19}$  eV. The reader is cautioned to remember, that in all these cases the flux is assumed to be constant.

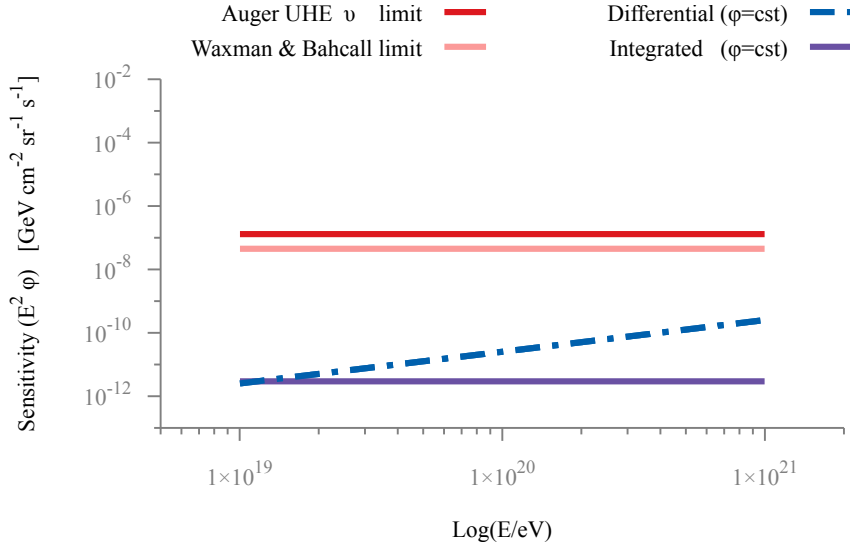


**Figure 5.1:** Comparison between the WB limit [Waxman & Bahcall 1998], PAO neutrino upper limit [PAO 2013c], and JEM-EUSO’s baryon sensitivity (the latter assuming a constant flux as in Eq.5.18), we also show the differential sensitivity. In all cases we used fiducial value of  $S_0 \sim 1.3 \times 10^{15} \text{ cm}^2$ .

### 5.1.2 Power law flux

Although the previous test illustrated the procedure, it is not realistic to expect a flat flux. A common test flux is the simple power law:

$$\Phi(E) = \Phi_0 \left( \frac{E}{\text{GeV}} \right)^\alpha$$

Following the discussion presented in § 1.2.2, typically  $\alpha$  is taken to be slightly above 2.

In [PAO 2013c] the integrated limit is calculated assuming a  $\alpha = -2$  and hence  $E^2\Phi(E) = \text{constant}$ . We follow this approach in the present work.

$$S_p^{int} = E^2\Phi(E) = \Phi_0 = \frac{N_p^S}{\int_{E_{thr}}^{E_{max}} E^{-2} \varepsilon_p(E) dE} \quad (5.21)$$

Since we are taking the exposure as piecewise constant in the energy interval  $\Delta E$ , we carry out explicitly the integral in the denominator

$$\begin{aligned} \int_{E_{thr}}^{E_{max}} E^{-2} \varepsilon_p(E) dE &= \sum_i \frac{\varepsilon_p(E_i)}{E_i} \cdot \left( \frac{1}{E_i} - \frac{1}{E_i \cdot 10^\delta} \right) \\ &= \left( 1 - \frac{1}{10^\delta} \right) \cdot \sum_i \frac{\varepsilon_p(E_i)}{E_i} \end{aligned} \quad (5.22)$$

Where  $\delta$  is the logarithmic interval where we are integrating (typically 0.1), and the sum runs over all the bins labeled by  $i$ . It is also straightforward to integrate eq.5.15 to calculate the differential limit:

$$\begin{aligned} N_p^{\mathbb{S}} &= \int_{\Delta E} \Phi^{\mathbb{S}}(E) \cdot \varepsilon(E) dE = \int_{\Delta E} \Phi_0 \left( \frac{E}{\text{GeV}} \right)^{\alpha} \cdot \varepsilon(E) dE \\ &= \frac{\Phi_0 \langle \varepsilon \rangle \text{GeV}}{\alpha + 1} \left( \frac{E}{\text{GeV}} \right)^{\alpha+1} \Big|_{\Delta E} \end{aligned} \quad (5.23)$$

This however is the same scenario as the one discussed in Eq. 5.15.

We point out that the choice of  $\alpha = -2$  is in slight disagreement with what is expected for neutrinos, where  $\alpha = -2.3$  is expected using IceCube results [Anchordoqui et al. 2013]. The results of this exercise can be seen in Fig.5.2. We see that the assumption of a power law flux has indeed increased our expected sensitivity.

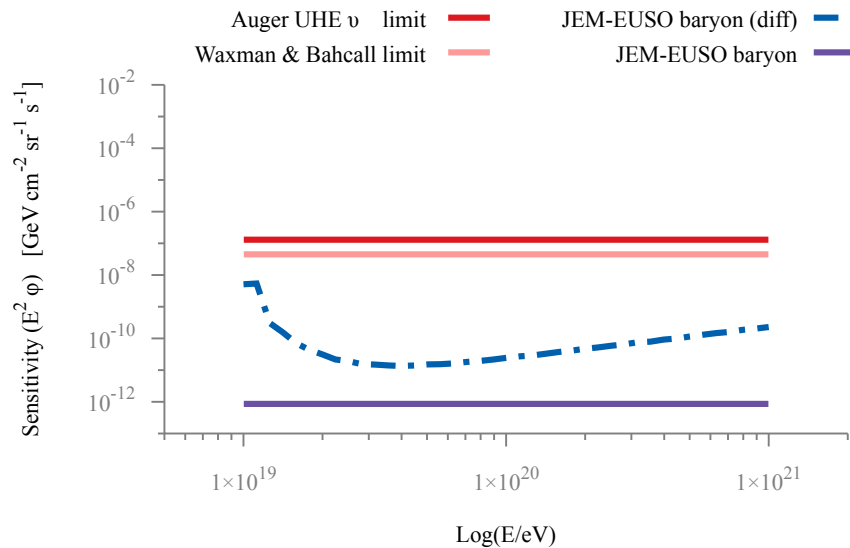


**Figure 5.2:** Comparison between the WB limit [Waxman & Bahcall 1998], PAO neutrino upper limit [PAO 2013c], and JEM-EUSO’s baryon sensitivity latter assuming a power law flux. We also show the JEM-EUSO’s differential sensitivity (see Eq. 5.15).

## 5.2 The neutrino sensitivity as a scaling of the baryon sensitivity

It is now clear, from the previous discussion, that the exposure plays a key role when calculating the expected sensitivity of a detector. This concept contains the specifics of a given experiment and can be directly used to estimate the number of expected events, using Eq.5.12 substituting the geometrical with the effective aperture. Clearly the discussion regarding the number of events will be strongly dependent on the speculated (measured) flux at hand.

In the case of JEM-EUSO the only exposure properly simulated/estimated, is the proton exposure [Adams et al. 2013a]. In this case, to take  $\mathcal{P}_{p \rightarrow EAS}(E_p) \sim 1$  is not so far-off. In other words, we expect extreme energetic protons to always interact in the atmosphere, even if they may go undetected.

In the neutrino case, we are expecting a decrease in the exposure mainly due to the fact that the neutrino interaction length is orders of magnitude longer than that for protons. Paraphrasing from [Supanitsky Medina-Tanco 2011]:

“The interaction length for protons is  $\lambda_p(10^{20} \text{ eV}) \sim 36 \text{ g cm}^{-2}$  [...] and for neutrinos is  $\lambda_\nu(10^{20} \text{ eV}) \sim 3.2 \times 10^7 \text{ g cm}^{-2}$ . The survival probability of an horizontal proton reaching the center of the FOV is  $\sim 5 \times 10^{-535}$ , whereas the corresponding probability for a neutrino is  $\sim 0.999$ ”

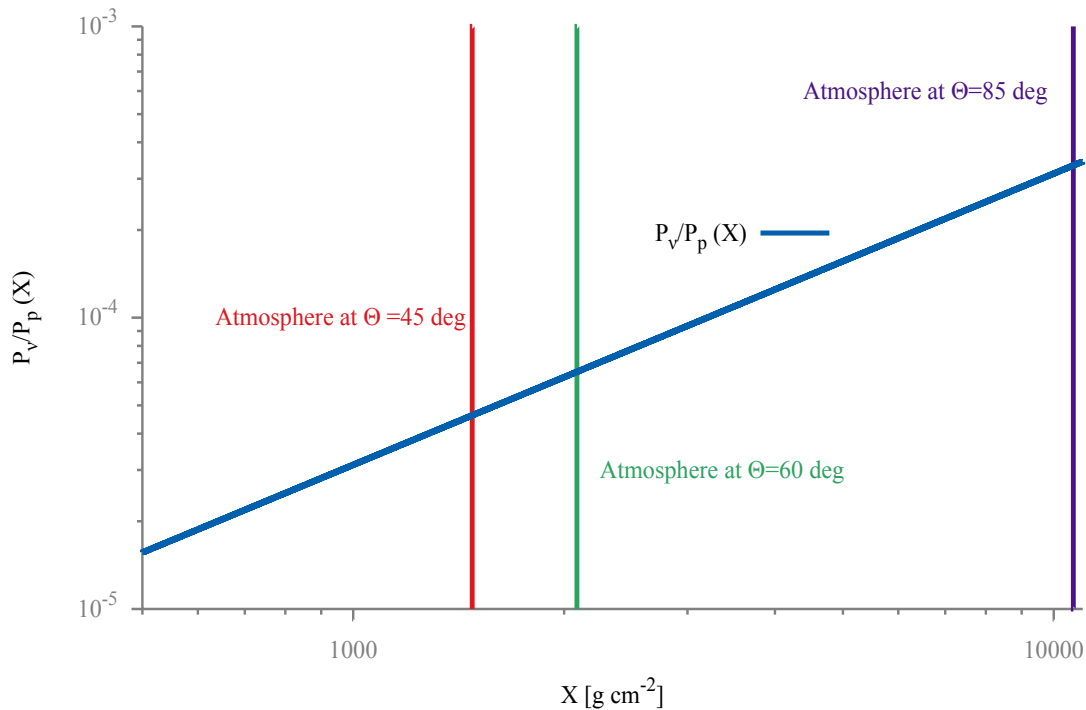


**Figure 5.3:** The ratio  $\frac{P_p(X)}{P_\nu(X)}$  of the proton’s probability of interaction to that of the neutrino, as a function of slant depth. Also shown are the integrated slant depth’s from the top of the atmosphere till the center of the FOV, for different zenith angles  $\Theta$ .

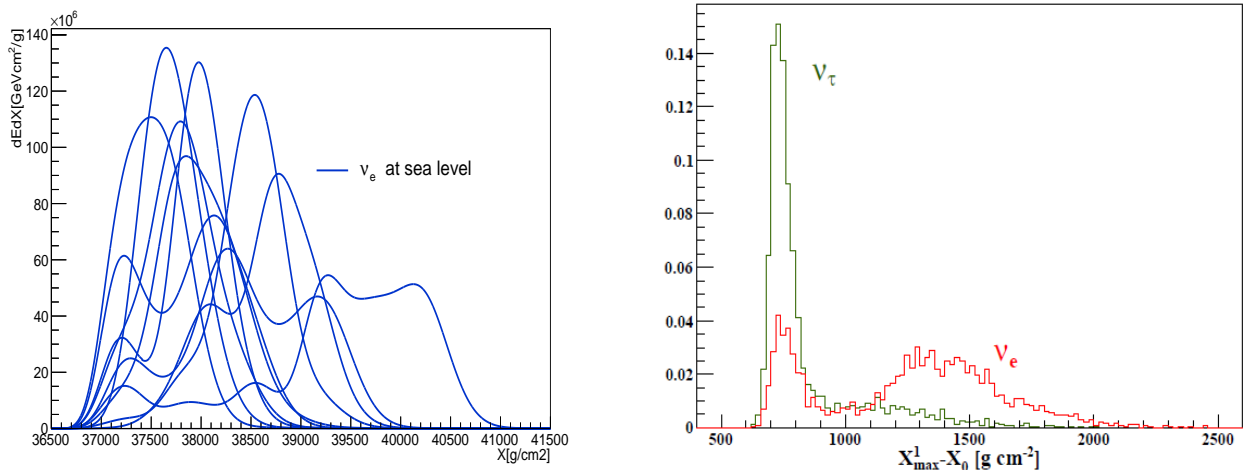


**Figure 5.4:** *Left:* Longitudinal profiles of horizontal ( $\Theta = 0^\circ$ ) neutrino showers. All showers were injected at the center of the FOV ( $X_0 = 36500 \text{ g cm}^{-2}$ ) with an energy of  $10^{20} \text{ eV}$ . *Right:* Distribution of the position of the first peak (in grammage) for electron and tau neutrino showers whose first interaction point is at sea level and on the vertical axis of JEMEUSO in Nadir mode. The neutrino energy is  $E = 10^{20} \text{ eV}$ . The histograms are normalized to unity. Reproduced from [Supanitsky & Guzmán 2013].

The change in the probability of interaction allows us to provide a first estimate on the expected change on the exposure. The ratio of the probability of a neutrino interacting within a slant depth of  $X$  (in  $\text{g cm}^{-2}$ ) to the corresponding probability for a proton is:

$$\frac{P_\nu(X)}{P_p(X)} = \frac{1 - e^{-\frac{X}{\lambda_\nu}}}{1 - e^{-\frac{X}{\lambda_p}}} \sim 1.6 \times 10^{-5} \div 3.3 \times 10^{-3} \quad \text{for } X \in [100, 11\,000] \text{ g cm}^{-2} \quad (5.24)$$

We show the ratio of these probabilities in Fig. 5.3. The reason we are selecting this range in  $X$  is because the probability of a proton surviving is already  $\sim 10^{-4}$  at  $250 \text{ g cm}^{-2}$ , which is half of the vertically integrated slant depth. Such atmospheric depths will, in principle, allow us to recognize the neutrino showers as deeply interacting particles. Unfortunately, this comes with a trade-off: deeply interacting showers may not have enough atmosphere in front of them to create a EAS before they reach the ground. This implies that, imposing a cut on the slant depth of the first interaction, poses a cut on the zenith angle  $\Theta$  that allows the development of the EAS. The latter has the side effect of reducing the solid angle by a fraction  $f_r(\Theta_{cut})$ . This reduction is simply:

$$f_r(\Theta_{cut}) = \frac{\Omega_{cut}}{\Omega_0} = \frac{\int_0^{\Theta_{cut}} \sin(2\Theta) d\Theta}{\int_0^{\frac{\pi}{2}} \sin(2\Theta) d\Theta} = \cos^2(\Theta_{cut}) \quad (5.25)$$

In the left side of Fig. 5.4 we show some examples of longitudinal profiles for horizontal  $\nu_e$  showers interacting at sea level in the center of the FOV. As can be seen in the right panel, typically a  $\nu_e$ -EAS would need at least  $\sim 1000 \text{ g cm}^{-2}$  after the first interaction  $X_0$  to create a detectable

fluorescence signal (first maxima  $X_{max}^1$ ). Sometimes even more atmospheric depth is needed.

Let us proceed calculating the probability that a neutrino survives till  $X_0$  and then interacts in the next  $\delta X$  of atmospheric grammage. This calculation is straightforward, and is given by:

$$P_\nu(\delta X | P_\nu(X_0)) = P_\nu(X_0)P_\nu(\delta X) = (e^{-\frac{X_0}{\lambda_\nu}})(1 - e^{-\frac{\delta X}{\lambda_\nu}}) \quad (5.26)$$

In addition, we now impose the condition that the shower has at least  $1000 \text{ g cm}^{-2}$  to develop inside the atmosphere. This is:

$$X_{atmo}(\Theta) - (X_0 + \delta X) \geq 1000 \text{ g cm}^{-2}$$

In this equation  $X_{atmo}(\Theta)$  is the total atmospheric depth, from the top of the atmosphere till the center of the FOV, along a track with zenith angle  $\Theta$ . We will also impose that the neutrinos interact at  $X_0 \gg \lambda_p$ . The idea is that during the reconstruction we should be able to recognize this high value of the first interaction and realize this is not a baryon-initiated shower. For the moment, we shall take  $X_0 \geq 250 \text{ g cm}^{-2}$ . This changes our requirement to:

$$\delta X \leq X_{atmo}(\Theta) - (X_0 + 1000) \text{ g cm}^{-2} \Big|_{X_0=250}$$

The latter imposes that  $\Theta \geq 45$  (see Fig. 5.3) else the shower will not have enough atmosphere in front of it after the first interaction. We introduce  $\delta X$  to provide a handle on the trade-off between the probability of interaction and our capability to see the shower.

We can now give a more realistic expected exposure and hence sensitivity by re-scaling the proton exposure by a factor that carries this information. We define:

$$f_{scale}(\Theta, \delta X) = \begin{cases} \frac{P_\nu(250)P_\nu(\delta X)}{P_p(250)} \cdot \cos^2(\Theta) & \text{if } \delta X \leq X_{atmo}(\Theta) + 1250 \text{ g cm}^{-2} \\ 0 & \text{if } \delta X > X_{atmo}(\Theta) + 1250 \text{ g cm}^{-2} \end{cases} \quad (5.27)$$

$f_{scale}$  directly incorporate the probability of a neutrino interacting within  $X_0$  and  $\delta X$  of atmosphere. Certainly  $P_p(X_0) \rightarrow 1$  faster than  $P_\nu(X_{atmo}(\Theta) - X_0)$ , however we keep the ratio since for the moment we will be scaling the proton exposure.

In other words, all other things equal, we only take into account neutrino EAS with a first interaction point, that allows the subsequent shower with at least  $1000 \text{ g cm}^{-2}$  of atmosphere in front of it. As it can be seen in Fig. 5.5 the dominating term is the cosine. Still at low  $\delta X$  the atmosphere is not deep enough for us to see at least the first maximum of the longitudinal profile (see right side of Fig. 5.4). Instead of multiplying  $f_{scale}$  times yet another factor to account for the  $X_{max}$  visibility, we select the value of  $\delta X$  that maximizes  $f_{scale}$ . We show some examples how  $f_{scale}$  behaves once  $\delta X$  is fixed Fig. 5.6.

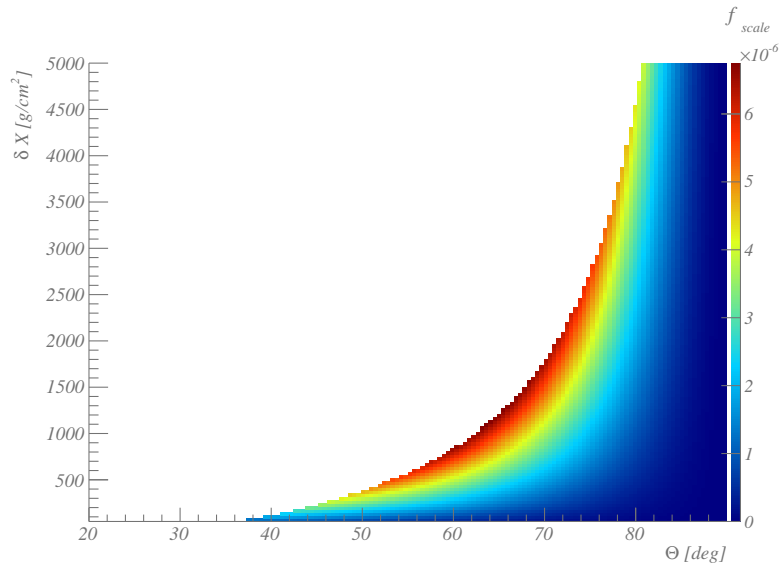


**Figure 5.5:** The scaling factor  $f_{scale}$  as a function of  $\Theta$  and  $\delta X$ .

As we illustrate in the right side of Fig. 5.4, it would be hardly justifiable to select  $\delta X \leq 1000 \text{ g cm}^{-2}$ , because then we would not be able to see the shower development till the first maximum. From Fig.5.5, we have that the angle and grammage that maximize  $f_{scale}$  are  $\Theta = 64.72^\circ$  and  $\delta X = 1188.63 \text{ g cm}^{-2}$ . The scale factor becomes:

$$f_{scale}(\Theta, \delta X)|_{\Theta \sim 65^\circ, \delta X \sim 1200 \text{ g cm}^{-2}} \approx 6.77 \times 10^{-6} \quad (5.28)$$

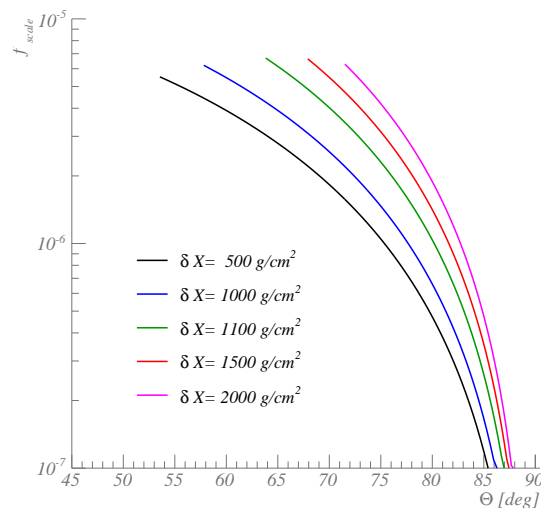


**Figure 5.6:** The scaling factor  $f_{scale}$  as a function of  $\Theta$  for fixed  $\delta X$ .

The effect of rescaling the proton exposure by such a factor is shown in Fig. 5.7. The problem with this procedure is that, as we show in the next section, due to the LPM effect, and the atmospheric depths at which the shower develops the trigger efficiency decreases dramatically, further worsening

the rescaled value that we are plotting. We already performed simulation studies for neutrino showers with  $\Theta = 80^\circ$  exclusively [Supanitsky & Guzmán 2013]. The results are shown in Fig. 5.8, where we see that  $\epsilon_{trig} = 0.8$  for  $E = 10^{19.5}$  eV and  $X_0 = 2000$ . Although we do not achieve full efficiency, we do achieve it at higher energies for this particular inclination angle. It is worth mentioning that our choice of parameters is arbitrary, and the case could be made for different cuts. For this reason we present a more thorough estimation in the next section.

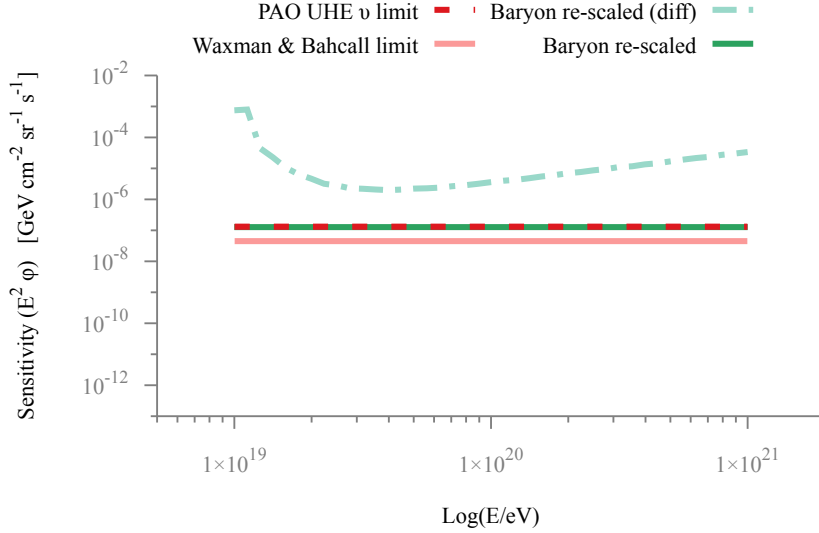


**Figure 5.7:** Comparison between reported values of the sensitivity for proton and the re-scaled sensitivity (see text). In this case  $f_{scale} = 6.77 \times 10^{-6}$ .

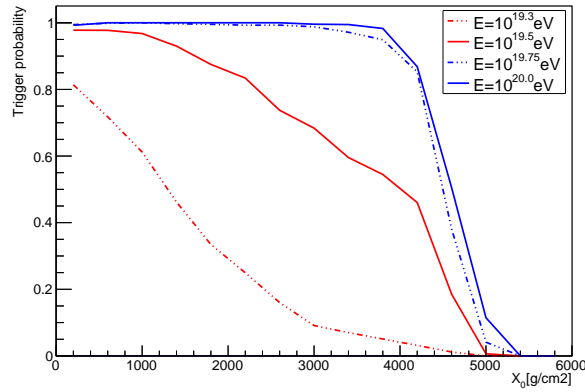


**Figure 5.8:** Triggering efficiencies for neutrino showers with their impact points (cores), coinciding with the center of the FOV at ground. In all cases  $\Theta = 80^\circ$ . Reproduced from [Supanitsky & Guzmán 2013].

### 5.2.1 Tilting

Before we conclude this re-scaling exercise, let us mention the case for the tilted mode. Kindly enough, Francesco Fenu [Fenu 2013] also provided us with the exposure curves for the tilted

mode from his PhD Thesis. We can also rescale them as we did in the previous section. Results are shown in Fig. 5.9. Unfortunately, and in disagreement to what is shown in [Kotera & Olinto 2011] [Medina-Tanco, et al. 2009] in this case even the proton exposure does not change dramatically enough for a significant energy range. Also here is shown the optimistic assumption of operating 5 years in the tilted mode. Hence, even this over optimistic scenario is already not enough to significantly enhance the sensitivity for neutrinos.

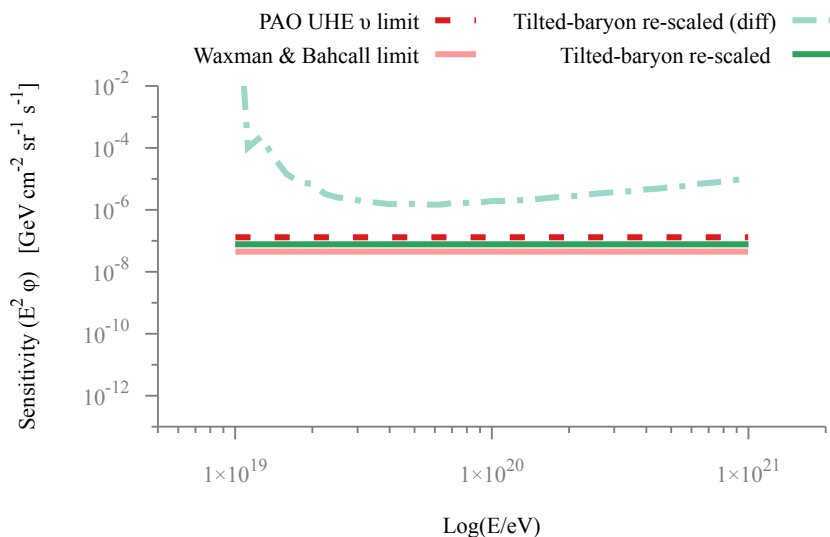


**Figure 5.9:** Comparison between reported values of the sensitivity for proton and the re-scaled sensitivity (see text) at a tilting angle of  $40^\circ$ . In this case  $f_{scale} = 6.77 \times 10^{-6}$ .

## 5.3 The neutrino exposure

With the discussion presented at the beginning of this chapter we are now ready to assess the right hand of Eq. 5.11 using computer simulations. These simulations will shed more light on the feasibility of detecting UHE neutrinos with JEM-EUSO, and realistically calculate the value for the upper limits JEM-EUSO could provide. By approximating the unknown value of the  $\epsilon'_\nu(E, \Theta, \vec{r}_{FOV})$  on eq. 5.11 with:

$$\epsilon'_\nu(E, \Theta, \vec{r}_{FOV}) \approx \frac{N_{trig}(E, \Theta, \vec{r}_{FOV})}{N_{inj}} \quad (5.29)$$

Here  $N_{trig}$  and  $N_{inj}$  are the number of neutrino showers triggered and injected respectively. To estimate  $\mathcal{P}_{\nu \rightarrow EAS}(E_\nu)$  we following [PAO 2013c] we use the corresponding neutrino-nucleon interaction cross-section  $\sigma^{CC}(E_\nu)$  and the nucleon mass  $m$ . This last step and the simplifications introduced in the last section, allow us to modify Eq. 5.11 to:

$$\begin{aligned}
\varepsilon_\nu(E_\nu) &= \int_T \eta(t) dt \int_{\Omega_0} \int_S \epsilon'_\nu(E, \Theta, \vec{r}_{FOV}) \otimes \mathcal{P}_{\nu \rightarrow EAS}(E_\nu) \cos \Theta dS d\Omega \\
&\approx \int_T \eta(t) dt \int_{\Omega_0} \int_S \frac{N_{trig}}{N_{inj}}(E_\nu, \Theta, \vec{r}_{FOV}) \otimes \mathcal{P}_{\nu \rightarrow EAS}(E_\nu) \cos \Theta dS d\Omega \\
&\approx T \eta_0 \pi S_0 \int_0^{\frac{\pi}{2}} \frac{N_{trig}}{N_{inj}}(E_\nu, \Theta) \cdot \sin(2\Theta) \cdot \mathcal{P}_{\nu \rightarrow EAS}(E_\nu) d\Theta \\
&\approx T \eta_0 \pi S_0 \int d\Theta \frac{N_{trig}}{N_{inj}}(E_\nu, \Theta) \cdot \sin(2\Theta) \cdot \left( \frac{\sigma^{CC}}{m} \int_0^{\delta X} dX \right) \Bigg|_{\delta X = X_{atmo}(\Theta) - (1000 + X_0)}
\end{aligned} \tag{5.30}$$

To “assure” that we will not confuse these showers with baryons, we will set a random the first interaction point above a threshold value that may make the “selection efficiency” close to the ideal case (i.e.  $\epsilon_{sel} = 1$ ). The selected threshold in slant depth is  $X_0^{thr} \geq 142$  [g cm<sup>-2</sup>] as suggested in [Supanitsky Medina-Tanco 2011]. Many combinations of energy and zenith angle that maximize the probability of a shower interacting after this minimum value of  $X_0$  will however make no visible track for the detector hence setting  $\epsilon'_\nu(E, \Theta, \vec{r}_{FOV}) = 0$ . Therefore we take the liberty of setting a simulation cut on the inclination angle. We take  $50^\circ \leq \Theta$ , which, as shown in Fig. 5.3, allows for at least 1000 g cm<sup>-2</sup> of atmospheric depth after the first interaction.

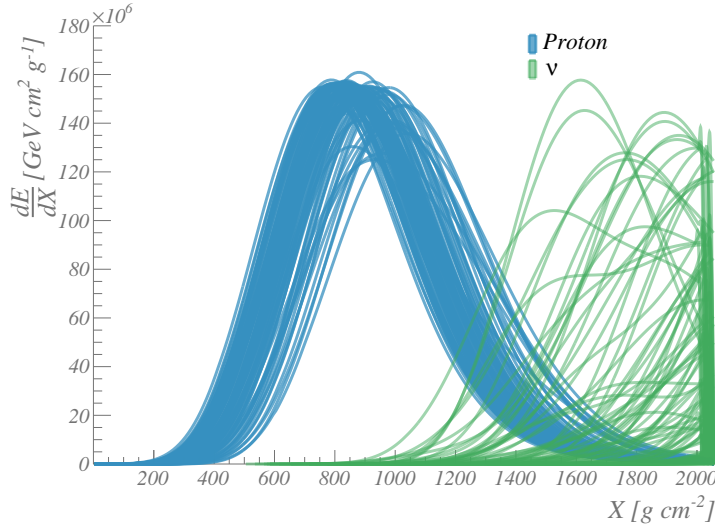


**Figure 5.10:** A comparison of the longitudinal profiles of EAS initiated by protons and neutrinos( $\nu$ ). For both primaries we show a subsample of 100 showers with an energy of  $10^{20}$  eV and  $\Theta \sim 60^\circ$ . In this particular example the neutrino simulations had a minimum interaction depth above  $450$  g cm<sup>-2</sup>.

We proceed in a similar way as in § 4. We simulate the charged current interaction between

the nuclei in the atmosphere and UHE- $\nu_e$ 's with fixed energies, i.e.  $10^{19.7}$ ,  $10^{19.8}$ ,  $10^{19.9}$ ,  $10^{20}$  and  $10^{20.5}$  eV. This is done via the PYTHIA [Sjöstrand et al. 2006] event generator, linked with the parton distribution functions CTnnlo10 [Lai et al. 2010]. We must be careful to remember that all neutrino cross-sections in our energy range of interest are well beyond measured values [Gandhi et al. 1998] [Palomares-Ruiz et al. 2006]. But for extrapolations based on the standard model we see that although a general increase with energy is observed, this increase in the cross section is not more than half an order of magnitude in the energy range we are interested.

Once we have a list of secondary particles created after the charged current interaction we inject them into the CONEX shower simulator. An example set of the longitudinal profiles of neutrino-initiated showers with  $\Theta = 60^\circ$ ,  $450 \text{ g cm}^{-2}$ , and  $E = 10^{20}$  is shown in Fig. 5.10.

The geometrical settings for each EAS are: a random polar angle and random inclination angle following a  $\sin(2\Theta)$  distribution. Though the latter is sampled in discrete intervals of  $10^\circ$  each. These conditions are summarized in Table 5.1. For the first interaction point we sampled  $X_0$  randomly within the interval  $[X_0^{thr}, X_{atmo}(\Theta) - (X_0^{thr} + 1000)]$  following a  $\left(1 - e^{-\frac{X_0}{\lambda_\nu}}\right)$  distribution. With these last specifications we rewrite Eq. 5.30 as:

$$\begin{aligned} \varepsilon_\nu(E_\nu) &\approx T\eta_0\pi S_0 \int d\Theta \frac{N_{trig}}{N_{inj}}(E_\nu, \Theta) \cdot \sin(2\Theta) \cdot \left( \frac{\sigma^{CC}}{m} \int_0^{\delta X} dX \right) \Bigg|_{\delta X = X_{atmo}(\Theta) - (1000 + X_0)} \\ &\approx T\eta_0\pi S_0 \sum_{\Theta} 2 \sin(2\Theta + 10^\circ) \cdot \sin(10^\circ) \cdot \frac{N_{trig}}{N_{inj}}(E_\nu, \Theta) \cdot \left( \frac{\sigma^{CC}}{m} \int_0^{\delta X} dX \right) \Bigg|_{\delta X = X_{atmo}(\Theta) - (1000 + X_0)} \end{aligned} \quad (5.31)$$

where we have performed the integral of  $\sin(2\Theta)$  and used  $\cos(\alpha) - \cos(\beta) = -2 \sin\left(\frac{\alpha+\beta}{2}\right) \sin\left(\frac{\alpha-\beta}{2}\right)$  to further simplify.

Finally using the tools developed in this thesis we inject the neutrino-initiated EAS into ESAF. To avoid border effects, i.e. to avoid showers exiting the FOV too early (before enough fluorescence light is produced) or entering the FOV too late (after the most of the fluorescence light is produced). Our results are shown in Fig. 5.11. As it can be seen in the aforementioned figure the “neutrino signal” is not saturating the detector even at  $10^{20}$  eV.

As explained in the present chapter the exposure is the fundamental information required to calculate the neutrino sensitivity for a EUSO like experiment. Once this information is at hand we can calculate the sensitivity following Eq. 5.21. This final calculation is shown in Fig. 5.12.

| $E$ [eV]    | $\Theta$ [deg] | Number of events |
|-------------|----------------|------------------|
| $10^{19.7}$ | 50 – 60°       | 1000             |
|             | 60 – 70°       | 1000             |
|             | 70 – 80°       | 1000             |
|             | 80 – 90°       | 1000             |
| $10^{19.8}$ | 50 – 60°       | 1000             |
|             | 60 – 70°       | 1000             |
|             | 70 – 80°       | 1000             |
|             | 80 – 90°       | 1000             |
| $10^{19.9}$ | 50 – 60°       | 1000             |
|             | 60 – 70°       | 1000             |
|             | 70 – 80°       | 1000             |
|             | 80 – 90°       | 1000             |
| $10^{20}$   | 50 – 60°       | 1000             |
|             | 60 – 70°       | 1000             |
|             | 70 – 80°       | 1000             |
|             | 80 – 90°       | 1000             |
| $10^{20.5}$ | 50 – 60°       | 1000             |
|             | 60 – 70°       | 1000             |
|             | 70 – 80°       | 1000             |
|             | 80 – 90°       | 1000             |

**Table 5.1:** The set of UHE- $\nu_e$  simulations, using PYTHIA as the event generator and CONEX as the shower generator. We will refer to this set of showers as the *Neutrino-Benchmark*.

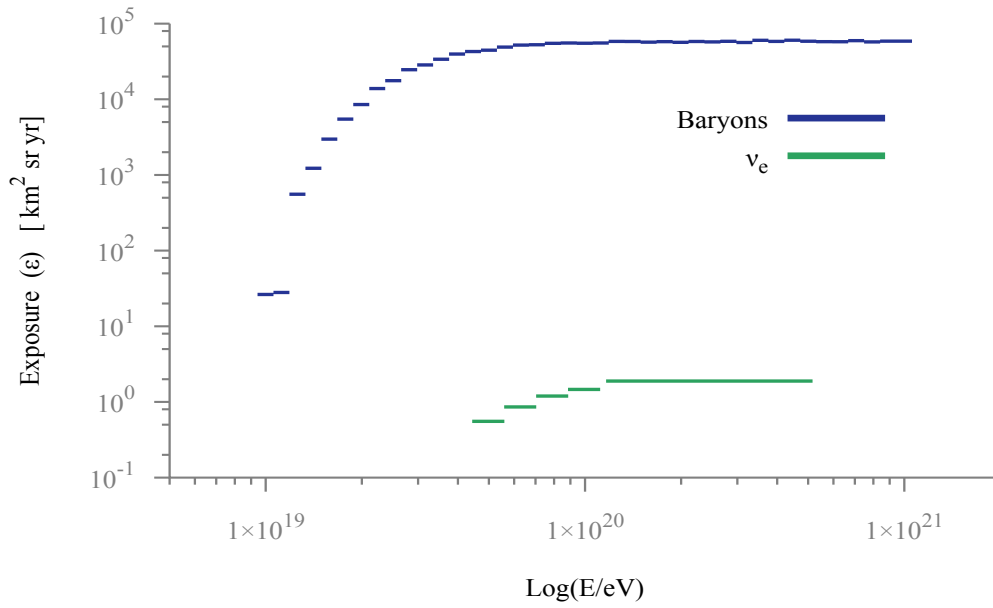


**Figure 5.11:** The neutrino exposure as a function of energy (following Eq. 5.31). Also shown is the baryon exposure (in blue) [Adams et al. 2013a].

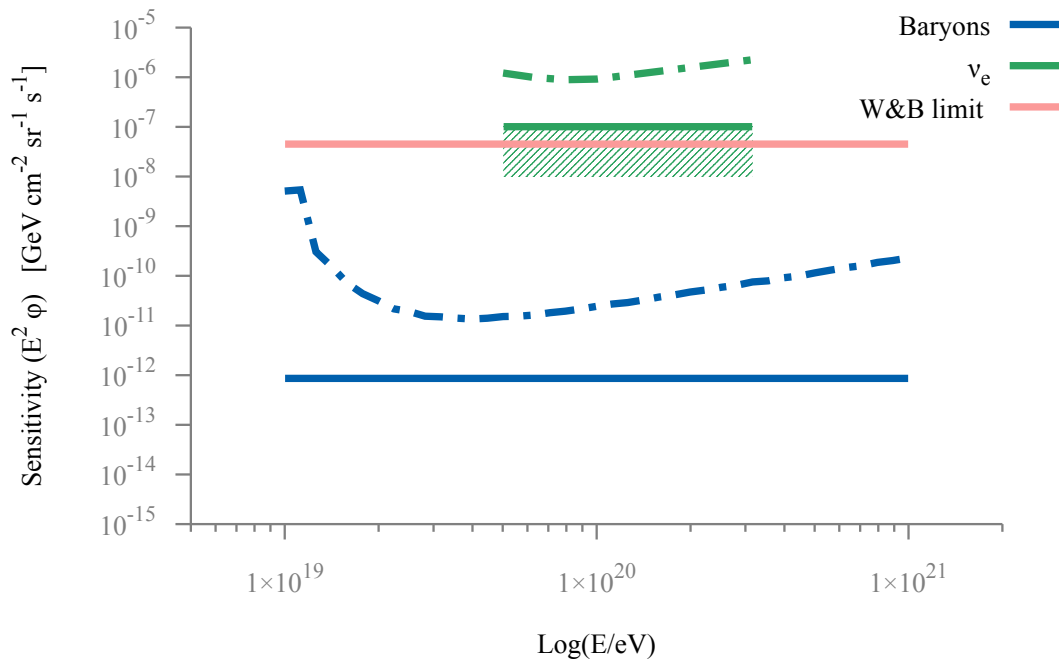


**Figure 5.12:** EUSO's neutrino sensitivity calculated with the exposure shown in Fig. 5.11. The shaded region represents an improved sensitivity in the case that the neutrino cross section increases as discussed in [Kusenko et al. 2002]. Also shown is the baryon sensitivity (in blue) [Adams et al. 2013a].

## 5.4 Reconstruction of EAS induced by a EE- $\nu$

As a final application of the tools developed in the present thesis we carried out a preliminary test of the reconstruction capabilities of the ESAF on the *Neutrino Benchmark*. We proceeded in the same way as we did for baryon or photon EECR primaries (presented in § 4). We use the default values of the reconstruction modules as if this was a blind test without prior knowledge of the nature of the primaries.

### 5.4.1 Angular reconstruction

The angular resolution for the *Neutrino Benchmark* is shown in Fig. 5.13. As it can be seen, despite we are operating at the zenith angle range where the angular resolution performs better (see § 4), the angular resolution for  $\nu_e$  is not within the requirements of the mission. Although we must emphasize that these requirements are set for charged EECR. We must however point out the fact that the triggering efficiency is already indicating a lack of signal thus bringing the angular reconstruction to the limits of its usability.

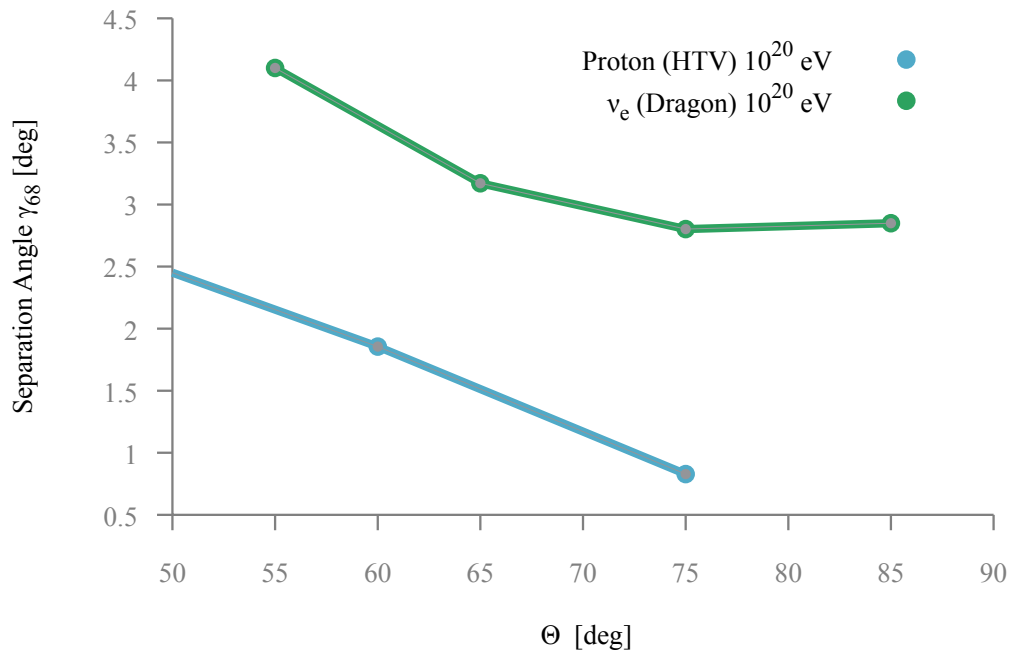


**Figure 5.13:** EUSO's angular reconstruction for neutrino initiated EAS. Also shown are the values for proton primaries as published in [Guzmán, Mernik et al. 2014].

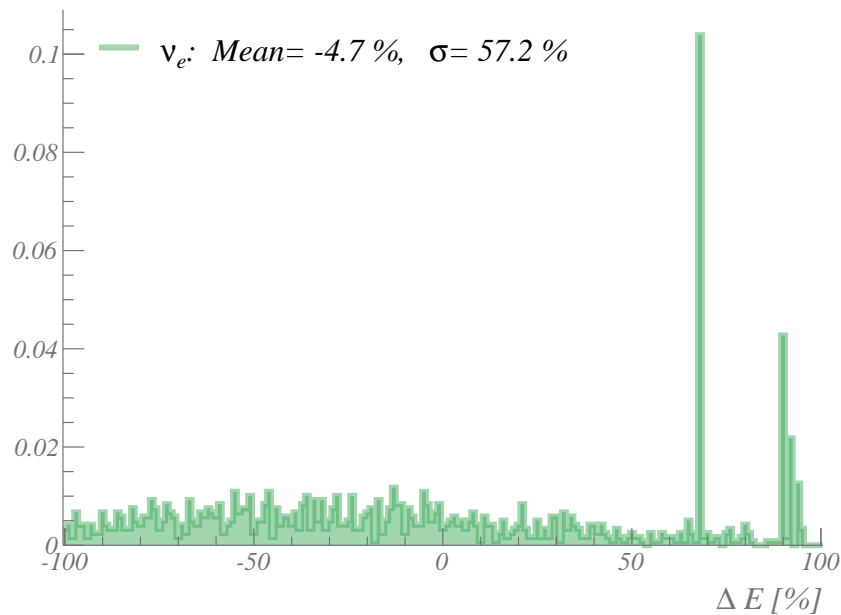


**Figure 5.14:** JEM-EUSO’s energy reconstruction error for neutrino initiated EAS using the output of the *PmtToShower Module*. See text to understand the mismatch between reconstructed and simulated energies. All energies from the *Neutrino-Benchmark* were used to produce this plot.

#### 5.4.2 Energy and longitudinal profile reconstruction

For the energy reconstruction we see a much worse performance, as shown in Fig. 5.14. This does not come as a surprise since the profile reconstruction module within ESAF is tuned for “typical” baryon-initiated EAS. The difference in atmospheric depth and overall shape of the longitudinal profile make this tool unsuitable for the task at hand. The main reason for the discrepancy between reconstructed energy and simulated energy of the primary, comes from the ill-suited fitting of the longitudinal profile with the GIL parametrization [Fenu 2013].

In Fig. 5.15 we show a comparison between simulated and reconstructed longitudinal profiles for some selected  $\nu_e$  events. Although this selection is arbitrary, it is useful to illustrate one of the systematic reasons for the discrepancy between the reconstructed and simulated shower profiles: the wrong estimation of the first interaction point. This factor plus the ill-suited GIL parametrization are the main culprits for the bad performance of the *PmtToShower Module* with  $\nu_e$  EAS. But let us remember that we are applying this module and the assumed models within, far beyond their usability realm.

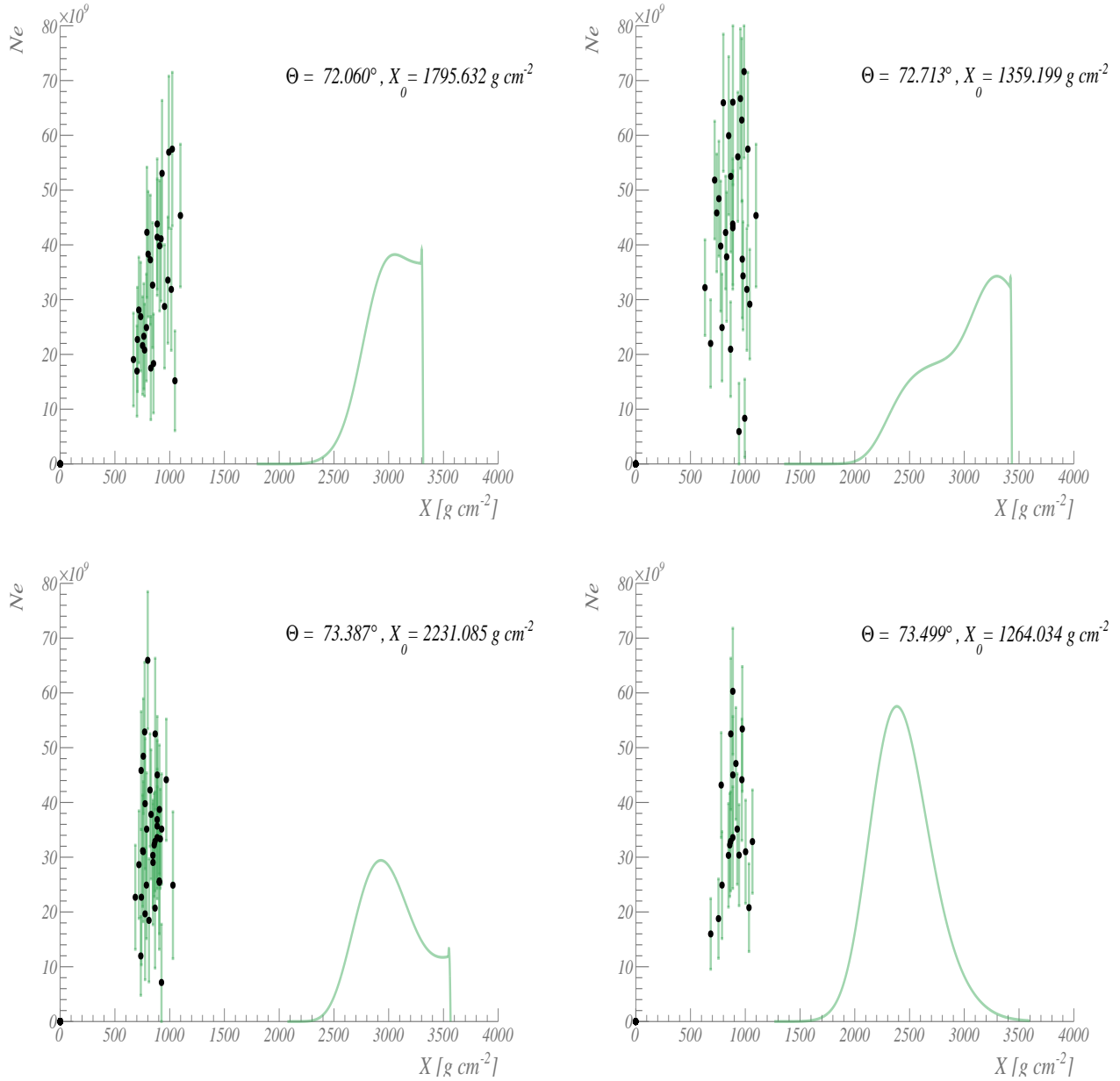


**Figure 5.15:** Some example of the difference between simulated and reconstructed points of the longitudinal profile. In the upper panel we see some examples with a relatively strong LPM effect where a shower maximum was not completely evident. And in the lower panel we see two examples of a more *regular* longitudinal profiles. All neutrinos in this figure were simulated with  $E = 10^{20}$  eV.

Despite this discouraging first preliminary attempt, a way of circumventing this problem may be relatively easy to implement. For example we can use the profiles reconstructed by the *PmtToShower Module* to perform a very coarse estimation of the energy by simply calculating the area underneath the reconstructed points (no fitting). This simple procedure is shown in Fig. 5.16. We can see a dramatic improvement in the energy reconstruction. However there is a strong systematic under estimation of the energy that requires further improvement. However such an improvement is out of the scope of the present work, since the main piece of missing information comes from estimation of the first interaction point. Or in other words, it requires the a technique to single out  $\nu_e$ -induced EAS. As we stated earlier, this is still an open issue and it is unclear if the fluorescence technique by itself is capable of providing enough information. The case has been made for Earth skimming neutrinos where it is postulated that the angular reconstruction will point out EAS propagating upwards [Palomares-Ruiz et al. 2006]. These results, however, have not yet been confirmed with simulations.

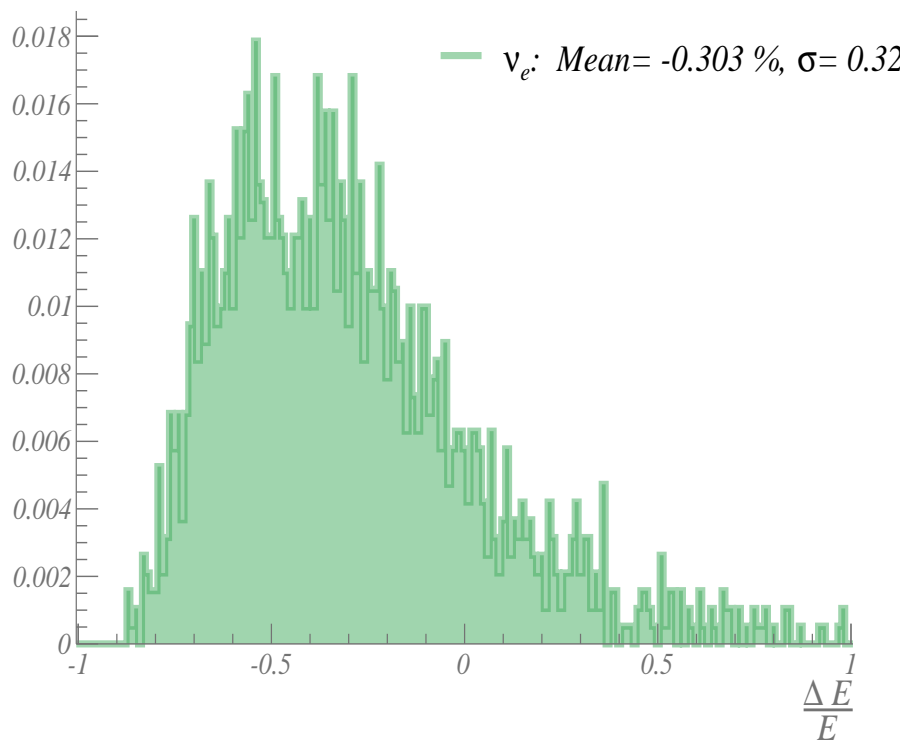


**Figure 5.16:** EUSO's energy reconstruction error for neutrino initiated EAS using a simple integration of the longitudinal profiles (see text). All energies from the *Neutrino-Benchmark* were used to produce this plot. The peaks in the distribution are artifacts introduced by the *PmtToShower Module*.



# 6

## PATHFINDER SIMULATIONS AND ANALYSIS

---

### Contents

---

|       |   |     |
|-------|---|-----|
| 6.1   | Statistical analysis of the EUSO-Balloon optics . . . . . | 139 |
| 6.1.1 | Definitions . . . . .                                     | 141 |
| 6.2   | Analysis of selected simulated scenarios . . . . .        | 143 |

---



## 6.1 Statistical analysis of the EUSO-Balloon optics

Due to problems in the manufacturing process of the mold for the intermediate lens, the EUSO-Balloon experiment flew only with two lenses [Von Ballmoos et al. 2015]. The addition of the wrongly-manufactured middle lens would have worsen the point spread function of the detector. To study the possible implications of this mismatch in the designed and manufactured configurations we conducted a statistical analysis of the observed scene. We did so by studying the 2 point correlation function for scenes observed in the Photo Detection Module (PDM) of the EUSO-Balloon. Different optics response configurations were used:

- (i) *Dirac's Delta Optical Response*
- (ii) *Designed Optical Response*
- (iii) *Manufactured Optical Response*

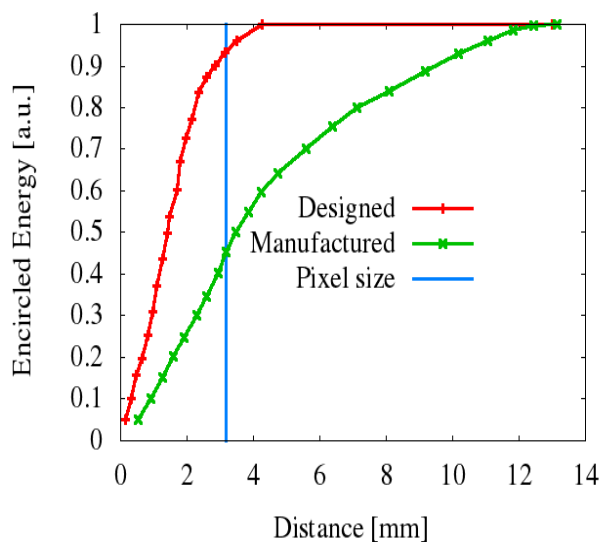
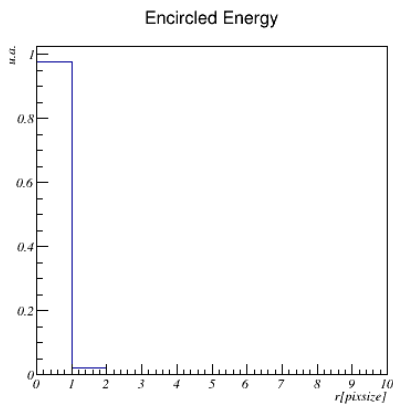
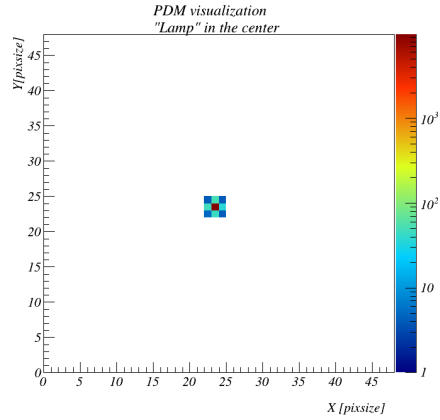


**Figure 6.1:** Comparison between the case (i) designed (red) and (ii) manufactured (green) optical responses. We show the average Encircled Energy as a distance from the center of the light spot. The blue line identifies the pixel size.

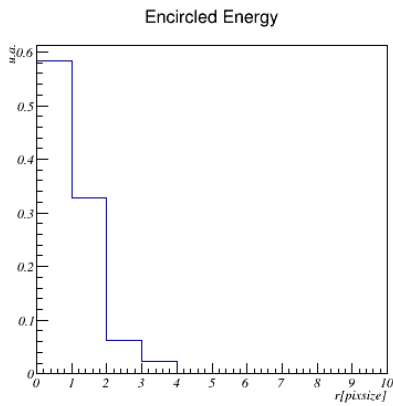
The difference in the encircled energy between the designed and manufactured optics cases can be seen in Fig. 6.1, and their respective impact on the image of an ideally illuminated pixel can be seen in Fig. 6.2. Also in Fig. 6.2 we re-binned the encircled energy in pixel size units to have a better idea of what the impact could be in the detector.



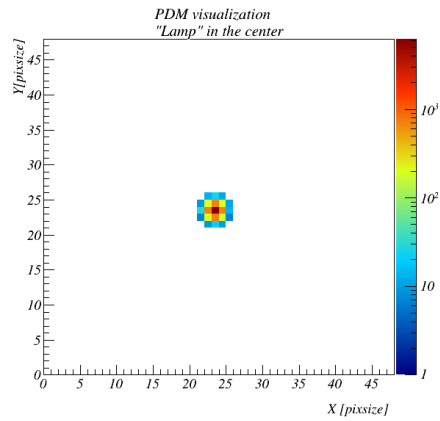
(a) Probability distribution for the designed optical response.



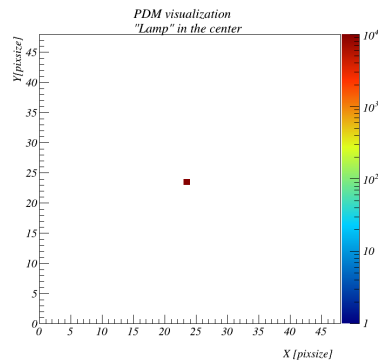
(b) Spot image of an ideal light source shining in the center pixel for the designed optical response.



(c) Probability distribution for the manufactured optical response.



(d) Spot image of an ideal light source shining in the center pixel for the manufactured optical response.



(e) Spot image of an ideal light source shining in the center pixel for a Dirac's delta optical response.

Figure 6.2

The objective of these tests was to quantify the impact of the difference between the manufactured and designed optics. As a consequence of the de-focusing introduced by the manufactured optics, the background was expected to behave quantitatively different. Particularly, we analyzed the spatial correlations of the balloon's Field of View (FoV).

### 6.1.1 Definitions

In this work, we used three different approaches to analyze the background fluctuations and their spatial correlation. The following definitions are based on [Moran 1950] and [Geary 1954]:

- **Point correlation function**, We define  $\mathbf{Pcf}(r, dr)_{x,y}$  at a point  $(x, y)$  as:

$$\mathbf{Pcf}(r, dr)_{x,y} = \frac{N_{pix}}{N_{\mathcal{R}(x,y)}} \frac{\sum_{(x',y') \subset \mathcal{R}(x,y)} (\gamma_{x,y} - \mu)(\gamma_{x',y'} - \mu)}{\sigma^2} \quad (6.1)$$

In this last expression  $\mathcal{R}(x, y)_{r+dr}$  is a ring of inner radius  $r$  and outer radius  $r + dr$ , centered at  $(x, y)$ ;  $N_{\mathcal{R}(x,y)}$  is the number of pixels inside this ring;  $\gamma_{x,y}$  is the amount of photons (photoelectrons, that is) integrated during a period of time  $\tau$ ; and  $\mu$  the PDM's mean value:

$$\begin{aligned} \sigma^2 &= \sum_{x,y} (\gamma_{x,y} - \mu)^2 \\ \gamma_{x,y} &= \sum_{gtu=0}^{\tau} pc(gt u) \\ \mu &= \frac{1}{N_{pix}} \sum_{x,y} \gamma_{x,y} \\ \gamma_{tot} &= \sum_{x,y} \gamma_{x,y} \end{aligned} \quad (6.2)$$

where  $N_{pix}$  is the total number of pixels in the PDM.

- **Two point correlation function**, The two point correlation function  $g(r, dr)$  corresponds to the sum of  $\mathbf{Pcf}(r, dr)_{x,y}$  over all pixels of the PDM:

$$g(r, dr) = \sum_{(x,y)} \mathbf{Pcf}(r, dr)_{x,y} \quad (6.3)$$

- **Moran's I**, We define  $\mathcal{I}(r)$  as:

$$\mathcal{I}(r) = \frac{N_{pix}}{\sum_{\vec{x}, \vec{x}'} W_{\vec{x}, \vec{x}'}(r)} \frac{\sum_{\vec{x}, \vec{x}'} W_{\vec{x}, \vec{x}'}(r) (\gamma_{\vec{x}} - \mu)(\gamma_{\vec{x}'} - \mu)}{\sigma^2} \quad (6.4)$$

Where  $\vec{x}$  is introduced as a shorthand for  $(x, y)$ . And the matrix  $W(r)$  of range  $N_{pix} \times N_{pix}$  is called the weight matrix. It codifies *a priori* the expected correlation between position  $\vec{x}$  and  $\vec{x}'$ . We will come back to  $W(r)$ 's definition after our next and last parameter.

- *Geary's C*, We define  $\mathcal{C}(r)$  as:

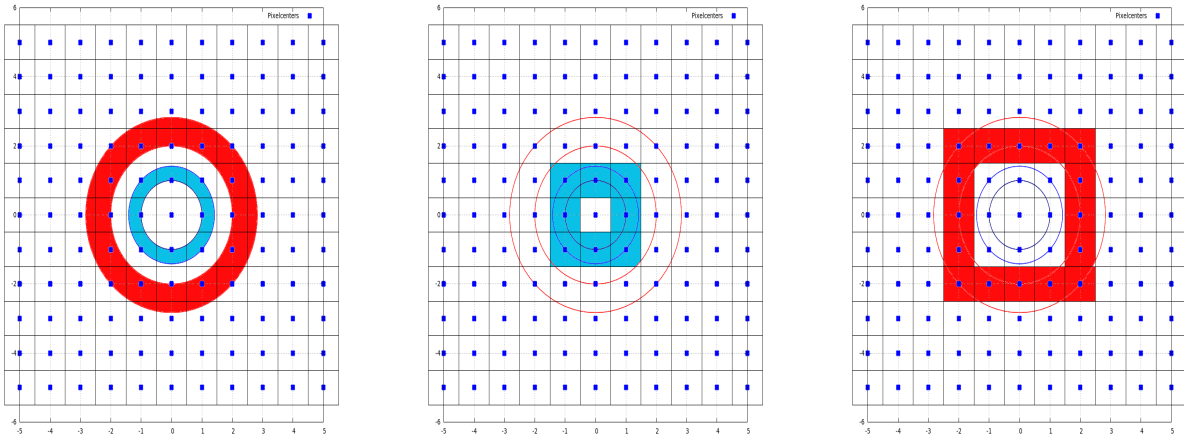
$$\mathcal{C}(r) = \frac{(N_{pix} - 1) \sum_{\vec{x}} \sum_{\vec{x}'} W_{\vec{x} \vec{x}'}(r) (\gamma_{\vec{x}} - \gamma_{\vec{x}'})^2}{\sum_{\vec{x}} \sum_{\vec{x}'} 2W_{\vec{x} \vec{x}'}(r) \sigma^2} \quad (6.5)$$

As it can be seen,  $\mathcal{I}(r)$  and  $\mathcal{C}(r)$  are quite similar, but the first compares the values with the overall mean and the second compares *adjacent* values. Hence providing more sensitivity to local variations or fluctuations.

The weight matrix is another way of setting the limits for the sum inside the ring. Both  $\mathcal{I}(r)$  and  $\mathcal{C}(r)$  are very sensitive to the definition of this matrix. There are different approaches to assign its values: first neighbors only, the inverse of the distance, the inverse of the square of the distance, etc. In these work we define the elements of  $W(r)$  as:

$$W_{\vec{x} \vec{x}'}(r) = \begin{cases} 1 & \text{if } r \leq \|\vec{x} - \vec{x}'\| \leq r + dr \\ 0 & \text{any other case} \end{cases} \quad (6.6)$$

Here the choice of  $dr$  is crucial to give a meaningful comparison between our 2 approaches. We choose  $dr \equiv r(\sqrt{2}-1)$ . This approach is valid only if we select  $r$  to be integer multiples of the pixel side. We choose this approach because the pixel side is the characteristic length (resolution). These choices translate into squared rings (as seen in Fig.6.3).



- (a) The two first rings from a pixel in the center of the image. (b) The first ring selects only the blue colored pixels. (c) The second ring selects the red colored pixels.

**Figure 6.3:** Graphical example of our selection of  $W(r)$ . Pixel centers with blue dots.

## 6.2 Analysis of selected simulated scenarios

Now that we have clear definitions, we proceed to calculate  $g(r, dr)$ ,  $\mathcal{I}(r)$  and  $\mathcal{C}(r)$  in the 3 different optical responses mentioned above, and the following lighting conditions (see Fig.6.4):

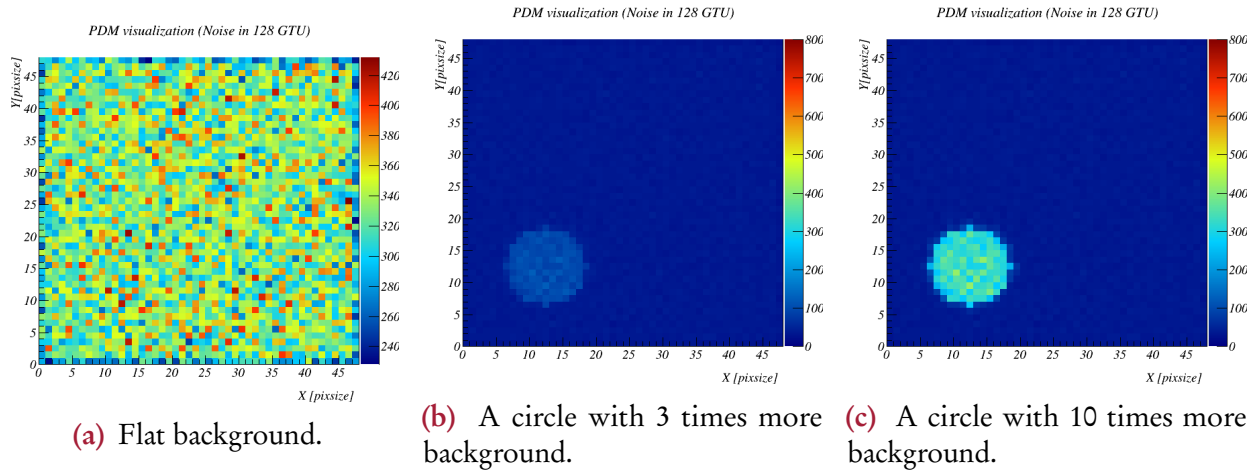


**Figure 6.4:** The (integrated) appearance of the manufactured PDM for different lighting conditions on top of flat a poissonian background with mean  $\mu = 2.6 \frac{\text{pc}}{\text{GTU}}$ . The image on the left is the pure flat background with no other source. It has a different scale on the color axis to enhance the fluctuations and the border effect, else the image would be completely blue, as the images on the right.

- **Ideal light source** We emulate an ideal lamp shining only in the center pixel of the PDM (see Fig. 6.2). The results of the statistical tests are shown in Fig. 6.5. As expected, only a barely perceivable deviation is seen between all three cases. This is explained by the fact that, regardless of the optics at hand, this unrealistic light source creates basically the same image on the focal surface (see Fig. 6.2).

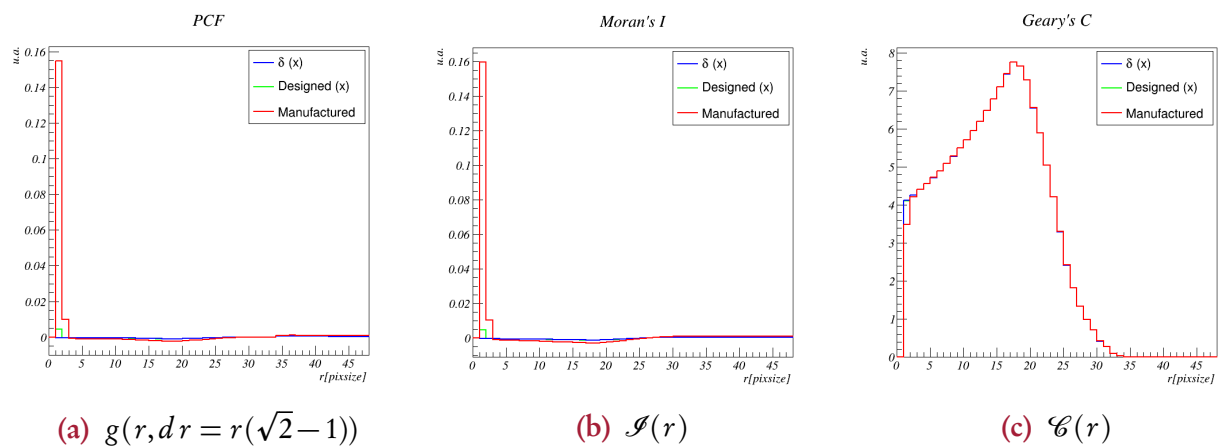


**Figure 6.5:** Comparison of  $g(r, dr = r(\sqrt{2}-1))$ ,  $\mathcal{I}(r)$  and  $\mathcal{C}(r)$  between the case (i) designed and (ii) manufactured optical responses, in red and green respectively. In blue we the Dirac's delta case.



of 40 km):

$$BGND(\vec{x}) = \begin{cases} Poisson(3(10) \times 2.6 \text{ pe/GTU}) & \text{if } r \leq \|\vec{x} - \vec{x}_0\| \leq r \\ Poisson(2.6 \text{ pe/GTU}) & \text{any other case} \end{cases}$$

Within this circle we increased the nominal background 3 and 10 times. As we see in Fig. 6.8 the structure that we introduced appears as a distinct feature in the statistical tests. And again the differences between manufactured and designed optics is barely noticeable.

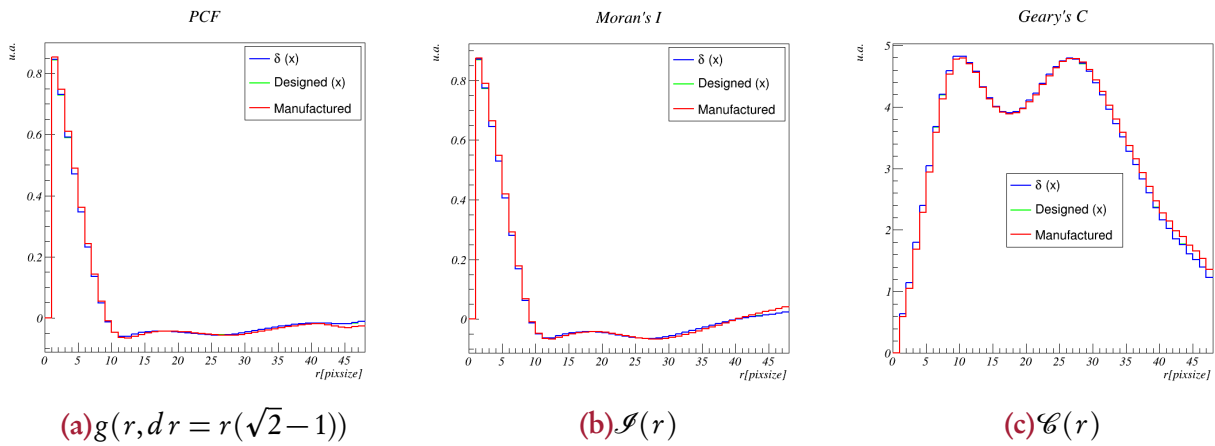


**Figure 6.8:** Comparison of  $g(r, dr = r(\sqrt{2}-1))$ ,  $\mathcal{I}(r)$  and  $\mathcal{C}(r)$  for a circle with 3 times higher background.

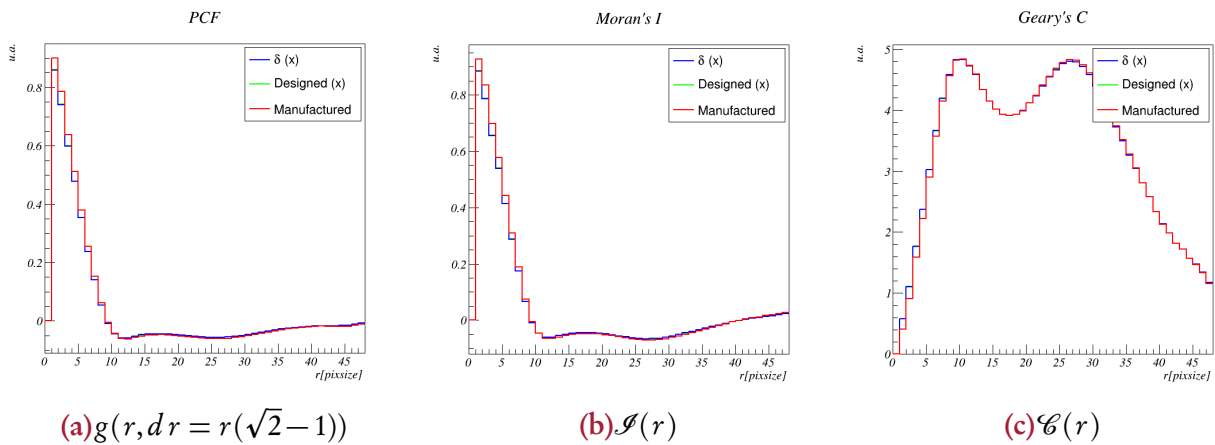


**Figure 6.9:** Comparison of  $g(r, dr = r(\sqrt{2}-1))$ ,  $\mathcal{I}(r)$  and  $\mathcal{C}(r)$  for a circle with 10 times higher background.

- **A heaviside function with 3 times higher value of the average background.** We introduced a step function satisfying:

$$BGND(x) = \begin{cases} Poisson(2.6 \text{ pe/GTU}) & \text{if } x < 0 \\ Poisson(3 \times 2.6 \text{ pe/GTU}) & \text{if } x \geq 0 \end{cases}$$

The idea this time is to simulate the passing of a larger structure in front of the FoV (a deck of clouds, an extended portion of the earth covered with snow, etc.). Again the statistical tests reveal this spatial component in the background (Fig. 6.10), but there is no distinct behavior between the different optics.

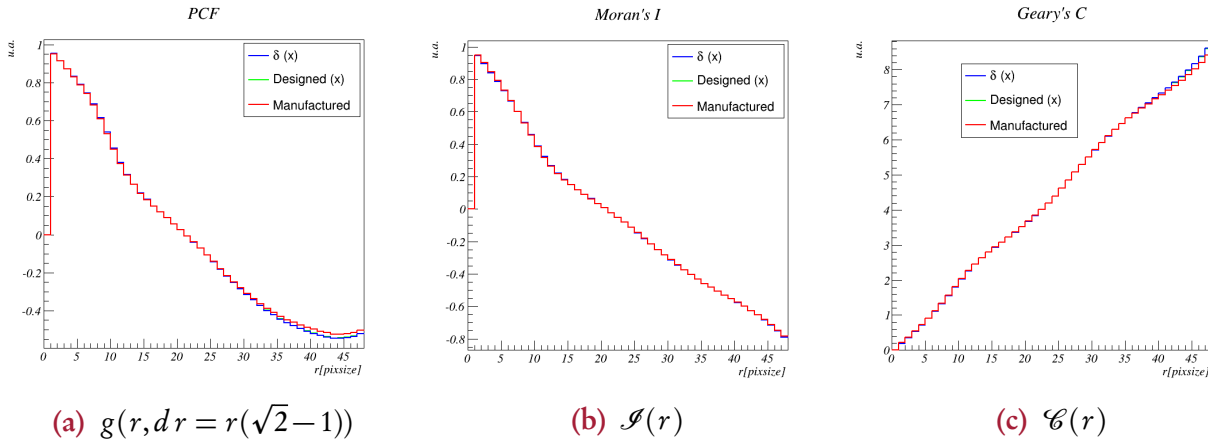


**Figure 6.10:** Comparison of  $g(r, dr = r(\sqrt{2}-1))$ ,  $\mathcal{I}(r)$  and  $\mathcal{C}(r)$  for a step function (in the X-axis) with 3 times higher background.

- **Circles with different sizes and an enhanced background.** Finally we have investigated the behavior of  $\mathcal{I}(r)$ ,  $\text{Pcf}(r)$ , and  $\mathcal{C}(r)$  by modifying the radius of the circle with a small background excess, i.e. within the circle the background is taken to be twice as intense. This is illustrated in Fig. 6.11.

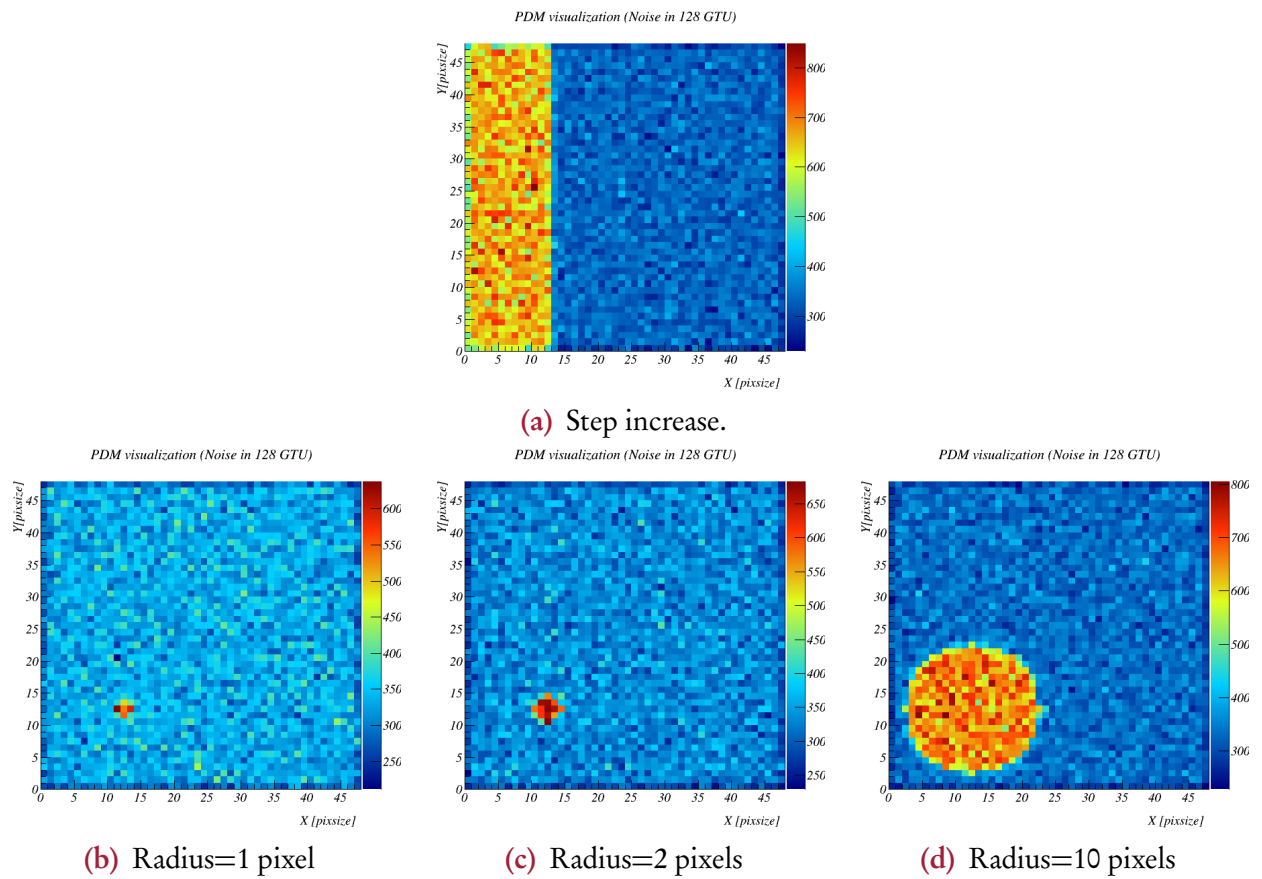
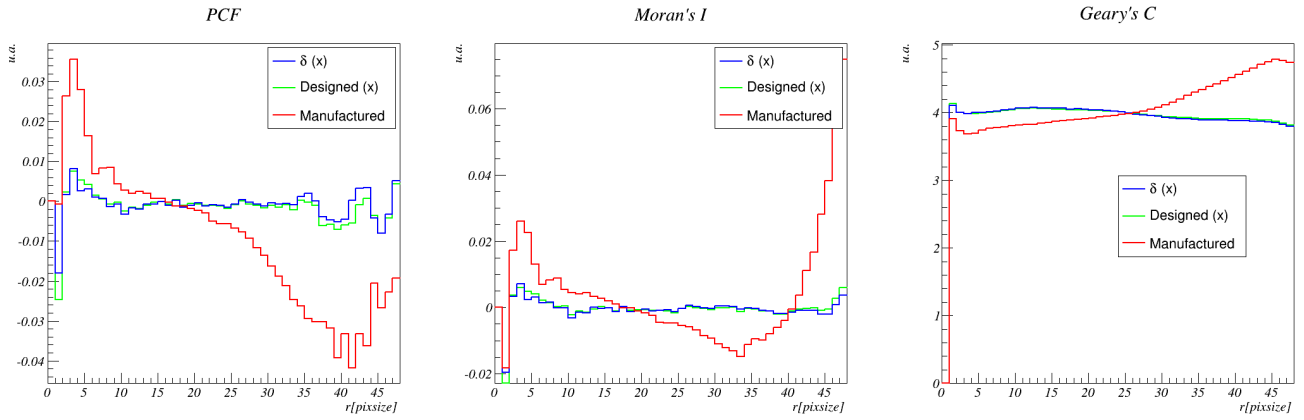
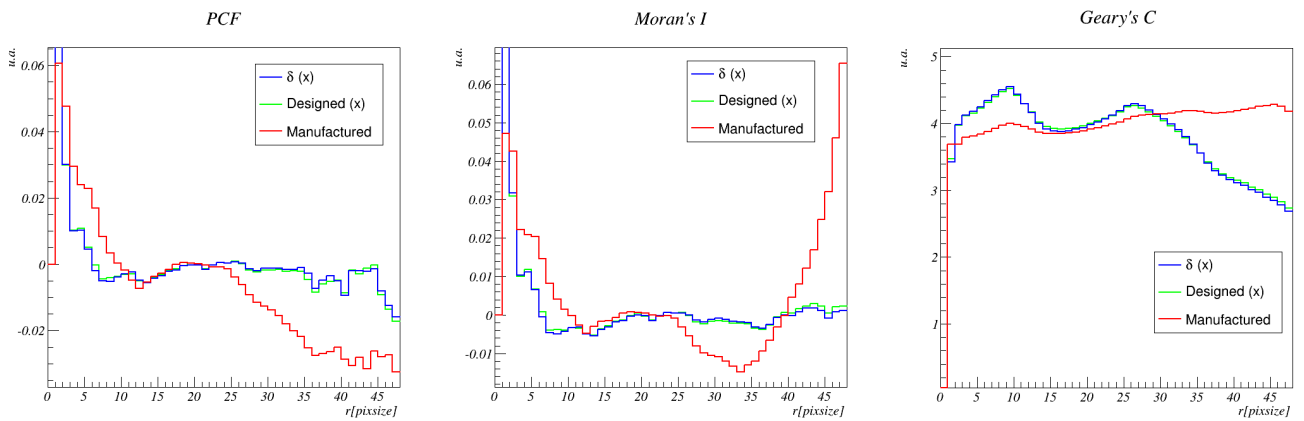


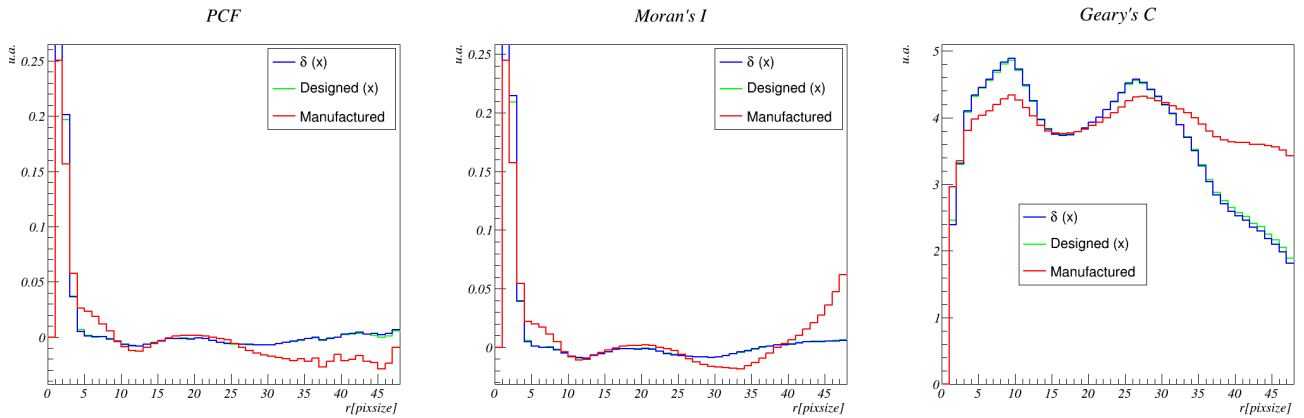
**Figure 6.11:** Test with special regions with twice the average background. (a) corresponds to a step function, whereas (b)(c)(d) radius with different circles.



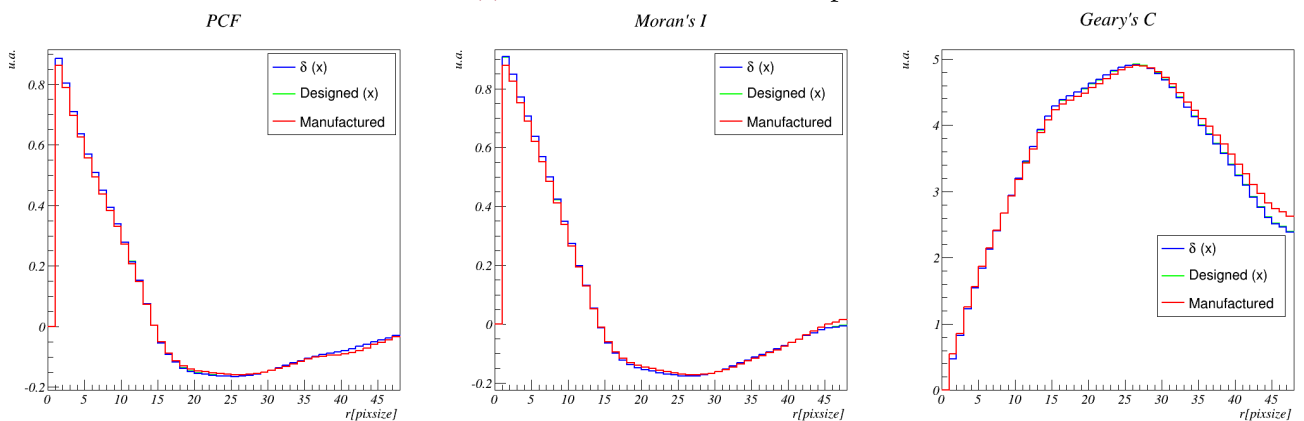
(a) Average background only.



(b) A circle with a radius of 1 pixel ( $SOG \approx .175$  m).



(c) A circle with a radius of 2 pixels.



(d) A circle with a radius of 10 pixels.

Figure 6.12: The impact of the different scenarios shown in Fig.6.11 on our statistical tests.

It is clear that in all conditions we are able to "perceive" a change in the underlying conditions in case there is a structured component in the background. Perhaps sometimes a simple look at the PDM image may suffice, for bright/dark enough spots. In the specific context of the EUSO-Balloon flight from Timmins Canada [Von Ballmoos et al. 2015], there are structured regions. Either man-made, like cities and mines, or natural ones like lakes, snow, etc. These regions will translate into a clear deviation from the expected behavior under the flat background conditions Fig. 6.13. Nevertheless, if there is a subtle but persistent perturbation of the background, we can detect it via these statistical tests.

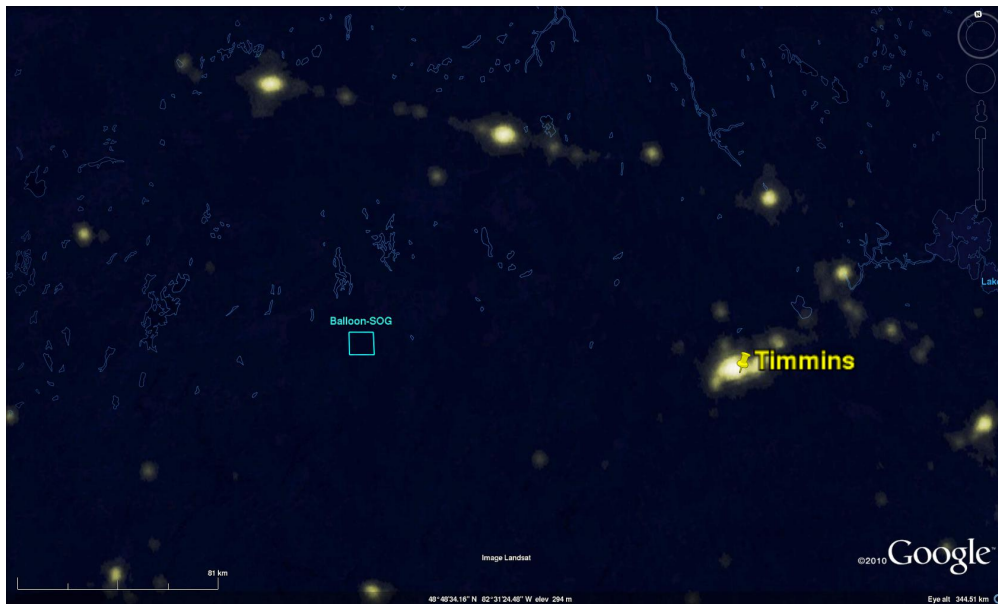


**Figure 6.13:** An aerial *night view* of the eastern area surrounding Timmins (taken from *Google-earth*). Barely visible are the outlines of mayor water bodies in the region. For comparison EUSO-Balloon's Spot-On-Ground (SOG) is drawn left to the center of the image.

The analysis presented here has shown that background observations of the 2014 EUSO-Balloon campaign fully maintain their value in spite of the missing lens. We are currently applying the analysis presented above to the data taken during the EUSO-Balloon campaign (Fig. 6.14). Once the calibration data will be produced and validated the results of our analysis will be released.

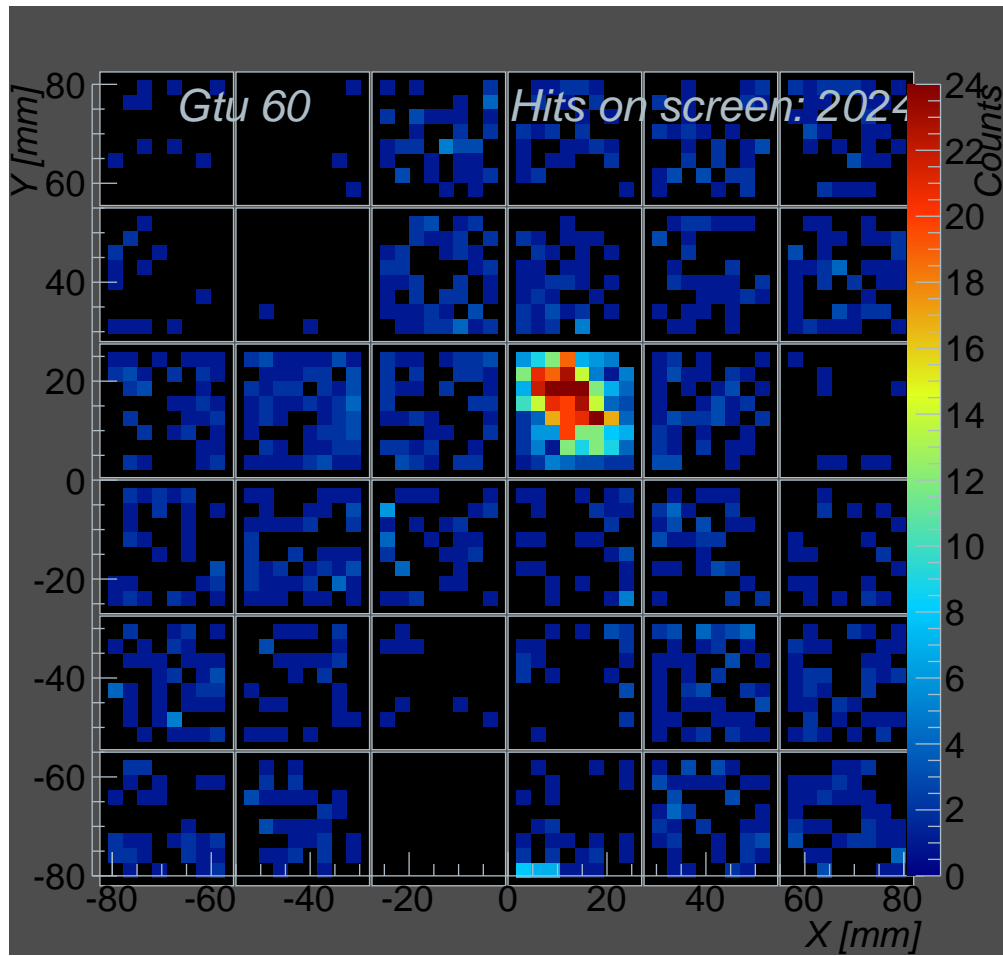


**Figure 6.14:** A snapshot of the image on the PDM of a laser shot captured by the EUSO-Balloon on August 24, 2014.

## SUMMARY & OUTLOOK

---

In this thesis we have presented a study, based on new techniques, developed to assess the performance of space-borne missions for the exploration of the Ultra High Energy Universe. We did focus on a specific example: the JEM-EUSO mission in its different configurations.

The first part of this work focused on the development of an innovative pattern recognition scheme within the ESAF simulation and analysis framework. This study resulted in the so-called *PWISE* and *PWISE-R* modules. As we demonstrated in § 4 and § 5, our pattern recognition technique has proven to be robust enough to produce solid results in different conditions of the event's incidence angle and energy. We highlight the fact that these techniques played a key-role in demonstrating that the science requirement for the angular resolution is satisfied by the current EUSO configuration.

In addition, these results were performed in “blind test” fashion, i.e. using automatic procedures applied to a large number of simulated events. Our exploration on the reconstruction of the incidence angle and energy of the events in the sample, as well as the application of “quality cuts” § 4.2.5 has provided the first decisive steps towards a robust analysis of the experimental data, allowing a better understanding of the experimental uncertainties and systematics. This can be translated into the improvement of the angular resolution for a given event depending on the specific features of the event. We must stress that the procedures for the developed “quality cuts” require no *a priori* knowledge of the nature of the event, nor do they require us to perform a fit and then refine it. Such a second iteration is foreseen, but even in the case where a first fitting is performed and then improved upon, our “quality cuts” will already impact the first iteration in a positive way. We wish also to observe that our study impacts on the optimization of the profile of the mission. As mentioned in the first chapter of this thesis, any EUSO-like mission will not collect the high events statistics of the sample studied in this work, due to the low flux in the energy interval where the mission is sensitive. This implies that on the real observed data, the analysis can and will be carried out on an event by event basis, and therefore our already robust analysis will be certainly improved. Great attention to the specifics of the status of the atmosphere and the detector will also play a major role in re-calibrating the signal seen by the detector and will point out to the most suitable set of parameters that should be used for the reconstruction.

The second main contribution of this work has been the development of tools to link the hybrid shower generator CONEX with the EUSO mission's software framework (ESAF). We stress that such a tool facilitates the use of different types of primaries and therefore different EAS profiles. The development of the specific CONEX-ESAF interface, allows studies which take into account fluctuations on the shower's development. In addition, the developed tools are available

as legacy code to other collaborators of the EUSO consortium who intend to perform other original studies. In addition, the use of an external EAS simulator allows the opportunity to re-use or share previously simulated EAS events. This reduces drastically the computing time involved in performing comparative simulations. The same set of simulated EAS can be in fact used for various detector configurations, allowing a comparison between different mission profiles, in view of maximizing the performance. As a first example of its usage, we simultaneously performed the angular and energy reconstruction of protons, iron nuclei and photons producing EAS. For the first time, we tested the techniques developed with a parametrized approach to the EAS, in a "more realistic" scenario. As expected deviations from the ideal case were observed and studied. Specifically for the energy reconstruction. However these deviations can be addressed systematics that can be corrected in the future. On the other hand, the angular reconstruction out-performed published results obtained with the previous version of the detector. This valuable result of the study is not due to the use of a hybrid EAS generator but, rather a result of the change of configuration, towards a circular optics.

In § 5 we concentrated ourselves in calculating the neutrino exposure with the key goal of estimating the sensitivity of JEM-EUSO to extremely energetic neutrinos. This is the first time such a study has been performed based on end-to-end simulations of the mission. This was only possible due to specific tools developed in this thesis. Nevertheless our work also relied upon existing state of the art dedicated software (CONEX, ROOT, PYTHIA, & ESAF). These software packages are used by the astroparticle and particle physics community at large. They are regularly tested, criticized, updated and improved by an increasing number of scientists. We hope our work will be a contribution, modest as it is, to the aforementioned scientific communities. However our results on the neutrino exposure are unprecedented

Actually, we regard our results as a conservative calculation of the overall exposure of the current JEM-EUSO configuration to neutrinos. We have shown that JEM-EUSO features a sensitivity for neutrino similar to current experimental limits. However our work have identified areas where future work can be undertaken to increase the exposure. For example, if we take into account up-going showers or make multi-peak search in the shower profile, we may increase the number of detectable events. Also nature plays a key role, if neutrino interaction cross sections at our energies of interest increase significantly, then JEM-EUSO would be capable of providing evidence for it.

Finally, in our thesis work, we prepared some statistical analysis that will provide a robust base for the analysis and interpretation of the background observed during the EUSO-Balloon 2014 campaign. We showed that the expected impact of the missing third lens is negligible from the point of view of the analysis. We are looking forward to apply these techniques to the validated data, once they will be available.

In the forthcoming years the EUSO's or JEM-EUSO's configuration will be finalized and the tests here presented will be further refined for the specifics of such configuration. Afterwards, once the mission is finally approved and flying, the analysis of the experimental data will be based upon this and similar works on the matter [Mernik 2014] [Fenu 2013]. We firmly believe that a EUSO like mission will be capable of opening the "particle channel" for astronomy. In addition, as in any novel scientific enterprise, there is always the potential of a serendipitous discovery, a true possibility when exploring the unknown.

---

*List of Key Publications*

During the writing of this thesis, I participated in the following scientific papers and conference proceedings as the primary author or one of the primary co-authors:

- ✱ “*Performances of JEM-EUSO: Angular Reconstruction*”, S. Biktemerova, **A. Guzmán**, T. Mernik, for the JEM-EUSO collaboration, *Experimental Astronomy*, (2014) (Erratum on July 2015).
- ✱ “*Ultra High Energy Photons and Neutrinos with JEM-EUSO.*”, **A. Guzmán**, G. Medina-Tanco, D. Supanitsky, for the JEM-EUSO collaboration *Experimental Astronomy*, (2013) (Erratum on July 2015).
- ✱ “*JEM-EUSO Observation in Cloudy conditions*”, **A. Guzmán**, G. Sáez-Cano, K. Shinozaki, for the JEM-EUSO collaboration. *Experimental Astronomy*, (2014).
- ✱ “*Performances and air-shower reconstruction techniques for the JEM-EUSO mission*”, M. Bertaina, P. Bobik, F. Fenu, **A. Guzmán**, T. Mernik, K. Shinozaki, *et al.* for the JEM-EUSO Collaboration, *Journal of Advances in Space Research*, (2014).
- ✱ “*The Peak and Window Searching Technique for the EUSO Simulation and Analysis Framework: Impact on the Angular Reconstruction of EAS*”, **A. Guzmán**, T. Mernik, A. Santangelo, G. Medina-Tanco, M. Bertaina, K. Shinozaki, F. Fenu, A. Gorgi, and JEM-EUSO Collaboration, *Journal of Physics Conference Series*, 409(1):012104, (2013).
- ✱ “*A study on JEM-EUSO’s trigger probability for neutrino-initiated EAS*”, **A. Guzmán**, A.D. Supanitsky, T. Mernik, F. Fenu, G. Medina-Tanco, A. Santangelo, and for the JEM-EUSO collaboration, 33<sup>rd</sup> International Cosmic Ray Conference, Rio de Janeiro, (2013).
- ✱ “*ESAF-Simulation of the EUSO-Balloon*”, T. Mernik, **A. Guzmán**, A. Santangelo, K. Shinozaki, N. Sakaki, C. Moretto, D. Monnier-Ragaigne, H. Miyamoto, S. Dagoret-Campagne, C. Catalano, P. Von Ballmoos, for the JEM-EUSO Collaboration, 33<sup>rd</sup> International Cosmic Ray Conference, Rio de Janeiro, (2013).
- ✱ “*Simulating the JEM-EUSO Mission: Expected Reconstruction Performance*” T. Mernik, **A. Guzmán**, F. Fenu K. Shinozaki, A. Santangelo, M. Bertaina, for the JEM-EUSO Collaboration, 33<sup>rd</sup> International Cosmic Ray Conference, Rio de Janeiro, (2013).
- ✱ “*Observation of neutrinos with JEM-EUSO: an updated view*”, E. Iwotschkin, A. Santangelo, **A. Guzmán**, T. Mernik, K. Shinozaki, J. Bayer, G. Medina-Tanco, A. V. Olinto, L. Wiencke, for the JEM-EUSO Collaboration, 34<sup>th</sup> International Cosmic Ray Conference, Den Haag, (2015).
- ✱ “*The Angular Resolution of the JEM-EUSO Mission: an updated view*” T. Mernik, **A. Guzmán**, A. Santangelo, K. Shinozaki, J. Bayer, E. Iwotschkin, M. Bertaina, F. Fenu, L. Wiencke, W. Painter, F. Sarazin, A. V. Olinto, G. Medina-Tanco for the JEM-EUSO Collaboration, 34<sup>th</sup> International Cosmic Ray Conference, Den Haag, (2015).
- ✱ “*The Expected Angular Resolution Performance of the Tilted JEM-EUSO Instrument*” T. Mernik, **A. Guzmán**, A. Santangelo, K. Shinozaki, J. Bayer, E. Iwotschkin, M. Bertaina, F. Fenu, for the JEM-EUSO Collaboration, 34<sup>th</sup> International Cosmic Ray Conference, Den Haag, (2015).

- ✱ “*The Angular Resolution of the JEM-EUSO Mission: an updated view*” T. Mernik, **A. Guzmán**, A. Santangelo, K. Shinozaki, J. Bayer, E. Iwotschkin, M. Bertaina, F. Fenu, L. Wiencke, W. Painter, F. Sarazin, A. V. Olinto, G. Medina-Tanco for the JEM-EUSO Collaboration, 34<sup>th</sup> International Cosmic Ray Conference, Den Haag, (2015).
- ✱ “*The simulation of cosmic rays in EUSO-Balloon: performances of the direction and energy reconstruction*” F. Fenu, M. Bertaina, **A. Guzmán**, K. Shinozaki, T. Mernik, J. Bayer, A. Santangelo, N. Sakaki, S. Bacholle, A. Jung, E. Parizot for the JEM-EUSO Collaboration, 34<sup>th</sup> International Cosmic Ray Conference, Den Haag, (2015).
- ✱ “*Evaluation of scientific performance of JEM-EUSO mission with Space-X Dragon option*” K. Shinozaki, A. Santangelo, J. Bayer, M. Bertaina, P. Bobík, M.J. Christl, P. Gorodetzky, **A. Guzmán**, E. Iwotschkin, G. Medina-Tanco, T. Mernik, A. Neronov, A.V. Olinto, B. Pastircák, M. Putiš, L. Wiencke, on behalf of the JEM-EUSO Collaboration, 34<sup>th</sup> International Cosmic Ray Conference, Den Haag, (2015).
- ✱ “*The JEM-EUSO energy and Xmax reconstruction performances*” F. Fenu, M. Bertaina, C. Vigorito, K. Shinozaki, **A. Guzmán**, T. Mernik, A. Santangelo, for the JEM-EUSO Collaboration, 34<sup>th</sup> International Cosmic Ray Conference, Den Haag, (2015).

### *Extended list of publications*

A more thorough list of scientific articles published during my PhD studies, in which I am listed as a co-author, follows:

1. P. Abreu, M. Aglietta, E. J. Ahn, I. F. M. Albuquerque, D. Allard, I. Allekotte, J. Allen, P. Allison, J. Alvarez Castillo, J. Alvarez-Muñiz, and et al. *Search for ultrahigh energy neutrinos in highly inclined events at the Pierre Auger Observatory*. Phys. Rev. D, 84(12):122005, December 2011.
2. Pierre Auger Collaboration, P. Abreu, M. Aglietta, E. J. Ahn, I. F. M. Albuquerque, D. Allard, I. Allekotte, J. Allen, P. Allison, J. Alvarez Castillo, and et al. *Anisotropy and chemical composition of ultra-high energy cosmic rays using arrival directions measured by the Pierre Auger Observatory*. J. Cosmology Astropart. Phys. , 6:22, June 2011.
3. Pierre Auger Collaboration, P. Abreu, M. Aglietta, E. J. Ahn, I. F. M. Albuquerque, D. Allard, I. Allekotte, J. Allen, P. Allison, J. Alvarez Castillo, and et al. *The effect of the geomagnetic field on cosmic ray energy estimates and large scale anisotropy searches on data from the Pierre Auger Observatory*. J. Cosmology Astropart. Phys. , 11:22, November 2011.
4. Pierre Auger Collaboration, P. Abreu, M. Aglietta, E. J. Ahn, I. F. M. Albuquerque, D. Allard, I. Allekotte, J. Allen, P. Allison, J. Alvarez Castillo, and et al. *The Lateral Trigger Probability function for the Ultra-High Energy Cosmic Ray showers detected by the Pierre Auger Observatory*. Astroparticle Physics, 35:266–276, December 2011. (Erratum on May 2012).
5. The Pierre Auger Collaboration, P. Abreu, M. Aglietta, E. J. Ahn, I. F. M. Albuquerque, D. Allard, I. Allekotte, J. Allen, P. Allison, J. Alvarez Castillo, and et al. *The Pierre Auger Observatory I: The Cosmic Ray Energy Spectrum and Related Measurements*. ArXiv e-prints, July 2011.

6. The Pierre Auger Collaboration, P. Abreu, M. Aglietta, E. J. Ahn, I. F. M. Albuquerque, D. Allard, I. Allekotte, J. Allen, P. Allison, J. Alvarez Castillo, and et al. *The Pierre Auger Observatory II: Studies of Cosmic Ray Composition and Hadronic Interaction models*. ArXiv e-prints, July 2011.
7. The Pierre Auger Collaboration, P. Abreu, M. Aglietta, E. J. Ahn, I. F. M. Albuquerque, D. Allard, I. Allekotte, J. Allen, P. Allison, J. Alvarez Castillo, and et al. *The Pierre Auger Observatory III: Other Astrophysical Observations*. ArXiv e-prints, July 2011.
8. The Pierre Auger Collaboration, P. Abreu, M. Aglietta, E. J. Ahn, I. F. M. Albuquerque, D. Allard, I. Allekotte, J. Allen, P. Allison, J. Alvarez Castillo, and et al. *The Pierre Auger Observatory IV: Operation and Monitoring*. ArXiv e-prints, July 2011.
9. P. Abreu, M. Aglietta, E. J. Ahn, I. F. M. Albuquerque, D. Allard, I. Allekotte, J. Allen, P. Allison, A. Almeda, J. Alvarez Castillo, and et al. *Measurement of the Proton-Air Cross Section at  $s=57\text{TeV}$  with the Pierre Auger Observatory*. Physical Review Letters, 109(6):062002, August 2012.
10. Pierre Auger Collaboration, P. Abreu, M. Aglietta, M. Ahlers, E. J. Ahn, I. F. M. Albuquerque, D. Allard, I. Allekotte, J. Allen, P. Allison, and et al. *A search for anisotropy in the arrival directions of ultra high energy cosmic rays recorded at the Pierre Auger Observatory*. J. Cosmology Astropart. Phys. , 4:40, April 2012.
11. Pierre Auger Collaboration, P. Abreu, M. Aglietta, M. Ahlers, E. J. Ahn, I. F. M. Albuquerque, D. Allard, I. Allekotte, J. Allen, P. Allison, and et al. *Description of atmospheric conditions at the Pierre Auger Observatory using the Global Data Assimilation System (GDAS)*. Astroparticle Physics, 35:591–607, April 2012.
12. Pierre Auger Collaboration, P. Abreu, M. Aglietta, E. J. Ahn, I. F. M. Albuquerque, D. Allard, I. Allekotte, J. Allen, P. Allison, J. Alvarez Castillo, and et al. *Search for signatures of magnetically-induced alignment in the arrival directions measured by the Pierre Auger Observatory*. Astroparticle Physics, 35:354–361, January 2012.
13. The JEM-EUSO Collaboration, :, J. H. Adams, Jr, S. Ahmad, J.-N. Albert, D. Allard, M. Ambrosio, L. Anchordoqui, A. Anzalone, Y. Arai, and et al. *The JEM-EUSO Mission: Status and Prospects in 2011*. ArXiv e-prints, April 2012.
14. J. H. Adams, S. Ahmad, J.-N. Albert, D. Allard, M. Ambrosio, L. Anchordoqui, A. Anzalone, Y. Arai, C. Aramo, K. Asano, and et al. *An evaluation of the exposure in nadir observation of the JEM-EUSO mission*. Astroparticle Physics, 44:76–90, April 2013.
15. M. Bertaina, P. Bobik, F. Fenu, F. Garino, A. Guzman, K. Higashide, G. Medina Tanco, T. Mernik, G. Saez Cano, A. Santangelo, and K. Shinozaki. *Performances of JEM-EUSO*. In European Physical Journal Web of Conferences, volume 53 of European Physical Journal Web of Conferences, page 9002, June 2013.
16. A. Guzman, T. Mernik, A. Santangelo, G. Medina-Tanco, M. Bertaina, K. Shinozaki, F. Fenu, A. Gorgi, and JEM-EUSO Collaboration. *The Peak and Window Searching Technique for the EUSO Simulation and Analysis Framework: Impact on the Angular Reconstruction of EAS*. Journal of Physics Conference Series, 409(1):012104, February 2013.
17. A. D. Supanitsky, G. Medina-Tanco, and A. Guzmán. *Ultra high energy photons and neutrinos with JEM-EUSO*. Experimental Astronomy, October 2013 (Erratum on July 2015).

18. M. Bertaina, S. Biktemerova, K. Bittermann, P. Bobik, D. Campana, F. Fenu, A. Gorgi, F. Guarino, A. Guzmán, K. Higashide, G. Medina-Tanco, T. Mernik, D. Naumov, M. Putis, M. D. Rodríguez Frías, G. Sáez Cano, A. Santangelo, K. Shinozaki, and S. Toscano. *Performance and air-shower reconstruction techniques for the JEM-EUSO mission*. *Advances in Space Research*, 53:1515–1535, May 2014.
19. S. Biktemerova, A. Guzman, and T. Mernik. *Performances of JEM-EUSO: angular reconstruction - The JEM-EUSO Collaboration*. *Experimental Astronomy*, February 2014 (Erratum on July 2015).
20. A. Guzmán, G. Sáez-Cano, and K. Shinozaki. *The JEM-EUSO observation in cloudy conditions*. *Experimental Astronomy*, July 2014.
21. J. H. Adams, S. Ahmad, J.-N. Albert, D. Allard, L. Anchordoqui, V. Andreev, A. Anzalone, Y. Arai, K. Asano, M. Ave Pernas, and et al. *Calibration aspects of the JEM-EUSO mission*. *Experimental Astronomy*, July 2015.
22. J. H. Adams, S. Ahmad, J.-N. Albert, D. Allard, L. Anchordoqui, V. Andreev, A. Anzalone, Y. Arai, K. Asano, M. Ave Pernas, and et al. *Performances of JEM-EUSO: energy and  $X_{max}$  reconstruction*. *Experimental Astronomy*, July 2015.
23. J. H. Adams, S. Ahmad, J.-N. Albert, D. Allard, L. Anchordoqui, V. Andreev, A. Anzalone, Y. Arai, K. Asano, M. Ave Pernas, and et al. *Science of atmospheric phenomena with JEM-EUSO*. *Experimental Astronomy*, July 2015.
24. J. H. Adams, S. Ahmad, J.-N. Albert, D. Allard, L. Anchordoqui, V. Andreev, A. Anzalone, Y. Arai, K. Asano, M. Ave Pernas, and et al. *The EUSO-Balloon pathfinder*. *Experimental Astronomy*, August 2015.

# BIBLIOGRAPHY

---

- [Aartsen et al. 2013] M. G. Aartsen et al.(IceCube Collaboration), *Probing the origin of cosmic rays with extremely high energy neutrinos using the IceCube Observatory*, Physical Review D 88, 112008 (2013).
- [Aartsen et al. 2014a] M. G. Aartsen et al.(IceCube Collaboration), *Observation of High-Energy Astrophysical Neutrinos in Three Years of IceCube Data*, Phys. Rev. Letters 113, 101101 (2014).
- [Aartsen et al. 2014b] Aartsen, M. et al. (IceCube Collaboration), *Search for a diffuse flux of astrophysical muon neutrinos with the IceCube 59-string configuration*, Phys. Rev. D 89, 062007 (2014).
- [Abbasi et al. 2014] Abbasi et al., the Telescope Array Consortium, *Indications Of Intermediate-Scale Anisotropy Of Cosmic Rays With Energy Greater Than 57 EeV In The Northern Sky Measured With The Surface Detector Of The Telescope Array Experiment* The Astrophysical Journal Letters, 790:L21 (5pp), (2014).
- [Abraham et al. 2008] J. Abraham, et al., Pierre Auger Collaboration, *Upper Limit on the Diffuse Flux of Ultrahigh Energy Tau Neutrinos from the Pierre Auger Observatory*, Phys. Rev. Lett. 100 211101 (2008).
- [Abraham et al. 2009] J. Abraham, et al., Pierre Auger Collaboration, *Limit on the diffuse flux of ultra-high energy tau neutrinos with the surface detector of the Pierre Auger Observatory*, Phys.Rev.D 79:102001, (2009).
- [Abraham, et al. 2010] Abraham, J. et al.(Pierre Auger Collaboration), *The Fluorescence Detector of the Pierre Auger Observatory*, Nucl.Instrum.Meth. A620 (2010).
- [Abreu et al. 2012] P. Abreu, et al., Pierre Auger Collaboration *Search for Point-Like Sources of Ultra-High Energy Neutrinos at the Pierre Auger Observatory and Improved Limit on the Diffuse Flux of Tau Neutrinos*, The Astrophysical Journal Letters, 755:L4 (2012).
- [Abu-Zayyad et al. 2012] T. Abu-Zayyad, et al., the Telescope Array Experiment *The surface detector array of the Telescope Array experiment* Nuclear Instruments and Methods in Physics Research Section A: Volume 689, Pages 87–97 (2012).
- [Ackermann et al. 2013] Ackermann et al., *Detection of the Characteristic Pion-Decay Signature in Supernova Remnants*, Science, 339, 807 (2013).
- [Adams et al. 2013a] Adams Jr., J.H. et al. (JEM-EUSO Collaboration), *An evaluation of the exposure in nadir observation of the JEM-EUSO mission*, Astroparticle Physics, 44 (2013).
- [Adams et al. 2013b] J.H. Adams, Jr., M.J. Christl, S.E. Csornac, F. Sarazin and L.R. Wiencke for the JEM-EUSO Collaboration, *“Ground Truth” calibration for the JEM-EUSO Mission* presented at the 2012 COSPAR Conference, submitted to Advances in Space Research Instrumentation and Methods for Astrophysics arXiv: 1302.5863[astro-ph.IM] (2013).
- [Adams et al. 2013c] J.H. Adams, Jr., R.M. Young, A. Olinto for the JEM-EUSO Collaboration, *JEM-EUSO Design for Accommodation on the SpaceX Dragon Spacecraft*, Proceedings of the International Cosmic Ray Conference 2013 Rio de Janeiro (2013).
- [Adams et al. 2015] James Adams for the JEM-EUOS collaboration, *The Calibration of EUSO Balloon using airborne light sources mounted to a Helicopter*, 34th Int. Cosmic Ray Conf. Proc. The Hague (2015).
- [Ahlers 2010] Ahlers, M., Anchordoqui, L. A, Gonzalez–Garcia, M. C. , Halzend, F., Sarkare, S., *GZK Neutrinos after the Fermi-LAT Diffuse Photon Flux Measurement*, Astroparticle Physics 34 (2010).
- [Ahmad et al. 2012] Salleh Ahmad, Pierre Barrillon, Sylvie Blin-Bondil, Sylvie Dagoret-Campagne, Christophe Dela Taille, Frederic Dulucq, Gisele Martin-Chassard, Yoshiya Kawasaki, Hiroko Miyamoto, Hirokazu Ikeda, Tatsunari Iguchi, Fumiyoshi Kajino, for the JEM-EUSO Collaboration, *SPACIROC: A Front-End Readout ASIC for JEM-EUSO Cosmic Ray Observatory*, Physics Procedia, Volume 37, p 1600–1607 (2012).
- [Alvarez & Compton 1933] Alvarez, Luis; Arthur H. Compton, *A positively charged component of cosmic rays*, Physical Review 43 (1933).
- [Anchordoqui et al. 2013] Luis A. Anchordoqui, Haim Goldberg, Morgan H. Lynch, Angela V. Olinto, Thomas C. Paul, Thomas J. Weiler, *Pinning down the cosmic ray source mechanism with new IceCube data*, <http://arxiv.org/abs/1306.5021> (2013).

- [Anchordoqui et al. 2002] Luis A. Anchordoqui, Jonathan L. Feng, Haim Goldberg, Alfred D. Shapere, *Neutrino Bounds on Astrophysical Sources and New Physics*, Phys.Rev.D66:103002, (2002).
- [Anderson 1933] Anderson, C.D. *The Positive Electron*, Phys. Rev. (1933) 43-49, (1933).
- [Anderson & Neddermeyer 1937] C.D. Anderson, S.H. Neddermeyer, *Note on the Nature of Cosmic-Ray Particles* Phys. Rev. 51 (1937).
- [Ando et al. 2013] Ando, S et al. *Colloquium: Multimessenger astronomy with gravitational waves and high-energy neutrinos*, Rev. Mod. Phys., Vol. 85, No. 4, October–December (2013).
- [Angelis 2010] de Angelis, A., *Domenico Pacini, uncredited pioneer of the discovery of cosmic rays*, Rivista del Nuovo Cimento33:713, (2010).
- [Angelis 2014] de Angelis, A., *Atmospheric ionization and cosmic rays: studies and measurements before 1912*, Astroparticle Physics Volume 53 (2014).
- [Asahi Glass Co, Ltd.] Asahi Glass Co, Ltd. Company Website <http://www.agc.com/kagaku/shinsei/cytop/en/>. Accessed January 12<sup>th</sup> 2015.
- [Auger 1939] Auger, P. , et al., *Extensive Cosmic-Ray Showers* Rev. Mod. Phys. 11, 288 (1939).
- [Ave et al. 2005] Ave, M. , Busca , N. , Olinto, A. ,Watson , A.A. , Yamamoto , T., *Cosmogenic neutrinos from ultra-high energy nuclei*, Astroparticle Physics 23 19-29 (2005).
- [Baltrusaitis et al. 1985] R.M. Baltrusaitis, R. Cady, G.L. Cassiday, R. Cooperv, J.W. Elbert, P.R. Gerhardy, S. Ko, E.C. Loh, M. Salamon, D Steck, P. Sokolsky, *The Utah Fly's Eye detector*, Nuclear Instruments and Methods in Physics Research Section A, Volume 240, Issue 2 (1985).
- [Bayer et al. 2011] J. Bayer, M. Bertaina, G. Distratis, F. Fenu, A. Santangelo, T. Schanz, C. Tenzer, for the JEM-EUSO Collaboration, *The Cluster Control Board of the JEM-EUSO mission*, Proceedings of the 32<sup>nd</sup> International Cosmic Ray Conference, Beijing (2011).
- [Bayer et al. 2013] J. Bayer, G. Distratis, D. Gotschall, A. Santangelo, C. Tenzer, M. Bertaina, M. Casolino, G. Osteria, for the JEM-EUSO Collaboration, *Second level trigger and Cluster Control Board for the JEM-EUSO mission*, Proceedings of the 33<sup>rd</sup> International Cosmic Ray Conference, Rio de Janeiro, Brazil, (2013).
- [Becquerel 1896] Becquerel, H., *Sur les radiations émises par phosphorescence (On the radiation emitted by phosphorescence)*, Comptes Rendus de l'Acad. des Sciences 122 420-421 (1896). Accessed via <http://gallica.bnf.fr/ark:/12148/bpt6k30780/f422.chemindefer> on 03/07/2014.,
- [Benson & Linsley 1981 ] Benson, R. and Linsley, J., *Satellite observation of cosmic ray air showers*, International Cosmic Ray Conference, 17th, Paris, France, July 13–25, Conference Papers. Volume 8 (1981).
- [Berat et al. 2010] C. Berat, S. Bottai, D. De Marco, S. Moreggia, D. Naumov, M. Pallavicini, R. Pesce, A. Petrolini, A. Stutz, E. Taddei, A. Thea, *Full Simulation of Space-Based Extensive Air Showers Detectors with ESAF*, Astroparticle Physics Volume 33, Issue 4, (2010).
- [Bergmann 2007] T. Bergmann, R. Engel, D. Heck, N. N. Kalmykov, S. Ostapchenko, T. Pierog, T. Thouw, K. Werner, *One-dimensional hybrid approach to extensive air shower simulation*, Astropart. Phys. Vol. 26, pp 420-432, astro-ph/0606564, (2007).
- [Bertaina et al. 2014] Bertaina, M.; Biktemerova, S.; Bittermann, K.; Bobik, P.; Campana, D.; Fenu, F.; Gorgi, A.; Guarino, F.; Guzmán, A.; Higashide, K.; Medina-Tanco, G.; Mernik, T.; Naumov, D.; Putis, M.; Rodríguez Frías, M. D.; Sáez Cano, G.; Santangelo, A.; Shinozaki, K.; Toscano, S., *Performance and air-shower reconstruction techniques for the JEM-EUSO mission*, Advances in Space Research, Volume 53, Issue 10, p. 1515-1535 (2014).
- [Bethermin 2011] Bethermin, M., *Counting the infrared galaxies, telling their story : statistical properties of the infrared galaxies at high redshift and origin of the cosmic infrared background*, PhD Thesis, Université Paris Sud - Paris XI. <https://tel.archives-ouvertes.fr/tel-00665256> (2011).
- [Bird et al. 1994] Bird, D.J., *The cosmic-ray energy spectrum observed by the Fly's Eye Experiment*, The Astrophysical Journal, 424:491-502 (1994).

- [Bird et al. 1995] Bird, D. J., Corbato, S. C., Dai, H. Y., Elbert, J. W., Green, K. D., Huang, M. A., Kieda, D. B., Ko, S. Larsen, C. G., Loh, E. C., Luo, M. Z., Salamon, M. H., Smith, J. D., Sokolsky, P., Sommers, P., Tang, J. K. K., Thomas, S. B., *Detection of a cosmic ray with measured energy well beyond the expected spectral cutoff due to cosmic microwave radiation*, *Astrophysical Journal*, Part 1 (ISSN 0004-637X), vol. 441, no. 1, p. 144-150 (1995).
- [Blandford & Ostriker 1978] R. D. Blandford, J. P. Ostriker, *Particle acceleration by astrophysical shocks*, *The Astrophysical Journal* 221, L29-L32 (1978).
- [Blümer et al. 2009] Blümer J., Engel R., Hörandel J., *Cosmic rays from the knee to the highest energies*, *Progress in Particle and Nuclear Physics* 63 293-338 (2009).
- [Blümer, Engel & Hörandel 2009] J. Blümer, R. Engel and J.R. Hörandel, *Cosmic rays from the knee to the highest energies*, *Prog. Part. Nucl. Phys.* 63 (2009).
- [Bonifazi 2009] C. Bonifazi, for the Pierre Auger Collaboration, *The angular resolution of the Pierre Auger Observatory*, *Nuclear Physics B (Proc. Suppl.)* 190 (2009).
- [Brueckner & Thieberg 1960] Brueckner, Keith A. and Thieberger, Reuben, *Nuclear Giant Dipole Resonance*, *Phys. Rev. Lett.* 4, 466 - Published 1 May (1960).
- [Bunner 1967] A.N. Bunner, *Cosmic Ray Detection by Atmospheric Fluorescence* PhD Tesis, Cornell University, Ithaca, NY, USA, (1967).
- [Caprioli & Spitkovsky 2014a] Caprioli, D., Spitkovsky, A., *Simulations of Ion Acceleration at Non-relativistic Shocks. I. Acceleration Efficiency*, *Astrophysical Journal*, 783, 91, (2014).
- [Caprioli & Spitkovsky 2014b] Caprioli, D., Spitkovsky, A., *Simulations of Ion Acceleration at Non-relativistic Shocks. II. Magnetic Field Amplification*, *Astrophysical Journal*, 794, 46, (2014).
- [Caprioli & Spitkovsky 2014c] Caprioli, D., Spitkovsky, A., *Simulations of Ion Acceleration at Non-relativistic Shocks. III. Particle Diffusion*, *Astrophysical Journal*, 794, 47, (2014).
- [Casolino 2013] M. Casolino, *Revised configuration of the JEM-EUSO instrument*, Presentation given at the JEM-EUSO's International Collaboration Meeting, June 2013.
- [Chadwick 1914] Chadwick, James, *Intensitätsverteilung im magnetischen Spektrum von  $\beta$ -Strahlen von Radium B+C*, *Verhandlungen der Deutschen Physikalischen Gesellschaft* 16: 383-391, (1914).
- [Clay 1927] Clay, J., *Penetrating radiation*, *Acad. Amsterdam Proc.* 30 1115-1127 (1927).
- [Clay 1932] Clay, J., *The Earth-magnetic effect and the corpuscular nature of (cosmic) ultraradiation*, *Proc. roy. Acad. Amsterdam*, 35, p. 1282 (1932).
- [Coulomb 1785] de Coulomb, C., *Troisième mémoire sur l'électricité et le magnétisme*, *Histoire de l'Académie Royale des Sciences*, pages 612-638, (1785).
- [Cowan & Reines 1956] Frederick Reines and Clyde L. Cowan, Jr., *The Neutrino* *Nature* 178, 446 (1956).
- [Curie 1898] Curie, P., Curie, M., and Gustave Bémont *Sur une nouvelle substance fortement radio-active, contenue dans la pechblende (On a new, strongly radioactive substance contained in pitchblende)*, *Comptes Rendus de l'Acad. des Sciences* 127, 1215- 1217 (1898).
- [Dagoret & Mot 2014] S. Dagoret, B. Mot, *BALLOON ASSEMBLY, INTEGRATION AND TESTS PLAN VERSION 2 (JUNE 2014) EUSO-AI-INST-251-LAL\_V2.8*. Accessed via EUSO-Balloon Website, <http://euso-balloon.1a1.in2p3.fr/>. Accessed Februar 2015.
- [Dragon] Space Exploration Technologies Corporation, official website <http://www.spacex.com/dragon>. Accessed February 18<sup>th</sup> 2015.
- [Engel et al. 2001] Engel, R. Seckel, D. & Stanev, T., *Neutrinos from propagation of ultrahigh energy protons*, *Phys. Rev. D*, Vol. 64, 093010 (2001).
- [EUSO-Balloon 2013] P. von Ballmoos, S. Dagoret, A. Santangelo, J.H. Adams, P. Barrillon, J. Bayer, M. Bertaina, F. Cafagna, M. Casolino, G. Distratis, M. Dupieux, A. Ebersoldt, T. Ebisuzaki, Ph. Gorodetzky, A. Haungs, A. Jung, Y. Kawasaki, G. Medina-Tanco, B. Mot, G. Osteria, E. Parizot, I.H. Park, P. Picozza, G. Prévôt, H. Prieto, M. Ricci, M.D. Rodríguez Frías, G. Roudil, V. Scotti, J. Szabelski, Y. Takizawa and K. Tsuno, *EUSO-BALLOON a pathfinder for detecting UHECR's from the edge of space*, *EPJ Web of Conferences* 53, 09003 (2013).

- [EUSO-Balloon 2015] The JEM-EUSO Collaboration, *EUSO-Balloon A pathfinder mission for JEM-EUSO*, EUSO-Balloon Website, <http://euso-balloon.la1.in2p3.fr/>. Accessed Februar 2015.
- [Facal San Luis 2013] Facal San Luis, P. For The Pierre Auger Collaboration, *The Distribution Of Shower Maxima Of UHECR Air Showers*, Proceedings of the 32<sup>nd</sup> International Cosmic Ray Conference , Beijing (2011).
- [Feldman & Cousins 1998] Gary J. Feldman and Robert D. Cousins, *A Unified Approach to the Classical Statistical Analysis of Small Signals*, Physical Reviews D57:3873-3889, (1998).
- [Fenu 2013] Fenu, F. *A Simulation Study of the JEM-EUSO Mission for the Detection of Ultra-High Energy Cosmic Rays* PhD Thesis, Eberhard Karls Universität Tübingen. Accessed via <https://publikationen.uni-tuebingen.de/xmlui/handle/10900/49955> (2013).
- [Fermi 1949] E. Fermi, *On the origin of cosmic radiation*, Phys. Rev. Vol 75, Numb 8 (1949).
- [Fermi 1934] Fermi, E., *Versuch einer Theorie der beta-Strahlen*, I. Zeitschrift für Physik 88: 161 (1934).
- [Gaisser 1997] Gaisser, T.K., *Neutrino astronomy: Physics goals, detector parameters*, OECD Megascience Forum, Taormina, Italy (1997). [arXiv:astro-ph/9707283](https://arxiv.org/abs/astro-ph/9707283)
- [Gandhi et al. 1996] Gandhi R, Quigg C., Reno M.H., *Ultrahigh-Energy Neutrino Interactions*, Astropart.Phys.5:81-110, (1996).
- [Gandhi et al. 1998] Raj Gandhi, Chris Quigg, Mary Hall Reno, and Ina Sarcevic *Neutrino interactions at ultrahigh energies* Phys. Rev. D 58, 093009 (1998).
- [Geant4 Collaboration 2003] S. Agostinelli, J. Allison, K. Amako, J. Apostolakis, H. Araujo, P. Arce, M. Asai, D. Axen, S. Banerjee, G. Barrand, F. Behner, L. Bellagamba, J. Boudreau, L. Broglia, A. Brunengo, H. Burkhardt, S. Chauvie, J. Chuma, R. Chytrcek, G. Cooperman, G. Cosmo, P. Degtyarenko, A. Dell'Acqua, G. Depaola, D. Dietrich, R. Enami, A. Feliciello, C. Ferguson, H. Fesefeldt, G. Folger, F. Foppiano, A. Forti, S. Garelli, S. Giani, R. Giannitrapani, D. Gibin, J.J. Gómez Cadenas, I. González, G. Gracia Abril, G. Greeniaus, W. Greiner, V. Grichine, A. Grossheim, S. Guatelli, P. Gumplinger, R. Hamatsu, K. Hashimoto, H. Hasui, A. Heikkinen, A. Howard, V. Ivanchenko, A. Johnson, F.W. Jones, J. Kallenbach, N. Kanaya, M. Kawabata, Y. Kawabata, M. Kawaguti, S. Kelner, P. Kent, A. Kimura, T. Kodama, R. Kokoulin, M. Kossov, H. Kurashige, E. Lamanna, T. Lampén, V. Lara, V. Lefebvre, F. Lei, M. Liendl, W. Lockman, F. Longo, S. Magni, M. Maire, E. Medernach, K. Minamimoto, P. Mora de Freitas, Y. Morita, K. Murakami, M. Nagamatu, R. Nartallo, P. Nieminen, T. Nishimura, K. Ohtsubo, M. Okamura, S. O'Neale, Y. Oohata, K. Paech, J. Perl, A. Pfeiffer, M.G. Pia, F. Ranjard, A. Rybin, S. Sadilov, E. Di Salvo, G. Santin, T. Sasaki, N. Savvas, Y. Sawada, S. Scherer, S. Sei, V. Sirotenko, D. Smith, N. Starkov, H. Stoecker, J. Sulkimo, M. Takahata, S. Tanaka, E. Tcherniaev, E. Safai Tehrani, M. Tropeano, P. Truscott, H. Uno, L. Urban, P. Urban, M. Verderi, A. Walkden, W. Wander, H. Weber, J.P. Wellisch, T. Wenaus, D.C. Williams, D. Wright, T. Yamada, H. Yoshida, D. Zschesche, the Geant4 Collaboration, *Geant4—a simulation toolkit*, Nuclear Instruments and Methods in Physics Research Section A: Accelerators, Spectrometers, Detectors and Associated Equipment, Volume 506, Issue 3, (2003).
- [Geary 1954] R. C. Geary, *The Contiguity Ratio and Statistical Mapping*, The Incorporated Statistician Vol. 5, No. 3, pp. 115-127+129-146 (1954).
- [Greisen 1966] Greisen, K., *End to the Cosmic-ray Spectrum?*, Physical Review Letters Vol. 16 Number 17 (1966).
- [Guzmán 2009] Guzmán Cabrera, Alejandro Daniel, *Mapeo de Objetos Extragalácticos sobre la superficie terrestre*, Tesis de licenciatura, Universidad Nacional Autónoma de México, Facultad de Física, (2009).
- [Guzmán, Mernik et al. 2014] A. Guzmán, T. Mernik, S. Biktemerova, for the JEM-EUSO Collaboration, *Performances of JEM-EUSO: angular reconstruction*, Experimental Astronomy, doi : 10.1007/s10686-013-9371-0, (2014).
- [Halzen & Gaisser 2014] Francis Halzen and Thomas K. Gaisser, *IceCube*, Annual Review of Nuclear and Particle Science, 64 101-123 (2014).
- [Han 2001] Han, Jin Lin, *Magnetic fields in our Galaxy: How much do we know? (II) Halo fields and the global field structure* AIP Conf.Proc.609:96-101,(2002).
- [Herschel 1800] Herschel, William *Experiments on the Refrangibility of the Invisible Rays of the Sun*, LL. D. F. R. S Philosophical Transactions of the Royal Society of London . 1800-01-01. 90:284–292 (1800).

- [Hess 1912 ] Hess, V.F. *Über Beobachtungen der durchdringenden Strahlung bei sieben Freiballonfahrten*, Phys. Z., 13, p. 10840 (1912).
- [ H.E.S.S 2014 ] H.E.S.S. Collaboration, *Diffuse Galactic gamma-ray emission with H.E.S.S.*, Accepted for publication at Physical Review D. arXiv: 1411. 7568 (2014).
- [Hillas 1982] Hillas, A. M., *Angular and energy distributions of charged particles in electron-photon cascades in air*, Journal of Physics G: Nuclear Physics Volume 8 Number 10p.1461 (1982).
- [Hillas 1984] A. M. Hillas, *The Origin of Ultra-High-Energy Cosmic Rays*, Ann. Rev. Astron. Astrophys. 22, 425 (1984).
- [HiRes 2011] Sokolsky P. for the HiRes Collaboration. *Final Results from the High resolution Fly's Eye (HiRes)*, Experiment Nuclear Physics B (Proc. Suppl.) 212–213 (2011) 74–78.
- [Hoffmann 2014] Hoffmann, F., *Werner Kolhörster (1887–1945): The German pioneer of cosmic ray physics*, Astroparticle Physics 53 (2014).
- [Homola et al. 2005] P. Homola, et al., *Simulation of ultra-high energy photon propagation in the geomagnetic field*, Computer Physics Communications Volume 173, Issues 1-2, Pages 71-90 (2005).
- [IceCube 2015] Aartsen, et al. The IceCube collaboration, *Atmospheric and Astrophysical Neutrinos above 1 TeV Interacting in IceCube*, Phys. Rev. D 91, 022001 (2015).
- [IceCube-Gen2] IceCube-Gen2 Collaboration, *IceCube-Gen2: A Vision for the Future of Neutrino Astronomy in Antarctica*, arXiv:1412.5106
- [Ikeda et al. 2013] Ikeda, D. et al. for the Telescope Array Collaboration, *Hybrid analysis for the Telescope Array*, EPJ Web of Conferences 53, 04006 (2013).
- [Ilina et al. 1992] Ilina, N. P., Kalmykov, N. N. and Prosin, V. V., *Cerenkov radiation and parameters of extensive air showers*, Sov. J. Nucl. Phys., vol. 55, p. 1540-1547 (1992).
- [Immerkaer 1998] Immerkaer, J., *Some remarks on the straight line Hough transform*, Pattern Recognition Letters 19 (1998).
- [JAXA] Japanese Space Agency official Website, <http://global.jaxa.jp/projects/rockets/htv/> Accessed February 18<sup>th</sup> 2015.
- [Jansso & Farrar 2012] Jansson, R. , Farrar, G. R., *A New Model of the Galactic Magnetic Field*, The Astrophysical Journal Volume 757 Number 14 (2012).
- [JEM-EUSO 2010] The JEM-EUSO Collaboration, *Report on the Phase-A Study*, (Purple Book). 2010
- [Johnson 1933] Johnson, Thomas H., *The azimuthal asymmetry of the cosmic radiation*, Physical Review 43 (1933).
- [Katz & Spiering 2012] Katz, U. & Spiering, C. *High-Energy Neutrino Astrophysics: Status and Perspectives*, Prog. Part. Nucl. Phys. 67 651, (2012).
- [Kawasaki et al. 2011] Kawasaki, Y., Casolino, M., Gorodetzky, P., Santangelo, A., Ricci, M., Kajino, F., Ebisuzaki, T., and the JEM-EUSO collaboration, *The focal surface of the JEM-EUSO instrument*, Astrophys. Space Sci. Trans., 7, 167-169, (2011).
- [Khrenov et al. 2001] Khrenov B.A. , Panasyuk M.I. , Alexandrov V.V. , Bugrov D.I. , Cordero A. , Garipov G.K. , Linsley J. , Martinez O. , Salazar H., Saprykin O.A., Silaev A.A., Surogatov D.V, Syromyatnikov V.S. , Villaseñor L. and Zepeda A., *Space Program KOSMOTEPETL (project KLYPVE and TUS) for the study of extremely high energy cosmic rays*, AIP Conference Proceedings, Volume 566, pp. 57–75 (2001).
- [Khrenov et al. 2004] B. A. Khrenov, V. V. Alexandrov, D. I. Bugrov, G. K. Garipov, N. N. Kalmykov, M. I. Panasyuk, S. A. Sharakin, A. A. Silaev, I. V. Yashin, V. M. Grebenyuk, D. V. Naumov, A. G. Olshevsky, B. M. Sabirov, R. N. Semenov, M. Slunechka, I. I. Skryl, L. G. Tkatchev, O. A. Saprykin, V. S. Syromyatnikov, V. E. Bitkin, S. A. Eremin, A. I. Matyushkin, F. F. Urmantsev, V. Abrashin, V. Koval, Y. Arakcheev, A. Cordero, O. Martinez, E. Morena, C. Robledo, H. Salazar, L. Villaseñor, A. Zepeda, I. Park, M. Shonsky, J. Zicha, *KLYPVE/TUS space experiments for study of ultrahigh-energy cosmic rays*, Physics of Atomic Nuclei November 2004, Volume 67, Issue 11, pp 2058-206 (2004).

- [Kotera et al. 2010] Kotera, K., Allard, D. & Olinto, A. V., *Cosmogenic neutrinos: parameter space and detectability from PeV to ZeV*, Journal of Cosmology and Astroparticle Physics Volume 2010 (2010).
- [Kotera & Olinto 2011] K. Kotera and A. V. Olinto., *The Astrophysics of Ultrahigh-Energy Cosmic Rays*, ARA&A 49, pp. 119-153 (2011).
- [Kusenko et al. 2002] Kusenko A, Weiler T J, *Neutrino Cross Sections and Future Observations of Ultrahigh-Energy Cosmic Rays*, Phys. Rev. Lett. 88 161101 (2002).
- [Lai et al. 2010] Hung-Liang Lai, Marco Guzzi, Joey Huston, Zhao Li, Pavel M. Nadolsky, Jon Pumplin, C.-P. Yuan, *New parton distributions for collider physics*, Phys.Rev.D82:074024, DOI: 10.1103/PhysRevD.82.074024 (2010).
- [Landau & Pomeranchuk 1953] L.D. Landau and I.Ya. Pomeranchuk, Dokl. Akad. Nauk SSSR 92 535, 735 (1953).
- [Lattes 1947] C.M.G. Lattes, H. Muirhead, G.P.S. Occhialini, C.F. Powell, *Processes involving charged mesons*, Nature 159 (4047) 694–69 (1947).
- [Letessier & Stanev 2011] Antoine Letessier-Selvon, Todor Stanev, *Ultrahigh Energy Cosmic Rays*, Rev. Mod. Phys, 83, 907-942 (2011).
- [Linsley 1963] J. Linsley, *Evidence for a primary cosmic-ray particle with energy  $10^{20}$  eV*, Phys. Rev. Lett. 10, 146–148 (1963).
- [LOWTRAN7 1986] F.X. Kneizys, E.P. Shettle, L.W. Abreu, J.H. Chetwynd, G.P. Anderson, W.O. Gallery, J.E.A. Selby, S.A. Clough, *Users guide to LOWTRAN 7*, Air Force Geophysics Laboratory, Public released document (1986). Retrieved from [www.dtic.mil/dtic/tr/fulltext/u2/a206773.pdf](http://www.dtic.mil/dtic/tr/fulltext/u2/a206773.pdf).
- [Manheim, Protheroe & Rachen 2001] Mannheim, K., Protheroe, R. J., Rachen, J. P., *On the cosmic ray bound for models of extragalactic neutrino production*, Physics Review D 63 023003, (2001).
- [Matthews et al. 2010] Matthews J. A. J., Mesler R., Becker B. R., Gold M. S. and Hague J. D., *A parameterization of cosmic ray shower profiles based on shower width*, Journal of Physics G: Nuclear and Particle Physics Volume 37 Number 2 (2010)
- [Mason et al. 1977] Mason, G. W., Bergeson, H. E., Cassiday, G. L., Chiu, T. W., Cooper, D. A., Elbert, J. W., *Observations of Extensive Air Showers by Air Fluorescence Description of Experimental Techniques*, Proceedings of the 15<sup>th</sup> International Cosmic Ray Conference (Budapest), Vol 8 (1977).
- [Medina-Tanco 2005] Medina-Tanco, G., *Ultra-high energy cosmic rays: from GeV to ZeV*, Proceedings of the Mexican School on Astrophysics arXiv:astro-ph/0607543 (2005).
- [Medina-Tanco, et al. 2009] Medina-Tanco, et al. for the JEM-EUSO collaboration, *JEM-EUSO Science Objectives*. 31st Int. Cosmic Ray Conf. Proc. Łódź (2009)
- [Mernik 2014] T. Mernik, *The Expected Angular Resolution of the JEM-EUSO Mission* PhD Thesis, Eberhard Karls Universität Tübingen. Accessed via <https://publikationen.uni-tuebingen.de/xmlui/handle/10900/58443> (2014).
- [Migdal 1956] Migdal, A. B. *Bremsstrahlung and Pair Production in Condensed Media at High Energies*, Physical Review Volume 103 Issue 6 p. 1811 (1956).
- [Millikan 1925] Robert Andrews Millikan, *High Frequency Rays of Cosmic Origin*, Nature 116, 823–825 (1925).
- [Mini-EUSO 2015] The JEM-EUSO Collaboration. Mini EUSO. Italian Collaboration Website, [http://jem-euso.roma2.infn.it/?page\\_id=818](http://jem-euso.roma2.infn.it/?page_id=818) Accessed February 17<sup>th</sup> 2015.
- [Mitsubishi] Mitsubishi Rayon Co., Ltd. Company Website <https://www.mrc.co.jp/english/products/plastics/>. Accessed January 12<sup>th</sup> 2015.
- [Moran 1950] Moran, P. A. P., *Notes on Continuous Stochastic Phenomena*, Biometrika 37 (1): 17–23. doi:10.2307/2332142 (1950).
- [NASA 2000] NASA's International Space Station website: <http://spaceflight.nasa.gov/spaceneeds/factsheets/pdfs/servmod.pdf> Accessed February 17<sup>th</sup> 2015.
- [NASA 2009] NASA's Space Station Imagery website: <http://spaceflight.nasa.gov/gallery/images/station/crew-20/html/iss020e031541.html> Accessed February 17<sup>th</sup> 2015.

- [NOAA & NASA 1976] NOAA, NASA *US Standard Atmosphere 1976*, U.S. Government Printing Office, Washington, D.C Retrieved from <http://www.pdas.com/atmos.html>.
- [Nagano et al. 2004] M. Nagano, K. Kobayakawa, N. Sakaki, K. Ando, *New measurement on photon yields from air and the application to the energy estimation of primary cosmic rays*, *Astroparticle Physics* 22 235-248 (2004).
- [Naumov 2003] Naumov, Dmitri, *SLAST Shower Initiated Light Attenuated to the Space Telescope. Manual*, Available online at [theor.jinr.ru/~naumov/professional/manual.pdf](http://theor.jinr.ru/~naumov/professional/manual.pdf). Accessed April 2015.
- [Nelson et al. 1985] Nelson, W. Ralph ; Hirayama, H. ; Rogers, David W.O. *The Egs4 Code System* SLAC-0265, (1985).
- [Nerling et al. 2006] F. Nerling, J. Blümer, R. Engel, M. Risse, *Universality of electron distributions in high-energy air showers - description of Cherenkov light production*, *Astroparticle Physics* 24:421-437,(2006).
- [Ostapchenko 2011] S. Ostapchenko, *Monte Carlo treatment of hadronic interactions in enhanced Pomeron scheme: QGSJET-II model* *Phys. Rev. D* 83, 014018 (2011).
- [Ostapchenko 2014] S. Ostapchenko, *LHC data on inelastic diffraction and uncertainties in the predictions for longitudinal extensive air shower development*, *S. Ostapchenko Physical Review D* 89, 074009 (2014).
- [Pacini 1912] D. Pacini, *La radiazione penetrante alla superficie ed in seno alle acque*, *Nuovo Cim.*, VI/3 93 (1912).
- [Palomares-Ruiz et al. 2006] Sergio Palomares-Ruiz, Andrei Irimia and Thomas J. Weiler, *Acceptances for Space-Based and Ground-Based Fluorescence Detectors, and Inference of the Neutrino-Nucleon Cross-Section above  $10^{19}$  eV*, *Phys.Rev.D*73:083003 (2006).
- [Panasyuk et al. 2014] M I Panasyuk, M Casolino, G K Garipov, T Ebisuzaki, P Gorodetzky, B A Khrenov, P A Klimov, V S Morozenko, N Sakaki, O A Saprykin, S A Sharakin, Y Takizawa, L G Tkachev, I V Yashin and M Yu Zotov, *The current status of orbital experiments for UHECR studies*, Summary of the rapporteur talk given by M.I. Panasyuk at ECRS-2014; to be published in the proceedings. Available online at: [arXiv:1501.06368](http://arxiv.org/abs/1501.06368)
- [PAO 2007] The Pierre Auger Collaboration, *Correlation of the Highest-Energy Cosmic Rays with Nearby Extragalactic Objects*, *Science* 9 November 2007: Vol. 318 no. 5852 pp. 938-943 (2007).
- [PAO 2010a] The Pierre Auger Collaboration, *Update on the correlation of the highest energy cosmic rays with nearby extragalactic matter*, *Astroparticle Physics* Volume 34, Issue 5 Pages 314–326 (2010).
- [PAO 2010b] The Pierre Auger Collaboration, *Measurement of the energy spectrum of cosmic rays above  $10^{18}$  eV using the Pierre Auger Observatory*, *Physics Letters B* 685:239-246,(2010).
- [PAO 2013a] The Pierre Auger Collaboration, *Anisotropy studies with the Pierre Auger Observatory*, *EPJ Web of Conferences* 53, 04011 (2013).
- [PAO 2013b] The Pierre Auger Collaboration, *Interpretation of the depths of maximum of extensive air showers measured by the Pierre Auger Observatory*, *Journal of Cosmology and Astroparticle Physics* Volume 2013 JCAP02(2013)026 (2013).
- [PAO 2013c] The Pierre Auger Collaboration, *Ultrahigh Energy Neutrinos at the Pierre Auger Observatory*, *Advances in High Energy Physics* 2013 708680 (2013).
- [PAO 2013c] The Pierre Auger Collaboration, *Ultrahigh Energy Neutrinos at the Pierre Auger Observatory*, *Advances in High Energy Physics*, vol. 2013 DOI:10.1155/2013/708680 (2013).
- [PAO 2015] The Pierre Auger Collaboration, *Searches for Anisotropies in the Arrival Directions of the Highest Energy Cosmic Rays Detected by the Pierre Auger Observatory*, *The Astrophysical Journal*, 804, 15 (2015).
- [PAO Event display] <http://www.auger.org/> Accessed August 26<sup>th</sup> 2014.
- [PAO-hybrid 2012] The Pierre Auger Observatory, *Measurement of the cosmic ray energy spectrum using hybrid events of the Pierre Auger Observatory*, *Eur. Phys. J. Plus* 127: 87 (2012).
- [Paschos 2007] E. A. Paschos, *Electroweak theory* Cambridge Univ. Press, 2007
- [Pauli 1930] Pauli, W., *Open letter to the group of radioactive people at the Gauverein meeting in Tübingen*, Accessed digitally via <http://microboone-docdb.fnal.gov/cgi-bin/RetrieveFile?docid=953;filename=pauliletter1930.pdf> on 27<sup>th</sup> November 2014.

- [Pierog & Heck 2011] D. Heck and T. Pierog, *Extensive Air Shower Simulation with CORSIKA: A User's Guide Version 6.980*, Karlsruhe Institut für Technologie, (2011).
- [Pierog 2013] Pierog, T., *LHC results and High Energy Cosmic Ray Interaction Models*, Journal of Physics: Conference Series 409 012008 (2013).
- [Ritter 1803] Ritter, J. W., *Versuche über das Sonnenlicht*, Ann. Phys., 12: 409–415. doi: 10.1002/andp.18030121205 (1803).
- [Rossi 1930a] Rossi, B., *Method of Registering Multiple Simultaneous Im pulses of Several Geiger's Counters*, Nature 125 636 (1930).
- [Rodríguez Frías et al. 2013] M.D. Rodríguez Frías, J.A. Morales de los Ríos, L. del Peral, G. Sáez-Cano, K. Shinozaki, H. Prieto, J. H-Carretero, M.D. Sabau, T. Belenguer, C. González Alvarado, M. Sanz Palomino, S. Briz, A.J. de Castro, I. Fernández, F. Cortés, F. López, J. Licandro, M. Reyes, E. Joven, K. Tsuno, T. Ogawa, O. Catalano, A. Anzalone6, F. Isgró, L. Valore, F. Guarino, M. Casolino, A. Cellino, M. Di Martino, M. Bertaina, R. Cremonini, F. Gola, F. Garino, B. Keilhauer A. Neronov and S. Wada for the JEM-EUSO Collaboration, *The Atmospheric Monitoring System of the JEM-EUSO space mission*, EPJ Web of Conferences 53, 10005 (2013).
- [Rossi 1930] Rossi, Bruno, *On the Magnetic Deflection of Cosmic Rays*, Physical Review 36 (3) (1930).
- [Rossi 1933] Rossi, Bruno, *Directional measurement on the cosmic rays near the geomagnetic equator*, Physical Review 45 (3) (1933).
- [Rossi 1959] B. Rossi, *High Energy Cosmic Rays*, Scientific American Volume 201, Issue 5 (1959).
- [Rouillé d'Orfeuil et al. 2014] Rouillé d'Orfeuil, B., Allard, D., Lachaud, C., Parizot, E., Blaksley, C., Nagataki, S., *Anisotropy expectations for ultra-high-energy cosmic rays with future high statistics experiments*, Astronomy & Astrophysics 567, A81 (2014).
- [Ryu et al. 1998] D. Ryu, H. Kang, and P.L. Biermann, *Cosmic magnetic fields in large scale filaments and sheets*, Astronomie and Astrophysics 335, 19 (1998).
- [Santangelo et al. 2013] A. Santangelo, P. Picozza, T. Ebisuzaki, for the JEM-EUSO Collaboration, *Status of the JEM-EUSO Mission* Proceedings of the 33<sup>rd</sup> International Cosmic Ray Conference, Rio de Janeiro (2013).
- [Schuster 2014] P. M. Schuster, *The scientific life of Victor Franz (Francis) Hess (June 24, 1883–December 17, 1964)* Astroparticle Physics 53 33–49 (2014).
- [Sciutto 1997] S. J. Sciutto, *AIRES: A minimum document*, Auger technical note GAP-97-029 (1997).
- [Sig et al. 2004] Günter Sigl, Francesco Miniati and Torsten A. Enßlin, *Ultrahigh energy cosmic ray probes of large scale structure and magnetic fields*, Physical Review D 70, 043007 (2004).
- [Sjöstrand et al. 2006] Torbjörn Sjöstrand, Stephen Mrenna, Peter Skands, *PYTHIA 6.4 Physics and Manual*, Journal of High Energy Physics 5 Vol 26 DOI: 10.1088/1126-6708/2006/05/026 (2006).
- [Smida 2014] Ramdomir Smida personal webpage. Image available at [http://www-hep2.fzu.cz/~smida/Auger-figures/Los\\_leones.jpg](http://www-hep2.fzu.cz/~smida/Auger-figures/Los_leones.jpg). Accessed 10<sup>th</sup> November 2014.
- [SpaceX] Space Exploration Technologies Corporation, official website <http://www.spacex.com/>. Accessed February 18<sup>th</sup> 2015.
- [Spiering 2012] Christian Spiering, *Towards high-energy neutrino astronomy*, Eur. Phys. J. H 37, 515–565 (2012)
- [Stanev 2010] Stanev, T., *High Energy Cosmic Rays*, Springer, Berlin, Heidelberg, New York, second edition, 2010.
- [Stecker 2005] Stecker, F.W., *A Note on High Energy Neutrinos from AGN Cores*, Physical Review D 72:107301, (2005).
- [Supanitsky & Guzmán 2013] Supanitsky, D., Guzman A., for the JEM-EUSO Collaboration, *Ultra High Energy Photons and Neutrinos with JEM-EUSO*, Special Issue of Experimental Astronomy (accepted for publication) (2013).
- [Supanitsky Medina-Tanco 2011] A D Supanitsky, G Medina-Tanco, et al. for the JEM-EUSO Collaboration, *Development of neutrino initiated cascades at mid and high altitudes in the atmosphere*, 32nd Int. Cosmic Ray Conf. Proc. Beijing (2011).

- [Taddei 2004] Taddei, E., *Studio di algoritmi per la ricostruzione della direzione degli sciami atmosferici in EUSO*, Master's thesis, Universita Degli Studi Di Firenze, (2004).
- [Tinyakov 2014] Tinyakov, Peter for the Telescope Array Collaboration, *Latest results from the telescope array*, Nuclear Instruments and Methods in Physics Research A 742 29–34 (2014).
- [Tokuno et al. 2012] H. Tokuno, Y. Tameda, M. Takeda, K. Kadota, D. Ikeda, M. Chikawa, T. Fujii, M. Fukushima, K. Honda, N. Inoue, F. Kakimoto, S. Kawana, E. Kido, J. N. Matthews, T. Nonaka, S. Ogio, T. Okuda, S. Ozawa, H. Sagawa, N. Sakurai, T. Shibata, A. Taketa, S. B. Thomas, T. Tomida, Y. Tsunesada, S. Udo, T. Abu-zayyad, R. Aida, M. Allen, R. Anderson, R. Azuma, E. Barcikowski, J.W. Belz, D.R. Bergman, S.A. Blake, R. Cady, B.G. Cheon, J. Chiba, E.J. Cho, W.R. Cho, H. Fujii, T. Fukuda, D. Gorbunov, W. Hanlon, K. Hayashi, Y. Hayashi, N. Hayashida, K. Hibino, K. Hiyama, T. Iguchi, K. Ikuta, T. Ishii, R. Ishimori, D. Ivanov, S. Iwamoto, C.C.H. Jui, O. Kalashev, T. Kanbe, K. Kasahara, H. Kawai, S. Kawakami, H.B. Kim, H.K. Kim, J.H. Kim, J.H. Kim, K. Kitamoto, K. Kobayashi, Y. Kobayashi, Y. Kondo, K. Kuramoto, V. Kuzmin, Y.J. Kwon, S.I. Lim, S. Machida, K. Martens, J. Martineau, T. Matsuda, T. Matsuura, T. Matsuyama, I. Myers, M. Minamino, K. Miyata, H. Miyauchi, Y. Murano, T. Nakamura, S.W. Nam, M. Ohnishi, H. Ohoka, K. Oki, D. Oku, A. Oshima, I.H. Park, M.S. Pshirkov, D. Rodriguez, S.Y. Roh, G. Rubtsov, D. Ryu, A.L. Sampson, L.M. Scott, P.D. Shah, F. Shibata, H. Shimodaira, B.K. Shin, J.I. Shin, T. Shirahama, J.D. Smith, P. Sokolsky, T.J. Sonley, R.W. Springer, B.T. Stokes, S.R. Stratton, T. Stroman, S. Suzuki, Y. Takahashi, M. Takita, H. Tanaka, K. Tanaka, M. Tanaka, G.B. Thomson, P. Tinyakov, I. Tkachev, S. Troitsky, K. Tsutsumi, Y. Tsuyuguchi, Y. Uchihori, H. Ukai, G. Vasiloff, Y. Wada, T. Wong, M. Wood, Y. Yamakawa, H. Yamaoka, K. Yamazaki, J. Yang, S. Yoshida, H. Yoshii, R. Zollinger, Z. Zundel, *New air fluorescence detectors employed in the Telescope Array experiment*, Nuclear Instruments and Methods in Physics Research Section A: Volume 676, , Pages 54–65 (2012).
- [Toscano et al. 2014] Toscano, S. et al. for the JEM-EUSO collaboration, *The atmospheric monitoring system of the JEM-EUSO instrument*, Experimental Astronomy (2014).
- [Von Ballmoos et al. 2015] Peter Von Ballmoos for the JEM-EUOS collaboration, *The EUSO-Balloon mission*, 34th Int. Cosmic Ray Conf. Proc. The Hague (2015).
- [Waxman & Bahcall 1998] Waxman, E. & Bahcall, J.N. , *High Energy Neutrinos from Astrophysical Sources: An Upper Bound*, Physical Review D, Volume 59, 023002 (1998).
- [Waxman & Bahcall 2001] Bahcall J , Waxman E, *High energy astrophysical neutrinos: The upper bound is robust* Physical Review D, Volume 64, 023002 (2001).
- [Wilson 1978] Robert W. Wilson, *The Cosmic Microwave Background Radiation*, Nobel Lecture, 8 December, 1978. Accessed online March 3<sup>rd</sup> 2015. [http://www.nobelprize.org/nobel\\_prizes/physics/laureates/1978/](http://www.nobelprize.org/nobel_prizes/physics/laureates/1978/)
- [Wulf 1909] Wulf,T., *On the radiation of high penetrating power that exists in the atmosphere*, Phys. Zeit. 1 152-15 (1909).
- [Yanasak et al. 2001] N. E. Yanasak , M. E. Wiedenbeck, R. A. Mewaldt, A. J. Davis, A. C. Cummings, J. S. George, R. A. Leske, E. C. Stone, E. R. Christian, T. T. von Rosenvinge, W. R. Binns, P. L. Hink, M. H. Israel, *Measurement of the Secondary Radionuclides  $^{10}\text{Be}$ ,  $^{26}\text{Al}$ ,  $^{36}\text{Cl}$ ,  $^{54}\text{Mn}$ , and  $^{14}\text{C}$  and Implications for the Galactic Cosmic-Ray Age*, The Astrophysical Journal Volume 563 Number 2 doi:10.1086/323842 (2001).
- [Yoshida et al. 1995] S. Yoshida et al. , *The cosmic ray energy spectrum above  $3 \times 10^{18}$  eV measured by the Akeno Giant Air Shower Array*, Astroparticle Physics 3 105-123, (1995).
- [Zatsepin & Kuz'min 1966] G. T. Zatsepin and V. A. Kuz'min, *Upper Limit of the Spectrum of Cosmic Rays*, Soviet Journal of Experimental And Theoretical Physics Letters, Volume 4 78, (1966).



# LIST OF FIGURES

|      |  |    |
|------|--|----|
| 1.1  | .....  | 4  |
| 1.2  | Ionizing radiation measurements by Kohlhörster and Hess. Reproduced from [Hoffmann 2014].  | 5  |
| 1.3  | The particle channel in astronomy. The filled curves represent the different components of the diffuse background spectrum of electromagnetic radiation [Betherrin 2011]. For comparison the flux of cosmic rays is also plotted. The Extreme Energy Cosmic Rays regime begins at the smallest shaded region, i.e. at energies above 50 EeV ( $5 \times 10^{19}$ eV). Figure modified from [Betherrin 2011].   | 7  |
| 1.4  | The energy spectrum of cosmic rays. Reproduced from [Blümer et al. 2009].  | 9  |
| 1.5  | Deflection of charged particles (protons) in the galactic magnetic field. In blue is shown the undeflected injection sites at the galactic halo. In red and green the arrival positions at $\sim 10$ EeV and $\sim 38$ EeV respectively [Guzmán 2009].   | 10 |
| 1.6  | Hillas diagram. Objects above the lines are capable of trapping Fe with $10^{20}$ eV (red), and protons with $E = 10^{20}$ eV (blue). Reproduced from [Kotera & Olinto 2011].  | 11 |
| 1.7  | Proton energy loss for photo pion production (purple), pair production (red) and due to the cosmological expansion (blue). Reproduced from [Kotera & Olinto 2011].   | 13 |
| 1.8  | Scheme of the development of an EAS. At ground level the most abundant component is the electromagnetic component, followed by the muonic one. Figure reproduced from [Letessier & Stanev 2011].   | 14 |
| 1.9  | The “universal” neutrino background. In the energy range where this works concentrate, we can see that there is already an expected contribution from EECR neutrinos as a by product of the GZK effect. Reproduced from [Spiering 2012].   | 19 |
| 1.10 | A summary of models of expected cosmological neutrino flux (see text). Data taken from [Aartsen et al. 2013], [Engel et al. 2001], [Kotera et al. 2010] and [Ahlers 2010].   | 22 |
| 1.11 | Charged current (left) and neutral (right) current interactions.   | 22 |
| 1.12 | The main components of the PAO. Upper image: one of the $\sim 1660$ water cherenkov tanks. Bottom left: The positions of the SD detectors in the final array configuration overlaid on a map of the Malargüe area. The FD’s field of view are indicated as shaded semicircles. Reproduced from [Abraham, et al. 2010]. Bottom right: the FD building located at Los Leones. Each of these buildings contains 6 UV-telescopes. Reproduced from [Smida 2014].  | 24 |
| 1.13 | The main components of the Telescope Array experiment. <i>Upper image:</i> one of the 507 scintillation counters. Overlaid on the picture is a diagram of the inner structure of the scintillator (white) separated by metal plates. Modified from [Abu-Zayyad et al. 2012]. <i>Bottom left:</i> The layout on ground of the TA experiment (distance between counters is 1.2 km) Reproduced from [Abu-Zayyad et al. 2012]. <i>Bottom right:</i> a sketch of new (not HiRes refurbished) FD designed for the TA experiment [Tokuno et al. 2012].  | 25 |
| 1.14 | <i>Left:</i> The measured energy spectra from HiRes and PAO. Reproduced from [PAO 2010b]. <i>Right:</i> Composition results from TA and PAO. Data taken from [Tinyakov 2014] [PAO 2013b] [Pierog 2013].  | 27 |
| 1.15 | Arrival directions in an Aitoff-Hammer projection of the sky in galactic coordinates, for HiRes a) and PAO b). Also plotted are the positions of nearby AGNs in the Veron catalogue. To the left: AGN are shown in black, uncorrelated data and correlated data is shown in blue and red boxes correspondingly. A lighter shadow intensity corresponds to a larger relative exposure. To the right 69 CRs with energy $E \geq 55 EeV$ detected by PAO are presented as black dots, while circles of radius $3.1^\circ$ are centered at the positions of the aforesaid AGN. In this figure a darker blue indicates a larger relative exposure. Figures a) and b) reproduced from [HiRes 2011] and [PAO 2010a] respectively. | 28 |
| 1.16 | <i>Upper panel:</i> An artistic depiction of the IceCube experiment. Reproduced from [Halzen & Gaisser 2014]. <i>Lower panel:</i> Recent constrains to the muon neutrino flux from the ICECUBE experiment compared to proposed models for cosmogenic UHE- $\nu$ [Aartsen et al. 2013].   | 30 |
| 2.1  | Artistic depiction of EUSO’s concept of operation. UV light originated by the EECR’s EAS, is observed from space. This allows for an unprecedented instantaneous exposure. Background image NASA   | 34 |

|      |   |    |
|------|---|----|
| 2.2  | Fraction of realizations which yield anisotropic results with significance larger than the abscissa for a) <b>4 EeV</b> model and b) <b>pure-Fe</b> , assuming the EUSO exposure. Different colors indicate different number of events above a certain energy. In blue are the results using the same realizations but with PAO exposure (and statistics). Reproduced from [Rouillé d'Orfeuil et al. 2014]. . . . .                           | 36 |
| 2.3  | a) The sky distribution of PAO events with $E > 52$ EeV (black dots) superimposed on top of the 2MRS objects (blue fuzzy circles). The blue solid line corresponds to the Super-Galactic Plane, and the dashed line is the field-of-view limit for the PAO. b) The values of $f_{min}$ and $P$ (see text) as a function of the maximum distance $D$ to the galaxies in the 2MRS catalog. Both figures are reproduced from [PAO 2015]. . . . . | 37 |
| 2.4  | Artistic depiction of JEM-EUSO's operational principle. The "fluorescence signal" (UV light) produced by the EAS is captured by a telescope mounted on the ISS. Reproduced from [JEM-EUSO 2010] and [Adams et al. 2013a]. . . . .   | 38 |
| 2.5  | Modifications to the JEM-EUSO nadir exposure by tilting the instrument at $20^\circ$ (red), $30^\circ$ (blue) and $40^\circ$ (green). Reproduced from [Fenu 2013]. . . . .  | 39 |
| 2.6  | Artistic depiction of JEM-EUSO summarizing the optics and focal surface layout. Notice that the original cylindrically symmetrical concept of the telescope is illustrated. In order to fit the telescope into the Japanese transfer vehicle, the shape of the telescope had to be modified (see Fig. 2.4). Reproduced from [JEM-EUSO 2010] . . . . .   | 41 |
| 2.7  | Comparison of PMMA's and Cytop's transmittance in the near UV/ visible. Data taken from [Asahi Glass Co, Ltd.]. . . . .   | 42 |
| 2.8  | Focal surface detector and its structure. Reproduced from [Kawasaki et al. 2011]. . . . .   | 43 |
| 2.9  | A diagram of the hierarchical scheme of the JEM-EUSO detector. Reproduced from [JEM-EUSO 2010].<br>44   |    |
| 2.10 | Atmospheric monitoring subsystem. Reproduced from [JEM-EUSO 2010]. . . . .  | 45 |
| 2.11 | <i>Upper panel:</i> a) A diagram showing the inner structure of the instrument Reproduced from [Dagoret & Mot 2014], and b) the EUSO-balloon gondola. Image credit Karine Mercier. <i>Lower panel:</i> EUSO-Balloon minutes before launch. Image credit Michael Wille. . . . .  | 48 |
| 2.12 | <i>Upper panel:</i> a) The Zvezda service module. Reproduced from [NASA 2000]. b) The nadir looking window that is foreseen to allocate the mini-EUSO experiment. Reproduced from [NASA 2009]. <i>Lower panel:</i> An schematic representation of the Mini-EUSO instrument. Reproduced from [Mini-EUSO 2015]. . . . .   | 49 |
| 2.13 | The Dragon spaceship berthed to the International Space Station. Image reproduced from [Dragon].  | 50 |
| 2.14 | The reallocation of the FS elements in the SpaceX EUSO design. In blue are shown the positions of the MAPMT superimposed on the outline of the FS for the HTV configuration. It can be seen that the newer design is more symmetric whilst conserving the monitored area. . . . .   | 51 |
| 2.15 | a) KLYPVE segmented mirror-concentrator and photo-detector. Viewed from the front side and viewed from the rear side. b) The foreseen docking spot on MRM1 on-board the Russian segment for the ISS. Both images reproduced from [Panasyuk et al. 2014]. . . . .  | 53 |
| 3.1  | An illustration of the concepts involved in the simulations with ESAF. . . . .  | 57 |
| 3.2  | The general structure of <i>Simu</i> as included in ESAF. . . . .   | 58 |
| 3.3  | <i>Left:</i> The (integrated) track of the moving spot produced by the fluorescence photons on the FS. <i>Right:</i> The <i>light curve</i> of the EAS's track on the left. This simulated example EAS has a proton primary with $E = 10^{20}$ eV and $\Theta = 60^\circ$ . . . . .   | 62 |
| 3.4  | The general structure of <i>Reco</i> as included in ESAF. *Measurements are foreseen to be interchangeable with the simulated data. . . . .   | 63 |
| 3.5  | The definition of the <i>MES</i> (see text). In red is also shown the definition of $\hat{\Omega}$ : the unitary vector parallel that characterizes the EAS's arrival direction. $\hat{\Omega}$ point in the opposite direction of the EAS's propagation. . . . .   | 65 |
| 3.6  | The Track Detector Plane: defined by the shower axis and the center of the detector. Its normal vector, $\hat{V}$ , is also shown. . . . .  | 67 |
| 3.7  | Geometrical illustration of the triangles referred by Eqs. 3.8, 3.7, and 3.9. . . . .   | 68 |
| 3.8  | A flow diagram representation of the <i>PMTToShowerReco</i> module. Modified from [Fenu 2013]. . .  | 74 |

- 4.1 *Left:* The (integrated) track of the *signal* photons **neglecting** the background. *Right:* Same as left but with the background included. The job of the pattern recognition is to extract the image on the left from the image on the right. . . . . 77
- 4.2 An example of the *pixel-trace* from a single pixel. On the *X*-axis we see the time in units of GTUs and in the *Y*-axis the photo electron counts. The highlighted counts are coming from the EAS. All other counts are background photons. . . . . 78
- 4.3 Illustration of the excess  $exc(n_1 + 1)$  added to the new sum  $Sum(n_1)$  when increasing the time window from  $\Delta t_{old}$  to  $\Delta t_{new}$ . (see text). . . . . 80
- 4.4 An illustration of *PWISE-R* technique. Here we show the points in the  $xt$  plane. The solid line is the result of the linear fit performed after the *PWISE* as a first stage (see text). . . . . 82
- 4.5 An illustration of *PWISE-R* technique. Here we show the points in the  $yt$  plane. The solid line is the result of the linear fit performed after the *PWISE* as a first stage (see text). . . . . 83
- 4.6 Energy deposition as a function of slant depth for a typical shower simulated using CONEX. Energy is  $10^{20}$  eV and zenith angle is  $60^\circ$ . . . . . 87
- 4.7 Diagram of the geometrical characteristics on the plane containing the EAS's track and the center of the Earth. The shower track (in red) is supposed to impact on the Earth's surface. Remember that the EAS's propagation is in the  $-\hat{\Omega}$  direction. . . . . 90
- 4.8 Diagram of the geometrical characteristics on the plane containing the EAS's track and the center of the Earth. The shower track (in red) has no impact point but rather a local height of maximum approximation  $h_{loc}$ . . . . . 91
- 4.9 Diagram of the relevant geometrical characteristics for the calculation of  $\zeta_{max}$  (see text). . . . . 92
- 4.10 Inheritance diagram for the *EventGenerator* class. The *ConexFileShowerGenerator* does not generate a new CONEX-simulated shower, but rather reads a CONEX output file and introduces the EAS into ESAF. . . . . 93
- 4.11 Our results for SLAST protons, as presented at [Guzmán, Mernik et al. 2014]. Here only *PWISE* was used as pattern recognition. . . . . 96
- 4.12 The normalized distribution of the reconstruction's error for SLAST proton showers at  $10^{20}$  eV (results presented in [Guzmán, Mernik et al. 2014]). In red the accumulated distribution is shown to illustrate how to calculate  $\gamma_{68}$ . . . . . 97
- 4.13 The longitudinal profiles of EAS initiated by protons and iron nuclei. For both primaries we show a subsample of 100 showers with an energy of  $10^{20}$  eV and  $\Theta = 60^\circ$ . The greater intrinsic fluctuation in proton initiated EASs can be clearly appreciated. . . . . 97
- 4.14 The angular resolution for proton and iron primaries using the *PWISE-R* technique and CONEX simulated showers with  $E = 5 \times 10^{19}$  eV. Results with the HTV configuration for protons at  $10^{20}$  eV are shown for comparison [Guzmán, Mernik et al. 2014]. . . . . 98
- 4.15 The angular resolution for proton and iron primaries using the *PWISE-R* technique and CONEX simulated showers with  $E = 10^{20}$  eV. Results with the HTV configuration for protons at  $10^{20}$  eV are shown for comparison [Guzmán, Mernik et al. 2014]. . . . . 99
- 4.16 A comparison of the longitudinal profiles of EAS initiated by protons and photons( $\gamma$ ). For both primaries we show a subsample of 100 showers with an energy of  $10^{20}$  eV and  $\Theta = 60^\circ$ . The abrupt end of the deeply penetrating photon EAS at  $\sim 2000$  g  $cm^{-2}$  marks the shower front reaching the ground. . . . . 100
- 4.17 The angular resolution for photon primaries. The apparent improvement upon hadronic primaries comes to the expense of losing events (non-triggering). Shown are simulated showers with  $E = 10^{20}$  eV. Results with the HTV configuration for protons at  $10^{20}$  eV are shown for comparison [Guzmán, Mernik et al. 2014]. . . . . 100
- 4.18 *Upper panel:* A scatter plot the distribution at the FS of the error in the angular reconstruction, primaries are protons with  $10^{20}$  eV. *Bottom panel:* The angular resolution of the same sample, restricting the results to showers with an impact position within 150 km from the center of the FoV. 102
- 4.19 *Upper panel:* A scatter plot showing the correlation between the number of selected points available for the *TrackDirection2* module and the error in the angular reconstruction. The energy for this data is  $10^{20}$  eV, and the particles simulated were all protons (CONEX). *Bottom panel:* The angular resolution obtained applying a quality cut in the **number of points selected**. For this plots only reconstructed showers with more than 20 points are shown. . . . . 103

|      |  |     |
|------|--|-----|
| 4.20 | An example of the reconstruction of the longitudinal profile of a proton-initiated EAS with an energy of $10^{20}$ eV and $\Theta = 60^\circ$ . The points represent the reconstructed longitudinal profile with the associated uncertainty. The solid line is the originally simulated EAS. . . . .   | 104 |
| 4.21 | The energy-reconstruction error distribution for the protons in our <i>CONEX-benchmark</i> data sample. . . . .  | 105 |
| 4.22 | The energy-reconstruction error distribution for the iron nuclei in our <i>CONEX-benchmark</i> data sample. . . . .  | 106 |
| 4.23 | The energy-reconstruction error distribution for the photons in our <i>CONEX-benchmark</i> data sample. . . . .  | 106 |
| 4.24 | The $\Delta X_{max}$ distribution for the protons in our <i>CONEX-benchmark</i> data sample. . . . .   | 108 |
| 4.25 | The $\Delta X_{max}$ distribution for the iron nuclei in our <i>CONEX-benchmark</i> data sample. . . . .   | 108 |
| 4.26 | The $\Delta X_{max}$ distribution for the photons in our <i>CONEX-benchmark</i> data sample. . . . .   | 109 |
| 5.1  | Comparison between the WB limit [Waxman & Bahcall 1998], PAO neutrino upper limit [PAO 2013c], and JEM-EUSO's baryon sensitivity (the latter assuming a constant flux as in Eq.5.18), we also show the differential sensitivity. In all cases we used fiducial value of $S_0 \sim 1.3 \times 10^{15}$ cm <sup>2</sup> . . . . .  | 120 |
| 5.2  | Comparison between the WB limit [Waxman & Bahcall 1998], PAO neutrino upper limit [PAO 2013c], and JEM-EUSO's baryon sensitivity latter assuming a power law flux. We also show the JEM-EUSO's differential sensitivity (see Eq. 5.15). . . . .  | 121 |
| 5.3  | The ratio $\frac{P_p(X)}{P_\nu(X)}$ of the proton's probability of interaction to that of the neutrino, as a function of slant depth. Also shown are the integrated slant depth's from the top of the atmosphere till the center of the FOV, for different zenith angles $\Theta$ . . . . .  | 122 |
| 5.4  | <i>Left:</i> Longitudinal profiles of horizontal ( $\Theta = 0^\circ$ ) neutrino showers. All showers were injected at the center of the FOV ( $X_0 = 36500$ gcm <sup>-2</sup> ) with an energy of $10^{20}$ eV. <i>Right:</i> Distribution of the position of the first peak (in grammage) for electron and tau neutrino showers whose first interaction point is at sea level and on the vertical axis of JEM-EUSO in Nadir mode. The neutrino energy is $E = 10^{20}$ eV. The histograms are normalized to unity. Reproduced from [Supanitsky & Guzmán 2013]. . . . . | 123 |
| 5.5  | The scaling factor $f_{scale}$ as a function of $\Theta$ and $\delta X$ . . . . .  | 125 |
| 5.6  | The scaling factor $f_{scale}$ as a function of $\Theta$ for fixed $\delta X$ . . . . .  | 125 |
| 5.7  | Comparison between reported values of the sensitivity for proton and the re-scaled sensitivity(see text). In this case $f_{scale} = 6.77 \times 10^{-6}$ . . . . .   | 126 |
| 5.8  | Triggering efficiencies for neutrino showers with their impact points (cores), coinciding with the center of the FOV at ground. In all cases $\Theta = 80^\circ$ . Reproduced from [Supanitsky & Guzmán 2013]. . . . .   | 126 |
| 5.9  | Comparison between reported values of the sensitivity for proton and the re-scaled sensitivity(see text) at a tilting angle of $40^\circ$ . In this case $f_{scale} = 6.77 \times 10^{-6}$ . . . . .   | 127 |
| 5.10 | A comparison of the longitudinal profiles of EAS initiated by protons and neutrinos( $\nu$ ). For both primaries we show a subsample of 100 showers with an energy of $10^{20}$ eV and $\Theta \sim 60^\circ$ . In this particular example the neutrino simulations had a minimum interaction depth above $450$ g cm <sup>-2</sup> . . . . .   | 128 |
| 5.11 | The neutrino exposure as a function of energy (following Eq. 5.31). Also shown is the baryon exposure (in blue) [Adams et al. 2013a]. . . . .  | 131 |
| 5.12 | EUSO's neutrino sensitivity calculated with the exposure shown in Fig. 5.11. The shaded region represents an improved sensitivity in the case that the neutrino cross section increases as discussed in [Kusenko et al. 2002]. Also shown is the baryon sensitivity (in blue) [Adams et al. 2013a]. . . . .  | 131 |
| 5.13 | EUSO's angular reconstruction for neutrino initiated EAS. Also shown are the values for proton primaries as published in [Guzmán, Mernik et al. 2014]. . . . .   | 132 |
| 5.14 | JEM-EUSO's energy reconstruction error for neutrino initiated EAS using the output of the <i>PmtToShower Module</i> . See text to understand the mismatch between reconstructed and simulated energies. All energies from the <i>Neutrino-Benchmark</i> were used to produce this plot. . . . .  | 133 |
| 5.15 | Some example of the difference between simulated and reconstructed points of the longitudinal profile. In the upper panel we see some examples with a relatively strong LPM effect where a shower maximum was not completely evident. And in the lower panel we see two examples of a more <i>regular</i> longitudinal profiles. All neutrinos in this figure were simulated with $E = 10^{20}$ eV. . . . .  | 134 |
| 5.16 | EUSO's energy reconstruction error for neutrino initiated EAS using a simple integration of the longitudinal profiles (see text). All energies from the <i>Neutrino-Benchmark</i> were used to produce this plot. The peaks in the distribution are artifacts introduced by the <i>PmtToShower Module</i> . . . . .  | 135 |

|      |  |     |
|------|--|-----|
| 6.1  | Comparison between the case (i) designed (red) and (ii) manufactured (green) optical responses. We show the average Energicled Energy as a distance from the center of the light spot. The blue line identifies the pixel size. . . . .  | 139 |
| 6.2  | . . . . .  | 140 |
| 6.3  | Graphical example of our selection of $W(r)$ . Pixel centers with blue dots. . . . .   | 142 |
| 6.4  | The (integrated) appearance of the manufactured PDM for different lighting conditions on top of flat a poissonian background with mean $\mu = 2.6 \frac{\text{pc}}{\text{GTU}}$ . The image on the left is the pure flat background with no other source. It has a different scale on the color axis to enhance the fluctuations and the border effect, else the image would be completely blue, as the images on the right. . . . . | 143 |
| 6.5  | Comparison of $g(r, dr = r(\sqrt{2} - 1))$ , $\mathcal{I}(r)$ and $\mathcal{C}(r)$ between the case (i) designed and (ii) manufactured optical responses, in red and green respectively. In blue we the Dirac's delta case. . . . .  | 143 |
| 6.6  | Zoom in for $g(r, dr = r(\sqrt{2} - 1))$ , and $\mathcal{I}(r)$ for the ideal light source . . . . .   | 144 |
| 6.7  | Comparison of $g(r, dr = r(\sqrt{2} - 1))$ , $\mathcal{I}(r)$ and $\mathcal{C}(r)$ between the case (i) designed and (ii) manufactured optical responses, in red and green respectively. In blue we the Dirac's delta case. . . . .  | 144 |
| 6.8  | Comparison of $g(r, dr = r(\sqrt{2} - 1))$ , $\mathcal{I}(r)$ and $\mathcal{C}(r)$ for a circle with 3 times higher background. . . . .  | 145 |
| 6.9  | Comparison of $g(r, dr = r(\sqrt{2} - 1))$ , $\mathcal{I}(r)$ and $\mathcal{C}(r)$ for a circle with 10 times higher background. . . . .   | 145 |
| 6.10 | Comparison of $g(r, dr = r(\sqrt{2} - 1))$ , $\mathcal{I}(r)$ and $\mathcal{C}(r)$ for a step function (in the X-axis) with 3 times higher background. . . . .   | 146 |
| 6.11 | Test with special regions with twice the average background.(a) corresponds to a step function, whereas (b)(c)(d) radius with different circles. . . . .   | 147 |
| 6.12 | The impact of the different scenarios shown in Fig.6.11 on our statistical tests. . . . .  | 148 |
| 6.13 | An aerial <i>night view</i> of the eastern area surrounding Timmins (taken from <i>Google-earth</i> ). Barely visible are the outlines of mayor water bodies in the region. For comparison EUSO-Balloon's Spot-On-Ground (SOG) is drawn left to the center of the image. . . . .   | 149 |
| 6.14 | A snapshot of the image on the PDM of a laser shot captured by the EUSO-Balloon on August 24, 2014. . . . .  | 150 |





# ACKNOWLEDGEMENTS

---

This work is the culmination of many years of hard work, effort and study. But the credit goes not only to me, but to every single person that has guided, supported, and taught me, both in Mexico and in Germany, throughout the whole adventure. I wish to express my deepest thanks to each and everyone of them, but specially to my mother who has devoted herself to her children: Gracias Mamá!

I would also like to thank my supervisors Gustavo Medina-Tanco and Andrea Santangelo for their irreplaceable contributions to my improvement and academic formation. Both of my supervisors have shared with me their passion for research and teaching, to pass-on what knowledge we have, and to profit from the collaborative work with fellow researchers. From my very first steps in research, Gustavo has been there supporting and providing invaluable guidance. Certainly without his input, my scientific and human development would be lacking. Since my arrival to the working group led by Andrea in Tübingen, I have bore witness to his passionate approach to knowledge in general, which permeates to each of the students that are fortunate enough to have him as a mentor. His constant support, trust, and experienced advice have driven the present work to a successful end.

I greatly benefited from working within the JEM-EUSO consortium. These colleagues offered not only their know-how, but also their kindness and friendship. It is the people like this, in the collaboration and outside of it, that make the scientific endeavor such an enjoyable privilege.

I see science as a collective effort, and as such, it benefits greatly from first hand interactions. Face to face conversations, discussions and presentations have a tremendous impact in the exchange of scientific ideas. Meeting researchers with different backgrounds and varying sets of skills has deepened my view of scientific activities and its potential. Therefore participation to symposiums, conferences, and workshops has played an essential role in my PhD education. To this end, I want also to acknowledge the support provided by the ESA Topical Team Activities, the DLR research grants, the Kepler Graduiertenkolleg funds and the University of Tübingen's ample support.

# Alejandro Daniel Guzmán Cabrera

## Curriculum Vitæ

|                |                            |
|----------------|----------------------------|
| Day of birth   | April 7 <sup>th</sup> 1984 |
| Citizenship    | Mexican                    |
| Marital Status | Single                     |

### Contact information

|   |  |
|---|--|
| 🏠 | Derendinger Str. 41, 72072 Tübingen, Germany |
| ☎ | +49 07071-29-75279                           |
| 📞 | +49 0176 30526788                            |
| ✉ | guzman@astro.uni-tuebingen.de                |

## EDUCATION

---

|                          |   |
|--------------------------|---|
| 2011 – Present           | <b>Doktor der Naturwissenschaften</b>   |
| Supervisor               | Andrea Santangelo   |
| Co-supervisor            | Gustavo Medina-Tanco  |
|                          | ASTROPARTICLE PHYSICS<br><i>Institut für Astronomie und Astrophysik<br/>Eberhard Karls Tübingen Universität</i> |
| Expected date of defense | October 2015  |
| 2009–2011                | <b>Maestro en Ciencias (Física)</b>   |
| Dissertation title:      | “Effects of atmospheric structures upon the detection of extensive air showers from UHECR”                      |
| Supervisor               | Gustavo Medina-Tanco  |
|                          | POSGRADUATE PROGRAM FOR SCIENCES<br><i>Universidad Nacional Autónoma de México (UNAM)</i>                       |
| 2008–2009                | <b>Tesis de Licenciatura</b>  |
| Dissertation title:      | “Mapping extragalactic objects in the Earth’s Sky using Charged Particles”                                      |
| Supervisor               | Gustavo Medina-Tanco  |
|                          | PHYSICS<br><i>UNAM</i>  |
| 2004 – 2008              | <b>Licenciatura en Física</b>   |
|                          | PHYSICS<br><i>UNAM</i>  |